

72<sup>nd</sup> ARFTG Microwave Measurement Symposium  
Fall 2008



Time Domain and Frequency  
Domain Measurement

December 9<sup>th</sup>-12<sup>th</sup> 2008  
Red Lion Hotel on the River – Jantzen Beach  
Portland, OR

*Dedicated to the memory of our friend and past ARFTG president  
Brian Pugh*



IEEE Catalog Number: CFP08ARG-CDR  
ISBN: 978-1-4244-2300-2  
Library of Congress: 2008902350



© 2008 IEEE. Personal use of this material is permitted. However, permission to reprint/republish this material for advertising or promotional purposes or for creating new collective works for resale or redistribution to servers or lists, or to reuse any copyrighted component of this work in other works must be obtained from the IEEE.

## **In memory of Brian Pugh**

Past ARFTG President and Executive Committee member



On November 14<sup>th</sup>, Brian Pugh and two colleagues at SiPort Inc. were fatally shot reportedly by a recently fired employee. Brian was caring, understanding, and a good listener – the last person you would think would be a target for this type of violence. Brian is survived by his wife Carol and two young children who were known to many of us as they traveled to multiple ARFTG meetings. We miss Brian and our thoughts and prayers turn to the welfare of his family.

## 72<sup>nd</sup> ARFTG Conference Organizers

*General Chair*

**Thomas Ruttan**

*Technical Program Chair*

**Leonard Hayden**

*Local Host*

**Evan Fledell**

## 71<sup>st</sup> ARFTG Conference Technical Program Committee

**Heidi Barnes**, Verigy

**Jon Martens**, Anritsu

**John Barr**, Verigy

**Nick Ridler**, NPL

**Dave Blackham**, Agilent

**Yves Rolain**, Vrije Universiteit Brussel

**Ali Boudiaf**, Focus Microwaves

**Dominique Schreurs**, KU Leuven

**Andrea Ferrero**, Politecnico di Torino

**Mohamed Sayed**, MMS

**Ron Ginley**, NIST

**Dima Smolyanski**, Tektronix

**Ed Godshalk**, Maxim

**Jean-Pierre Teyssier**, University of Limoges

**Brett Grossman**, Intel

**David Walker**, NIST

**Holger Heuermann**, FH Aachen

**Ken Wong**, Agilent

**Kooho Jung**, Cascade Microtech

**John Wood**, Freescale Semiconductor

**Tom Ruttan**, Intel

## 72<sup>nd</sup> ARFTG Conference Technical Session Chairs

*Session A: Time Domain Measurement*

**Brett Grossman**

*IF 1: Time Domain and Linear Network Measurement*

**Evan Fledell**

*Session B: Linear Network Measurement*

**Ken Wong**

*Session C: Non-Linear Network Analysis Applications*

**Jean-Pierre Yessier**

*IF 2: Non-Linear Network Measurement*

**Evan Fledell**

*Session D: Non-Linear Network Test Equipment*

**John Wood**

*Session E: Spectrum and Noise Measurement*

**Tom Ruttan**

*IF3: Calibration and Power Measurement*

**Evan Fledell**

*Session F: Calibration*

**Nick Ridler**

## The 2008 ARFTG Executive Committee (ExCom)

*President*

**Leonard Hayden**, Cascade Microtech

*Vice President and  
Electronic Communications*

**Ronald Ginley**, NIST

*Secretary and Publicity*

**Nick Ridler**, NPL

*Treasurer (Transition In)*

**David Walker**, NIST

*Treasurer (Transition Out)*

**Ken Wong**, Agilent Technologies

*Exhibits*

**Joseph L. Tauritz**, Universiteit Twente

*Workshops*

**Jean-Pierre Teyssier**, University of Limoges

*Nominations, Awards*

**John Wood**, Freescale Semiconductor

*Technical (Transition In)*

**Mohamed Sayed**, MMS

*Technical (Transition Out)*

**Thomas G. Ruttan**, Intel

*Membership*

**Raymond W. Tucker, Jr.**, Retired

*Education Chair*

**Dominique Schreurs**, K.U. Leuven

*Standards*

**Uwe Arz**, PTB

*MTT-S Liaison*

**Charles Wilker**, DuPont

*Publications*

**David Blackham**, Agilent Technologies

## Ex-Officio

*Executive Secretary*

**Jim L. Taylor**

*ARMMS Liaison*

**Roger Hopper**

# 72<sup>nd</sup> ARFTG Measurement Conference Agenda

Thursday December 11, 2008

## Session A: Time Domain Measurement

Brett Grossman, Session Chair

### **Gating Effects in Time Domain Transforms**

J. Dunsmore, Agilent Technologies, Inc., Santa Rosa, United States

### **Measurements of Characteristic Impedance of High Frequency Cables with Time Domain Reflectometry (TDR)**

L. Navarro, E. Mayevskiy, T. Chaire, Tyco Electronics Corporation, Wilsonville, United States

### **Comparison Between Root-Impulse-Energy and Vector Network Analyzer Methods for Measuring Loss on Printed Circuit Boards**

M. Harper, N. Ridler, M. Salter, National Physical Laboratory, Teddington, United Kingdom

## Interactive Forum 1: Time Domain and Linear Network

### Measurement

Evan Fledell, Session Chair

### **Time-domain and mechanical assessments of 1.0 mm coaxial air lines**

M. Horibe, M. Shida, K. Komiyama, AIST, Tsukuba, Japan

### **Hidden Problems in Precise Calibration on Microstrip**

J. Raboch, K. Hoffmann, Z. Skvor, P. Hudec, Czech Technical University in Prague, Prague 6, Czech Republic

### **A Simple Method for Extreme Impedances Measurement - Experimental Testing**

M. Randus, K. Hoffmann, Czech Technical University in Prague, Prague, Czech Republic

## Session B: Linear Network Measurement

Ken Wong, Session Chair

### **Wideband measurement of extreme impedances with a multistate reflectometer**

A. Lewandowski<sup>2</sup>, D. LeGolvan<sup>1</sup>, R. A. Ginley<sup>1</sup>, T. M. Wallis<sup>1</sup>, A. Imtiaz<sup>1</sup>, P. Kabos<sup>1</sup>, <sup>1</sup>National Institute of Standards and Technology, Boulder, United States, <sup>2</sup>Warsaw University of Technology, Warsaw, Poland

### **Statistical Measurement Techniques for Equivalent Source Mismatch of 1.85 mm Power Splitter**

T. M. Wallis<sup>1</sup>, A. Lewandowski<sup>2</sup>, <sup>1</sup>NIST, Boulder, United States, <sup>2</sup>Warsaw University of Technology, Warsaw, Poland

### **An Envelope Domain Measurement Test Setup to Acquire Linear Scattering Parameters**

E. Zenteno<sup>1</sup>, M. Isaksson<sup>1</sup>, N. Keskitalo<sup>1</sup>, D. Wisell<sup>2</sup>, O. Andersen<sup>3</sup>, <sup>1</sup>University of Gävle, Gävle, Sweden, <sup>2</sup>Ericsson AB, Stockholm, Sweden, <sup>3</sup>Ericsson AB, Gävle, Sweden

## Session C: Non-Linear Network Analysis Applications

Jean-Pierre Teyssier, Session Chair

### **Microwave characterization of optically modulated photo-induced switches with a passivation layer using an LSNA**

C. Roda Neve<sup>1</sup>, G. Poesen<sup>2</sup>, D. Schreurs<sup>3</sup>, J. Raskin<sup>1</sup>, J. Stiens<sup>2</sup>, R. Vounckx<sup>2</sup>, <sup>1</sup>UCL, Louvain-la-neuve, Belgium, <sup>2</sup>VUB, Brussels, Belgium, <sup>3</sup>K.U.Leuven, Leuven, Belgium

### **Nonlinear Network Analysis for Modern Communication Devices and Systems**

E. Zenteno<sup>1</sup>, O. Andersen<sup>3</sup>, M. Isaksson<sup>1</sup>, N. Keskitalo<sup>3</sup>, D. Wisell<sup>2</sup>, <sup>1</sup>University of Gävle, Gävle, Sweden, <sup>2</sup>Ericsson AB, Stockholm, Sweden, <sup>3</sup>Ericsson AB, Gävle, Sweden

### **RF Waveform metrology for characterization of non-linear amplifiers**

D. A. Humphreys<sup>1</sup>, G. Watkins<sup>2</sup>, K. Morris<sup>2</sup>, J. Miall<sup>1</sup>, <sup>1</sup>National Physical Laboratory, Teddington, United Kingdom, <sup>2</sup>Bristol University, Bristol, United Kingdom

## Interactive Forum 2: Non-Linear Network Measurement

Evan Fledell, Session Chair

### **Power Amplifier Behavioral Modeling Performance Comparison of the LSNA and the modulation-domain system**

P. N. Landin<sup>1</sup>, C. Fager<sup>2</sup>, M. Isaksson<sup>1</sup>, K. Andersson<sup>2</sup>, <sup>1</sup>University of Gävle, Gävle, Sweden, <sup>2</sup>Chalmers University of Technology, Göteborg, Sweden

### **Simultaneous Measurement of High and Low Frequency Response of Non-Linear Microwave Circuits**

G. Avolio<sup>1</sup>, G. Pailloncy<sup>2</sup>, D. Schreurs<sup>1</sup>, M. Vande Bossche<sup>2</sup>, B. Nauwelaers<sup>1</sup>, <sup>1</sup>K.U.Leuven, Leuven, Belgium, <sup>2</sup>NMDG nv, Bornem, Belgium

### **Design and Testing of a Software Feedback Loop for RF Power Leveling**

X. Cui, T. P. Crowley, National Institute of Standards and Technology, Boulder, United States

## Session D: Non-Linear Network Test Equipment

John Wood, Session Chair

### **Load-Pull + NVNA = Enhanced X-Parameters for PA Designs with High Mismatch and Technology-Independent Large-Signal Device Models**

G. Simpson<sup>1</sup>, J. Horn<sup>2</sup>, D. Gunyan<sup>2</sup>, D. E. Root<sup>2</sup>, <sup>1</sup>Maury Microwave Corporation, Ontario, United States, <sup>2</sup>Agilent Technologies, Santa Rosa, United States

### **A New Technique for Decreasing the Characterization Time of Passive Load-Pull Tuners to Maximize Measurement Throughput**

C. Roff<sup>2</sup>, J. Graham<sup>1</sup>, J. Sirois<sup>1</sup>, B. Noori<sup>1</sup>, <sup>1</sup>Freescale Semiconductor, Inc., Tempe, United States, <sup>2</sup>Cardiff University, Cardiff, United Kingdom

### **Inexpensive Solution to Double RF Bandwidth of Vector Signal Generator**

D. Schreurs, J. Alonso Romero, J. Martinez San Roman, M. Homayouni, G. Avolio, B. Nauwelaers, K.U.Leuven, Leuven, Belgium

Friday December 12, 2008

## Session E: Spectrum and Noise Measurement

Tom Ruttan, Session Chair

### **Real-Time Spectrum Analysis reveals Time Domain Characteristics of Frequency Domain Signals**

T. C. Hill, Tektronix. Inc., Beaverton, United States

### **Using Spectrum Analyzer to Determine Frequency Modulation Accuracy of a Synthesizer and Its measurement Uncertainty**

Y. B. Lee, Anritsu Company, Morgan Hill, United States

### **In-Situ Silicon integrated tuner for automated On-wafer MMW noise parameters extraction of Si HBT and MOSFET in the range 60-110GHz.**

Y. Tagro<sup>1</sup>, D. Gloria<sup>1</sup>, S. Boret<sup>1</sup>, Y. Morandini<sup>1</sup>, G. Dambrine<sup>2</sup>, <sup>1</sup>STMicroelectronics, Crolles, France, <sup>2</sup>IEMN, Villeneuve d'ascq, France

### **A New Noise Parameter Measurement Method Results in More than 100x Speed Improvement and Enhanced Measurement Accuracy**

G. Simpson<sup>1</sup>, D. Ballo<sup>2</sup>, J. Dunsmore<sup>2</sup>, A. Ganwani<sup>1</sup>, <sup>1</sup>Maury Microwave Corporation, Ontario, United States, <sup>2</sup>Agilent Technologies, Santa Rosa, United States

## Interactive Forum 3: Calibration and Power Measurement

Evan Fledell, Session Chair

### **Comparison of On-Wafer Multiline TRL and LRM+ Calibrations for RF CMOS Applications**

A. Rumiantsev<sup>1</sup>, S. L. Sweeney<sup>2</sup>, P. L. Corson<sup>2</sup>, <sup>1</sup>SUSS MicroTec Test Systems GmbH, Sacka, Germany, <sup>2</sup>IBM Microelectronics, Essex Junction, United States

### **A General Closed-Form Solution to Multi-Port Scattering Parameter Calculations**

P. Wittwer<sup>2</sup>, P. J. Pupalakis<sup>1</sup>, <sup>1</sup>LeCroy Corporation, Chestnut Ridge, United States, <sup>2</sup>University of Geneva, Geneva, Switzerland

### **Benchmarking Comparison of Thermal and Diode Sensors for Pulsed Power Measurements**

S. Somasundaram Meena<sup>1</sup>, C. Baylis<sup>2</sup>, L. Dunleavy<sup>3</sup>, <sup>1</sup>University of South Florida, Tampa, United States, <sup>2</sup>Baylor University, Waco, United States, <sup>3</sup>Modelithics, Inc, Tampa, United States

## Session F: Calibration

Nick Ridler, Session Chair

### **Reciprocity-based multiport de-embedding and an analysis of standard sensitivity**

J. Martens, Anritsu Company, Morgan Hill, United States

### **Traceability of VNA Measurements**

K. Wong, Agilent Technologies, Inc., Santa Rosa, United States

### **The Influence of Calibration Substrate Boundary Conditions on CPW Characteristics and Calibration Accuracy at mm-Wave Frequencies**

A. Rumiantsev<sup>1</sup>, R. Doerner<sup>2</sup>, E. M. Godshalk<sup>3</sup>, <sup>1</sup>SUSS MicroTec Test Systems GmbH, Sacka, Germany, <sup>2</sup>Ferdinand-Braun-Institut fuer Hoehstfrequenztechnik (FBH), Berlin, Germany,

<sup>3</sup>Maxim Integrated Products, Inc., Sunnyvale, United States

### **Software Solutions for Linear and Non-Linear Microwave Measurements and Calibrations**

A. Ferrero, V. Teppati, M. Garelli, S. Bonino, U. Pisani, Politecnico di Torino, Torino, Italy

# Gating Effects in Time Domain Transforms

Joel Dunsmore *Member IEEE*,

Agilent Technologies, 1400 Fountaingrove Parkway, Santa Rosa, CA, 95403

*Abstract: Gating is well known in modern VNAs for improving or isolating responses from multiple reflections in the frequency and time domain. However, the particular details of how positions of selections of the gate start and stop values, as well as gate shapes, aliasing and masking effects are not well documented. This paper presents an explanation of gate band-edge effects due to renormalization effects, and masking effects, and provides recommendations for improving the effectiveness of gating.*

## I TIME DOMAIN GATING

Time domain gating refers to the process of selecting a region of interest in a portion of the time domain, removing unwanted responses, and displaying the result in the frequency domain. Gating can be thought of as multiplying the time domain response by a mathematical function with a value of one over the region of interest, and zero outside this region[1,2]. The gated time domain function can then be forward transformed to display the frequency response without the effect of the other responses in time. The gating effects, however, are somewhat subtle in their response and there are consequences of the gating function that are not readily apparent.

In practice, the gating is not a “brick-wall” function. The gate function can be arbitrarily sharp, as its frequency response is not limited by the measured data. However the time-gated response would also have sharp transitions in the time domain, and the frequency response will have ringing associated with this sharp transition (as the displayed frequency response is typically limited to the measured data region). Because of this, the gating function is windowed in the frequency domain before being transformed to the time domain. For a rectangular time gating function centered at  $t = 0$ , the Fourier transform can be calculated analytically, with the result that the gate frequency response will have a  $\sin(\omega)/\omega$  or  $\text{sinc}(\omega)$  function. The width of the sinc main-lobe is inversely proportional to the width of the time gate. If the center of the gate time is not at  $t = 0$ , the resulting Fourier transform produces a response that corresponds to the sinc function multiplied by a complex exponential factor, namely  $\text{sinc}(\omega) \cdot e^{j\omega t}$ . This is windowed in the frequency domain by a Kaiser-Bessel window that sets the maximum gate transition slope in the time domain. The gate function is then transformed to the time domain and multiplied by the time domain response, before being transformed back to the frequency domain. Equivalently, the time-gated frequency response may be determined by convolving the gate frequency response by the measured frequency response, and this view of the gating allows a more intuitive understanding of one of the subtle gating effects.

A curious effect of the gating function occurs at the endpoints of the time-gated frequency-domain response: these endpoint regions are lower by 6 dB. The 6 dB offset can be understood by comparing the center point and last point of a gated frequency response of a unit function  $F(\omega)=1$ . The time domain response will approach a delta function,  $f(t)=\delta(t)$ . In the convolution of the gate frequency response  $G(\omega)$  with the original frequency response  $F(\omega)$ , the gated value at any frequency  $\omega_1$  can be determined by multiplying the original frequency response by the reverse of the gating frequency function centered at that frequency, and summing the result (this being the definition of convolution):

$$F_g(\omega_1) = \sum_{n=-N}^N F(n \cdot \Delta\omega) \cdot G(\omega_1 - n \cdot \Delta\omega) \quad (1)$$

For the center point (zero frequency, or DC) of a gated frequency response where the time gate is centered at  $t=0$ , the response is the sum of a multiplication of the sinc function (which is the gate frequency response as described above) with the original measured frequency response. For the case of the last frequency point (highest), the sinc function is centered on the last data point, and half the gate function is multiplied by zero (for frequencies above  $\omega = N \cdot \Delta\omega$ ), and does not add to the sum. Thus, the last data point will be one-half the value of the DC point, or 6 dB lower. This creates the unfortunate result that any gating will distort the last points (and first points in band pass mode) of the gated frequency response.

The VNA time domain, however, compensates for this roll-off through a post-gate renormalization. The post-gate renormalization is a function determined by creating a frequency response that is unit magnitude. A pre-gate window is applied to this unit-response that is the same as the pre-transform window applied to the normal frequency response data. This unity-magnitude frequency response is convolved with the gate frequency response, to generate the final normalizing frequency response. The time-gated frequency response is divided by this function to remove the roll-off effects of the time gating. This normalizing function works perfectly for a unit time response at the center of the gate. However, if the gate is not symmetrical around the time function, then the result will show errors in the gated response when compared to the original frequency response.

It is instructional to view the actual gate shape in the time domain, which can be done using a function not normally available in commercial VNAs. The gate shape may be generated by creating a delta-like frequency response ( $F(0)=1$ ;  $F(\omega)=0$  for  $\omega \neq 0$ ), applying gating, and

transforming the result to the time domain to see the actual gate shape. This is useful in understanding how the gate shape affects the gated response.

Figure 1 shows the gating function for various gate center times. Figure 2 shows a unit frequency response ( $F(\omega)=1$ ) in the time domain, with gates applied at various gate times. Note that the time domain response is nearly unchanged as the time-gate fully encompasses the impulse at all three center times. The abrupt changes in the side-lobe levels of Figures 6a and 6b are likely due to the re-normalization effect. Without re-normalization, one would expect the side-lobe levels to be greatly reduced outside of the gate window. Figure 6c shows the frequency response after gating. Here there is a substantial difference in the response at high frequency for the different

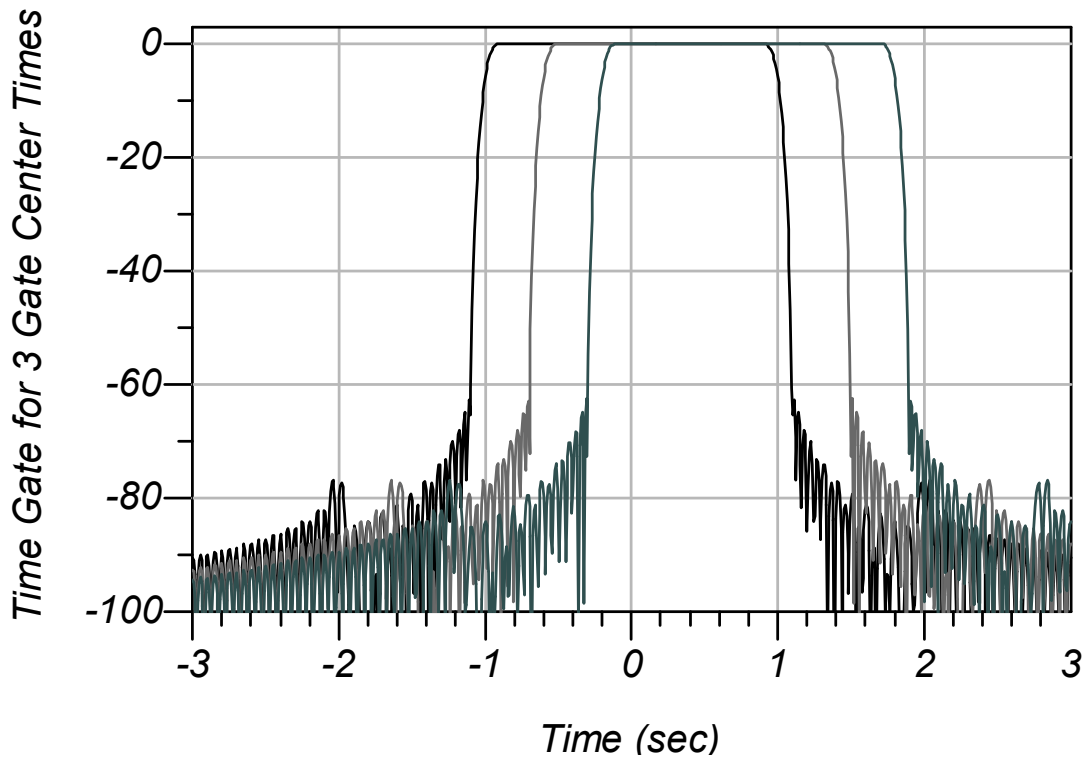


**Figure 1: Time Gate shape for various gate center time choices**

gate center times. It is clear that normalization is optimal when the gate is centered on the response being gated.

The gated response may be viewed in time domain by taking the IFT and displaying the result. In fact, it is almost always required to first view the time domain response to assign proper gating start and stop values: the transform function is turned on, and the resultant time domain response is displayed, and the gate start and stop are set. Next gating is turned on. The transform is turned

off, and the time-gated frequency response is shown in the figure 3. A study of the time domain response of an example of composite responses of several component elements will show how time gating can be used to separate the responses in time and display the individual frequency

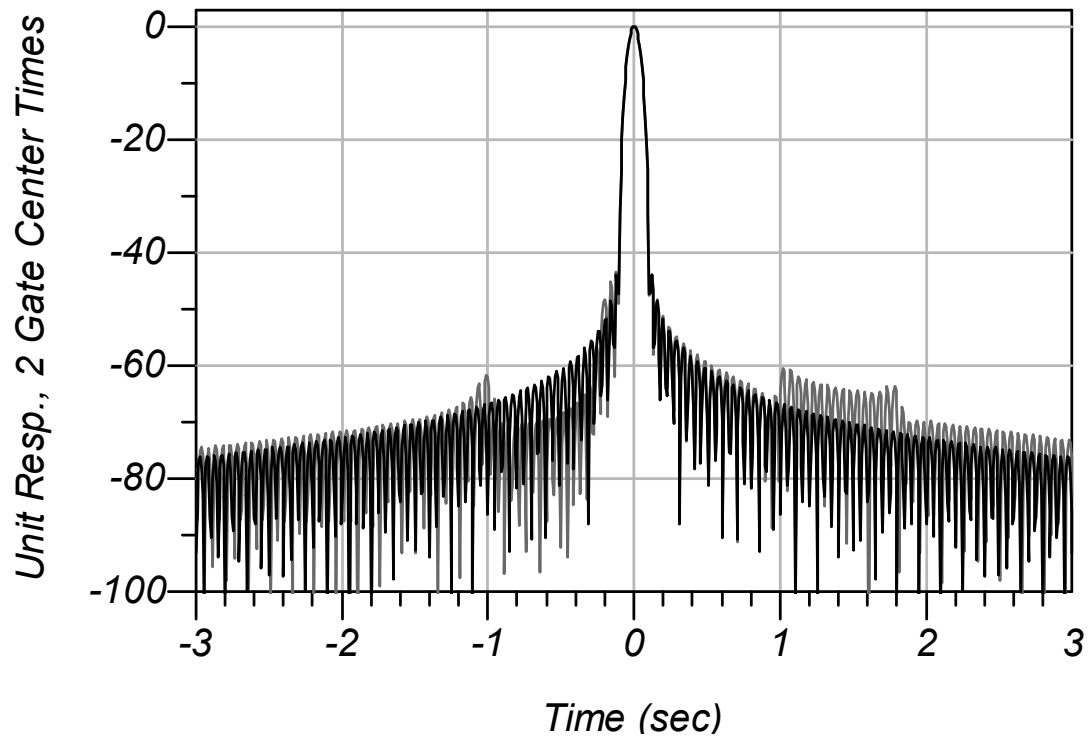


Figure 2: Gated Time Domain Unit Response for various gate center times

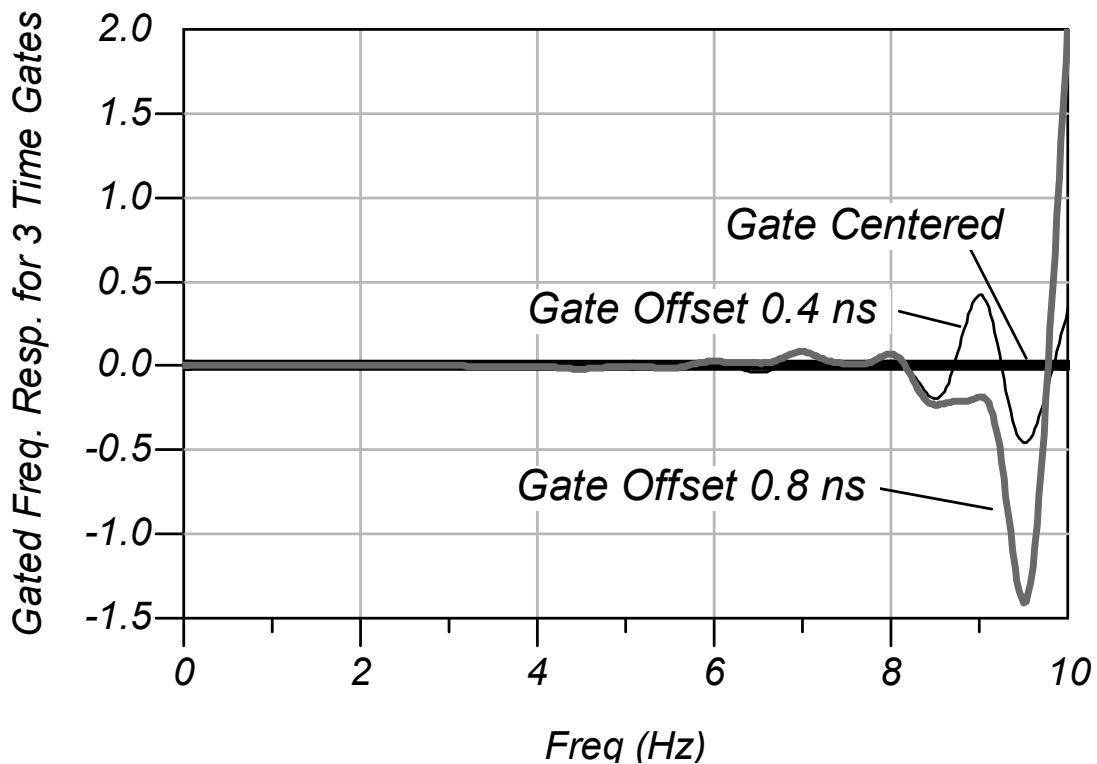
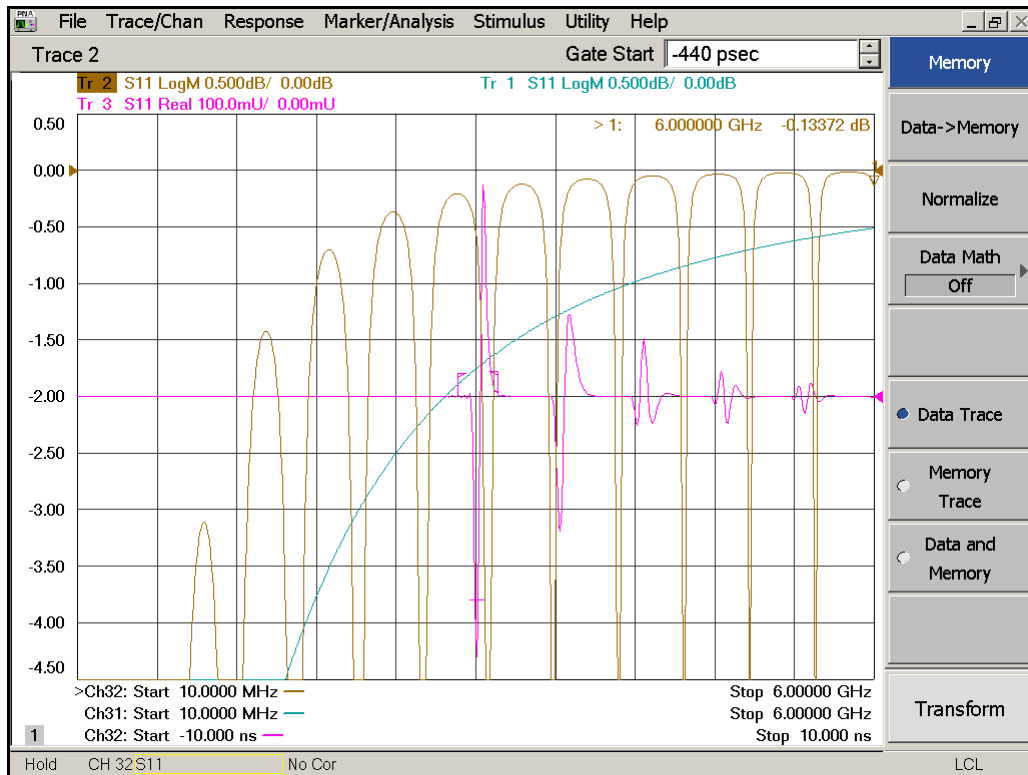
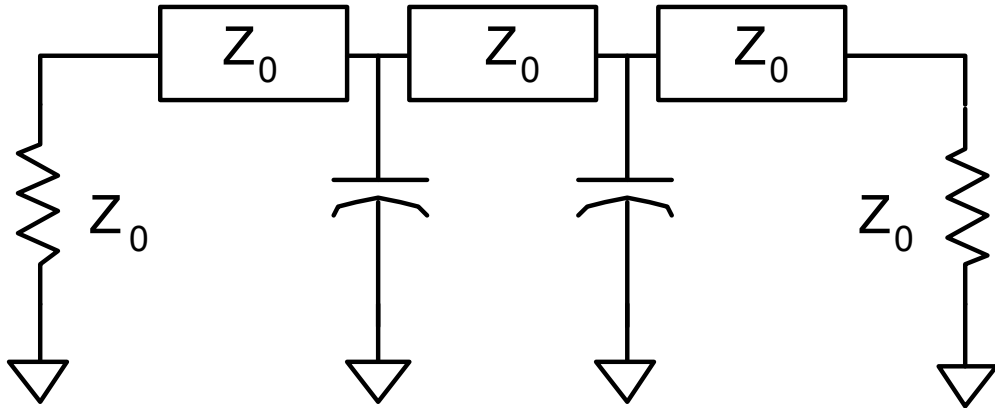


Figure 3: Frequency response after gating, showing the edge effects

responses of the component elements, but with some distortion due to masking effects [3].

This effect can be seen more distinctly in a case where we use gating to remove the effects of unwanted reflections. Consider the circuit of figure 4. In this circuit, we have two identical capacitors. Figure 5 shows the frequency response of the two capacitors (yellow), and of just a single capacitor (blue), and the time domain response of the two capacitors (Magenta)



**Figure 4 (above) Circuit of two capacitors.  
 Figure 5 (below) Frequency response (yellow) of two caps. Frequency response (blue) of just 1 cap. Time domain (Magenta) of two caps.**

Figure 6 below shows the effect of gating centered around the time response of just the first capacitor. You can see that the response is within 0.2 dB of the ideal response of just a single capacitor (blue trace).

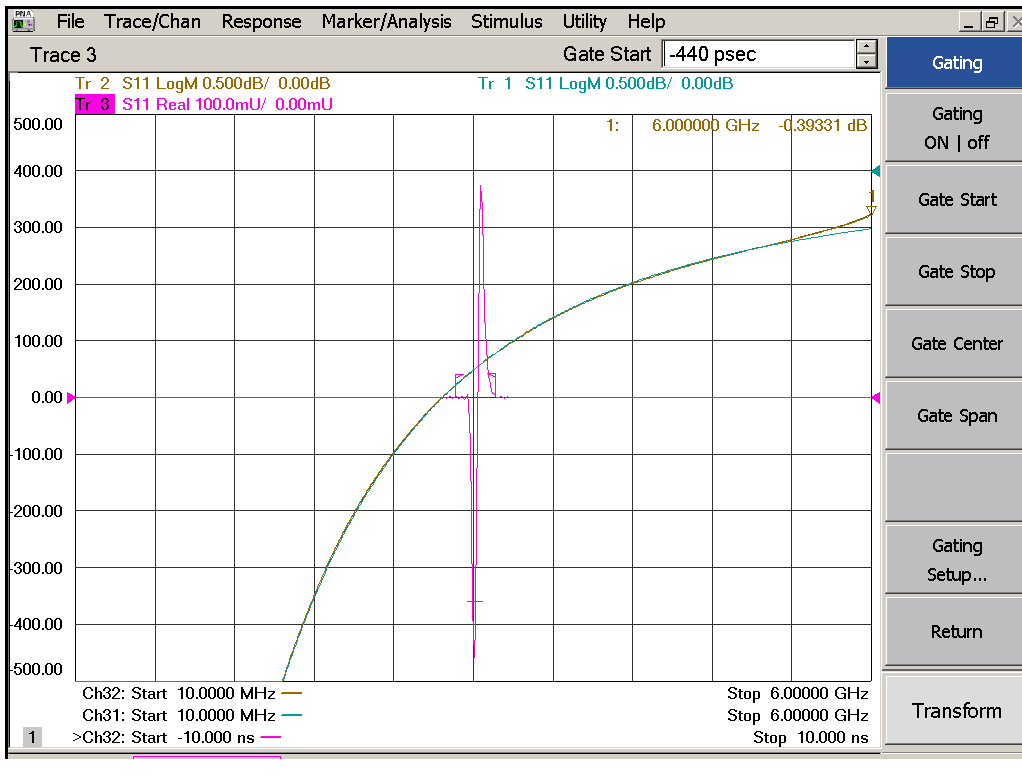


**Figure 6, Time gated response of just the first capacitor.**

Figure 7 shows the result of moving the time gate start down to -5 nsecs, so that the time gate is no longer centered on the response of the first capacitor. In this plot we can see that there is substantial end effect, associated with the fact that the gate window is not centered on the discontinuity.

The end effect can be minimized by setting the discontinuity to be centered at zero time. The zero time can be set by using port extensions on the network analyzer to reset the reference plane of the VNA. When the reference plane is reset, the end effects will disappear, as shown in figure 8.

**Conclusion:**

Time gating renormalization causes band edge effects if the time gates are not centered on the desired response. Port extension can compensate nearly completely for this effect.

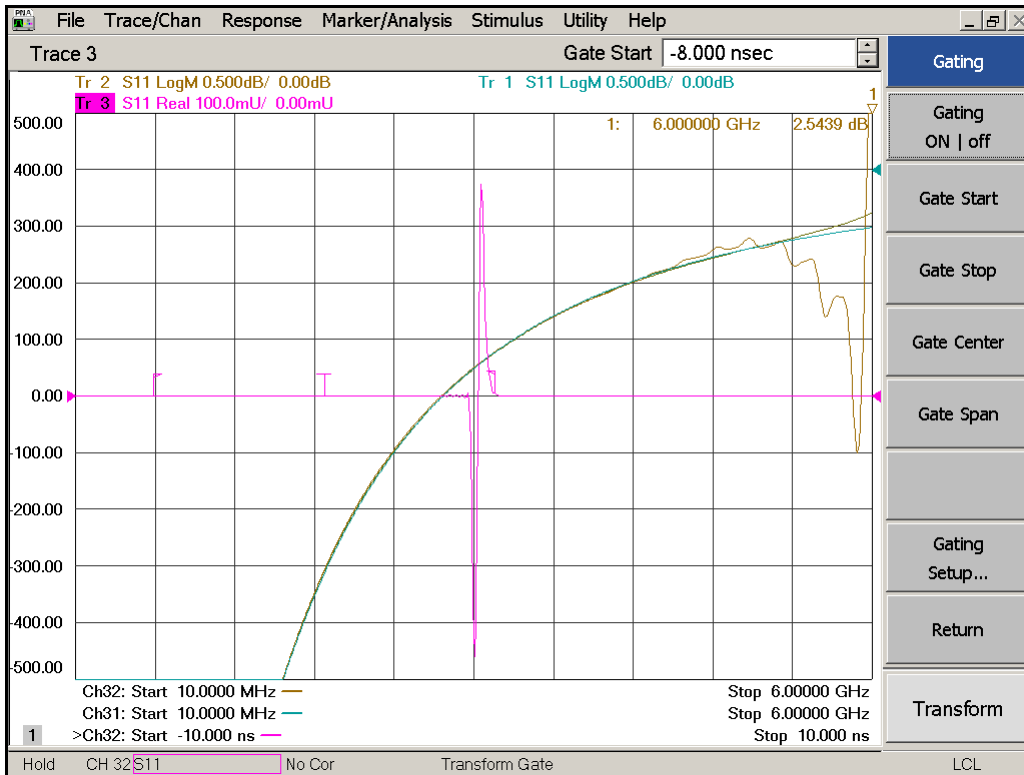


Figure 7: Frequency response with offset gates

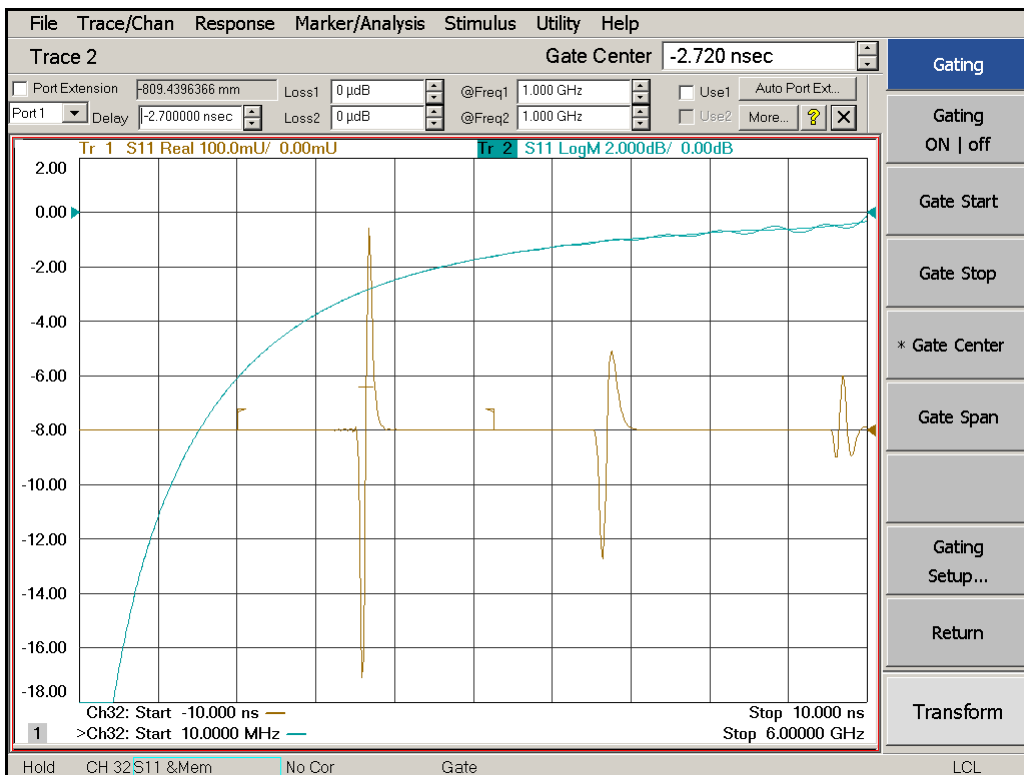


Figure 8: Frequency response with offset gates, and port extension to set the discontinuity at the center of the gate.

## References:

---

- [1] Sharrit, D, "Vector network analyzer with integral processor", US Patent No. 4,703,433
- [2] Rytting, D., "Let Time-domain Provide Additional Insight into Network Behaviour", Hewlett-Packard RF & Microwave Measurement Symposium and Exhibition, April 1984
- [3] K Lu, T. Brazil, "A Systematic Error Analysis of HP8510 Time-Domain Gating Techniques with Experimental Verification", 1993 IEEE MTT-S Digest, pg 1259.

# Measurements of Characteristic Impedance of High Frequency Cables with Time Domain Reflectometry (TDR)

Luis Navarro, Eugene Mayevskiy, and Timothy Chairat

Precision Interconnect  
Tyco Electronics  
Wilsonville, OR 97070, USA

**Abstract**—A new methodology for measuring the cable characteristic impedance ( $Z_0$ ) is presented. The approach employs a least square fit to extract accurate and repeatable  $Z_0$  values from the TDR measurements. The RLGC circuit modeling explores various cable losses and shows that the proposed approach agrees with the transmission line theory. A frequency domain plot of  $Z_0$  measurements correlates with the new methodology. The proposed methodology equips a test engineer with a quantifiable and efficient way to evaluate the cable performance as a function of environmental and physical changes.

**Keywords**—characteristic impedance; time domain reflectometry; coaxial cable; telegrapher's equations

## I. INTRODUCTION

The time domain reflectometry oscilloscope (TDR) oscilloscope is traditionally a tool of choice to measure time domain characteristic impedance of cables. When impedance is measured with a TDR oscilloscope, the generator produces a time domain square waveform with a fast rising edge. Only a short region near the rising edge of the waveform is used, so that part of the waveform looks like a step on the oscilloscope's screen. This step is used to measure impedance because when the step propagates through a cable, it results in reflections, which are directly related to the amplitude and duration of a physical discontinuity. Even though the principal operation of the TDR instruments is the same in many platforms, there is a variety of methodologies used in industry to interpret the oscilloscope's readout.

The major issue in the interpretation of the results is that the impedance curve in general exhibits a slope due to the cable loss. For example, the beginning of the TDR data can show  $48\Omega$  impedance whereas the end of the cable can be  $52\Omega$ . In such a case, is it the average, or the start or the end value that needs to be reported as the characteristic impedance? What about impedance deviations due to reflections or process variations? Hence, the test engineer working with TDR oscilloscope has to make an intelligent decision about what impedance value to report. The industry techniques can vary from a simple oscilloscope measurement of the absolute impedance with the cursors to the sophisticated impedance

measurement algorithms aimed to eliminate undesired losses and reflections in interconnect and in the measurement system.

Perhaps the simplest way to measure characteristic impedance of cables is to specify the time range and find out if the measured impedance exhibits expected results. This approach is often used for compliance testing in various communication standards such as SATA<sup>®</sup>, InfiniBand<sup>®</sup>, or DisplayPort<sup>®</sup>. Those standards specify impedance masks relative to reference time position, which is usually found by measuring open or short from the test adaptor. A displayed TDR waveform shows discontinuities due to the physical features of the measured cable. These physical features, such as fixture footprints, mated connectors, and solder points, help to define a mask that is applicable for a specific application.

For example in a SATA cable, the reflections from a mated connector in the cable assembly can occupy approximately 300-500ps of the TDR response. Hence, the SATA compliance test specification procedures require to measure and record maximum and minimum cable differential impedance values in the first 500ps of cable response following any vestige of the connector response [1]. By doing this, the impedance of the beginning of the cable is captured, and the loss behavior of the cable is ignored. Although, the specification limits can be very well defined, the question about the real value of the characteristic impedance can be left open.

The institute for printed circuits test methods manual (IPC-TM 650) describes impedance measurements of transmission lines using a calibration standard and a defined region [2]. The method corrects for the high-frequency loss exhibited by the TDR connecting cable and allows measuring impedance almost as accurate as the standard used in calibration process. The major drawback of this method, however, is that measured impedance is an averaged impedance value of the specified region. Given that the displayed characteristic impedance is changing due to the cable loss, such results will be highly dependent on the region used in the measurements as illustrated in Fig. 1.

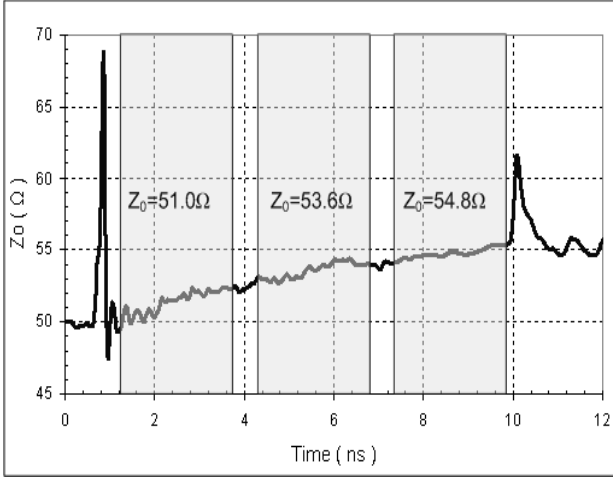


Figure 1. Impedance of a coaxial cable measured at different regions; the reflections from the launch and the end of the cable are excluded. Note that the impedance slope due to loss mechanism in the cable is causing three different regions to have three different characteristic impedance average values.

More rigorous techniques, such as the one described by Bechhover [3], try to tackle the major sources of the discrepancies such as reflections and attenuation due to high frequency losses by applying vigorous algorithms that minimize undesired effects, such as inverse scattering method followed by the inverse filtering. Although, this methodology can be very helpful in determining the location of the cable discontinuity or failure, the impedance value obtained is dependent on at least two assumptions that are not true in the real cables. First, impedance inverse scattering method assumes a lossless behavior of the cable measured. Second, the inverse filtering assumes that a high frequency loss in the system is uniform. However, the real cable assembly has both a non-uniform losses and significant reflections that affect the accuracy of the algorithms used.

In this paper we present a new method of measuring characteristic impedance  $Z_0$ , which involves capturing the waveform of impedance as a function of time in a Time Domain Reflectometer (TDR), defining the cable impedance measurement region that includes only cable impedance variations, performing a least square fit to the measured characteristic, and finally extrapolating the impedance result to the time location of the reference plane as shown in Fig. 2. The measured impedance is essentially extrapolation of the curve fit to the launch time point. This point represents impedance that would be seen by the transmitter if someone could connect a cable to it without any reflections. The new methodology offers several advantages over the other methodologies used in industry such as, repeatability, independence on physical properties of the cable, and provides a quantifiable way to evaluate the cable characteristic impedance of a cable as a function of environmental changes.

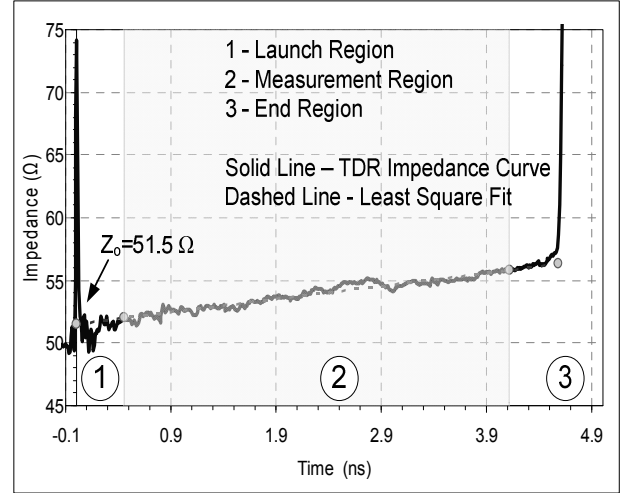


Figure 2. Impedance of a coaxial cable measured using the launch point extrapolation technique; the reflections from the launch (1) and the end (3) of the cable are excluded from the measurement zone (2) and the characteristic impedance is measured from the least square fit extrapolation to the time position of the reference plane.

The paper starts from the discussion about the physical effects of losses in time and in frequency domains. Then the impedance measurement methodology is explained in details. Finally, the validity of the measurement technique will be explored by analyzing the accuracy, sensitivity, and repeatability results from the measurements of the test cables.

## II. PHYSICAL EFFECTS

When no loss is present, the cables can be viewed as lossless transmission lines. The behavior of the lossless transmission line can be described by two major characteristics: characteristic impedance  $Z_0$  in Ohms ( $\Omega$ ) and propagation delay in seconds per meter (Tpd). The governing equations for these characteristics can be derived from the telegrapher's equations [4] and they are listed below:

$$Z_0 = \sqrt{\frac{L}{C}} \quad (1)$$

$$T_{pd} = \sqrt{L \cdot C} \quad (2)$$

Where  $L$  is inductance per unit length in Henries (H/m) and  $C$  is capacitance per unit length in Farads (F/m).

In the presence of loss, (1) and (2) change to the following representations:

$$Z_0 = \sqrt{\frac{R + j\omega L}{G + j\omega C}} \quad (3)$$

$$\gamma = \sqrt{(R + j\omega L)(G + j\omega C)} \quad (4)$$

Where R is the series component of the loss per unit length in Ohms ( $\Omega/m$ ), G is the shunt component of the loss per unit length in Siemens (S/m) and  $\gamma$  is the propagation function. The loss elements in (3) and (4) are frequency dependent, and that frequency dependency can be farther expressed as:

$$R(f) = R_{DC} + R_{AC}\sqrt{f} \quad (5)$$

$$G(f) = G_{DC} + G_{AC} \cdot f \quad (6)$$

Where  $f$  is the frequency of operation in Hertz (Hz) and subscripts DC and AC indicate low and high frequency dependent series loss and shunt loss terms in Ohms ( $\Omega$ ) and

Siemens (S) respectively. The loss representations (5) and (6) are often used in commercially available measurement-based model extractors such as IConnect software by Tektronix Inc. [5]. Having defined the loss model for the cables, let's look at how time and frequency impedance responses are affected by these loss contributors. Accurate RLGC models can be used to "remove" the various losses by setting them to zero and analyzing the cable performance both in time and in frequency domains.

#### A. Time Domain

First, a 50 $\Omega$  coaxial cable was measured using a TDR oscilloscope, and then IConnect model extraction software was used to generate a general measurement-based RLGC model. The resulting correlation of the models with the measurements in time and frequency domains are shown in Fig. 3 and Fig. 4 respectively. Finally, the loss parameters in (5) and (6) are used to analyze physical effects of various losses.

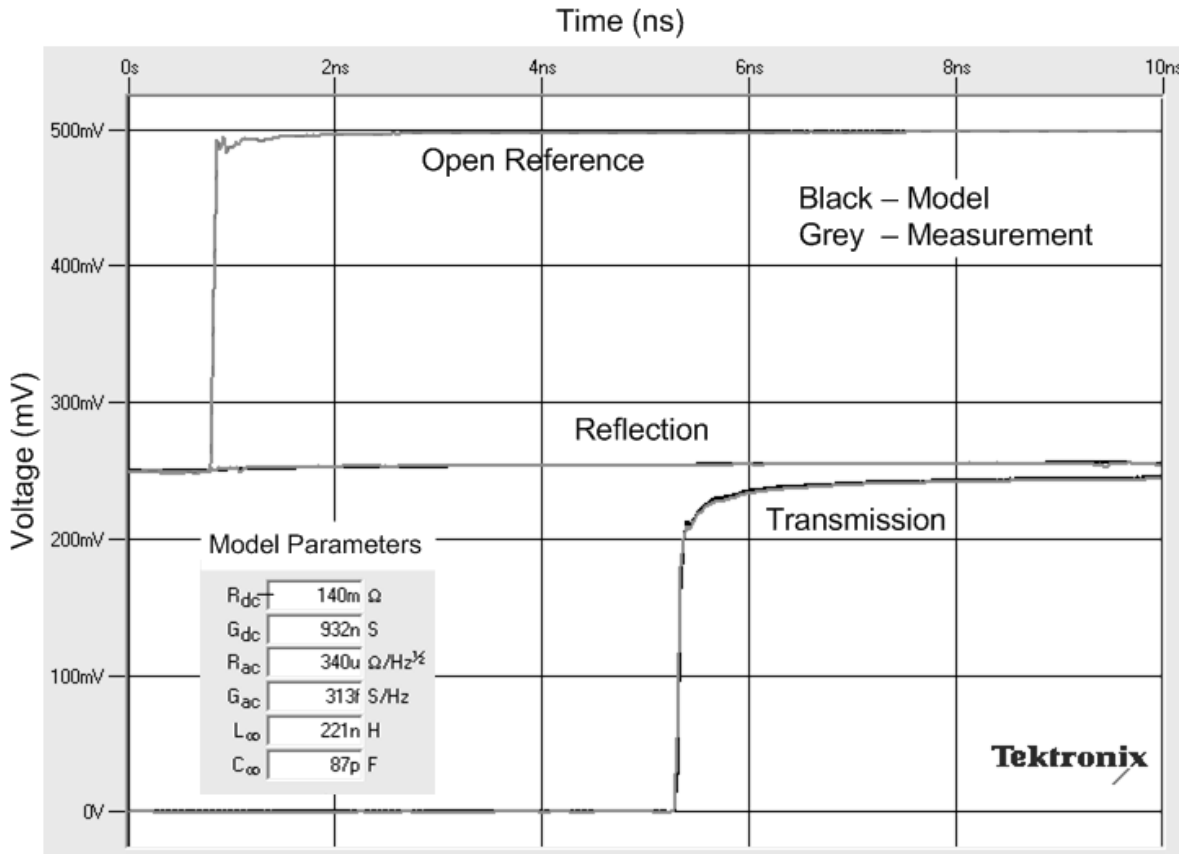


Figure 3. RLGC model correlation with the measurements in time domain. Note the transmission rise time degradation and a slight increase in reflection waveform profile due to the losses. The RLGC model parameters are listed in the legend.

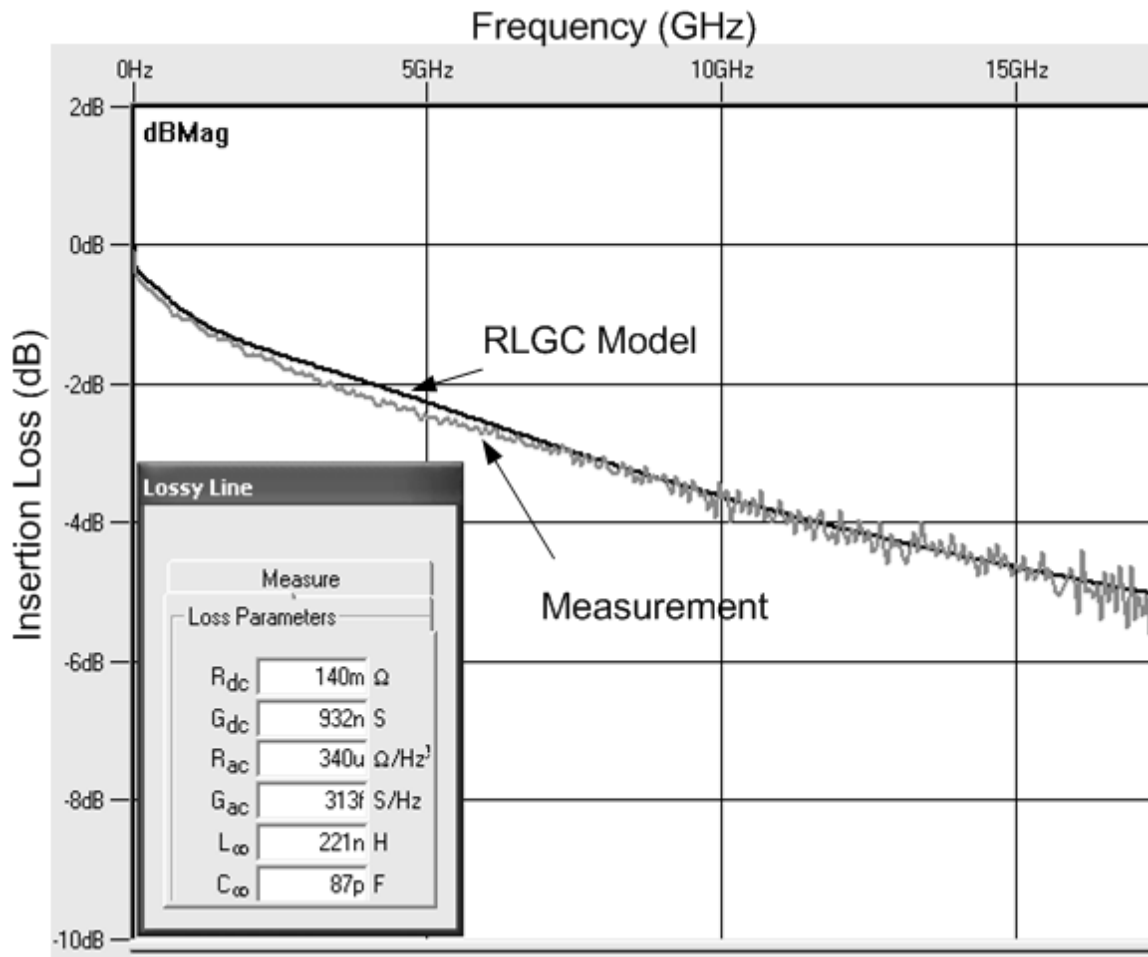


Figure 4. RLGC model correlation in frequency domain. Note the excellent correlation for insertion loss. The RLGC model parameters are listed in the legend.

The model parameters can be easily adjusted to look at the “idealized” behavior. So, setting the G components to zero in (6) eliminates the dielectric loss, which in real life would mean that air dielectric is used in the cable design. Whereas, setting the R components to zero in the (5) would eliminate the conductor loss. If both loss components are set to zero, then the resulting response will be the same as the one from lossless transmission line. Therefore, the loss model obtained from TDR measurements is modified to derive three more models: lossless, series loss only, and a shunt loss only. The loss parameters are listed in the Table 1.

TABLE I. LOSSY PARAMETERS DERIVED FROM THE “ALL LOSSES” CABLE MODEL SHOWN IN FIGURES 3 AND 4.

Parameter	All Losses	Lossless	Series Loss Only	Shunt Loss Only
R <sub>dc</sub> (Ω)	140m	0	140m	0
R <sub>ac</sub> (Ω/Hz <sup>1/2</sup> )	340u	0	340u	0
G <sub>dc</sub> (S)	932n	0	0	932n
G <sub>ac</sub> (S/Hz)	313f	0	0	313f
L (H)	221n	221n	221n	221n
C (F)	87p	87p	87p	87p

The impedance profiles of such models are shown in Fig. 5 and a few conclusions can be drawn from the figure.

Since the removal of the shunt loss elements (“Series Loss Only” case) resulted in a greater upward change in the impedance slope, the slope of the TDR impedance can be linked to the series loss elements of (5). Hence, the positive slope would be an indicator of the domination of the series loss in the cable assembly. On the other hand, the shunt conductance (“Shunt Loss Only” case) results in the downward impedance change, and if such behavior is observed it can be attributed to the high dielectric loss. Since cables normally are designed to have very low dielectric loss, the upward slope in the impedance profile is usually observed in TDR measurements. When there is no loss present (“Lossless” case), the TDR impedance profile is flat.

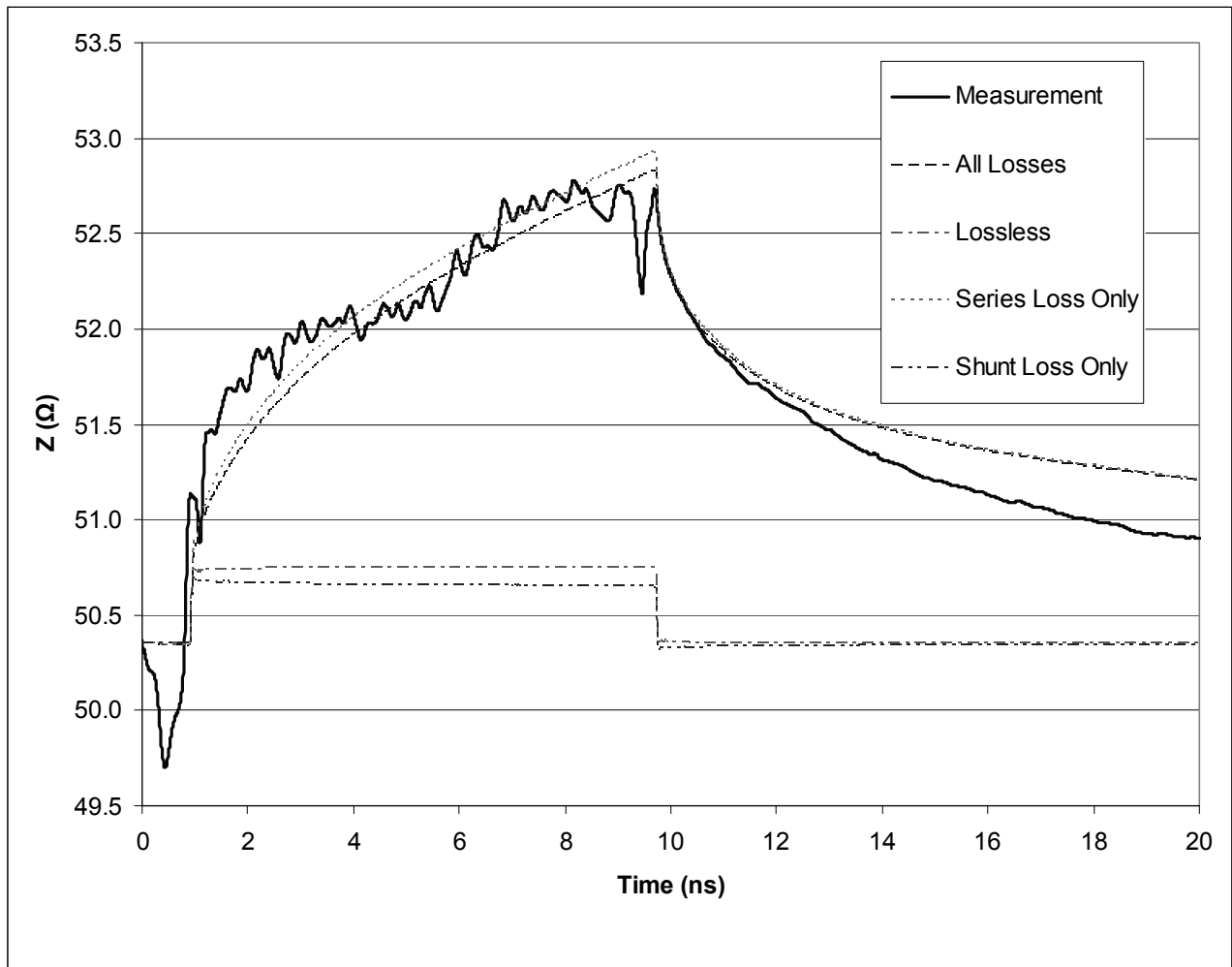


Figure 5. Removal of the various loss components in the cable. The removal of the shunt losses results in more upward slope of the data, whereas the removal of the series losses results in the downward slope.

Another prominent effect is the curvature waveforms that have high series loss in the TDR impedance data. The dielectric loss waveform does not show a significant curvature<sup>1</sup>. The source of this curvature is the frequency dependent loss of the cable because the model parameters show that  $G_{ac}$  part is relatively small compared with  $G_{dc}$  part (313fS/Hz vs. 932nS), while the  $R_{ac}$  is much greater compared with  $R_{dc}$  part (340uΩ/Hz<sup>1/2</sup> vs. 140mΩ). This can be even better visible when the model parameters are substituted in the equations (5) and (6). The total R impedance at 30 MHz, is about 589,000 percent higher than the original  $R_{dc}$  part, while the total G part at the same frequency is only 113 percent higher of the original  $G_{dc}$  value.

To verify this observation, model's parameters can be alternated to decrease the frequency dependent loss in the series component and to increase the frequency dependent loss in the shunt component. The result of this alternation is shown in Fig. 6 where the arrows indicate the direction of the curvature increase. When the series frequency dependent loss ( $R_{ac}$ ) was set to zero while the constant term ( $R_{dc}$ ) in (5) was set to 2Ω (a value corresponding to the total resistive loss at 30 MHz), the curvature disappeared, whereas when the shunt frequency depended term ( $G_{ac}$ ) was increased significantly, the impedance waveform had pronounced increased curvature.

<sup>1</sup> Normal loss will result in a concave curve (frown), while extremely high dielectric loss in respect with copper loss may show a convex curve (smile), this is not likely to happen. However, undesirable variations of impedance as a function of length due to center conductor or dielectric diameter as well as relative permittivity can show an unwelcome "smile".

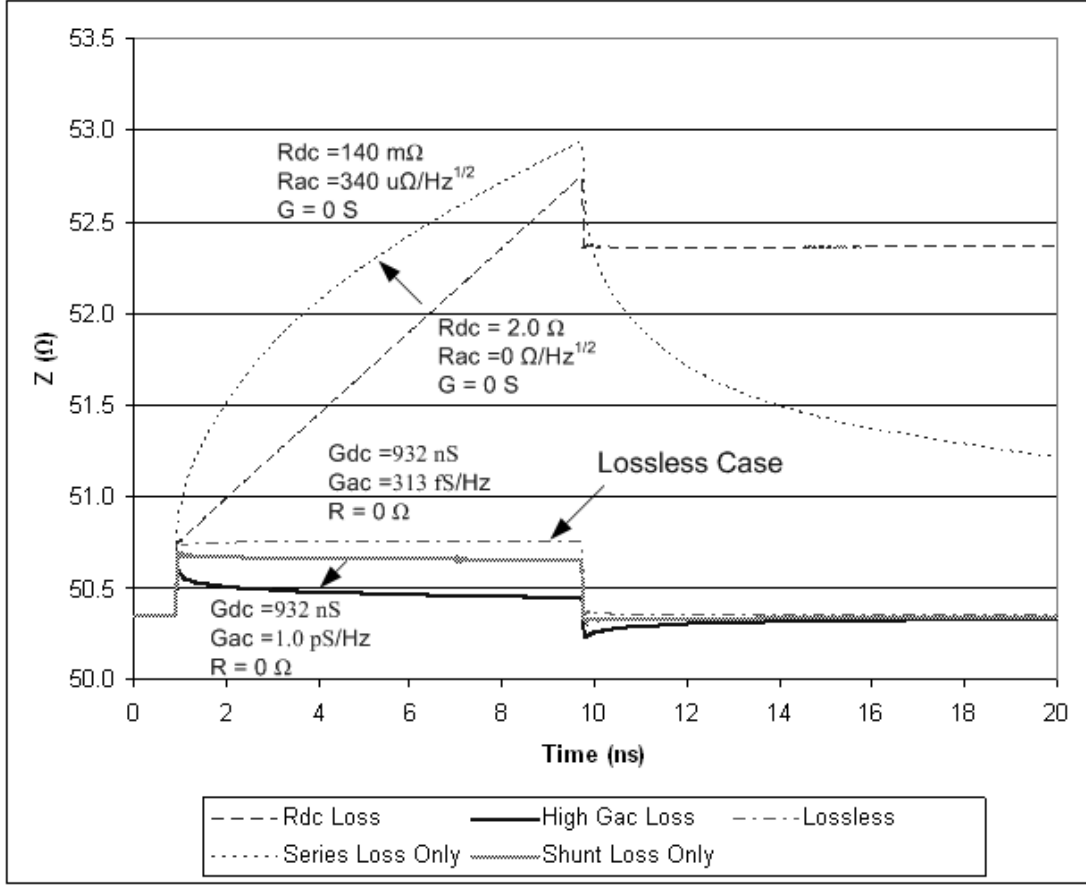


Figure 6. TDR waveform curvatures as a result of the frequency dependent loss components. The arrows indicate the curvature increase as the loss is increasing.

Lastly, it can be observed that all impedance waveforms start from the same impedance point, and then they deviate after being affected by the loss. Hence, the beginning value represents the impedance seen by the transmitter and is important for matching purposes. Moreover, the starting point of this impedance is located at a time when the TDR step enters the cable under test and therefore has the highest frequency content. This value should relate to the high frequency value of the impedance. To visualize this effect we will look at the frequency domain in the next section of the paper.

### B. Frequency Domain

To observe the frequency domain trends, (3) can be used. At the low frequencies the series loss term dominates, and (3) can be rewritten as:

$$Z_o = \sqrt{\frac{R + j\omega L}{j\omega C}} \quad (7)$$

At the high frequencies the L and C terms become more prominent and the asymptote reaches the lossless transmission line value expressed by (1). The loss model defined in the Table 1 along with (1), (3), and (7) can be used to plot high,

medium, and low frequency trends respectively in the frequency domain as shown in Fig. 7.

Fig. 7 shows that for the cable used in the experiment, the low frequency transition happens at the frequencies below 100kHz. The cable impedance is approaching the high frequency asymptote after about 2MHz. The VNA measurement data, which starts at 40MHz, is also approaching the high frequency asymptote, and the deviations from this line can be explained by reflections that come from the cable's connectors.

Since observations in time and in frequency domain indicate that the starting point of cable impedance in the TDR waveform does not have strong dependency on the cable loss and represents the high frequency asymptote, the extrapolated value of the measured impedance waveform to the launch time point can be used as a practical representation of the cable characteristic impedance.

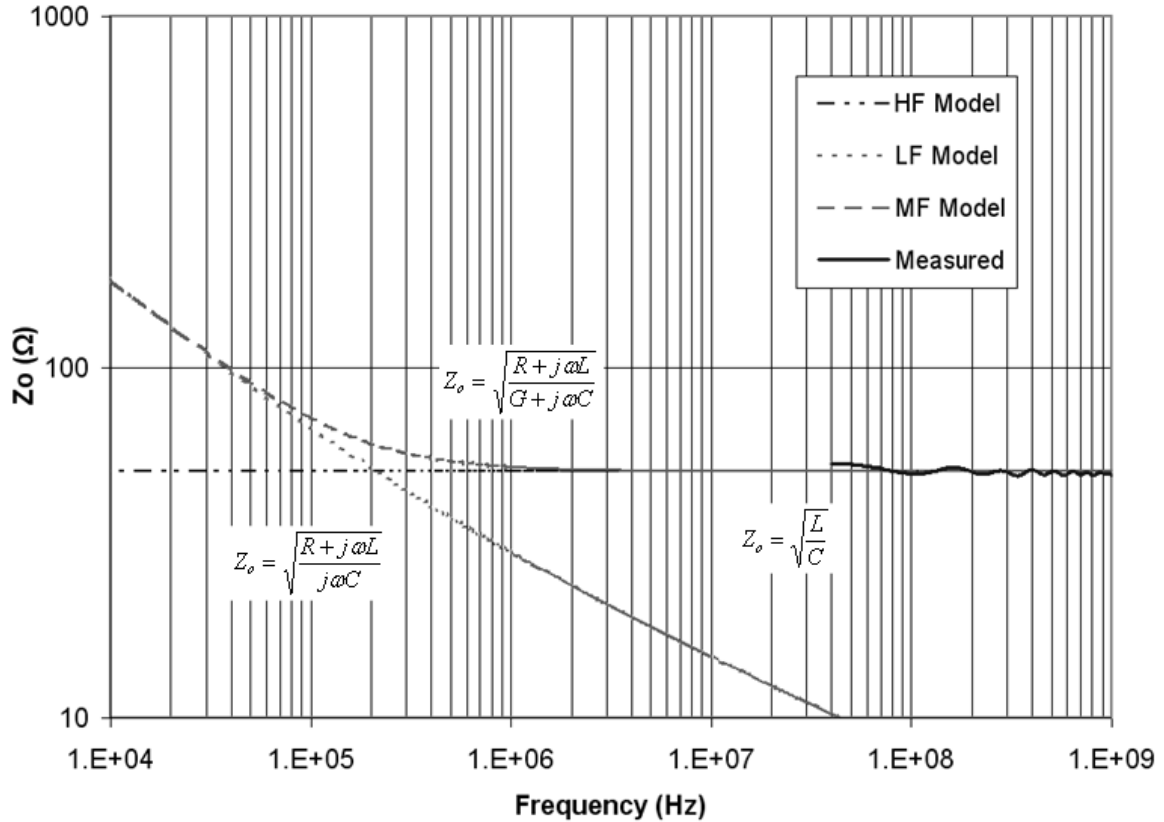


Figure 7. Frequency Domain Plot of Characteristic Impedance of the RLGC cable model asymptotes and the measurements with the VNA. Note the high frequency asymptote and the VNA measurements approaches the lossless representation of the measured data. HF is high frequency trend. LF is low frequency trend. MF is middle frequency trend.

### III. METHODOLOGY DESCRIPTION

To measure the characteristic impedance with the proposed technique, the time domain reflection data has to be acquired first. This can be done with a TDR capable oscilloscope or with a Vector Network Analyzer (VNA). In case of the VNA measurement, the data needs to be converted into time domain using the inverse of the Fast Fourier transformation (IFFT). Often the beginning and the end of the time domain reflection data from the cable measurements are affected by the connector reflections. These reflections are superimposed on the cable response and need to be excluded from the cable impedance data. Then a linear or higher order least squares fit can be performed on the data between the launch and the end exclusion zones. Finally, the plot of the least squares fit is extrapolated to time  $t = T_0$  where the open end of the launching fixture is. The curve fit intercept with the impedance axis at that time is then defined as the measured characteristic impedance of the cable ( $Z_0$ ).

Fig. 8 shows the results of the impedance measurements of three coaxial cables having different characteristic impedances. Note that in all cases the impedance slope linear trends are very well defined.

### IV. METHODOLOGY VALIDATION

Initial measurements performed indicated that the measurements were repeatable enough to perform a Design of Experiments to characterize the sensitivity of the measurements. Later on, additional measurements were made to quantify the repeatability. Finally, the accuracy was verified using independent measurements of capacitance. These results are shown below.

#### A. Sensitivity

The first investigation was to study the sensitivity of the impedance measurement to choices on how to make the measurements. The variables were as follows: #1 the test method (TDR or TDT<sup>2</sup>), #2 whether the far end sample was open or terminated into 50Ω and #3 the variation introduced by the equipment setup.

<sup>2</sup> Typically, the TDR measurement is made with the far end of the transmission line open. At times, the far end may be terminated in its characteristic impedance to measure the transmitted waveform. This is known as TDT (Time domain transmission). Some TDR measurements are made with the far end shorted. These are conditions that may affect the quality of the measurement.

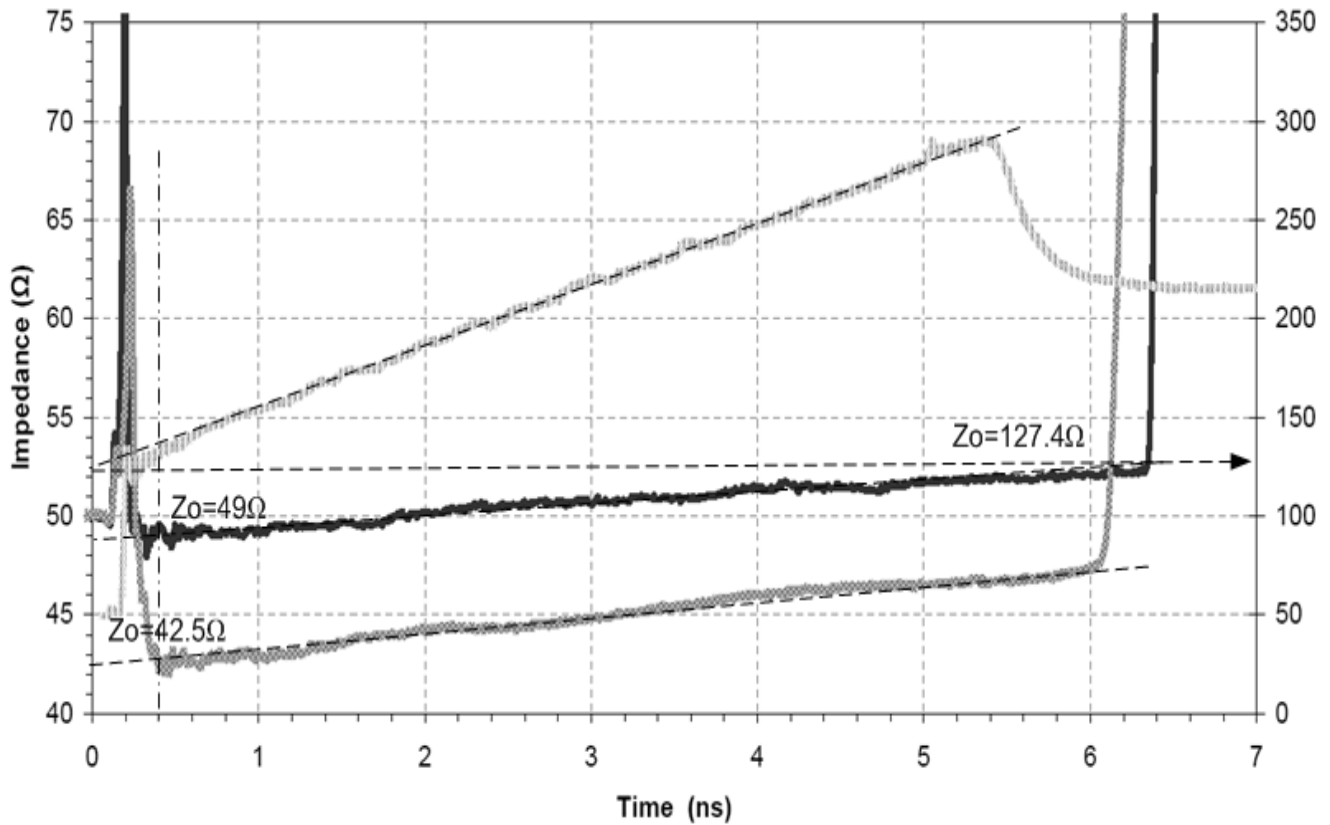


Figure 8. Impedance measurements of a three coaxial cables having different characteristic impedances. Note that the top waveform is plotted on the secondary axis on the right.

This was accomplished by measuring two coax transmission lines, 50Ω and 75Ω nominally and designing a full factorial 16 trial experiment design.

Since we have four variables (A=Coax impedance, B=TDR or TDT method, C=Open or 50Ω and D=setup 1 and 2) and two values each, it takes 16 trials ( $2^4$ ) to measure the effect of those variables and all possible interactions.

Fig. 9 shows the sensitivity (Effects) of the measurement contributed by the different variables, A the coax type (50Ω or 75Ω), B test method (TDR or TDT), C termination (open or 50Ω). The tests were repeated twice, so the last variable D represented setup.

Statistics teaches us to determine a criterion using a Student-t distribution to determine if the effect is significant based on the correct sample size (16), the standard deviation of the data (0.3Ω) and the significant economic resolution we desire for this experiment (0.7Ω). If any variable is above the criterion we can state that we have 95% confidence that it is significant (5% Alpha error) and 99% that we did not miss a significant effect (1% Beta error). The calculated criterion is 0.263Ω.

The results of the experiment are shown on Fig. 9. Total of 16 numbers are obtained as a result of processing the measurements. The first one is the average impedance of 63.13Ω. Rows 1 through 15 are the contributions of the

variables (A, B, C, D) to the different values used (75Ω and 50Ω coax, TDR or TDT, open end or terminated, setup) and their interactions (AB, AC, AD...ABC, ABD...ABCD). The Effects column is the difference between the two values of the variables.

Thus the measured difference of 25.56Ω between the nominal 75Ω and 50Ω coax is close to the expected value. Variable C (open or terminated end) is the next most significant value of the effect, but below the criterion threshold at 0.18Ω or 0.7% of the coax difference. Variable B (Test method TDR or TDT) and variable D (setup) were 0.63% and 0.47% of the coax difference. This gave a solid indication that the method is quite insensitive to the chosen variables.

### B. Repeatability

The repeatability of the measurement is demonstrated by measuring 36 coaxes using two different Tektronix oscilloscopes (“Production TDS8200” and “Engineering TDS8200”). Both instruments were calibrated using a 50Ω standard. Each coaxial cable was serialized and measured at random.

Thus we have three sets of 36 points: two sets (A#1 and A#2) measured with Engineering TDS8200 and a third set (B#1) measured with a Production TDS8200. The sets are ordered according to their serial number and plotted against each other in a scatter plot.

Response: Impedance Zo

### Measurement Sensitivity Analysis

Sort	Contrasts	μ	μ/σ	Average	Effects
1	A		15	63.131568	Coax
2	C			25.561188	Open or Terminated
3	-AB			0.1768199	
4	B			-0.167811	TDR or TDT
5	D			0.125573	Setup
6	ABD			-0.112572	
7	-BD			-0.101452	
8	-AC			0.1004689	
9	ABC			0.0877894	
10	-AD			0.0629353	
11	-BC			0.0438326	
12	-CD			0.0357233	
13	ACD			0.0207341	
14	BCD			-0.007553	
15	-ABCD			-0.001762	

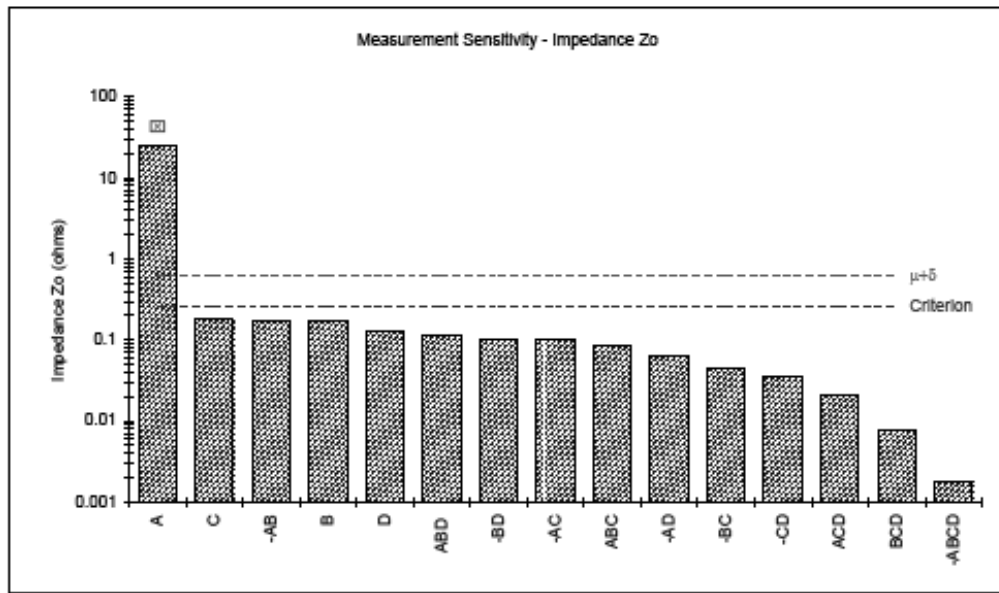


Figure 9. Experiment design results. Top table is the numerical values of the effects for different variation and the bottom plot shows their comparison on the log scale.

Fig. 10 shows the plot of set A#1 as the x axis and set B#1 as the y axis. Fig. 11 shows the plot of set A#1 as the x axis and set A#2 as the y axis.

Clearly, if the correlation was perfect, all 36 points will lie on the  $y=x$  line. The deviation from the straight line is the measurement error/noise. We can measure the imperfection by drawing a least square fit line based on the 36 points and drawing a “sausage” around the line encompassing all the points except the one deviating farthest from the line. The width of the “sausage” is an estimate of sigma or standard

deviation. The slope of the line should be close to 1 and the y intercept (or offset) measures the bias from one instrument to the other.

Another significant measure of the repeatability is the ratio of the length of the “sausage” to its width. This is the ability of the system to discriminate two measurements that are close together. It can be shown that a discrimination of 6:1 correspond to a correlation coefficient of 98% or  $R^2$  of .96. This is the minimum desirable discrimination for a suitable measurement system.

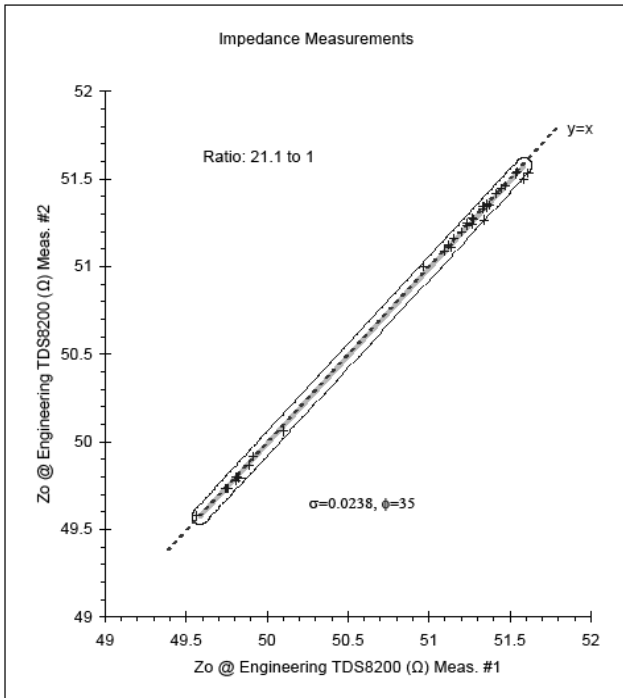


Figure 10. Same instrument scattering plot. The ratio of 21:1 is consistent with a correlation coefficient of 99.8%. The estimate of sigma is 0.024Ω.

Note the two populations between 49.5Ω and 51.5Ω. The ratio of 21:1 is consistent with a correlation coefficient of 99.8%. The estimate of sigma is 0.024Ω.

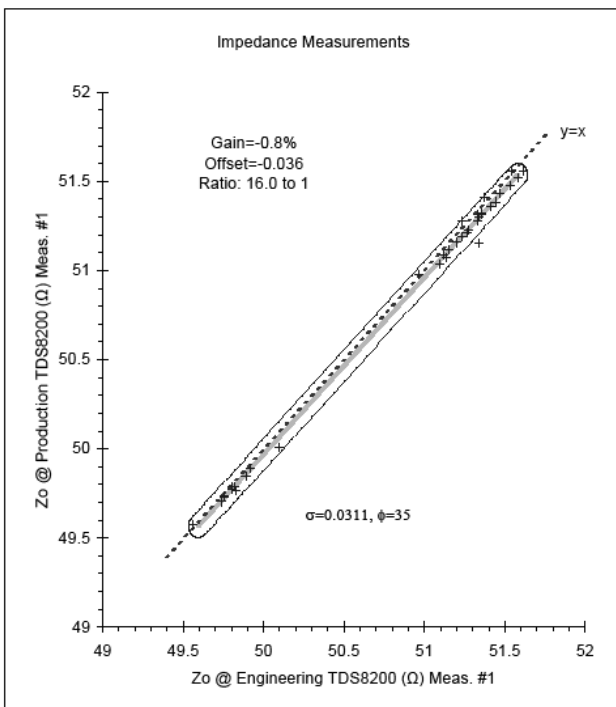


Figure 11. Different instrument scatter plot. The discrimination is 16:1 or a correlation coefficient of 99.7%. The estimate of sigma is 0.03Ω.

In this case the discrimination is 16:1 or a correlation coefficient of 99.7%. The estimate of sigma is 0.03Ω. The measurements in the Engineering instrument are an average of 0.036Ω below the measurements recorded in the Production instrument over a range of 2Ω (49.5Ω to 51.5Ω).

### C. Accuracy

Two independent ways were used to check the accuracy of the measurements. The first one was to measure the impedance of a precision termination resistor at the end of a semi-rigid transmission line and compare it with the reading measured using a 5 digit digital multi-meter (DMM). The results are as follows:

TDR method: Within  $\pm 0.014\Omega$  of 50.50Ω

TDT method: Within  $\pm 0.002\Omega$  of 50.50Ω

The second method was to compare the capacitance measured with a capacitor meter on a semi-rigid line<sup>3</sup> with the capacitance as calculated by measuring the impedance and the time delay using the following equation derived from (1) and (2):

$$C = \frac{T_d}{Z_0} \quad (8)$$

where  $T_d$  is the time delay in picoseconds, and  $Z_0$  the characteristic impedance in Ohms measured using the launch point extrapolation technique. The results are as follows:

Calculated capacitance: 286pF

Measured capacitance: 290pF

Difference: -1.4%

Previous measurements made using standard techniques of impedance zone averaging generated calculated capacitance values consistently 20 to 30% lower than what was measured using a capacitance meter. Since the time delay measurements were in agreement with the dielectric constant of the measured transmission lines, the characteristic impedance had to be too high. In addition, there was a variation depending on the zone where the average was measured due to the DC resistance of the sample.

## V. CONCLUSIONS

In this paper the time and frequency domain cable loss effects were analyzed and the launch point extrapolation methodology to measure the cable characteristic impedance was presented. The methodology provides an effective way to perform accurate and repeatable measurements of the cable characteristic impedance. The methodology can be applied to measure the cables of various length and physical properties. It produces repeatable results regardless of the variations of impedance as a function of cable length. It can also benefit an

<sup>3</sup> A semi-rigid line is in general more stable than the flexible coax.

engineer by providing a quantifiable way to evaluate cable changes as a function of temperature, humidity, stress and other environmental forces that will affect cable performance.

#### ACKNOWLEDGMENT

The authors thank Paul Hamilton and Tatyana Gushtyuk from Tyco Electronics Wilsonville, OR, who provided generous help with various measurements and paper revision.

#### REFERENCES

- [1] Serial ATA International Organization, *Serial ATA International Organization: Serial ATA Revision 2.6, Section 6.5.2.4*, February 2007.
- [2] TDR Test Method Task Group (D-24a), *Characteristic Impedance of Lines on Printed Boards by TDR*, IPC-TM-650 TEST METHODS MANUAL, 2.5.5.7, March 2004.
- [3] E. Bechhoefer and Jun Yu, *Algorithm Development to Ascertain the true Characteristic Impedance of a Wire for Wire Diagnostics*, IEEEAC paper #1104, January 4, 2005.
- [4] D. Derickson and M. Müller et al. *Digital Communications Test and Measurement*. Prentice Hall, 2008, pp. 659-661.
- [5] Tektronix, Inc. Beaverton, OR 97077, USA; [www.tek.com](http://www.tek.com).

# Comparison Between Root-Impulse-Energy and Vector Network Analyzer Methods for Measuring Loss on Printed Circuit Boards

Matthew R Harper, Nick M Ridler, *Senior Member, IEEE*, and Martin J Salter, *Member, IEEE*

**Abstract**— This paper presents a comparison of two methods for measuring the electrical loss for transmission lines on printed circuit boards (PCBs). The two methods are (i) the Root Impulse Energy (RIE) method which is a time-domain reflectometry (TDR)-based method using a pulse generator and a sampling oscilloscope and (ii) a method based on the use of a vector network analyzer (VNA) to measure the  $S$ -parameters of the line in the frequency domain. Results and uncertainties obtained by the two methods for connectorized microstrip lines on flexible FR4 are presented and compared.

**Index Terms**—Printed circuit testing, Scattering parameters, Time domain reflectometry.

## I. INTRODUCTION

The need to measure electrical loss of transmission lines on Printed Circuit Boards (PCBs) has arisen as data speeds in computers and communication systems have increased. Loss limits the bandwidth of a circuit and hence the speed at which the system can operate reliably [1, 2]. Measurement of this loss is important, both at the design stage and on the production floor, as part of the manufacturing quality control process. The IPC (the trade association for the electronics interconnect industry) [3] is proposing several possible methods for measuring PCB loss [4]. In this paper we implement two of these – the Root Impulse Energy (RIE) method and the Vector Network Analyzer (VNA) method – and make a comparison between the two.

Both techniques are used to measure the loss of three sets of microstrip lines fitted with SMA connectors on two flexible FR4 PCBs with nominally identical loss (making a total of six lines altogether). The two PCBs are identified as ‘#140’ and ‘#170’. The approximate lengths of the lines are listed in Table I. Sections II and III describe the techniques and present the results with uncertainties for the RIE- and VNA-based methods, respectively. The VNA results for the lines are further processed in Section IV in order to obtain loss values for comparison with those measured directly using the RIE method. Our conclusions are presented in Section V.

TABLE I  
PCB LINE LENGTHS

Line	Length, <sup>1</sup> mm (inches)
Short	125 (5)
Medium	250 (10)
Long	375 (15)

## II. RIE METHOD

The RIE method [4] uses Time Domain Reflectometry (TDR) to measure the difference in loss between two identically constructed PCB transmission lines of different length: a longer ('test') line and a shorter ('reference') line. Identical step pulses are injected into each of the lines with the far ends open circuited and the reflected step pulses are captured using a sampling oscilloscope. A measure of the energy contained in the reflected step, termed the RIE value ( $E$ ), is calculated as the square root of the integral of the squared derivative of the time domain voltage waveform  $V(t)$

$$E = \sqrt{\int \left(\frac{d}{dt} V(t)\right)^2 dt}.$$

The ratio between the RIE values of the test and reference lines,  $E_{test}$  and  $E_{ref}$ , will be proportional to the extra loss introduced by the additional length of the test line. Expressing this ratio in dB and dividing by twice the length difference (the pulses travel to the end of the lines and back) gives the RIE loss per unit length ( $\Lambda$ ) of the PCB line pair

$$\Lambda = \frac{1}{2(l_{test} - l_{ref})} 20 \log_{10} \left( \frac{E_{test}}{E_{ref}} \right) \quad (1)$$

where  $l_{test}$  and  $l_{ref}$  are the lengths of the two lines.

TDR measurements were made on each of the three lines on the two flexible FR4 PCBs using a combination of a sampling oscilloscope and a pulse generator as shown in Figure 1. The TDR sampling head used was a Tektronix SD-20 installed in a Tektronix CSA803A communications signal analyzer (oscilloscope) mainframe via an extension cable. A short length of SMA cable was used to connect the sampling head to

<sup>1</sup> Throughout this paper length values are expressed in millimeters, with approximate values in inches given alongside in parentheses.

the SMA input of the line being measured. The SD-20 uses a feed-through loop to accept a pulse from an external pulse generator for the TDR stimulus. The majority of the measurements were carried out using the nominal 150 ps rising step from a Wavetek 9530 oscilloscope calibrator. Some additional measurements were also carried out using the nominal 500 ps rising step from the Wavetek 9530 and the rising step calibration output of the CSA803A mainframe. The actual steps, as measured at the SMA cable output using an SD-32 sampling head, are shown in Figure 2. It was found that the typically 15 ps rising step of the calibration output had degraded to 28 ps after transfer through the feed-through loop and the SMA cable. Waveforms were acquired over 50 ns intervals with 2048 points per waveform. Oscilloscope averaging was set to four. Only single waveforms were acquired (as opposed to the averages of multiple acquired waveforms).

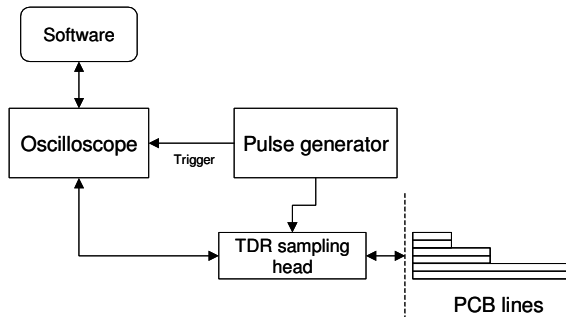


Fig 1: Schematic of the RIE measurement system used at NPL.

To calculate the RIE value, logic noise was first removed from the waveform according to [4] using the repetitive filtering algorithm

$$B_j = \frac{A_2 + \sum_{i=1}^j (2^{i-1} \cdot A_i)}{2^j}$$

where  $j$  is the index of an element in the waveform,  $A_j$  are the points of the input waveform and  $B_j$  are the points of the filtered waveform. Successive repetitions of the algorithm (setting  $A_j = B_j$  before each repetition) produce further filtering. For the 2048-point waveforms used here, the recommended number of six repetitions was used [4]. After filtering, the waveform was interpolated to 10,000 points, also in accordance with [4], before differentiation and integration was applied to obtain the RIE value.

As each PCB has three lines, there are three possible combinations of test and reference line. Therefore three values of RIE loss per unit length can be calculated using equation (1) and an average taken. If the SMA connectors are identical then effects of the connectors on the TDR step pulses will cancel out during the RIE calculation; therefore the RIE loss per unit length is purely for the transmission line itself.

A number of contributions to the uncertainty of the RIE loss

measurement have been identified and quantified. Table II lists these with the typical order of magnitude given as standard uncertainties. (Variability of pulse generator here means the difference between two nominally identical pulse generators.) It can be seen that currently the dominant contribution is the reproducibility of the returned values between different line pairs. Other likely uncertainty contributions that have been identified but not quantified and so not included in our analysis include, but are not limited to, the effect of the smoothing algorithm, the overall response of the TDR sampling module, differences in the nominally identical SMA connectors and detailed knowledge of the step pulse shape.

The two PCBs (#140 and #170) were each measured using the 150 ps step and the results are given in Table III. The uncertainties,  $U(\Lambda)$ , are for approximately 95% confidence.

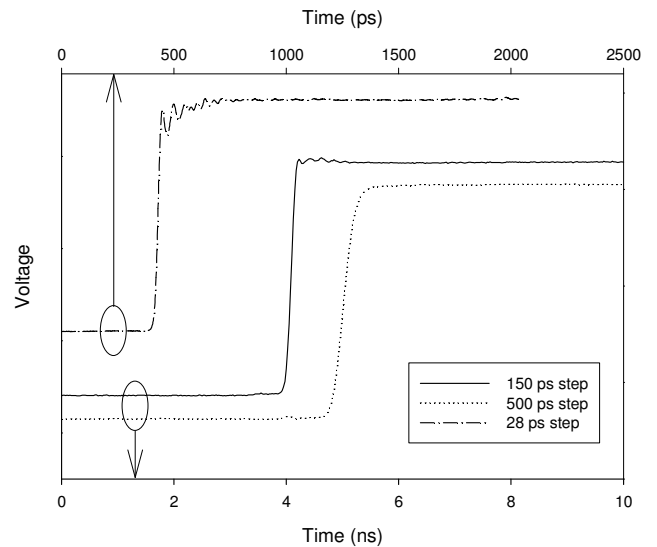


Figure 2: Comparison of the three step pulses used for TDR measurements. The pulses have been offset for clarity. The time axis for the fastest step is at the top of the plot.

TABLE II  
UNCERTAINTY CONTRIBUTIONS FOR RIE METHOD

Contribution	Standard uncertainty order of magnitude dB/mm
Repeatability of measurement	$10^{-5}$
Repeatability of connection	$10^{-5}$
Reproducibility between line pairs	$10^{-3}$
Length of line	$10^{-5}$
Choice of differentiation method	$10^{-5}$
Choice of integration method	$10^{-6}$
Variability of pulse generator	$10^{-4}$

TABLE III  
RIE LOSS ( $\Lambda$ ) MEASURED WITH A 150 PS STEP

PCB	$\Lambda$ dB/mm (dB/inch)	$U(\Lambda)$ dB/mm (dB/inch)
#140	0.006 7 (0.17)	0.001 0 (0.03)
#170	0.006 5 (0.17)	0.001 4 (0.04)

In addition, #140 was measured with the 500 ps and 28 ps steps. The results are given in Table IV, again with uncertainties,  $U(\Lambda)$ , for approximately 95% confidence. It can be seen that the measured RIE loss increases as the risetime of the step pulse decreases i.e. as the step becomes faster. This is expected since a step with shorter risetime contains more high frequency components than a step with longer risetime and the loss of a PCB transmission line increases with frequency. Nevertheless, it demonstrates the importance of specifying the step risetime used when defining an RIE measurement.

TABLE IV  
RIE LOSS ( $\Lambda$ ) MEASURED WITH STEPS OF VARIOUS RISETIMES FOR #140

Step risetime (ps)	$\Lambda$ dB/mm (dB/inch)	$U(\Lambda)$ dB/mm (dB/inch)
500	0.004 4 (0.11)	0.000 6 (0.02)
150	0.006 7 (0.17)	0.001 0 (0.03)
28	0.007 7 (0.20)	0.003 0 (0.08)

### III. VNA METHOD

In the VNA method a 2-port VNA is used to measure the  $S$ -parameters of a length of PCB transmission line as a function of frequency and a frequency dependent measure of the loss of the line is calculated from the  $S$ -parameters. The VNA method used in this paper differs somewhat from that given by the IPC in that a correction is applied to take into account the mismatch between the VNA and the PCB line. This correction uses all four measured  $S$ -parameters of the line.

The dissipative component of attenuation<sup>2</sup> [5] at a particular frequency for a 2-port device in the forward direction (expressed in dB),  $A_{dF}$ , is given by

$$A_{dF} = 10 \log_{10} \left( \frac{P_{IN1}}{P_{OUT2}} \right) = 10 \log_{10} \left( \frac{1 - |S_{11}|^2}{|S_{21}|^2} \right)$$

whilst the corresponding quantity in the reverse direction,  $A_{dR}$ , is

$$A_{dR} = 10 \log_{10} \left( \frac{P_{IN2}}{P_{OUT1}} \right) = 10 \log_{10} \left( \frac{1 - |S_{22}|^2}{|S_{12}|^2} \right).$$

In these equations  $P_{IN1}$  is the net power accepted at port 1 and  $P_{OUT2}$  is the power dissipated in a matched load connected to port 2 and similarly for  $P_{IN2}$  and  $P_{OUT1}$ . For a section of reciprocal transmission line, the mean of these two attenuation values provides an estimate of the dissipative component of attenuation,  $A_d$ , depending on all four  $S$ -parameters of the line as follows

<sup>2</sup> The attenuation of a 2-port device is the insertion loss of the device in a matched system. It can be considered to have two components: one associated with the dissipation of energy and one associated with mismatch.

$$A_d = \frac{1}{2} (A_{dF} + A_{dR}) \\ = \frac{1}{2} 10 \log_{10} \left( \frac{(1 - |S_{11}|^2)(1 - |S_{22}|^2)}{|S_{12}S_{21}|^2} \right).$$

If the line is of length  $l$ , the loss per unit length  $L$  is given by

$$L = \frac{A_d}{l} = \frac{1}{2l} 10 \log_{10} \left( \frac{(1 - |S_{11}|^2)(1 - |S_{22}|^2)}{|S_{12}S_{21}|^2} \right) \quad (2)$$

In order to estimate the uncertainty in the determination of  $L$ , first we obtain the sensitivity coefficients using partial differentiation

$$c_{|S_{11}|} = \frac{\partial L}{\partial |S_{11}|} = -\frac{4.3429}{l} \frac{|S_{11}|}{(1 - |S_{11}|^2)} \\ c_{|S_{22}|} = \frac{\partial L}{\partial |S_{22}|} = -\frac{4.3429}{l} \frac{|S_{22}|}{(1 - |S_{22}|^2)} \\ c_{|S_{21}|} = \frac{\partial L}{\partial |S_{21}|} = -\frac{4.3429}{l} \frac{1}{|S_{21}|} \\ c_{|S_{12}|} = \frac{\partial L}{\partial |S_{12}|} = -\frac{4.3429}{l} \frac{1}{|S_{12}|} \\ c_l = \frac{\partial L}{\partial l} = -\frac{L}{l}.$$

Then, using the law of propagation of uncertainty [6] and ignoring any correlation that may exist between the input quantities, the standard uncertainty in the loss,  $u(L)$ , is given by

$$u(L) = \sqrt{c_{|S_{11}|}^2 u^2(|S_{11}|) + c_{|S_{22}|}^2 u^2(|S_{22}|) + c_{|S_{21}|}^2 u^2(|S_{21}|) + c_{|S_{12}|}^2 u^2(|S_{12}|) + c_l^2 u^2(l)}$$

where  $u(|S_{11}|)$ ,  $u(|S_{22}|)$ ,  $u(|S_{21}|)$  and  $u(|S_{12}|)$  are the standard uncertainties in the magnitudes of the  $S$ -parameters and  $u(l)$  is the standard uncertainty in the length of the line. Assuming the output quantity  $L$  is normally distributed, and the effective degrees of freedom is sufficiently large, for a coverage interval with a coverage probability of approximately 95% a coverage factor  $k=2$  can be used and the expanded uncertainty in the loss is given by

$$U(L) = 2u(L). \quad (3)$$

All four  $S$ -parameters of the three PCB transmission lines on each of the two PCBs were measured in the frequency domain using a VNA from 100 MHz to 20 GHz in 100 MHz steps. The VNA was calibrated using a TRL/LRL based calibration scheme using NPL's Primary Impedance Measurement System (PIMMS) [7].

For each line, the loss per unit length (dB/mm) was

calculated from the measured  $S$ -parameters using equation (2) and the corresponding expanded uncertainty was calculated using equation (3). The standard uncertainties in the magnitude of the  $S$ -parameters and in the lengths of the lines were estimated and used to calculate the uncertainty in  $L$ . Figure 3 shows the resulting loss per unit length ( $L$ ) values for the short and long lines on #140 as a function of frequency together with error bars representing the corresponding expanded uncertainties. Similar results were obtained for the medium line on #140 and for all the lines on #170. Generally, the losses per unit length for all six lines on the two PCBs agree within the stated uncertainties. An exception to this is shown in Figure 3 where the loss determined for the long and short line disagree above about 12 GHz. The loss determined for the long line shows a smooth variation with frequency whilst that for the short line shows a more irregular frequency dependence. The reason for this is not fully understood and requires further investigation but could include the onset of higher-order modes propagating along the line. Table V lists some values of the loss  $L$  measured for the long line on #140 together with the corresponding uncertainties,  $U(L)$ , for approximately 95% confidence.

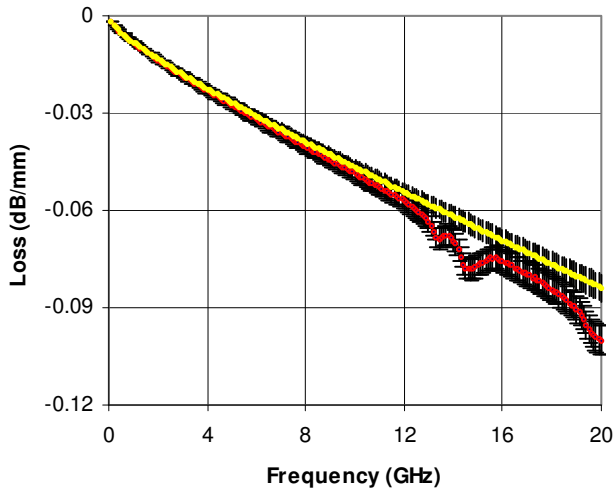


Figure 3: Loss per unit length for short and long length transmission lines on PCB #140. The loss varies smoothly with frequency for the long line but shows a more irregular variation with frequency for the short line.

TABLE V  
VNA LOSS ( $L$ ) MEASURED FOR LONG LINE ON PCB #140

Frequency (GHz)	$L$ (dB/mm (dB/inch))	$U(L)$ (dB/mm (dB/inch))
0.1	0.001 90 (0.048 2)	0.000 07 (0.001 7)
10	0.046 7 (1.187)	0.002 3 (0.058)
20	0.083 8 (2.19)	0.004 2 (0.11)

Figure 4 shows the return loss corresponding to  $S_{11}$  for one of the PCB transmission lines. This is representative of the return loss seen at either end of all six lines on the two PCBs.

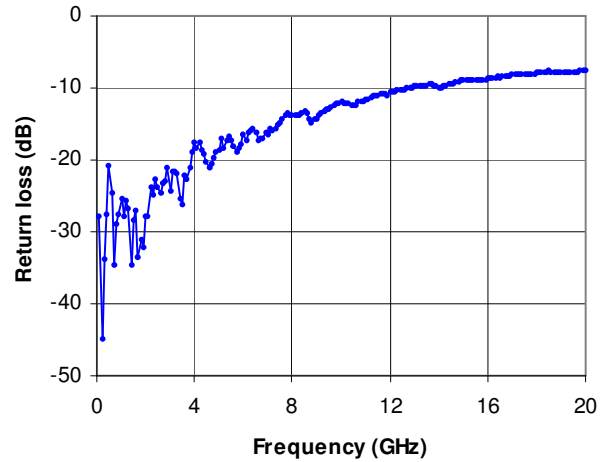


Figure 4: Typical input return loss for the PCB lines.

#### IV. COMPARISON BETWEEN THE TWO METHODS

The RIE method quantifies PCB loss as a single value by considering the differences in energy between injected step pulses reflected from open-circuited PCB test lines of varying lengths (equation (1)). On the other hand, the VNA method quantifies PCB loss as a function of frequency by swept frequency excitation of a PCB test line (equation (2)). To compare the methods we can consider the total energy transmitted through a line during a VNA measurement by integrating the relevant  $S$ -parameters over frequency<sup>3</sup>. Doing this for both a test and reference line, taking the ratio in dB and dividing by the length difference provides an RIE loss-per-unit-length  $\Lambda_{VNA}$  for comparison with the TDR-derived value  $\Lambda$ . The expression for  $\Lambda_{VNA}$  is shown in equation (4). We note that, although the  $S$ -parameters express ratios of output power to input power, the ratio used in calculating  $\Lambda_{VNA}$  causes the input power values to cancel out and so only the measured output powers contribute (assuming identical input powers in each case). We also note that the VNA-based RIE method is single pass, as opposed to the double pass of the TDR-based RIE method, when determining RIE loss per unit length.

The VNA-based RIE loss-per-unit-length  $\Lambda_{VNA}$  is given by

$$\Lambda_{VNA} = \frac{1}{l_{test} - l_{ref}} 20 \log_{10} \frac{\sqrt{\int_0^{f_{MAX}} R_{test}(f) df}}{\sqrt{\int_0^{f_{MAX}} R_{ref}(f) df}} \quad (4)$$

where  $R_{test}(f)$  and  $R_{ref}(f)$  measure the energy transmitted at frequency  $f$  during one pass along the test and reference line respectively,  $f_{MAX}$  is the maximum frequency of interest and  $l_{test}$  and  $l_{ref}$  are the lengths of the test and reference lines. The quantities  $R_{test}(f)$  and  $R_{ref}(f)$  are calculated from the

<sup>3</sup> Recall that the raw measured data for the VNA method consists of all four  $S$ -parameters of the PCB line over a particular frequency range.

S-parameters of the test and reference line respectively as follows<sup>4</sup>

$$R(f) = \frac{|S_{12}S_{21}|}{\sqrt{(1-|S_{11}|^2)(1-|S_{22}|^2)}}.$$

From equation (4) it is apparent that  $\Lambda_{VNA}$  will be dependent on the frequency range over which the integration is carried out. In order to make a valid comparison with  $\Lambda$  this frequency range should match the frequency content of the step pulse.

The frequency content of a step pulse is often estimated using the following equation

$$\beta \approx \frac{0.35}{\tau} \quad (5)$$

where  $\tau$  is the 10% to 90% risetime of the step and  $\beta$  is the bandwidth (defined as the point at which the spectral content of the step pulse is 3 dB down from its value at dc). For a particular RIE pulse, the following procedure can thus be used to calculate a value of  $\Lambda_{VNA}$  for comparison with  $\Lambda$  for one of the PCBs:

- calculate the bandwidth of the pulse from equation (5) and take this to be  $f_{MAX}$  in equation (4)
- calculate  $\Lambda_{VNA}$  for each pair of test and reference lines on the PCB from equation (4) using this value of  $f_{MAX}$
- calculate the average value of  $\Lambda_{VNA}$  over the three combinations of test and reference on the PCB.

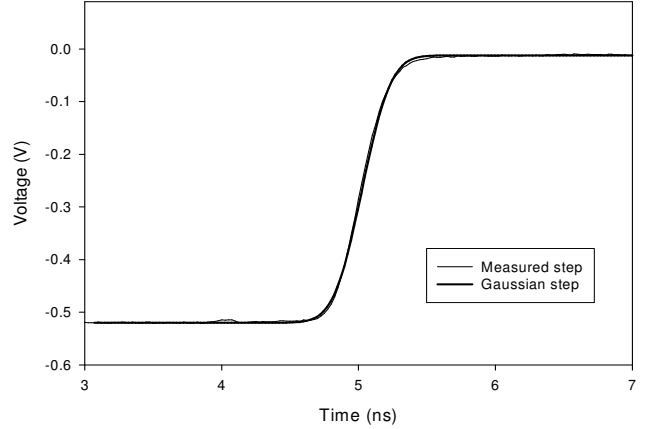
The values of  $\Lambda_{VNA}$  thus obtained for the three different pulses used in the RIE method for PCB #140 are shown in Table VI together with the corresponding values of  $\Lambda$ .

It can be seen that  $\Lambda$  and  $\Lambda_{VNA}$  are in good agreement for the 500 ps pulse but diverge as the pulse risetime gets shorter. The reason for this is that equation (5) is derived for Gaussian step pulses but the shorter risetime (faster) pulses used here are less well approximated by Gaussian steps (Figure 5). Therefore two pulses of equal risetimes but different shape can be expected to produce different RIE loss values due to their differing bandwidths (frequency content).

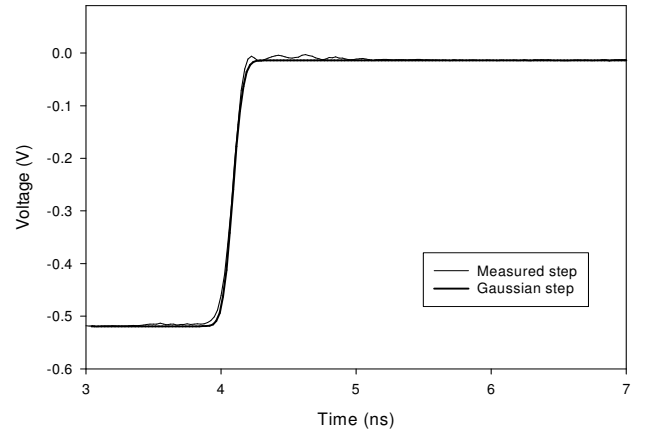
TABLE VI  
COMPARISON OF  $\Lambda_{VNA}$  WITH  $\Lambda$   
WITH UPPER FREQUENCY OF PULSES DETERMINED BY GAUSSIAN ASSUMPTION

Step		RIE loss per unit length dB/mm (dB/inch)	
Risetime (ps)	Bandwidth (GHz)	$\Lambda_{VNA}$	$\Lambda$
500	0.7	0.004 2 (0.11)	0.004 4 (0.11)
150	2.3	0.008 1 (0.21)	0.006 7 (0.17)
28	12.5	0.019 2 (0.48)	0.007 7 (0.20)

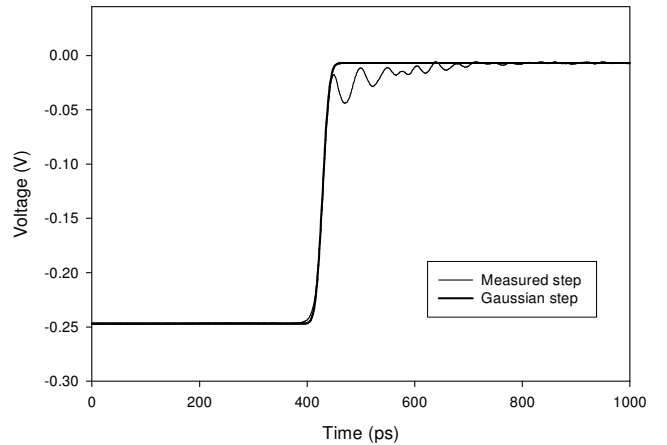
<sup>4</sup>  $R$  represents an average (geometric mean) of the ratio of output power to net input power taken in the forward and reverse directions.



(a): 500 ps pulse compared with Gaussian step



(b): 150 ps pulse compared with Gaussian step



(c): 28 ps pulse compared with Gaussian step

Figure 5: The TDR step pulses as measured at the input to the test lines, compared with modeled Gaussian steps. The steps become less Gaussian as the risetime decreases.

To obtain a more accurate estimate of the frequency content of the faster step pulses, their 3 dB points were determined directly from the Fast Fourier Transforms (FFTs) of their derivatives (Figure 6) and these new values used in the

calculation of  $\Lambda_{VNA}$ . The results are given in Table VII, again with the corresponding values measured directly by the RIE method ( $\Lambda$ ), showing that the agreement between the two methods has greatly improved. We note that the accuracy of these results is affected by the frequency resolution of the VNA measurements (100 MHz/point) and the achievable frequency range and resolution when taking FFTs of the RIE method measurements (20 GHz epoch, 20 MHz/point).

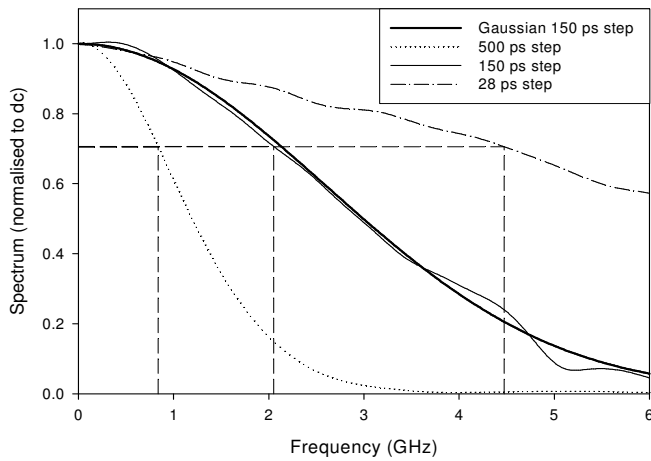


Figure 6: Determination of the step bandwidths. The 3dB point ( $1/\sqrt{2}$ ) of each step is marked by dashed lines. A Gaussian 150 ps step has been included to illustrate the frequency shift of the 3 dB point.

TABLE VII  
COMPARISON OF  $\Lambda_{VNA}$  AND  $\Lambda$

WITH UPPER FREQUENCY OF PULSES DETERMINED FROM ENERGY SPECTRUM

Step		RIE loss per unit length dB/mm (dB/inch)	
Risetime (ps)	Bandwidth (GHz)	$\Lambda_{VNA}$	$\Lambda$
500	0.8	0.004 5 (0.11)	0.004 4 (0.11)
150	2.0	0.007 5 (0.19)	0.006 7 (0.17)
28	4.5	0.011 9 (0.30)	0.007 7 (0.20)

## V CONCLUSION

Two methods have been considered for the determination of PCB line loss: a time domain method (RIE method) and a frequency domain method (VNA method). These methods measure the loss in the transmission lines by taking into account the mismatch component due to the launch mechanism (for the RIE method by normalizing to a reference line and for the VNA method by applying a mismatch correction). Both have been applied to the determination of loss in two nominally identical FR4 PCBs and estimates of the measurement uncertainty have been given in each case. For comparison of the two methods, calculation of RIE loss-per-unit-length values from the VNA method results has been demonstrated and these show good agreement with the values obtained directly by the RIE method. It is apparent that not only the risetime of the step pulse used but also its shape have a significant effect on the RIE loss values obtained using TDR.

## VI ACKNOWLEDGEMENTS

The authors would like to thank Polar Instruments for supplying the two PCB test sets, Mr Güner Ibrahim for performing the VNA measurements and Emma Sayer for her help with the TDR measurements.

## REFERENCES

- [1] International Technology Roadmap for Semiconductors (ITRS), [www.itrs.net](http://www.itrs.net).
- [2] Eric Bogatin, "Signal Integrity – simplified", Prentice-Hall, Upper Saddle River, NJ, 2004.
- [3] IPC – "Association Connecting Electronics Industries", [www.ipc.org](http://www.ipc.org)
- [4] IPC TM-650 Test Methods Manual, Method 2.5.5.12: Signal Propagation Loss", Working draft, rev. 0.5, November 2007, <http://www.ipc.org/CommitteeDetail.aspx?Committee=D-24B>.
- [5] D M Kerns and R W Beatty, "Basic theory of waveguide junctions and introductory microwave network analysis", Pergamon Press Inc, New York, 1967.
- [6] Guide to the expression of uncertainty in measurement", 2<sup>nd</sup> Edition, ISO, Geneva, 1995.
- [7] N M Ridler, "A review of existing national measurement standards for RF and microwave impedance parameters in the UK", IEE Colloquium Digest, No 99/008, pp 6/1-6/6, February 1999.

# Time-domain and mechanical assessments of 1.0 mm coaxial air lines

Masahiro Horibe, Masaaki Shida, Koji Komiyama

National Metrology Institute of Japan, National Institute of Advanced Industrial Science and Technology,  
Tsukuba, Ibaragi, 305-8563, Japan

**Abstract**— This paper presents an assessment of 1.0 mm coaxial air lines for use as reference impedance standards at microwave and millimeter-wave frequencies in frequency domain and time-domain measurements. The time-domain measurement has proved effective in the assessment of air lines [1]. Here, the assessments are performed for air lines in 1.0 mm line size and are based primarily on mechanical measurements and use several different types of time-domain reflection measurements with commercial Vector Network Analyzers (VNAs). This paper includes a comparison between the results obtained by these time-domain measurement options and mechanical measurement for reflections and electrical lengths. Frequency domain measurements up to 110 GHz are also included to complete the assessment.

**Index Terms**—Coaxial air lines, impedance standards, characteristic impedance, electrical delay, mechanical assessment, time-domain network analysis, 1.0 mm line size.

## I. INTRODUCTION

This paper reports on an investigation using time-domain reflection measurements to significantly improve the evaluation of unsupported coaxial air lines at millimeter-wave frequencies up to 110 GHz. Unsupported precision air dielectric coaxial transmission lines (i.e., air lines) are used as reference standards in impedance measurements at RF, microwave and millimeter-wave frequencies [2]–[4]. These air lines do not contain the dielectric support beads that typically position the center conductor inside the outer conductor. Here the center conductor is held only by the test ports of the measuring instrument to which it is connected. The absence of support beads means that the properties of air lines more closely approach the ideal properties.

To use an air line as a reference standard, it is necessary to know the characteristic impedance of the line. For example, values of characteristic impedance and phase are required in residual error evaluations [6] and in calibration schemes that use a Vector Network Analyzer (VNA) (i.e., TRL [5]).

At the accuracy levels now being required by end users, it is important to consider the departure of characteristics from ideal values. This implies the precise determination of the mechanical and material properties of the line's conductors. The mechanical properties (i.e., diameters and lengths) of the conductors are measured with air-gauging [7] and laser-gauging [8] instruments such that both center and outer conductor can be measured separately for unsupported air lines.

The characterization of air lines has been limited thus far to the mechanical measurement of the diameters of the line's

conductors and several national metrology institutes (NMIs) have developed diameter measurement capabilities using air-gauging and laser-gauging techniques specifically for measuring unsupported air lines. In addition to diameter measurements, the length of air line is also important and to obtain the length, we use a three-axis measuring machine. These diameter and length values then allow us to determine a mechanically-derived value for the characteristic impedance,  $Z_{\text{mech}}$ , and electrical phase-related delay of the line using:

$$Z_0 = \frac{1}{2\pi} \sqrt{\frac{\mu}{\epsilon}} \ln\left(\frac{b}{a}\right) \approx 59.939045 \times \ln\left(\frac{b}{a}\right) \quad (\Omega)$$
$$\text{delay} = \ell \sqrt{\mu\epsilon} \approx 3.336723 \cdot \ell \quad (\text{ps})$$

where:  $b$  = diameter of outer conductor (mm)  
 $a$  = diameter of center conductor (mm)  
 $l$  = length of outer conductor (mm)  
 $\epsilon$  =  $\epsilon_0\epsilon_r$   
 $\mu$  =  $\mu_0\mu_r$

The values of the constants are  $\epsilon_r = 1.000649$  for air at standard conditions (temperature 23 °C, relative humidity 50%, and pressure 1013.25 hPa) [9, 10] and  $\mu_r = 1$  (to six decimal places, for air at standard conditions).  $\epsilon_0$  is the permittivity of free space (defined as  $(c^2\mu_0)^{-1} = 8.854\,187\,817 \dots \times 10^{-12} \text{ Fm}^{-1}$ ) and  $\mu_0$  is the permeability of free space (defined as  $4\pi \times 10^{-7} \text{ Hm}^{-1}$ ).

Such mechanical characterization, however, does not evaluate other effects that, at millimeter-wave frequencies, can contribute significantly to the overall impedance of the air line – for example, reflections caused by the connectors at the ends of the line or variations in the conductivity of the line's elements. These effects will be observed when the line is used for high frequency electrical measurements, so it is desirable to include them when evaluating the line's characteristics and this requires electrical in addition to the mechanical measurements [1].

Traditional frequency-domain measurements of the  $S$ -parameters do not provide a direct measure of the magnitudes of these effects individually. Rather, they provide a measure of the combination of all such effects at any given frequency. Since these reflections are separated in distance, a more useful way of observing each effect separately is by making measurements in the time (i.e., distance) domain.



Fig. 1 1.0 mm coaxial air lines

TABLE I  
AIR LINE DESCRIPTIONS

Nominal line length	Manufacturer	Model number	Serial number
11 mm	Rosenberger	01S101-K011	84000
12 mm		01S101-K012	83995
16 mm		01S101-K016	84004

Three different types of time-domain measurement were included in this investigation:

- i) Band-pass;
- ii) Low-pass Impulse;
- iii) Low-pass Step.

These results are first compared to those obtained by mechanical measurements to assess the reliability and accuracy of the time-domain measurements. Finally, in addition to mechanically derived characteristics, some frequency-domain data are presented before and after ‘gating out’ in the time-domain, the effects due to the connectors and other discontinuities of the air lines.

## II. Air lines as impedance standards

All of the above tests leading to the establishment of S-parameter standards in 1.0 mm line sizes were carried out using three precision air lines with different nominal lengths (Fig. 1). The specifications of each line are described in Table I. All lines were of the same physical type, as described below:

- Insertable (i.e., with a male connector at one end and a female connector at the other end)
- Unsupported (i.e., containing no dielectric support beads to hold the center conductor in place)
- Nominal characteristic impedance of 50 ohms
- 1.0 mm line size, with nominal outer conductor internal



Fig. 2 Diameter measurement system for air lines

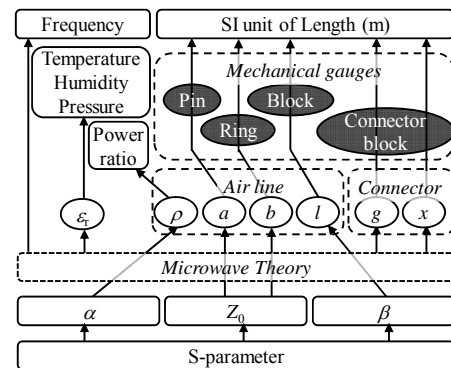


Fig. 3 Traceability chart of S-parameter standards in NMIJ

diameter of 1.000 mm and nominal center conductor diameter of 0.434 mm [11]

- Fitted with 1.0 mm precision coaxial connectors [11]
- Nominal length of 11 mm, 12 mm and 16 mm.

## III. Mechanical Assessments

The outer diameter of the center conductor,  $a$ , and the inner diameter of the outer conductor,  $b$ , were measured using the Air Gauge Measurement System (AGMS) shown in Fig. 2 and a Laser Gauge Measurement System (LGMS) described elsewhere [12]. With these systems a 1.0 mm line size can be measured in lengths to 20 mm. In the AGMS measurements, the ends of the air lines were connected to the adapters using a torque wrench to obtain the mechanical distortions typical of the line in use [13]. The value of  $b$ , around both connector ends, was observed by a three-axis measuring machine (3DCMM). The length,  $l$ , of the outer conductor was also measured using the 3DCMM when the line was connected to adapters.

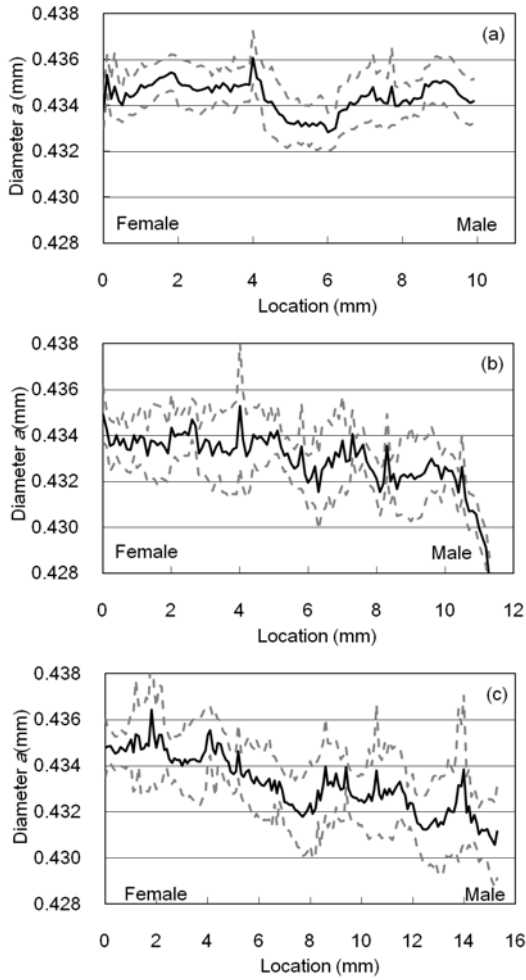


Fig. 4 Measurement results for diameter  $a$  of (a) 11 mm, (b) 12 mm and (c) 16 mm long air lines in 1.0 mm line size. Solid lines indicate the calibrated values and broken lines indicate the expanded uncertainties.

TABLE II

AVERAGE AND EXTREME VALUES OF OUTER DIAMETER

Line length	$a(\text{mm})$		
	Avg.	Min- $U(k=2)$	Max+ $U(k=2)$
11	0.4344	0.4372	0.4372
12	0.4340	0.4265	0.4380
16	0.4337	0.4300	0.4400

Other sources of reflection characteristics in air lines are gaps,  $g$ , and eccentricities,  $x$ , in the connectors. The gaps arise around mated surfaces due to varying pin-depths when the adapters are mated to the air line. The eccentricity of the air line was taken to be that of connectors on adapters and devices mated to the line. The eccentricity and pin-depth of test port adapters were evaluated using an optical displacement meter [14].

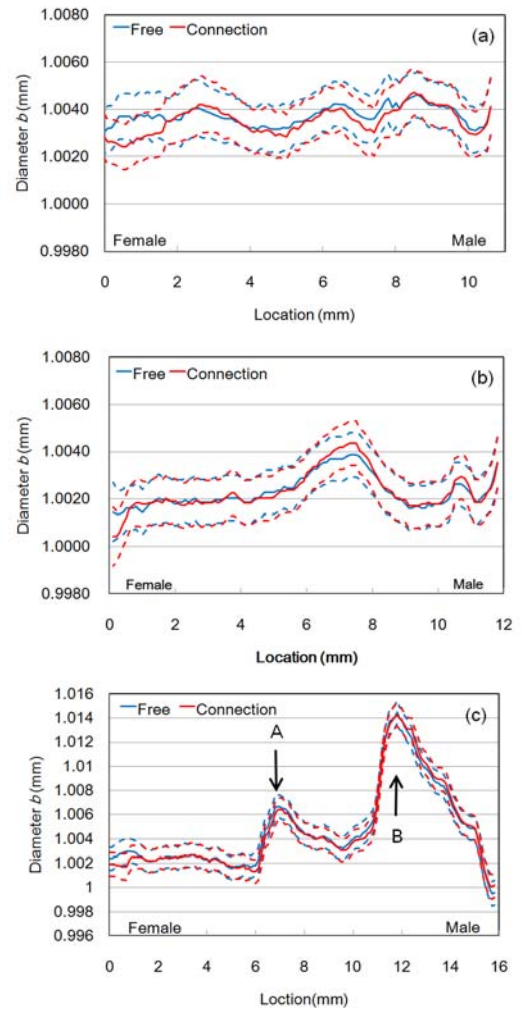


Fig. 5 Measurement results for diameter  $b$  of (a) 11 mm, (b) 12 mm and (c) 16 mm long air lines with (black lines) and without (gray lines) the connection to adapters at specified torques. Solid lines indicate the calibrated values and broken lines indicate the expanded uncertainties.

TABLE III

AVERAGE AND EXTREME VALUES OF INNER DIAMETER

Line length	$b(\text{mm})$		
	Avg.	Min- $U(k=2)$	Max+ $U(k=2)$
11	1.0017	0.9993	1.0073
12	1.0007	0.9980	1.0033
16	1.0034	1.0006	1.0151

In this way we were able to establish a traceability chart for the characterization of air lines, as shown in Fig. 3. In addition to the dimensions of the lines, these characterizations have taken into account the effects of frequency, temperature, relative humidity and atmospheric pressure.

TABLE IV  
LENGTH AND ELECTRICAL DELAY MEASUREMENTS

Nominal length	Length $l$ (mm)	Uncertainty ( $k=2$ ) ( $\mu\text{m}$ )	Delay (ps)	Uncertainty ( $k=2$ ) (ps)
11 mm	10.9929	1.7	36.680	0.006
12 mm	12.1335	1.7	40.486	0.006
16 mm	16.6764	1.7	55.645	0.006

#### A. Diameter measurements of center conductors

Figure 4 shows the measurement results of diameter  $a$  for air lines when connected to the center conductors used in adapters. The averaged value of diameter  $a$  was obtained from six measurements around the circumference at each location along the length of each line. This average value was  $0.4344 \text{ mm} \pm 0.5 \mu\text{m}$  for all center conductors with an uncertainty of  $3.0 \mu\text{m}$ . A major source of uncertainty was poor diameter uniformity. The difference between extreme values was approximately  $3.0 \mu\text{m}$  in the circumferential direction and  $4.0 \mu\text{m}$  in the length direction for a single line. Overall the maximum difference between extreme values of diameter  $a$  was less than  $10 \mu\text{m}$ . This is summarized in Table II.

#### B. Diameter measurements of outer conductors

Figure 5 shows the measurement results of  $b$  for air lines not connected and connected to the adapter at the specified torque of  $0.50 \text{ N}\cdot\text{m}$ . The resulting diameter deformations were observed near the connector ends and, at the female end, were between  $1.0 \mu\text{m}$  and  $2.0 \mu\text{m}$  for all air lines. The averaged value of diameter  $b$  was  $1.0000 \text{ mm} \pm 4.0 \mu\text{m}$  with an uncertainty of  $3.0 \mu\text{m}$ . This average was obtained by six measurements around the circumference at each location in length direction. Here too a major source of uncertainty was poor longitudinal diameter uniformity. The difference between extremes was  $3.0 \mu\text{m}$  in the circumferential direction. Longitudinal uniformity was good for the 11 mm long air line but for the 12 mm long air line the variation of  $b$  was greater than  $4.0 \mu\text{m}$ , and for the 16 mm air line, greater than  $15 \mu\text{m}$ . The locations of the extreme values on the 16 mm long line are indicated in Fig. 5(c) as 'A' and 'B' and are typically  $1.005 \text{ mm}$  and  $1.014 \text{ mm}$ , respectively. Table III summarizes these results.

#### C. Length measurements of air lines

The results of length measurements are summarized in Table V. The length is used to determine the electrical delay of the air line using equation (2). The uncertainty of length was  $1.7 \mu\text{m}$  for all lines. The major source of this is the systematic uncertainty of 3DCMM, but this contributes only  $0.006 \text{ ps}$  to the electrical delay ( $S_{12}$ ) and typically  $0.2^\circ$  to the phase offset ( $S_{21}$ ) of the air line. Of more significance, when

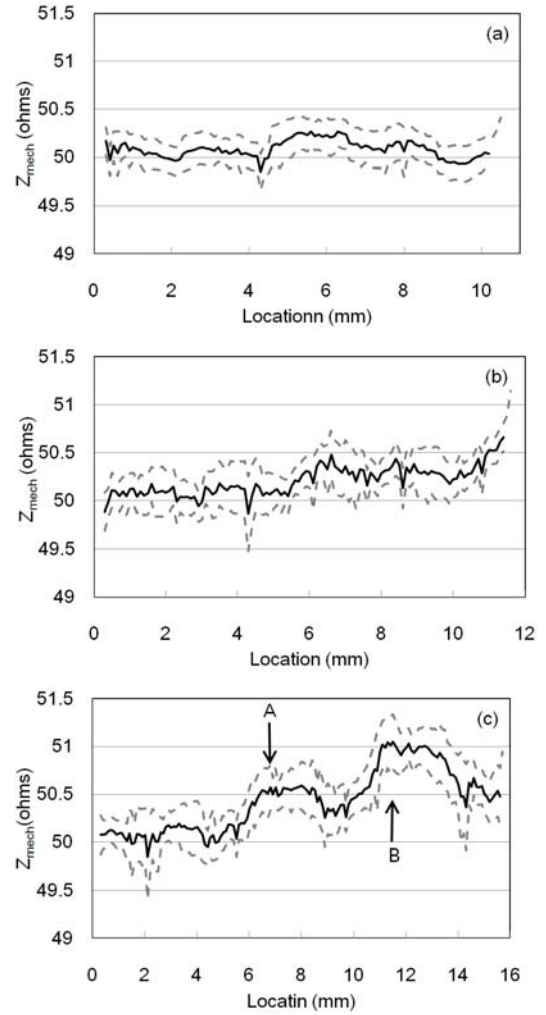


Fig. 6 Calculated mechanically-derived characteristic impedances of (a) 11 mm, (b) 12 mm and (c) 16 mm long air lines in 1.0 mm line size. Solid lines indicate the calibrated values and broken lines indicate expanded uncertainties.

TABLE V  
AVERAGE AND TWO EXTREME VALUES OF MECHANICALLY-DERIVED CHARACTERISTIC IMPEDANCE OF AIR LINE

Line length	$Z_0(\Omega)$		
	Avg.	Min- $U(k=2)$	Max+ $U(k=2)$
11	50.09	49.67	50.43
12	50.21	49.48	50.13
16	50.43	49.41	51.34

the air line was connected to the adapter it was observed that length was shortened as well as diameter  $b$ . The length compression was approximately  $12.0 \mu\text{m}$ , which was equivalent to  $1.6^\circ$  in the phase transmission characteristics of air line at  $110 \text{ GHz}$ .

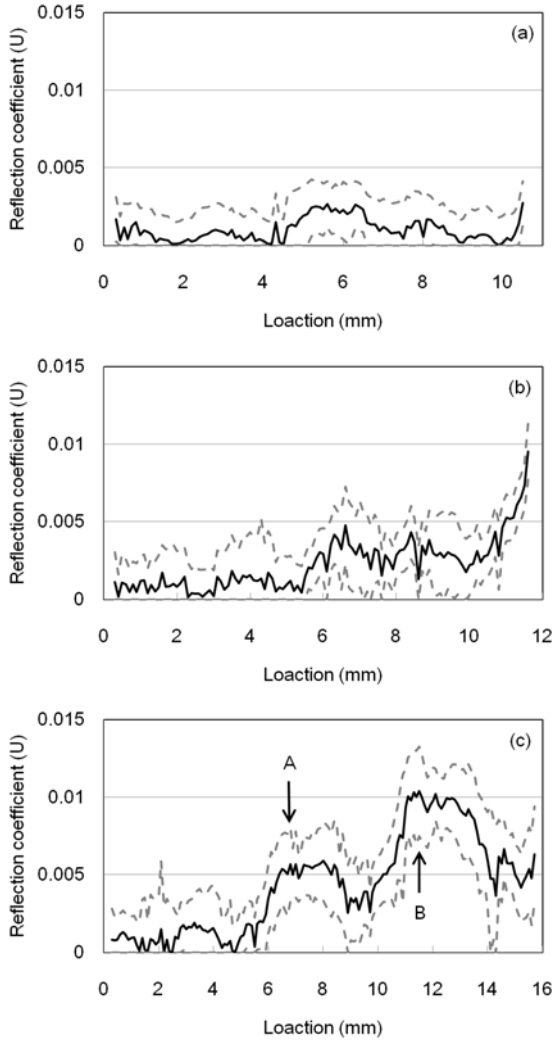


Fig. 7 Mechanically-derived reflection coefficient of (a) 11 mm, (b) 12 mm and (c) 16 mm long air lines in 1.0 mm line size. Solid lines indicate the calibrated values and broken lines indicate expanded uncertainties.

TABLE VI

AVERAGE AND TWO EXTREME VALUES OF MECHANICALLY-DERIVED REFLECTION COEFFICIENT OF AIR LINE

Line length	$\Gamma$   (mU)		
	Avg.	Min- $U(k=2)$	Max+ $U(k=2)$
11	1.0	0.0	4.2
12	2.2	0.0	11.3
16	4.3	0.0	13.3

#### D. Mechanically-derived characteristic impedance

The values of  $a$  and  $b$  are used to determine a value of characteristic impedance,  $Z_0$ , using equation (1). The value of  $Z_0$  is plotted in Fig. 6 with uncertainty limits, and then summarized in Table VI. The uncertainty of  $Z_0$  was also

TABLE VII

LOCATION OF REFLECTION POINT IN 16 MM LONG AIR LINE

Peak	Location		$\Gamma$   (mU)
	(mm)	(ps)	
A	6.8	22.7	5.7
B	11.5	38.4	10.4

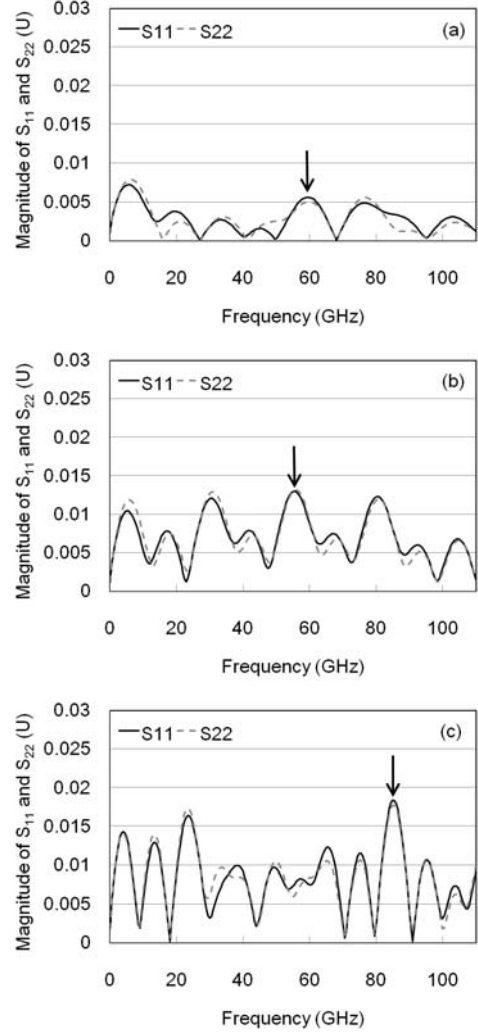


Fig. 8 Magnitude of mechanically-derived S parameters,  $S_{11}$  and  $S_{22}$ , of (a) 11 mm, (b) 12 mm and (c) 16 mm long air lines in 1.0 mm line size. Solid lines indicate the calibrated values and broken lines indicate expanded uncertainties.

calculated using the uncertainties of  $a$  and  $b$  on the basis of the method reported in Ref [15]. The value of  $Z_0$  was typically  $50 \Omega$  in the 11 mm air line with a maximum variation of  $0.4 \Omega$  even when the expanded uncertainty was taken into account. In the 12 mm long air line, as shown in Fig. 6(b), the value of  $Z_0$  is seen to be  $0.5 \Omega$  higher than nominal  $Z_0$  at the male end of air line. This higher impedance was caused by a reduced diameter  $a$  of the center conductor. In the 16 mm long air line,

TABLE VIII  
VNA DESCRIPTIONS AND CONFIGURATIONS

Hard ware	N5250 PNA
Calibration kit	85059A
Calibration method	Offset short
Test port Port1 – Port2	Male - Female
Frequency range	0.1 to 110 GHz (0.1 GHz-step)
Number of points	1100
IF Band Width	100 Hz

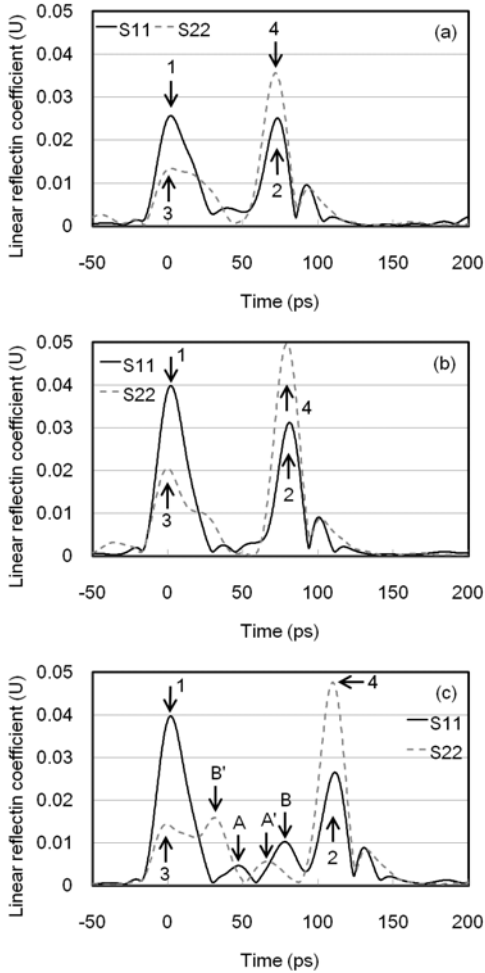


Fig. 9 Results of time-domain band-pass measurements for (a) 11 mm, (b) 12 mm and (c) 16 mm long air lines. Black solid and gray broken lines indicate the traces of  $S_{11}$  and  $S_{22}$ .

shown in Fig. 6(c), the value of  $Z_0$  at peaks 'A' and 'B' is seen to be  $0.5 \Omega$ ,  $1.0 \Omega$  higher than nominal  $Z_0$ . This higher impedance is attributed to the increased diameter  $b$  in contrast to the 12 mm long air line. Taking into account the expanded uncertainty, the maximum value of  $Z_0$  reaches  $50.86 \Omega$  in 16 mm long air line.

TABLE IX  
REFLECTION PEAKS IN TIME-DOMAIN BAND-PASS MEASUREMENTS

Line length	Peak number	Location		$ \Gamma $ (mU)	Delay (ps)
		ps	mm		
11	1	2.1	0.3	25.6	35.5
	2	73.1	10.9	25.1	
	3	2.1	0.3	13.5	34.8
	4	71.7	10.7	35.5	
12	1	2.1	0.3	39.8	39.5
	2	81.0	12.1	31.2	
	3	-0.2	0.0	20.6	39.8
	4	79.4	11.9	49.7	
16	1	2.1	0.3	39.7	54.6
	2	111.3	16.7	26.5	
	3	-0.9	-0.1	14.3	55.4
	4	109.9	16.5	47.7	
	A	47.1	7.1	4.6	
	B	77.8	11.7	10.2	
	A'	66.0	9.9	5.5	
	B'	31.2	4.7	15.9	

TABLE X  
ELECTRICAL DELAY ANALYSIS FROM MECHANICAL AND TIME-DOMAIN MEASUREMENTS

Line length	delay (ps)		
	Electrical	Mechanical	Difference
11	35.5 (1 / 2)*	36.7	-1.2
	34.8 (3 / 4)*		-1.9
12	39.5 (1 / 2)*	40.5	-1.0
	39.8 (3 / 4)*		-0.7
16	54.6 (1 / 2)*	55.6	-1.0
	55.4 (3 / 4)*		-0.2

\*The values in brackets indicate the start and end locations to determine the electrical values in the time-domain.

TABLE XI  
REFLECTION ANALYSIS FOR MECHANICAL AND TIME-DOMAIN MEASUREMENTS AT REFLECTION PEAKS IN 16 mm LONG AIR LINE

Peak number	$\Gamma$ (mU)		
	Electrical	Mechanical	Difference
A	4.6	5.7	-1.1
A'	5.5		-0.2
B	10.2	10.4	-0.2
B'	15.9		5.4

#### E. Mechanically-derived reflection coefficient

The values of  $Z_0$  were transformed to values of absolute magnitude of reflection coefficients on the basis of the calculation reported in Ref[16]. The reflection coefficient is plotted as a function of lengthwise location in Fig. 7. For the 11 mm air line the value is less than 5.0 mU even if we include the expanded uncertainty. For the 12 mm and 16mm long air lines, the value of reflection coefficient reached 10 mU. At peaks 'A' and 'B' on the 16 mm line the values reach 5 mU and 10 mU respectively as shown in Fig. 7(c). By taking into account the uncertainty, the maximum reflection value of

TABLE XII  
ANALYSIS OF MECHANICAL AND TIME-DOMAIN MEASUREMENTS AT  
REFLECTION PEAKS IN 16 MM LONG AIR LINE

Peak number	Location (ps)		
	Electrical	Mechanical	Difference
A	23.6 (1 / A)*	22.7	0.9
A'	21.5 (A' / 4)*		-1.2
B	38.9 (1 / B)*	38.4	0.5
B'	39.4 (B' / 4)*		1.0

\*The values in brackets indicate the start and end locations to determine the peak locations from the female connector ends in the time-domain.

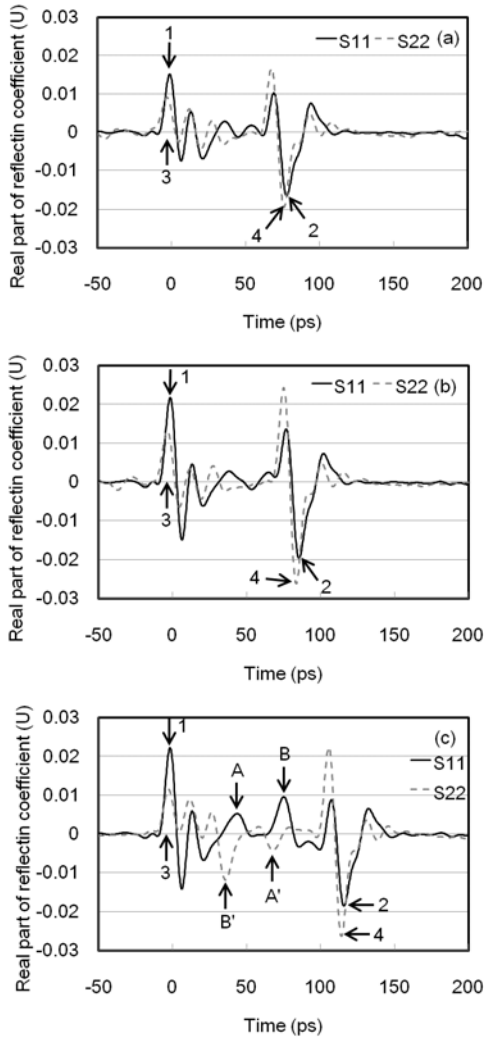


Fig. 10 Results of time-domain low-pass impulse measurements for (a) 11 mm, (b) 12 mm and (c) 16 mm long air lines. Black solid and gray broken lines indicate the traces of  $S_{11}$  and  $S_{22}$ .

13.3 mU is obtained for the 16 mm long air line as shown in Table VI.

TABLE XIII  
REFLECTION PEAKS IN TIME-DOMAIN LOW-PASS IMPULSE  
MEASUREMENTS

Line length	Peak number	Location		$ \Gamma $ (mU)	Delay (ps)
		ps	mm		
11	1	-1.3	-0.2	15.1	39.6
	2	77.8	11.7	-16.4	
	3	-3.1	-0.5	9.1	39.6
	4	76.0	11.4	-19.5	
12	1	-1.8	-0.3	21.8	43.7
	2	85.6	12.8	-19.7	
	3	-3.6	-0.5	13.2	43.6
	4	83.5	12.5	-26.1	
16	1	-1.8	-0.3	22.2	58.8
	2	115.8	17.4	-18.6	
	3	-2.7	-0.4	11.5	58.5
	4	114.2	17.1	-26.3	
	A	43.7	6.5	5.2	
	B	75.1	11.3	9.6	
	A'	67.8	10.2	-4.2	
	B'	35.8	5.45	-11.8	

#### F. Mechanically-derived S parameters

In addition to these calculations, the mechanically-derived S-parameters, as a function of frequency, have been calculated on the basis of the cascade model reported in Ref[12, 13]. For the 1.0 mm line size used here, the resistivity of the conductor was defined as  $9.0 \mu\Omega\text{cm}$ . Figure 8 shows the magnitudes of  $S_{11}$  and  $S_{22}$  for the three air lines as determined from mechanical measurements. The variation in values of  $S_{11}$  and  $S_{22}$  is attributed to the non-uniformity of diameters  $a$  and  $b$  along the lines. By taking the expanded uncertainty into account, the maximum value of reflection coefficient in the air line of 16 mm length reaches to 18.4 mU as shown in (c). No effects of reflections at the connector ends can be seen in this analysis.

### III. TIME-DOMAIN MEASUREMENTS

The time-domain measurements employed commercial VNAs and offered three different options for measuring reflections and characteristic impedances: band-pass, low-pass-impulse and low-pass-step. The descriptions and configurations of the VNAs are summarized in Table II. For all measurements reported here, the female ends of the air lines were connected to port 1 of the VNA and the male ends to port 2.

Time-domain measurements provide a useful tool for investigating the electrical properties of transmission lines as a function of distance. Each time-domain mode has specific characteristics for such an analysis. For example, the band-pass and low-pass impulse modes are well suited to determining the locations of sources of reflection. By

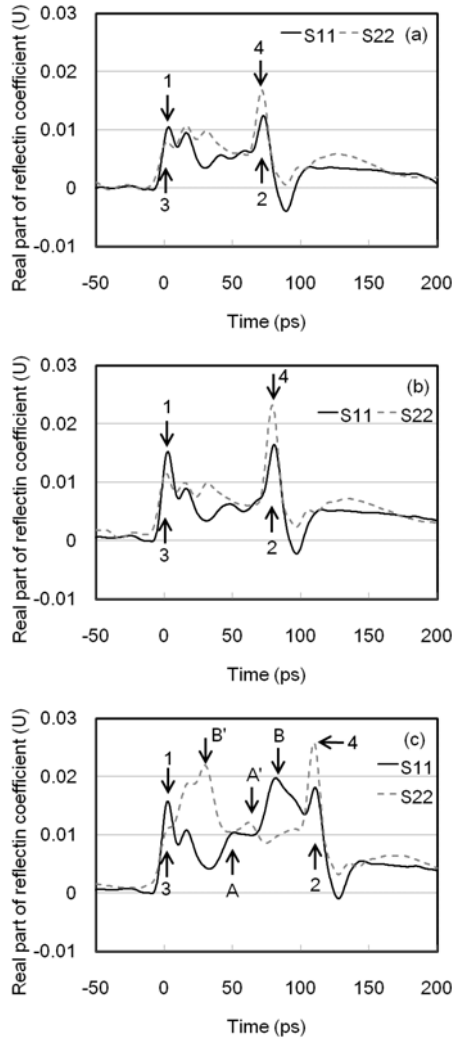


Fig. 11 Results of time-domain low-pass step measurements for (a) 11 mm, (b) 12 mm and (c) 16 mm long air lines. Black solid and gray broken lines indicate the traces of  $S_{11}$  and  $S_{22}$ .

detection of positive and/or negative peaks in the low-pass impulse mode, changes in the characteristic impedance of the air lines are estimated. The low-pass step mode also provides information concerning the characteristic impedance. The investigation in this report has focused on the potential for using these time-domain modes to characterize precision coaxial air lines as impedance references.

#### A. Band-pass Mode

Linear reflection coefficients in relation to size and location of reflection peaks were obtained with the time-domain band-pass mode as shown in Fig. 9 and summarized in Table IX. The maximum observed differences in the measured electrical delay times for  $S_{11}$  and  $S_{22}$  were less than 1.0 ps. Note in the figure the larger values of reflection for the female connectors (i.e., peak '1' or '4') in all cases, being typically 40

TABLE XIV  
REFLECTION PEAKS IN TIME-DOMAIN LOW-PASS STEP  
MEASUREMENTS

Line length	Peak number	Location		$ \Gamma $ (mU)	Delay (ps)
		ps	mm		
11	1	3.5	0.5	10.4	34.7
	2	72.8	10.9	12.4	
	3	2.3	0.3	7.9	34.6
	4	71.5	10.7	16.9	
12	1	2.8	0.4	15.2	38.9
	2	80.6	12.1	16.4	
	3	1.4	0.2	11.5	38.9
	4	79.2	11.9	23.2	
16	1	2.8	0.4	15.8	53.9
	2	110.6	16.6	18.1	
	3	4.6	0.7	11.3	52.5
	4	109.7	16.4	25.8	
	A	48.3	7.2	10.0	
	B	81.7	12.2	19.7	
	A'	61.9	9.3	12.1	
	B'	30.1	4.5	22.0	

mU compared with approximately 30 mU for the male connectors. This could be due to the slotted contact on the female connector ends. On the 11 mm air line the value of 30 mU observed for peak '2' was higher compared with the other lengths (i.e., 25 mU) and may be due to the shrinking diameter of center conductor in that line (cf. Fig. 4(b)).

Table X summarizes the electrical delays calculated from time-domain analysis and from mechanical length measurements of air lines. The electrically derived values agreed with the mechanically-derived values to within 1.9 ps. For the 16 mm air line, peaks 'A' and 'B' in the  $S_{11}$  traces and 'A' and 'B' in  $S_{22}$  traces are summarized in Table XI. The electrically derived reflection coefficients at locations 'A' and 'B' were 4.6 mU and 10.2 mU, respectively, in good agreement with the values of 5.7 mU and 10.4 mU obtained mechanically. The locations of peak 'A' and 'B' were found to be 22.6 ps and 37.9 ps from the female end, which agreed well with the value of 22.7 ps and 38.4 ps determined mechanically and listed in Table XII.

From these observations, it is clear that in the millimeter-wave frequency range time-domain band-pass measurements can significantly improve the characterization of air line electrical performance over that obtained from mechanical measurements alone.

#### B. Low-pass Impulse Mode

The results for the time-domain low-pass impulse measurements for all air lines are shown in Fig. 10 and summarized in terms of the observed reflection peaks in Table XIII. The low-pass impulse response can indicate the 'reactive' nature (i.e., either capacitive or inductive) of changes in the characteristic impedance along the air line in terms of the real part of the measured reflection coefficient. For example, the observed positive and negative peaks at each test port

indicated a change in the characteristic impedance of the air lines with respect to the nominal value of 50 ohms. In addition, for the 16 mm line, peaks were found at the locations of the large diameter of outer conductor (i.e., peak ‘A’ and ‘B’ in Table XIII). The relative sizes of peaks ‘A’ and ‘B’ indicate that the characteristic impedance of the line section in 16 mm air line was higher than the nominal characteristic impedance. This was consistent with the measured values of  $Z_{\text{mech}}$  for this section of the line, being 50.5 ohms and 51.0 ohms at ‘A’ and ‘B,’ respectively.

Based on these observations, it is considered that the time-domain low-pass impulse response for analysis of the characteristic impedance of an air line can be just as useful in the millimeter-wave frequency range as it is in the microwave frequency range.

### C. Low-pass Step Mode

Measurements of the time-domain low-pass step response are shown in Fig. 11. In Table XIV these results are summarized, as before, in terms of the observed reflection peaks. As with the low-pass impulse response, the low-pass step response can indicate the ‘reactive’ nature of changing impedance along an air line as well as the characteristic impedance as a function of line length. For example, in the 16 mm line, peaks ‘A’ and ‘B’ were the responses to the high impedance section of air line caused by the larger diameter of outer conductor – the values for these peaks (i.e. 10 mU and 20 mU) are equivalent to a characteristic impedance of 51.0 ohms and 52.0 ohms respectively, which agreed well with the value of  $Z_{\text{mech}}$  for this section of the line (i.e., 51.0 ohms).

## IV. FREQUENCY-DOMAIN MEASUREMENTS

Reflection coefficients determined from frequency-domain measurements for each air line are shown in Fig. 12. The values were approximately 100 mU at frequencies up to near 110 GHz. The ripples on the observed traces are due to reflections caused by a combination of the reflections at each end of the line and at inhomogeneities along its length. As we saw above the mechanically-derived reflection coefficients shown in Fig. 7, and the mechanically-derived magnitudes of  $S_{11}$  and  $S_{22}$  shown in Fig. 8, were approximately 15 mU, which values are one order lower than the values obtained in frequency domain measurements.

A much higher reflection coefficient is noted at frequencies above 70 GHz, especially for 16 mm long air line (Fig. 12c). This may indicate the presence of VNA systematic error (i.e., port match error), which may be larger than that in the microwave frequency region. However, these frequency-domain measurements could only indicate the overall characteristics of the air lines. By taking into account the time-

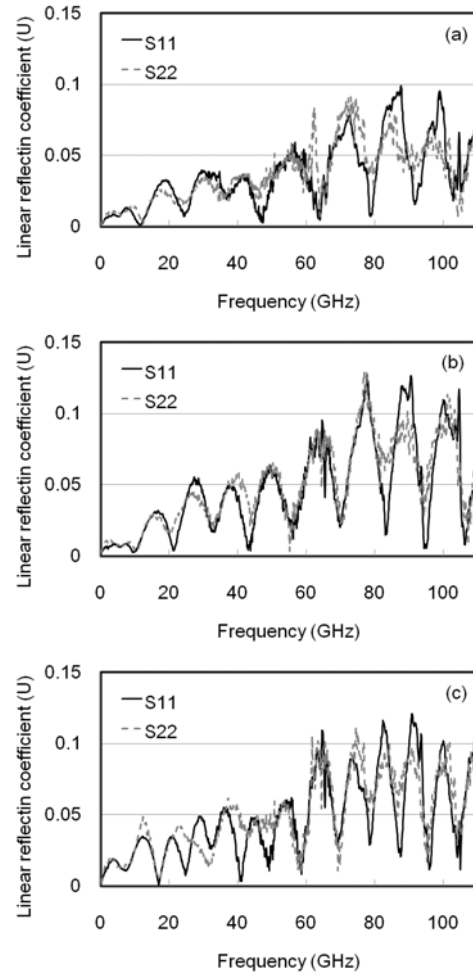


Fig. 12 Results of frequency-domain measurements for (a) 11 mm, (b) 12 mm and (c) 16 mm long air lines. Black solid and gray broken lines indicate the traces of  $S_{11}$  and  $S_{22}$ .

domain band pass measurements of Fig. 9, the peak values of  $S_{11}$  and  $S_{22}$  derived from electrical measurements are in general agreement with the values obtained here by combining the reflection characteristics at both connector ends (i.e., approximately 80 mU).

Clearly the observed characteristics of the lines are dominated by the effects of the connectors at both ends. The time-gate technique can be used to separate the characteristics of the line section from those due to the connectors [1]. This is illustrated in Fig. 13 where the maximum reflection peaks on the frequency-domain response, because of time gating, are found to eliminate the reflection characteristics of connector ends. The configurations used for the time-gating process are given in Table XV.

TABLE XV  
CONFIGURATIONS OF TIME-DOMAIN MEASUREMENTS FOR  
FREQUENCY-DOMAIN ANALYSIS

Resolution [17]	17.743 ps / 5.318 mm
Gating time start / stop (ps)	11mm: 32 / 52 12mm: 30 / 62 16mm: 29 / 91

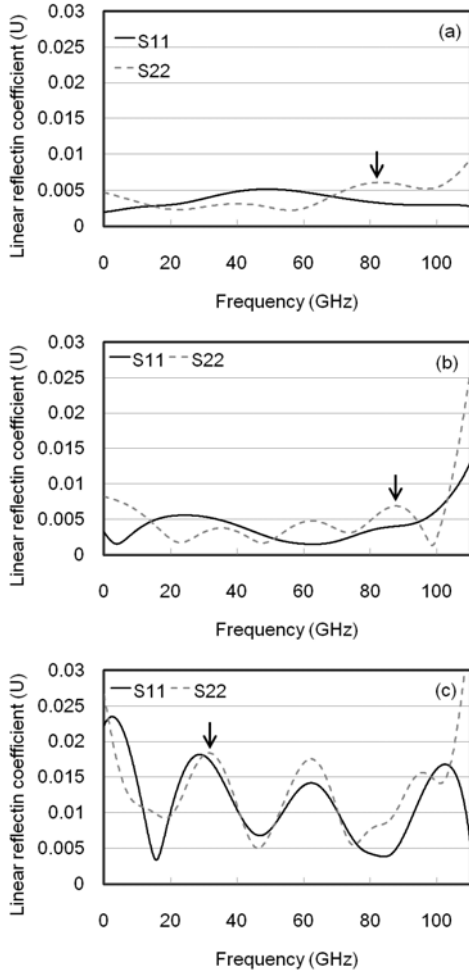


Fig. 13 Results of frequency-domain measurements with time-gate for (a) 11 mm, (b) 12 mm and (c) 16 mm long air lines. Black solid and gray broken lines indicate the traces of  $S_{11}$  and  $S_{22}$ .

Figure 13 shows the linear reflection coefficients obtained in the frequency-domain after applying the time-gate to all air line measurements. The arrows indicate the maximum reflection peaks for the measurement of each air line in the frequency range from 10 GHz to 100 GHz. The responses exhibit band edge effects (i.e., below approximately 10 GHz and above approximately 100 GHz) that result in artificially high values of reflection coefficient. This is due to the gating process. These band edge regions have been excluded in the determination of the maximum peak of reflection coefficient. These electrical reflection coefficient

TABLE XVI  
REFLECTION PEAKS ANALYSIS FROM MECHANICAL AND TIME-GATED  
FREQUENCY-DOMAIN MEASUREMENTS

Line length	$S_{11}$ or $S_{22}$ (mU)		
	Electrical	Mechanical	Difference
11	6.2	5.7	0.5
12	6.9	13.1	-6.2
16	18.4	18.4	0.0

values representing the electrical performance of the air line in the absence of the connectors could be compared with the maximum mechanically-derived  $S_{11}$  (or  $S_{22}$ ) coefficients between 10 GHz and 100 GHz (the same frequency range as in the frequency domain measurements with time-gate). These values are shown in Table XVI, which demonstrates that the electrically-derived reflection coefficients agreed with the mechanically-derived values to within 0.5 mU, except for 12 mm long air line. In that line, the mechanically-derived  $S_{11}$  (or  $S_{22}$ ) assumed a constant diameter of center conductor along the length. The effect, previously mentioned, of the reduced diameter of the center conductor at the male connector end is eliminated from the electrically-derived values because they were gated out.

In the above results, it has been shown that, by using time- and frequency-domain electrical assessments of air lines, additional information can be obtained that supplements the traditional characterizations of air lines in terms of mechanical measurements. It was found that, having ‘gated-out’ the connectors on the air lines, a reflection coefficient derived from electrical measurements shows very good agreement with a reflection coefficient derived from the traditional mechanical measurements. In addition, the ‘reactive’ nature of changing impedance can be determined using time-domain low-pass methods. The low-pass impulse method also provides an indication of changes in characteristic impedance along the length of the air lines. The locations of reflection sources along the length of the air line could be identified clearly. The signal delay times derived from electrical measurements agree well with those derived from mechanical measurements. Time-domain assessments are not only very useful for determining characteristic impedance of air lines, but also an effective technique for analyzing the characteristics near connector interfaces at millimeter-wave frequencies.

While there is an inherent limit to resolution in the time-domain method, by using the various time-domain options on the VNA, the detailed characteristics of air lines can be determined. Such determinations can be used to supplement the information gained from mechanical measurements of lines.

For 1.0 mm coaxial air lines it is clear that the connector interfaces are a significant issue in metrology (corresponding to Ref. [18]). The reflection characteristics resulting from the connector interfaces in air lines and/or calibration standards

and systematic errors in the VNA are major factors in determining the reflection characteristics of 1.0 mm coaxial air lines.

## VI. CONCLUSION

The results reported here show that the mechanical and electrical assessment of 1.0 mm coaxial air lines can yield values of reflection characteristic and electrical delay equivalent to within approximately 1.0 mU and 1.0 ps, respectively. The mechanical assessments of dimensions, i.e., diameters and lengths of conductors, were performed by AGMS, LGMS and 3DCMM. The electrical determinations were performed by VNAs. Three time-domain measurement methods, conventional frequency-domain measurements, and time-gated frequency-domain measurements up to 110 GHz were included.

Using the mechanical assessments the characteristics of air lines along their lengths could be successfully defined. However, the reflection characteristics near connector ends remained unknown at millimeter-wave frequencies. It has been shown that sources of reflection along the lengths of air lines could be clearly identified using both band-pass and/or low-pass time-domain methods. The results were consistent with those obtained by mechanical measurements for those characteristics that can be derived from such measurements. The low-pass impulse response makes it possible to quantify changes in characteristic impedance along the length of the air line.

The time-gate technique was used successfully to distinguish between reflections due to the various components of the air line – i.e., connectors and the section of precision line used to provide a definition of the characteristic impedance. This enabled a frequency-domain assessment of the line to be made with effects due to connectors effectively removed from the measurements. The resulting value for the electrical reflection in the line section of the air line agreed well with the mechanically-derived S parameter,  $S_{11}$  (or  $S_{22}$ ) determined from the measurement of the diameters and length for 1.0 mm coaxial air lines.

## REFERENCES

- [1] M. Horibe and N. Ridler, "Using time-domain measurements to improve assessments of precision coaxial air lines as standards of impedance at microwave frequencies," *70th ARFTG Conference Digest*, pp. 84-90, Nov. 2007.
- [2] B. O. Weinschel, "Air-filled coaxial lines as absolute impedance standards", *Microwave Journal*, Vol 7, pp 47-50, April 1964.
- [3] I. A. Harris and R. E. Spinney, "The realization of high-frequency impedance standards using air spaced coaxial lines", *IEEE Trans*, Vol IM-13, No 4, pp 265-272, December 1964.
- [4] K. H. Wong, "Using precision coaxial air dielectric transmission lines as calibration and verification standards", *Microwave Journal*, Vol 31, pp 83-92, December 1998.
- [5] G. F. Engen and C. A. Hoer, "Thru-Reflect-Line: an improved technique for calibrating the dual six-port automatic network analyzer", *IEEE Trans*, Vol MTT-27, No 12, pp 987-993, December 1979.
- [6] "Guidelines on the evaluation of Vector Network Analysers (VNA)", *EURAMET/cg-12/v.01 (previously EA-10/12)*, July 2007. (Available from www.euromet.org.)
- [7] J. C. Evans and I. G. Morgan, "Principles of pneumatic gauging", National Physical Laboratory Notes on Applied Science, No 34, 1964.
- [8] A. Spizzamiglio, "The continuous measurement of the diameter of the steel wire intended for steel-cord", *Proceedings of the International Conference on Wires & Cables*, Florence, Italy, 4-5 October 1995.
- [9] L. Essen, et al., "The Refractive Index and Dielectric Constants of Air and its Principal Constituents at 24,000 Mc/s," *Proc. Phys. Soc. B* 64, pp. 862 - 875, 1951.
- [10] W. Wagner and A. Pruss, "International Equations for the Saturation Properties of Ordinary Water Substance. Revised According to the International Temperature Scale of 1990." *J. Phys. Chem. Reference Data*, 22, pp. 783 - 787, 1993.
- [11] "Radio-frequency connectors – part 31: RF coaxial connectors with inner diameter of outer conductor 1,0 mm (0,039 in) with screw coupling – Characteristic impedance 50 ohms (type 1,0)," *IEC 61169-31*, September 1999.
- [12] M. Horibe, M. Shida, and K. Komiyama, "Development of Evaluation Techniques for Air Lines in 3.5 mm and 1.0 mm Line Sizes," to be published in *IEEE Trans. on Instrum. Meas.*.
- [13] M. Horibe, M. Shida, and K. Komiyama, "S-parameters of Standard Airlines Whose Connector Is Tightened with Specified Torque," *IEEE Trans. on Instrum. Meas.* Vol. 56, no. 2, pp. 401 – 405, Apr. 2007.
- [14] M. Horibe, M. Shida and K. Komiyama, "Assessing the Repeatability of RF and Microwave Connectors in High-frequency Precision Measurements," *Proceedings of the 23<sup>rd</sup> International Conference on Electrical Contacts (ICEC2006)*, pp. 203 - 208, June 2006.
- [15] M. Horibe, and N. Ridler, "Comparison between Two National Metrology Institutes of Diameters and Characteristic Impedance of Coaxial Air Lines," to be published in *IEEE Trans. on Instrum. Meas.*.
- [16] M. Horibe and N. Ridler, "Summary report of Reference Air line bilateral comparison between NPL and NMIJ" NMIJ-AIST unpublished report, July 2007.
- [17] Agilent Technologies, Time Domain Analysis Using Network Analyzer, *Application Note 1287-12*, Mar. 2007.
- [18] M. Horibe, M. Shida and K. Komiyama, "Quantitative Understanding of the Mated Interface Characteristics of Precision Coaxial Connectors at Microwave and Millimeter-Wave Frequencies," *71st ARFTG Conference Digest*, pp. 120-130, June. 2008.

# Hidden Problems in Precise Calibration on Microstrip

Jiri Raboch, Karel Hoffmann, Zbynek Skvor and Premysl Hudec

Czech Technical University in Prague, Faculty of Electrical Engineering,

Technicka 2, 166 27 Prague 6, Czech Republic

E-mail: hoffmann@fel.cvut.cz, rabocj1@fel.cvut.cz, skvor@fel.cvut.cz

**Abstract** — A study of calibration problems on microstrip with respect to interaction of electromagnetic fields around SMA to microstrip launcher and microstrip short was carried out in frequency band up to 26 GHz. Omni Spectra SMA to microstrip launcher, 50  $\Omega$  microstrip line on Arlon CuClad 223 0.508 mm thick substrate and microstrip shorts with reflective wall above the upper side of substrate as a calibration elements were used for simulations in CST Microwave Studio. Strong influence of dimensions of shorts and distance between the shorts and the launcher on simulated calibration data was observed. Reasonable dimensions of the short and the distance between the short and the launcher making possible correct precise calibration were determined.

## I. INTRODUCTION

Many kinds of correction methods for s-parameter vector measurements have been developed since Hackborn and Rehnmark suggested a calibration process for vector network analyzer (VNA) systems, [1], [2]. In all calibration methods values of elements of various error models are determined on the basis of measurement of calibration data obtained by measurement of calibers like Open, Short, Load, Thru, Line, etc. It is always supposed and necessarily demanded so that values of elements of an error model were constant during calibration and subsequent measurement. Surprisingly great systematic errors can be removed in such cases. The demand of constant values of elements error model also means that they are independent on the caliber connected to VNA. It is simple to satisfy in non radiating structures like a coaxial line. However, the situation is more complicated in case of measurement on an open structure like a microstrip line. A launcher connecting the microstrip line with the coaxial line of a port of the VNA more or less radiates and some higher order modes occur in the vicinity of the launcher. If a caliber is placed too close to this area the electromagnetic field around the launcher can interact with that of the caliber. Such an interaction may differ during calibration and measurement and thus may result in strong changes of calibration data obtained by measurement of the caliber, and dramatic increase of measurement uncertainty.

The purpose of this paper is to clear up this issue and to give some practical recommendation to minimize these problems.

The analysis was done for Omni Spectra SMA to microstrip launcher, see Fig. 1, connected to a 50 $\Omega$  microstrip line

realized on Arlon CuClad 223 0.508 mm thick substrate with  $\epsilon_r = 2.33$ . CST Microwave Studio was used for simulations.

First of all simulations of reflection coefficient at the coaxial part of the launcher for different dimensions of the microstrip Short and different distances between the Short and the launcher were carried out. Then dimensions of a microstrip Short providing satisfactory electrical parameters were determined. Finally with this Short placed in different distances from the launcher the reflection coefficients at the coaxial part of the launcher were simulated.

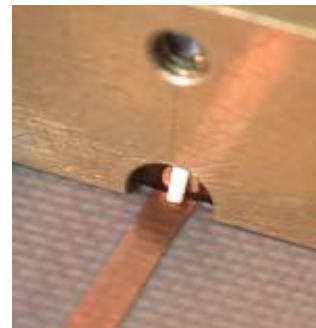


Fig. 1. SMA to microstrip launcher.

## II. FIRST SIMULATIONS

The first simulation was made with the microstrip Short placed at the edge of the microstrip at the distance of 25 mm from the launcher, see Fig. 2. The height of the metal sheet above the upper side of the substrate was 5 mm and the width was 20 mm.

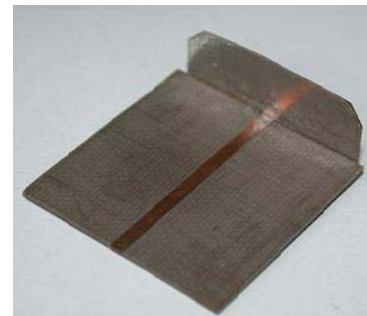


Fig. 2. Microstrip Short.

Fig. 3 displays magnitude of electric field in the structure at frequency 22.8 GHz. The structure clearly radiates especially when the maximum of electric intensity standing wave on the microstrip occurs on the launcher. Simulations have revealed that up to 30% of energy fed into SMA connector may leak out of the structure.

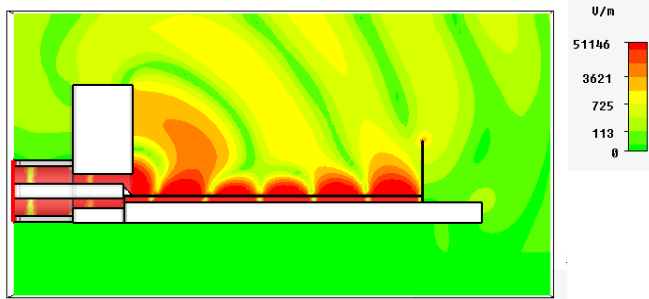


Fig. 3. Distribution of magnitude of electrical field in the analyzed structure at frequency 22.8 GHz.

Further simulations were made for different heights of the microstrip Shorts. The width of the metal sheet was 23 mm. The highs of the Shorts above the upper side of the substrate were 0 mm, 2.5 mm, 5 mm and 10 mm. The results of simulations are displayed in Fig. 4 to Fig. 6

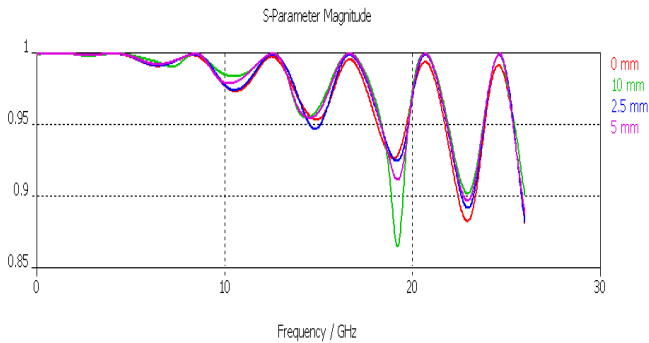


Fig. 4. Reflection coefficient at the input of the launcher of microstrip Shorts with different metal sheet height placed at the distance 25 mm from the launcher.

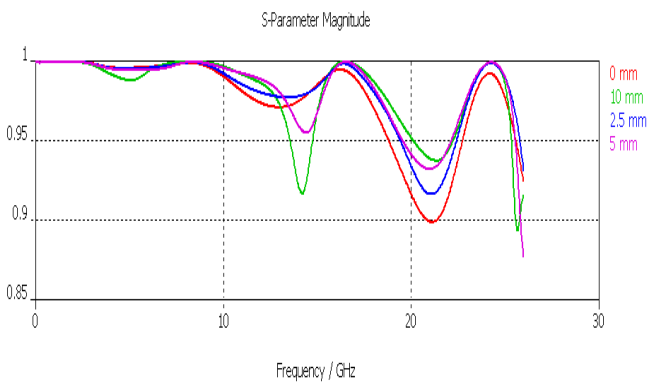


Fig. 5. Reflection coefficient at the input of the launcher of microstrip Shorts with different metal sheet height placed at the distance 12.5 mm from the launcher.

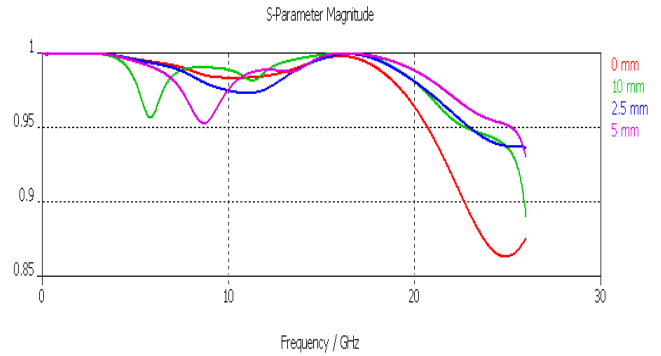


Fig. 6. Reflection coefficient at the input of the launcher of microstrip Shorts with different metal sheet height placed at the distance 6.25 mm from the launcher.

It can be seen that Shorts with different height create different reflection coefficients. The phenomenon is more significant for Shorts close to the launcher. It is obvious that some interactions between near field and also radiated field of the launcher and the Short occur. However the differences in reflection coefficients can be caused both the interaction of the field of the launcher and different (may be insufficient) dimensions of the Shorts. Therefore it was decided to determine dimensions of the metal sheet of the Short to form sufficiently good electrical properties of the Short.

### III. MICROSTRIP SHORT

Proper dimensions of the Short were determined by simulation. Shorts with different height were placed at edge of the substrate. Reflection coefficients calculated at the distance 25 mm from the Shorts at microstrip line were calculated and transformed to the reference plane of the shorts using CST Microwave Studio, see Fig. 7. It can be seen the shorts with height of metal plane equal or higher than 5 mm have practically acceptable parameters. Therefore the Short with the height of the metal sheet 5 mm was chosen for further simulations.

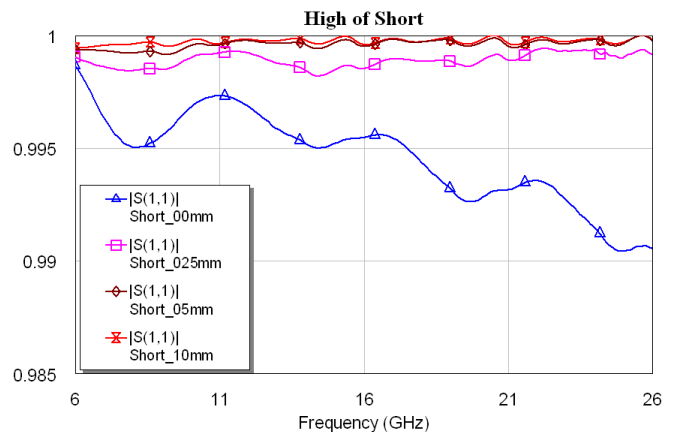


Fig. 7. Microstrip Shorts reflection coefficients magnitudes with different heights of metal sheet.

#### IV. POSITIONING OF SHORT

A short with proper dimensions does its job in calibration well as far as its electromagnetic field does not interact with other parts of calibration setup. Having obtained dimensions of the Short, minimum distance of the short from the launcher remains to be determined.

The whole structure consisting from the launcher connected to the Short through a microstrip of certain length can be considered as one object and analyzed by the electromagnetic field simulator. However, it can be also considered as a cascade connection of two blocks - the launcher with the microstrip line as the first block and the Short as the second block. The later approach neglects electromagnetic coupling.

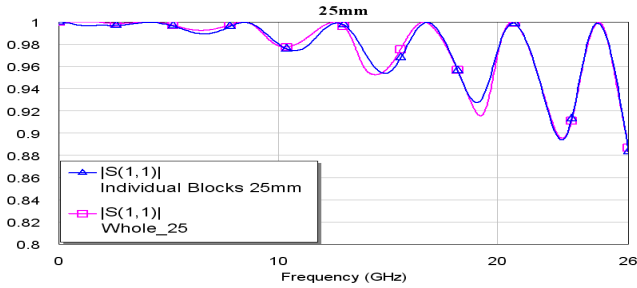


Fig. 8. Reflection coefficient of the cascade of two blocks compared to the reflection coefficient of the whole structure. The length of the microstrip is 25 mm.

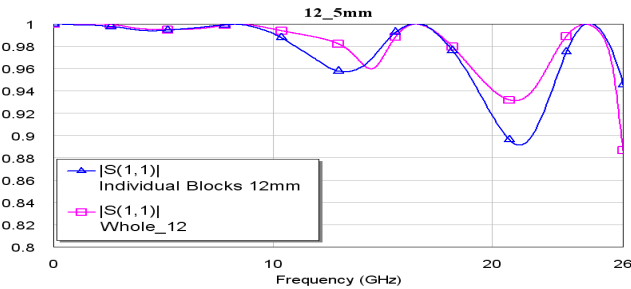


Fig. 9. Reflection coefficients of the cascade of two blocks compared to the reflection coefficient of the whole structure. The length of the microstrip is 12.5 mm.

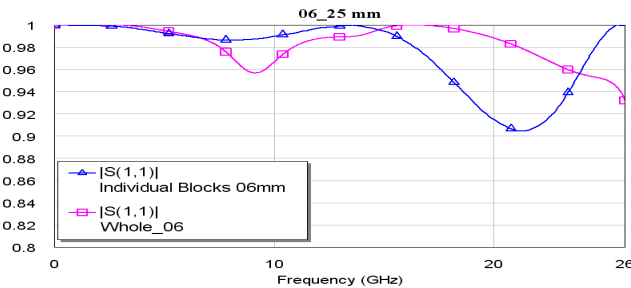


Fig. 10. Reflection coefficients of the cascade of two blocks compared to the reflection coefficient of the whole structure. The length of the microstrip is 6.25 mm.

Both blocks can be simulated to obtain their s-parameters and then calculate s-parameter (reflection coefficient) of the cascade using some circuit simulator, AWR Microwave Office in our case. Simulated reflection coefficients at the input of the launcher should be identical for the whole structure and for both blocks in cascade in case that the Short does not influence the electromagnetic field distribution near the launcher. Comparing results of both simulations minimum distance between the launcher and the Short can be determined.

The results of simulations show Fig. 8 to Fig. 10. It can be seen that distances 12.5 and 6.25 mm are not reasonable. The difference caused by direct coupling in the case of 25 mm spacing is negligible when compared to other errors, and therefore the 25 mm spacing proved to be enough.

#### V. CONCLUSION

Microwave measurements in open structures require good knowledge of electromagnetic effects. It has been observed that the structure consisting of coaxial to microstrip launcher, a piece of microstrip line and a microstrip short may exhibit strong radiation and mutual couplings. These couplings between launcher and calibers that can not be easily implemented into systematic error correction schemes should be minimized during measurement setup design. Fullwave electromagnetic simulation proved to be an efficient way to provide for that.

Experimental study has been carried out for OmniSpectra SMA microstrip launcher and a 50 ohm microstrip line on Arlon CuClad233 0.508 mm thick substrate. 5 mm height of the metal plane and a minimum spacing of 25 mm between the launcher and the Short have been found as a reasonable recommendation for practical measurements. It is suggested to use a similar algorithm for other calibers.

#### ACKNOWLEDGEMENT

This work has been conducted at the Department of Electromagnetic Field of the Czech Technical University in Prague and supported by the research program MSMT6840770015 "Research of Methods and Systems for Measurement of Physical Quantities and Measured Data Processing" of CTU in Prague sponsored by the Ministry of Education, Youth and Sports of the Czech Republic and by the Czech Science Foundation under Grant 102/08/H027 "Advanced Methods, Structures and Components of Electronic Wireless Communication" (presentation).

#### REFERENCES

- [1] R. A. Hackborn, "An automatic network analyzer system," *Microwave J.*, pp 45-52, May 1968.
- [2] S. Rehnmark, "On the Calibration Process of Automatic Network Analyzer Systems," *IEEE Trans. on MTT*, vol. MTT-22, pp. 457-458, April 1974.

# A Simple Method for Extreme Impedances Measurement – Experimental Testing

Martin Randus, Karel Hoffmann

Czech Technical University in Prague, Technicka 2, 166 27 Prague 6, Czech Republic  
E-mail: randum1@fel.cvut.cz, hoffmann@fel.cvut.cz

**Abstract** — This paper directly follows and extends [1], where a novel method for measurement of extreme impedances is described theoretically. In this paper experiments proving that the method [1] can significantly improve stability of a measurement system are described. Using Agilent PNA E8364A vector network analyzer (VNA) the method is able to measure reflection coefficient with stability improved 36-times in magnitude and 354-times in phase compared to the classical method of reflection coefficient measurement. Further, validity of the error model and related equations stated in [1] are verified by real measurement of SMD resistors (size 0603) in microwave test fixture. Values of the measured SMD resistors range from 12 k $\Omega$  up to 330 k $\Omega$ . A novel calibration technique using three different resistors as calibration standards is used. The measured values of impedances reasonably agree with assumed values.

**Index Terms** — Calibration, impedance measurement, microwave circuits, microwave measurements, nanotechnology.

## I. INTRODUCTION

Measurement of extreme impedances – impedances with magnitude of the corresponding reflection coefficient approaching to unity – becomes more and more important due to emerging microwave devices based on carbon nanotubes [2]-[4] as well as due to need for impedance measurements in biological applications.

Classical measurement of impedances by measuring reflection coefficient of the impedance provides poor resolution for impedances that are substantially smaller or substantially greater than a reference impedance of a vector network analyzer (VNA), that is usually 50  $\Omega$  [5], [6].

Limited stability of VNA itself (drifts) together with limited reproducibility of connection of a device under test (DUT) and calibration standards are the most limiting factors in extreme impedances measurements.

In [1] a novel method for measurement of such extreme impedances, which substantially increases sensitivity of the measurement to changes in the value of the measured impedance, was introduced.

Scope of this paper is to bring results of experimental testing of the method [1]. Tests were focused on stability of the measurement system and ability to measure high impedances. The paper shows that the method is able to significantly improve stability of the measurement system and to measure extreme impedances.

Moreover, a novel calibration technique suitable for measurement of extreme impedances is introduced. The

method is using three resistors of different value as calibration standards.

## II. THEORY

Arrangement of idealized measurement system realizing the developed method [1] is depicted in Fig. 1.

The method is based on subtracting a reference reflection coefficient  $\Gamma_{ref}$  from reflection coefficient of the DUT  $\Gamma_x$ , amplifying this difference by an amplifier with gain  $G$  and measuring the resulting signal by a standard VNA as a transmission coefficient  $T_{21}$ .

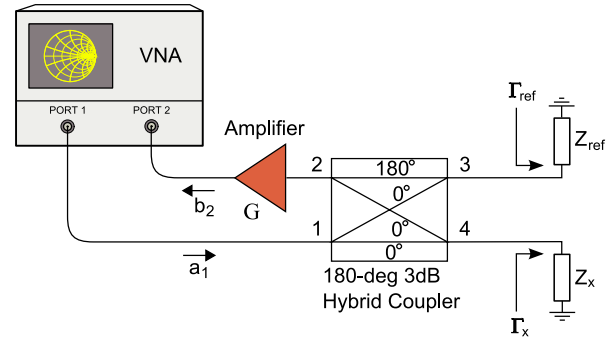


Fig. 1. Arrangement of the measurement system – ideal components.

In the case of ideal components of the measurement system the measured transmission coefficient  $T_{21}$  is given by equation

$$T_{21} = \frac{G}{2} (\Gamma_x - \Gamma_{ref}). \quad (1)$$

From this equation value of the reflection coefficient  $\Gamma_x$  of the DUT is

$$\Gamma_x = \frac{2T_{21}}{G} + \Gamma_{ref}. \quad (2)$$

Value of the transmission coefficient  $T_{21}$  is measured with uncertainty  $\Delta T_{21}$  which will cause that the true value of the reflection coefficient  $\Gamma_x$  of the DUT is changed by  $\Delta \Gamma_x$

$$\Gamma_x + \Delta \Gamma_x = \frac{2}{G} (T_{21} + \Delta T_{21}) + \Gamma_{ref}. \quad (3)$$

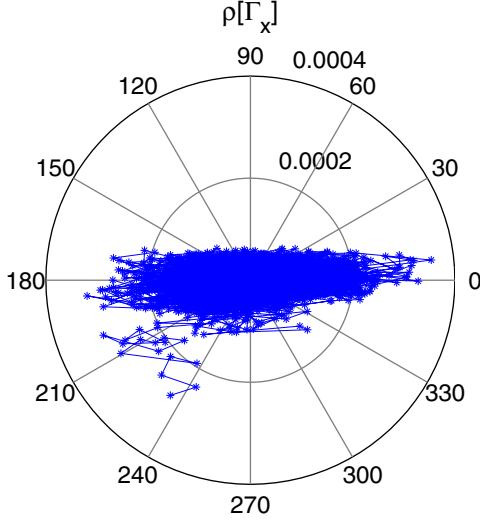


Fig. 2. Spreading of the measured values of the reflection coefficient  $\Gamma_x$  of the SMA female open end around the average value when using the classical method for the measurement, 3201 points acquired during 94 minutes under stable conditions.

By subtracting equations (2) and (3) we obtain the value of uncertainty of the measured reflection coefficient

$$\Delta\Gamma_x = \frac{2\Delta T_{21}}{G}. \quad (4)$$

It is obvious that by using amplifier with high gain  $G$  the uncertainty of the VNA can be significantly reduced. Maximal value of gain that can be used is limited by the difference of the reference reflection coefficient  $\Gamma_{ref}$  and the reflection coefficient  $\Gamma_x$  of the DUT and by hardware requirements and constraints of a VNA used.

### III. EXPERIMENTAL VERIFICATION OF MEASUREMENT SYSTEM STABILITY IMPROVEMENT

Reduction of uncertainty of the measured reflection coefficient  $\Gamma_x$  described by equation (4) was experimentally verified.

In the first part of the experiment a fully warmed up VNA Agilent PNA E8364A was calibrated by OSM method at the end of a female SMA connector connected to the VNA by a flexible test cable Agilent 85133. Male calibration standards Open, Short and Broadband Load from Agilent 85052C 3.5mm Precision Calibration Kit were used.

Then the VNA was during 94 minutes in CW mode collecting 3201 data points of a measured reflection coefficient of the open end of the female SMA connector. The measurement was done at frequency 1.56675 GHz which is the frequency that was used in the second part of the experiment. IF bandwidth was set to 1 Hz and generator

power level was set to -7 dBm. Room temperature did not change more than  $(29.5 \pm 0.5) ^\circ\text{C}$ .

To show variations of the measured values of the reflection coefficient  $\Gamma_x$  of the DUT an operator  $\rho$  calculating distance of a data point  $d_i$ ,  $i = 1, 2, \dots, N$  from an average value of data points set was established by equation

$$\rho[d_i] = d_i - \frac{1}{N} \sum_{j=1}^N d_j. \quad (5)$$

The 3201 calculated values of  $\rho[\Gamma_x]$  ( $N = 3201$ ) acquired during the 94 minutes period under stable conditions are depicted in polar plot in Fig. 2.

The average measured value was  $\Gamma_{x,AVG} = 1.007 \angle -0.96^\circ$  (absolute accuracy of this value is not important for this experiment). The difference between the maximal and the minimal measured value of the reflection coefficient  $\Gamma_x$  was  $6.719\text{E-}4$  in magnitude and  $0.017^\circ$  in phase.

In the second part of the experiment the same measurement under the same conditions was done by the developed method. Arrangement of the measurement system is depicted in Fig. 3.

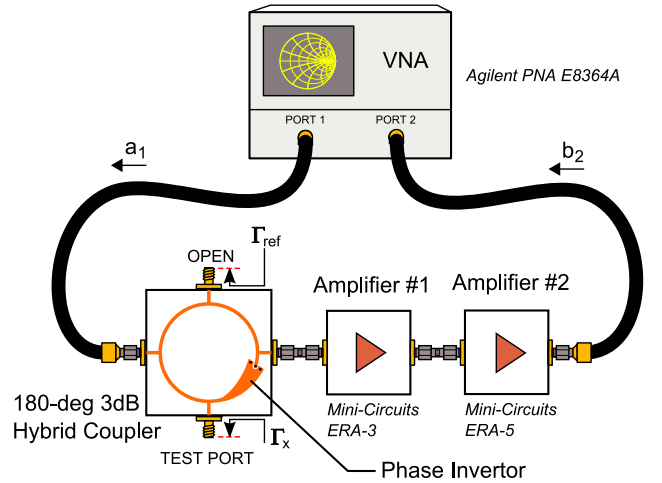


Fig. 3. Arrangement of the measurement system for demonstration of improvement of measurement system stability.

Microstrip 180-degree 3dB hybrid coupler with phase inverter was used. The reference arm was terminated simply by SMA female open end of the SMA flange connector of the coupler. Two amplifiers with ICs Mini-Circuits ERA-3 and ERA-5 providing overall gain 35.27 dB ( $G = 58.01$ ) were used.

The VNA was used for measurement of the transmission coefficient  $T_{21}$

$$T_{21} = \frac{b_2}{a_1}, \quad (6)$$

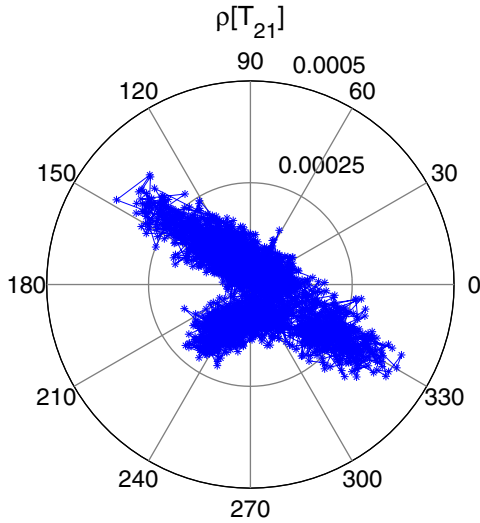


Fig. 4. Spreading of the measured values of the transmission coefficient  $T_{21}$ , 3201 points acquired during 94 minutes under stable conditions.

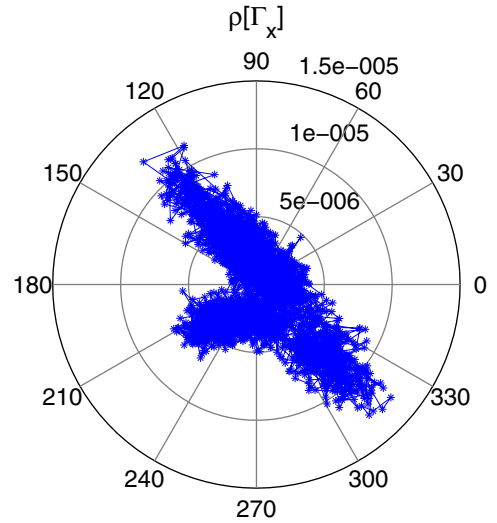


Fig. 5. Spreading of the calculated values of the reflection coefficient  $\Gamma_x$  of the SMA female open end around the average value when using the developed method for the measurement, 3201 points acquired during 94 minutes under stable conditions.

where  $b_2$  and  $a_1$  are voltage waves measured by test and reference receivers of the VNA. No correction was applied in the VNA.

Measurement was done at frequency 1.56675 GHz. This is the frequency where the measured transmission coefficient  $T_{21}$  reaches its minimum – the reference reflection coefficient  $\Gamma_{ref}$  and reflection coefficient  $\Gamma_x$  of the DUT are mutually very well subtracted. Generator power level was set to -40 dBm. The rest of the conditions remained the same.

The system was calibrated at the test port of the hybrid coupler (see Fig. 3) by the same calibration standards as in the first part of the experiment. Parameters of an error model [1] and corrected values were calculated with MATLAB software using equations from [1] and [7].

However, it should be emphasized that OSM calibration technique is not suitable for this method since principle of subtraction of the reference and the measured reflection coefficient will not work well for at least two of the three calibration standards (moreover, in the case of the Agilent 85052C calibration kit calibration standards Open and Short do not provide open end termination and short termination in the reference planes because the calibration standards include also a short section of coaxial line). Generator power level must be set to sufficiently low value to ensure that amplifiers operate in small signal region even during the calibration.

The most convenient calibration technique for the developed method will be introduced in section IV.

Spreading of values of the measured transmission coefficient  $T_{21}$ , calculated by (5) is depicted in Fig. 4.

The average measured value was  $T_{21,AVG} = 0.144 \angle -167.75^\circ$ . Difference between the maximal and the minimal measured value of the transmission coefficient  $T_{21}$  was  $18.031E-4$  in magnitude and  $0.016^\circ$  in phase. The difference in phase is the same as in the case of direct measurement of the reflection coefficient  $\Gamma_x$  by VNA. The difference in magnitude is even 2.66-times larger.

Subsequently, values of the reflection coefficient  $\Gamma_x$  of the female open end of the SMA flange connector (DUT) of the hybrid coupler were calculated (using equation (7) in [1]) from the measured values of the transmission coefficient  $T_{21}$ . Spreading of values of the calculated reflection coefficient  $\Gamma_x$  calculated by (5) is depicted in Fig. 5.

The average value of the calculated reflection coefficient  $\Gamma_x$  was  $\Gamma_{x,AVG} = 1.003 \angle -0.91^\circ$  (absolute accuracy of this value is not important for this experiment). The difference between the maximal and the minimal calculated value of the reflection coefficient  $\Gamma_x$  was  $0.185E-4$  in magnitude and  $4.680E-5^\circ$  in phase, that is more than 36-times better stability of the magnitude of the reflection coefficient  $\Gamma_x$  and more than 354-times better stability of the phase. The radius of the area  $\rho[\Gamma_x]$  was decreased more than 26-times (compare the scale on the radial axes in Fig. 2 and Fig. 5).

The experiment proved that the developed method is capable of outstanding improvement of stability of the measurement system which is necessity for measurement of extreme impedances.

#### IV. EXPERIMENTAL RESULTS OF EXTREME IMPEDANCES MEASUREMENT

This section describes a real measurement of several SMD resistors of size 0603. Their values, ranging from 12 k $\Omega$  up to 330 k $\Omega$ , can be considered as extreme impedances.

Arrangement of the measurement system is depicted in Fig. 6.

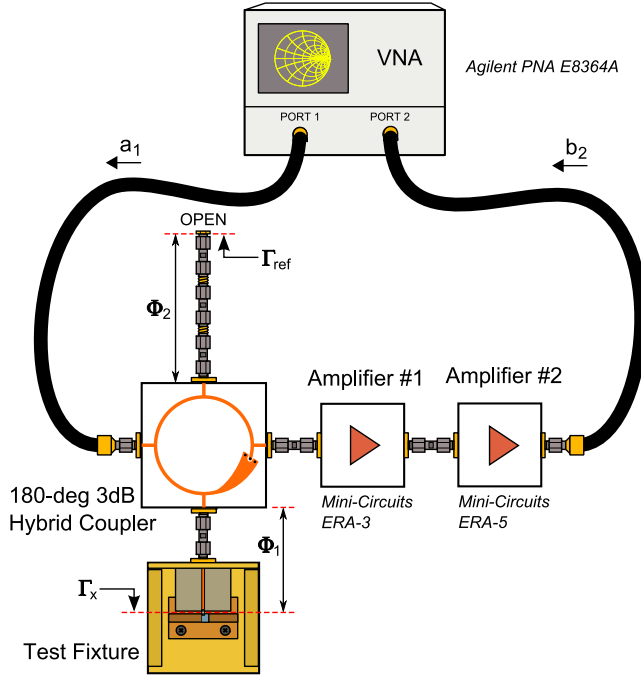


Fig. 6. Arrangement of the measurement system for measurement of extreme impedances of SMD resistors.

Most of the arrangement is the same as in the experiment described in section III. Only the reference and the test branch were modified.

In the test branch of the hybrid coupler a microwave test fixture for measurement of SMD components was connected. Electrical length from the port of the hybrid coupler to a reference plane of the measurement, lying in the position of the SMD resistor, is  $\Phi_1$ .

In the reference branch an open-ended coaxial line formed by male-male and female-female SMA adaptors was used. Electrical length of this line is  $\Phi_2$  and  $\Phi_2 \approx \Phi_1$  with difference less than  $10^\circ$  at the operating frequency.

Measurements were performed in CW mode at frequency 1.796 GHz. This is the frequency where the measured transmission coefficient  $T_{21}$  reaches its minimum – the reference reflection coefficient  $\Gamma_{ref}$  and the reflection coefficient  $\Gamma_x$  are mutually very well subtracted. At this frequency the overall gain of the amplifiers is 35.03 dB ( $G = 56.41$ ). Generator power level was set to -40 dBm. IF bandwidth was set to 10 Hz, 101 points were acquired during 8.94 seconds in each measurement.

For all calculations an average value of the measured transmission coefficient  $T_{21}$  was used.

Calibration of the measurement system was performed by a novel technique using three different resistors. SMD resistors of the same size 0603 with values 11 k $\Omega$ , 76 k $\Omega$  and 1 M $\Omega$  were used for calibration. These values were chosen so that they uniformly describe area of Smith chart where the measured impedances lie.

Moreover, using these high values of resistors enables that magnitude of the measured transmission coefficient  $T_{21}$  does not change too much during calibration. Thus, nonlinearities of the amplifiers as well as nonlinearities of the receivers of the VNA do not have any significant effect on accuracy of the results.

By using the SMD resistors as both calibration standards and DUTs, describing the standards as purely resistive impedances and assuming the same parasitics of all the resistors the parasitics become an integral part of the test fixture and are eliminated by calibration and correction. Thus, in ideal case, the measured values of impedances of the resistors can be expected to be purely real impedances.

A DC resistance of the used resistors was assumed to be the true value of their impedance and in the case of the calibration standards it was used for their description.

Results of the measurement are in Table I. The results exhibit reasonable agreement between the measured and the true (DC) values of extreme impedances of the SMD resistors up to 240 k $\Omega$ .

For higher resistor values the values of the measured impedances differ significantly from the supposed (DC) values. It was experimentally determined that the connection reproducibility of the used test fixture ranges from  $3.3E-5$  to  $1.3E-3$ . Therefore, it can be supposed that these measurements are affected by limited connection reproducibility of the used test fixture.

#### V. CONCLUSION

A method for measurement of extreme impedances described in [1] was experimentally tested and successfully verified. The method can significantly improve stability of the measurement system which is necessity for measurement of extreme impedances.

The experiment was done in CW mode at frequency 1.56675 GHz. Difference between the maximal and minimal measured value of the reflection coefficient of SMA female open end termination during 94 minutes under stable conditions was reduced more than 36-times in magnitude, more than 354-times in phase and the radius of the area in Smith chart where all the measured points were situated was decreased more than 26-times when compared with the direct method of reflection coefficient measurement by VNA.

Functionality of the method [1] was demonstrated on measurement of several SMD resistors size 0603 with values

TABLE I  
MEASURED IMPEDANCES OF SMD RESISTORS AT FREQUENCY 1.796 GHz

Resistor	DC Resistance / k $\Omega$	Measured Impedance	
		Re / k $\Omega$	Im / k $\Omega$
Cal. Std. #1	11.00	-	-
DUT #1	12.01	13.16	1.13
DUT #2	12.97	13.45	-0.21
DUT #3	16.08	14.84	-0.79
DUT #4	18.57	19.17	-2.70
DUT #5	22.23	24.90	-0.83
DUT #6	26.87	31.18	1.15
DUT #7	34.08	35.88	0.09
DUT #8	42.50	38.45	3.82
DUT #9	52.10	56.56	11.01
DUT #10	62.10	61.66	12.26
Cal. Std. #2	75.70	-	-
DUT #11	90.70	92.74	3.58
DUT #12	99.30	79.43	-11.56
DUT #13	150.20	132.50	-4.12
DUT #14	239.70	208.80	-6.79
DUT #15	329.50	202.36	323.39
Cal. Std. #3	1004.00	-	-

ranging from 12 k $\Omega$  up to 330 k $\Omega$ . The experiment was done in CW mode at frequency 1.796 GHz. A novel calibration technique using three different resistors as calibration standards was introduced. SMD resistors with values 11 k $\Omega$ , 76 k $\Omega$  and 1 M $\Omega$  were used as calibration standards in order to uniformly describe an area of Smith chart where the values of DUT resistors are situated. The measured values of impedance exhibit reasonable accuracy of measurement being influenced by limited connection reproducibility of the test fixture. This random effect now represents a crucial problem in absolute measurement of extreme impedances. Further improvement of absolute measurement of extreme impedances is not possible without solving this problem.

Fortunately, the limited connection reproducibility of the test fixture need not pose a serious problem in relative measurements [4]. In this case improvement of measurement system stability described above means a significant breakthrough.

#### ACKNOWLEDGEMENT

This work has been conducted at the Department of Electromagnetic Field of the Czech Technical University in Prague and supported by research program MSMT6840770015 "Research of Methods and Systems for Measurement of Physical Quantities and Measured Data Processing" of CTU in Prague sponsored by the Ministry of

Education, Youth and Sports of the Czech Republic and by the Czech Science Foundation under Grant 102/08/H027 "Advanced Methods, Structures and Components of Electronic Wireless Communication" (presentation).

#### REFERENCES

- [1] M. Randus, and K. Hoffmann, "A simple method for extreme impedances measurement," *2007 ARFTG Int. Conference*, December 2007.
- [2] P. J. Burke, Z. Yu, S. Li, and C. Rutherglen, "Nanotube technology for microwave applications," *2005 IEEE MTT Int. Microwave Symp.* 2005.
- [3] Z. Yu, C. Rutherglen, and P. J. Burke, "Microwave nanotube transistor operation at high bias," *Applied Physics Letters*, 88, 233115. 2006.
- [4] Z. Yu, and P. J. Burke, "Microwave transport in metallic single-walled carbon nanotubes," *Nano Letters*, 5, pp. 1403-1406, 2005.
- [5] Agilent Technologies, *Impedance Measurement Handbook*, Agilent Technologies Co. Ltd., July 2006, P/N 5950-3000.
- [6] H. Tanbakuchi, M. Richter, and M. Whitener, "Design of scanning capacitance microscope," *2006 ARFTG Int. Conference*, November 2006.
- [7] Agilent Technologies, *Specifying Calibration Standards and Kits for Agilent Vector Network Analyzers (Application Note 1287-11)*, Agilent Technologies Co. Ltd., April 2006, P/N 5989-4840EN.

# Wideband measurement of extreme impedances with a multistate reflectometer\*

Arkadiusz Lewandowski, Denis LeGolvan, Ronald A. Ginley, T. Mitchell Wallis, Atif Imtiaz, and Pavel Kabos

**Abstract**—We present a technique for accurate wideband measurements of one-port devices with extreme impedances. Our technique uses a reflectometer with variable parameters (states) to obtain redundant measurements of the extreme impedance device. We process these measurements using statistical techniques that allow us to exploit the redundancy in order to increase the measurement bandwidth and reduce the measurement uncertainty. We demonstrate our technique for a simple setup containing a power splitter and an unknown variable reference impedance connected to one of its arms and an unknown extreme-impedance device connected to its other arm. The variable reference impedance is realized as either a set of mechanical standards or an electronically tunable impedance. Measurement results show that the repeatability of the reference impedance values is essential for achieving increased accuracy.

**Index Terms**—broadband measurements, calibration, high impedance loads

## I. INTRODUCTION

THE implementation of nanotechnology into high speed/frequency electronics allows for new opportunities and exciting developments in the field. On the other hand, it also introduces new challenges, particularly for high frequency metrology [1], [2], [3]. These challenges are related mostly to the fact that the nanoscale devices are usually made from composite materials, and scaling down to nanoscale increases their DC resistivity and leads to a complex frequency response. The DC resistivity can reach values from a few to hundreds of kilohms. This brings the magnitude of the reflection coefficient of these devices to almost one when measured with 50  $\Omega$  reference impedance vector network analyzers (VNA). Consequently, high accuracy in the measurement of large reflection coefficients is required in order to determine the impedance of the measured devices meaningfully and accurately.

Obtaining high accuracy in VNA measurement of reflection coefficients with magnitude close to one, forms a particular challenge. It requires a large dynamic range for the VNA receivers along with accurate calibration techniques. As the dynamic range of modern VNAs constantly increases, the ultimate limitation to the accuracy in the measurement of reflection coefficients with large magnitudes comes from the

calibration techniques. This accuracy is limited primarily by the uncertainty with which we determine the mismatch of the VNA port. This uncertainty, referred to as residual source match, results in measurement errors that increase as the magnitude of the reflection coefficient of the measured device approaches one [4].

The issue of measuring extreme loads has previously been addressed in the literature [5]. Recently Randus and Hoffmann [6] introduced an elegant and simple method for measurement of extreme impedances based on a standard VNA and a 180 degree 3 dB hybrid coupler. The approach is based on subtracting two signals, one reflected from a reference high impedance load and the second reflected from the unknown high impedance device. The transmitted signal through this system is proportional to the difference of the reflection coefficients. Consequently, by measuring an amplified version of this transmission, the difference between the two reflection coefficients can be accurately characterized.

The drawback to this approach is that it is limited to the frequency band in which the coupler introduces a phase shift of 180 degrees to one of the reflected signals. Consequently, we expect the accuracy of this approach to deteriorate outside of the designated coupler band.

In this paper, we present an extension of the approach introduced in [6] that allows for broadband measurements of extreme impedances. We increase the measurement bandwidth by replacing the fixed reference impedance with a set of reference impedances with different phase shifts. Consequently, the ability of our approach to characterize the reflection coefficient of an unknown high-impedance device is not limited by the phase shifting properties of the coupler, and is determined instead by the phase shifts realized by the reference impedance.

As we do not have to rely on the phase shifting properties of the hybrid, we replace it with a simple three-port power splitter. We terminate two of the splitter ports with the reference and unknown impedance, respectively, and measure the input reflection coefficient. This setup forms a multistate reflectometer as introduced in [7]. Since we measure the reflection coefficient instead of the transmission through the coupler, as suggested in [6], our setup can be easily extended to two-port measurements.

We present measurement results for two cases: with the variable reference impedance realized as either a set of mechanical standards or an electronically tunable impedance. The measurement results show that the repeatability of the reference impedance states is essential for achieving increased accuracy.

Arkadiusz. Lewandowski is with the Warsaw University of Technology. He is currently a Guest Researcher at the National Institute of Standards and Technology, Boulder, CO 80305 USA (phone: 303-497-4665; fax: 303-497-3970; e-mail: A.Lewandowski@ieee.org).

Denis LeGolvan, Ronald A. Ginley, T. Mitchell Wallis, Atif Imtiaz and Pavel Klabos are with the Electromagnetic Division, National Institute of Standards and Technology, Boulder, CO 80305.

\*This work is a publication of the National Institute of Standards and Technology (NIST), an agency of the U.S. government, and is not subject to U.S. copyright.

## II. THEORY

Our measurement setup is shown in Fig. 1. The input (port 1) of the power splitter is connected directly to the VNA. The unknown extreme impedance is connected to port 2 of the splitter (measurement port) and the set of reference standards is sequentially connected to port 3 of the splitter (reference port). The details of the measurement procedure will be described later on in the text. We start with the analysis of the ideal case to demonstrate the principle of our approach.

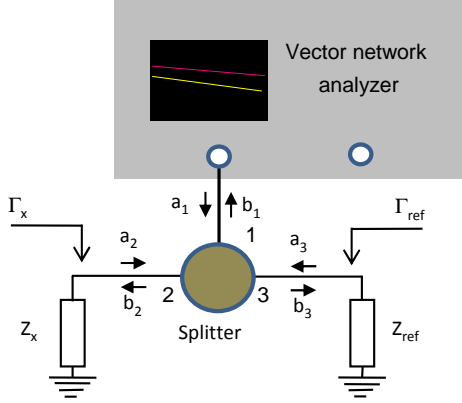


Figure 1. Measurement setup.

For this purpose, we will use an ideal Wilkinson power divider in place of the power splitter in Fig. 1. The  $S$ -matrix of the ideal Wilkinson divider at the center frequency is

$$[S] = \frac{-j}{\sqrt{2}} \begin{bmatrix} 0 & 1 & 1 \\ 1 & 0 & 0 \\ 1 & 0 & 0 \end{bmatrix}. \quad (1)$$

The VNA measures the reflection coefficient  $\Gamma_m$  at port 1 of the divider, which can be expressed as:

$$\Gamma_m = -\frac{1}{2}(\Gamma_{ref} + \Gamma_x). \quad (2)$$

The graphical representation of  $\Gamma_m$  in the complex plane for a continuously changing phase of the reflection coefficient  $\Gamma_{ref}$  and the reflection coefficient  $\Gamma_x = 1$  is shown in Fig. 2. The reflection coefficient  $\Gamma_m$ , as measured by the VNA in this ideal case, represents points on the circle of radius  $\frac{1}{2}$  with the center of the circle representing the position of the unknown reflection coefficient  $\Gamma_x$ . From this simple picture, we see that the magnitude of the measured reflection coefficient varies between zero and one depending on the phase and the magnitude of the reference reflection coefficient  $\Gamma_{ref}$ . Consequently, for a given set of reflection coefficients  $\Gamma_{ref,i}$ , for  $i = 1, \dots, N$ , we obtain an overdetermined set of linear equations described by (2) that can be statistically solved to obtain  $\Gamma_x$ . Provided that the values of  $\Gamma_{ref,i}$  uniformly cover the Smith chart, magnitudes of these linear combinations cover the entire range from zero to one, which moves the measurement of the reflection coefficient of the extreme impedance closer to the

center of the Smith chart and improves the accuracy of the measurement of such devices.

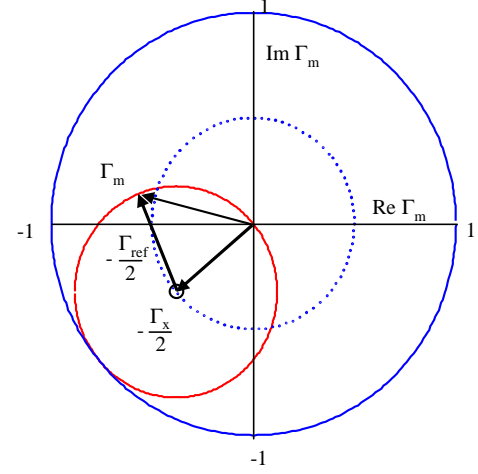


Figure 2. Graphical representation of the measured reflection coefficient  $\Gamma_m$  in the complex plane for continuously varying phase of the reference reflection coefficient  $\Gamma_{ref}$ . The reflection coefficient  $\Gamma_m$  is for ideal case a circle with the center in  $-\frac{\Gamma_x}{2}$ , where  $\Gamma_x$  is the reflection coefficient of the measured device.

## III. MEASUREMENT

In the previous section we explained the principles of our approach using the ideal Wilkinson divider. As the Wilkinson divider operates in a narrow frequency band and becomes highly mismatched out of this band, we tested our approach with a broadband two-resistor power splitter. The scattering matrix of an ideal two-resistor splitter is

$$[S] = \begin{bmatrix} 0 & 1/2 & 1/2 \\ 1/2 & 1/4 & 1/4 \\ 1/2 & 1/4 & 1/4 \end{bmatrix}. \quad (3)$$

Although the splitter ports are not well isolated, the device has an interesting property. Rewriting (2) with (3), we obtain

$$\Gamma_m = \frac{\frac{1}{4}(\Gamma_{ref} + \Gamma_x)}{1 - \frac{1}{4}(\Gamma_{ref} + \Gamma_x)}. \quad (4)$$

Consequently, for  $\Gamma_{ref} = -\Gamma_x$  we have the input reflection coefficient  $\Gamma_m = 0$ . Hence, we see that combinations of loads with equal magnitudes and opposite phase shifts are transformed to a matched load, which allows us to move the measurement of these loads to the center of the Smith chart.

Our experiment consisted of two parts. In the first part, we investigated the properties of the impedance transformation through the splitter for different pairs of extreme impedances. In the second part, we performed a complete calibration of the entire measurement system and characterized some unknown highly reflective devices.

In the first part of our experiment, the VNA was calibrated with a standard one-port calibration method (four offset shorts, an open, and a load) and the power splitter used was characterized by use of the approach [8], described in a different

paper presented at this conference. We connected different pairs of highly reflective devices to the ports of the splitter and measured the reflection coefficient. The measurements were performed in the frequency range from 200 MHz to 50 GHz. Fig. 3 shows the measured frequency dependence of the reflection coefficient  $\Gamma_m$  for one particular case of two offset shorts of the same length used as the the device-under-test (DUT) and the reference standard. The magnitude of the measured reflection coefficient varies from about 0.3 to about 0.95 as a function of frequency and demonstrates that there are reference impedances that transform the measured extreme impedance to a position closer to the center of the Smith chart.

In the second part of our experiment we performed a complete calibration of our measurement setup and then characterized some unknown highly reflective devices. The VNA measured uncorrected reflection coefficient in the frequency range from 200 MHz to 50 GHz. During the calibration procedure we measured a set of known calibration standards (four offset shorts, load and open). For each calibration standard attached to the measurement port we connected a number of unknown reference standards to the reference port of the splitter and each time we measured the uncorrected reflection coefficient. We used two different sets of reference standards. The first set consisted of six mechanical devices (another set of four offset shorts, a load and an open), while the second set was realized with an electronically tunable impedance standard. During the measurement, an unknown device was connected to the measurement port of the splitter, and measured for different reference standards on the other port of the splitter. Details of the calibration and correction procedure follow.

#### IV. ANALYSIS

Our measurement system has three ports: two of the ports (ports 2 and 3) are terminated with the measurement and reference device, respectively, while the measurements are taken at the third port (port 1). In the notation of Fig. 1, we have

$$\begin{aligned} b_1 &= S_{11}a_1 + S_{12}a_2 + S_{13}a_3, \\ b_2 &= S_{21}a_1 + S_{22}a_2 + S_{23}a_3, \\ b_3 &= S_{31}a_1 + S_{32}a_2 + S_{33}a_3, \end{aligned} \quad (5)$$

along with boundary conditions

$$\begin{aligned} a_2 &= \Gamma_x b_2, \\ a_3 &= \Gamma_{ref} b_3. \end{aligned} \quad (6)$$

Solving this system of equations for the uncorrected reflection coefficient  $\Gamma_m = \frac{b_1}{a_1}$  measured by the VNA gives

$$\begin{aligned} \Gamma_m &= \frac{S_{11} - \Gamma_x \Delta_{11,22} - \Gamma_{ref} \Delta_{11,33} + \Gamma_x \Gamma_{ref} \Delta}{1 - \Gamma_x S_{22} - \Gamma_{ref} S_{33} + \Gamma_x \Gamma_{ref} \Delta_{22,33}} = \\ &= \frac{E_1 + E_2 \Gamma_x + E_3 \Gamma_{ref} + E_4 \Gamma_x \Gamma_{ref}}{1 - E_5 \Gamma_x - E_6 \Gamma_{ref} - E_7 \Gamma_x \Gamma_{ref}}, \end{aligned} \quad (7)$$

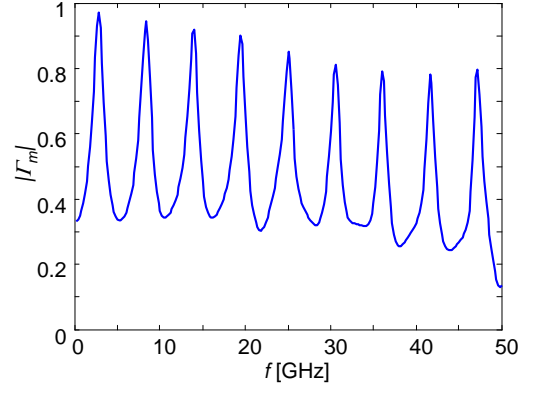


Figure 3. Reflection coefficient at the input of the splitter terminated with offset shorts of similar length.

where  $\Delta$  represents the determinant of the system's three-port  $S$ -matrix, and  $\Delta_{ii,jj}$  is a determinant defined by

$$\Delta_{ii,jj} = \begin{vmatrix} S_{ii} & S_{ij} \\ S_{ji} & S_{jj} \end{vmatrix}. \quad (8)$$

For a set of  $N$  reference reflection coefficients  $\Gamma_{ref,i}$  with  $i = 1, \dots, N$ , our system is described by  $4 + N$  parameters, since parameters  $E_3, E_4, E_6$  and  $E_7$  in (7) appear in products with  $\Gamma_{ref}$ .

In our calibration approach, we treat the system as a one-port reflectometer with variable parameters. Each set of reflectometer parameters (states) is realized by connecting a different reference standard. For a reference standard with reflection coefficient  $\Gamma_{ref,i}$ , the reflectometer can be described by

$$\Gamma_m = \frac{F_{1i} + F_{2i} \Gamma_x}{1 - F_{3i} \Gamma_x}, \quad (9)$$

where parameters  $F_{1i}, F_{2i}$  and  $F_{3i}$  are defined as

$$\begin{aligned} F_{1i} &= \frac{E_1 + E_3 \Gamma_{ref,i}}{1 - E_6 \Gamma_{ref,i}}, \\ F_{2i} &= \frac{E_2 + E_4 \Gamma_{ref,i}}{1 - E_6 \Gamma_{ref,i}}, \\ F_{3i} &= \frac{E_5 + E_7 \Gamma_{ref,i}}{1 - E_6 \Gamma_{ref,i}}. \end{aligned} \quad (10)$$

For each state of the reflectometer, we measure a set of calibration standards with known reflection coefficients and use standard one-port calibration methods to obtain parameters  $F_{1i}, F_{2i}$  and  $F_{3i}$ . Consequently, for  $N$  different values of  $\Gamma_{ref,i}$  we obtain  $3N$  parameters describing our system. Note that for  $N > 3$ , some of those parameters are correlated, as our system is then described by only  $4 + N < 3N$  parameters. These correlations can be exploited to increase the robustness of the calibration, but such optimizations will not be addressed in this paper.

In the measurement procedure, we measure a device-under-test (DUT) for the same set of reflectometer states. For each state we obtain the DUT parameters  $\Gamma_{x,i}$  by simply inverting

(9) and using parameters  $F_{1i}$ ,  $F_{2i}$  and  $F_{3i}$  obtained in the calibration. In order to estimate  $\Gamma_x$  we use a weighting procedure. We assume that the reflectometer states are perfectly repeatable and the errors in the measurement of  $\Gamma_{x,i}$  come from noise in each uncorrected measurement  $\Gamma_{m,i}$ . Assuming that the variance of errors in the uncorrected measurements is the same for each state, we can write

$$\Gamma_x = \frac{\sum_{i=1}^N \frac{1}{|D_i|^2} \Gamma_{x,i}}{\sum_{i=1}^N \frac{1}{|D_i|^2}}, \quad (11)$$

where

$$D_i = \frac{\partial \Gamma_{x,i}}{\partial \Gamma_{m,i}}, \quad (12)$$

and can be determined from (9).

## V. RESULTS AND DISCUSSION

In order to verify our approach, we performed a complete calibration of the system and then measured the reflection coefficient of a flat short. The magnitude and phase of the corrected flat short reflection coefficient are shown in Fig. 4 and Fig. 5, respectively, and are compared with a direct one-port measurement. The solid lines with squares and triangles represent the splitter measurement with states realized as mechanical standards and electronic tunable impedance, respectively, whereas the solid line with circles depicts the direct measurement.

Ideally, a flat short has a reflection coefficient of  $-1$ , and in all cases the measurement results are close to that value. We see very close agreement between the direct measurement and the splitter measurement with the electronically tunable reference standard. The differences in the magnitude are less than 0.2 %, while the differences in phase are within  $0.6^\circ$ . In order to conclude which measurement is more accurate, an uncertainty analysis for both measurement approaches needs to be performed. This will be the topic of further research.

The measurement performed with the mechanical reference standards does not agree as well with the direct measurement and exhibits some fairly regular ripples. The differences in magnitude are of order of 1 %, whereas the differences in phase are also within  $0.6^\circ$ . To understand the origin of the observed ripple pattern we performed a simple measurement of the input reflection coefficient of the splitter terminated with two offset shorts of similar length. We disconnected and reconnected the devices between the measurements. The difference of two such measurements is shown in Fig. 6. We used the same offset shorts for which we performed the measurement shown in Fig. 3. We see that the difference in  $\Gamma_m$  due to reconnection of the devices can be of the order of 0.25 % which, considering the attenuation of the splitter of approximately 12 dB, corresponds to changes of around 0.5 % in the reflection coefficients  $\Gamma_x$  and  $\Gamma_{ref}$ . The periodic spikes in the reconnection error are also correlated with the maxima of the reflection coefficient in Fig. 3. This indicates

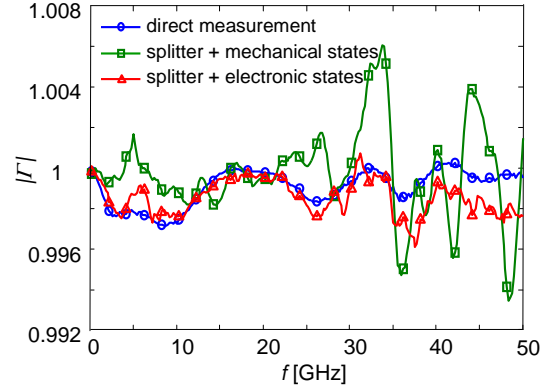


Figure 4. Magnitude of the reflection coefficient for a flat short: direct measurement (blue line with circles), splitter measurement with mechanical states (green line with squares), and splitter measurement with electronic states (red line with triangles).

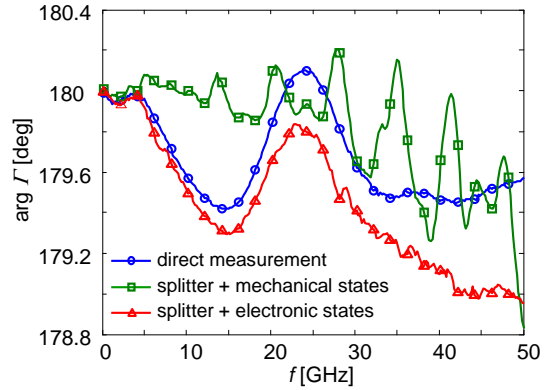


Figure 5. Phase of the reflection coefficient for a flat short: direct measurement (blue line with circles), splitter measurement with mechanical states (green line with squares), and splitter measurement with electronic states (red line with triangles).

that the observed ripples in the magnitude and phase result from connector repeatability errors that become larger as the magnitude of reflection coefficient approaches one [9].

## VI. CONCLUSIONS

We have demonstrated the basic principle of a simple approach for measurement of extreme impedances, extending the technique introduced in [6]. We used a multistate reflectometer realized as a power splitter with one of its arms terminated with a variable reference impedance and the other arm terminated with an unknown extreme-impedance device. This approach transforms the reflection coefficient of the extreme impedance closer to the center of the Smith chart, which may possibly improve the accuracy of the measurement. By using a variable reference impedance with different phase shifts the transformation does not rely on the phase shifting properties of the power splitting device as in [6], which allows us to increase the measurement bandwidth. The use of multiple reference standards provides redundant measurements that,

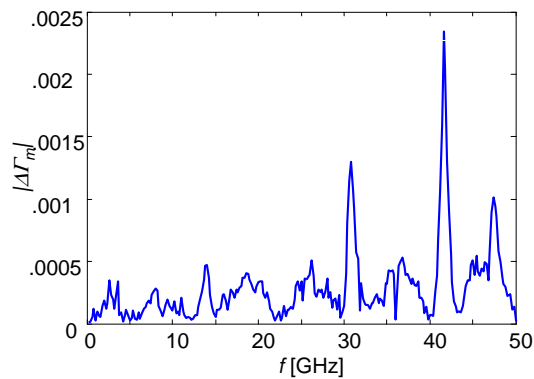


Figure 6. Magnitude of the difference (connection error) of reflection coefficients for an offset short at the reference port and a similar offset short at the measurement port for two consecutive reconnections of both devices. Note that the spikes in the connection error correspond to the maxima of the reflection coefficient for the same reference/device configuration as shown in Fig. 3.

combined with the weighting scheme we proposed, can also lead to increased measurement accuracy. Further study of the uncertainties of both measurement approaches is needed in order to quantify the accuracy improvement of our technique.

The single port measurement we described can also be extended to two-port measurement schemes. Such a two-port scheme would include two multistate reflectometers with the DUT connected between their device ports.

## VII. ACKNOWLEDGMENT

This research was partially supported by the DARPA Center on Nanoscale Science and Technology for Integrated Micro/Nano-Electromechanical Transducers (iMINT) funded by DARPA/MEMS S&T Fundamentals Program (HR0011-06-1-0048).

## REFERENCES

- [1] Z. Yu, and P. J. Burke, "Microwave transport in metallic single-walled carbon nanotubes," *Nano Letters*, 5, pp. 1403-1406, 2005.
- [2] Z. Yu, C. Rutherglen, and P. J. Burke, "Microwave nanotube transistor operation at high bias," *Applied Physics Letters*, 88, 233115. 2006.
- [3] P. Rice, T. M. Wallis, S. E. Russek, and Pavel Kabos, "Broadband Electrical Characterization of Multiwalled Carbon Nanotubes and Contacts," *Nano Letters*, 7, pp. 1086-1090, 2007.
- [4] "Reflectometer measurements - revisited", Anritsu Application Note 11410-00214.
- [5] H. Tanbakuchi, M. Richter, and M. Whitener, "Design of scanning capacitance microscope," *Digest of 2006 ARFTG Int. Conference*, November 2006.
- [6] M. Randus, K. Hoffmann, "A Simple Method for Extreme Impedances Measurement," *Digest of 2007 ARFTG Int. Conference*, December 2007.
- [7] Oldfield, B., "A multistate reflectometer", *IEEE Trans. Instrum. Meas.*, vol. 34, 1985, pp. 198-201.
- [8] T. M. Wallis, A. Lewandowski, "Statistical Measurement Techniques for Equivalent Source Mismatch of 1.85 mm Power Splitter", *Digest of 2008 ARFTG Int. Conference*, December 2008.
- [9] J. R. Juroshek, "A Study of Measurements of Connector Repeatability Using Highly Reflecting Loads (Short Paper)", *IEEE Trans. Microw. Theory Tech.*, vol. 35, 1987, pp. 457-460.

# Statistical Measurement Techniques for Equivalent Source Mismatch of 1.85 mm Power Splitter

T. Mitch Wallis, Arkadiusz Lewandowski

**Abstract**—The equivalent source mismatch ( $\Gamma_G$ ) of a 1.85 mm coaxial power splitter was characterized by use of two statistical measurement techniques. The first technique, originally described by Juroshek [1], uses a modified one-port calibration method to determine  $\Gamma_G$ . The second method uses two-port measurements of the splitter with one of the ports loaded with a series of calibration standards. This second, “indirect” method provides measurements of S-parameters for the three-port device that can subsequently be used to calculate  $\Gamma_G$ . Measurements of  $\Gamma_G$  made with the two techniques are in good agreement. This demonstrates that the value of  $\Gamma_G$  of a splitter can be determined by statistical measurement techniques, thus providing the possibility of exploiting redundant measurements to reduce the effect of random measurement errors. Analysis of repeated measurements of  $\Gamma_G$  shows that the effect of random measurement errors is lower for the indirect method than for the Juroshek method.

**Index Terms**—broadband measurements, calibration, equivalent source mismatch, microwave power splitters

## I. INTRODUCTION

A variety of microwave power measurement techniques rely on three-port devices such as directional couplers and power splitters. For example, three-port splitters are key components of direct power comparison systems [1], [2]. More generally, three-port devices are used in a variety of applications for power leveling. In a direct power comparison measurement, an accurate measurement of the effective source mismatch ( $\Gamma_G$ ) of a power splitter is necessary to account for reflections between the splitter and the device under test as well as the finite directivity of the splitter.  $\Gamma_G$  can be determined from the following equations [2]:

$$\Gamma_G = S_{22} - \frac{S_{12}S_{23}}{S_{13}} \quad (1)$$

$$\Gamma_G = S_{33} - \frac{S_{13}S_{32}}{S_{12}} \quad (2)$$

where equation (1) refers to  $\Gamma_G$  for port 2 and equation (2) refers to  $\Gamma_G$  for port 3.  $S_{ij}$  are the complex, three-port scattering parameters (S-parameters). This paper follows the convention that port 1 is the input port of the power splitter and port 2 and port 3 are the output ports.

T. Mitch Wallis is with the Electromagnetic Division, National Institute of Standards and Technology, Boulder, CO 80305 USA (phone: 303-497-5089; e-mail: mwallis@boulder.nist.gov).

Arkadiusz Lewandowski is with the Warsaw University of Technology. He is currently a Guest Researcher at the National Institute of Standards and Technology, Boulder, CO 80305 USA.

This work is a publication of the National Institute of Standards and Technology (NIST), an agency of the U.S. government, and is not subject to U.S. copyright.

Several approaches to direct measurement of  $\Gamma_G$  of three-port devices have been reported [1], [3], [4]. Additionally, several measurement techniques have been reported that use a conventional two-port network analyzer to determine the S-parameters of a three-port device [5], [6], [7]. Once the S-parameters are known,  $\Gamma_G$  can be determined via equations (1) and (2). Generally, the direct measurement techniques are less complex, require fewer connects and do not require a two-port calibration of the network analyzer, but the direct measurement techniques do not provide the full characterization of the three-port S-parameters. This paper summarizes the determination of  $\Gamma_G$  for a 1.85 mm coaxial power splitter using two different methods. Specifically, the methods described in references [1] and [5] are extended by use of redundant measurements. Throughout the paper, the extension of the direct method introduced by Juroshek in [1] will be referred to as the “Juroshek method” and the extension of the method introduced in [5] will be referred to as the “indirect method.” The two methods produce measurements of  $\Gamma_G$  that are in good agreement with one another. Moreover, repeated measurements with both methods using variable numbers of standards demonstrate how redundant measurements can reduce the effect of random measurement errors. Specifically, the effect of random measurement errors is found to be significantly lower for the indirect method. However, the use of redundant measurements is more effective in reducing this effect for the Juroshek method.

## II. MEASUREMENT METHODS

Two measurement methods were used to determine  $\Gamma_G$  of a commercial 1.85 mm coaxial power splitter between 200 MHz and 67 GHz. Nominally, the splitter delivers one quarter of the power input at port 1 to each of the two output terminals (port 2 and port 3). The first method is the Juroshek method [1]. The measurement setup is shown schematically in Figure 1(a). In this method, two ports of the splitter are connected to an uncalibrated two-port network analyzer, while the third port of the splitter acts as the measurement port of an equivalent one-port network analyzer. Calibration standards are then connected to this equivalent measurement port and a one-port calibration is performed.  $\Gamma_G$  can be shown to be the source match as determined by the one-port calibration. The approach reported here extends the original work presented in [1] in that redundant measurements are used here to reduce the effect of random measurement errors. Specifically, six one-port calibration standards are used: four offset shorts, along with an open and a matched load. Note that this system is over-

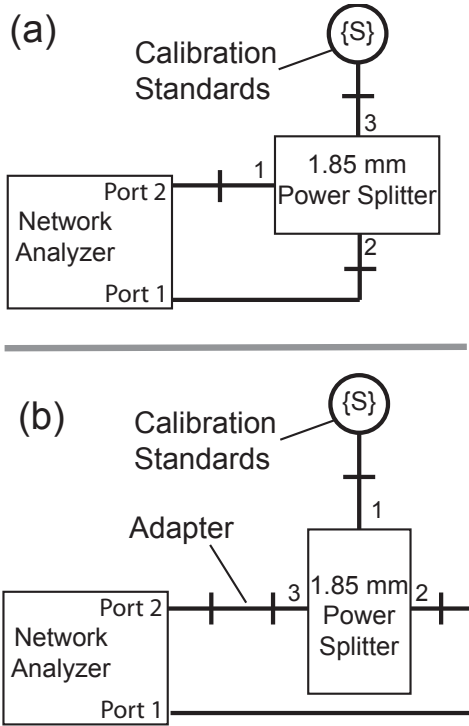


Figure 1. Schematic diagrams of the two methods used in this paper for measuring  $\Gamma_G$ . (a) The Juroshek method is based on reference [1] and uses a conventional, uncalibrated two-port network analyzer as an equivalent one-port analyzer. Note that the configuration for measuring  $\Gamma_G$  for port 3 is shown. To measure  $\Gamma_G$  for port 2, port 2 and port 3 must be swapped. (b) The indirect method extends reference [5]. This method requires a calibrated two-port network analyzer. Note that the calibration standards are connected to port 1 (the input port) and an adapter is required in order to provide compatibility with an insertable two-port calibration.

determined: only three standards are required to determine the source match of an equivalent one port analyzer. Thus, the calibration is completed by use of a statistical approach based on the weighted linear least squares technique and the Bauer-Penfield method [8].

The indirect method used here extends the approach of reference [5]. The underlying strategy of this method is as follows. First, five of the nine three-port S-parameters for the device along with products of the remaining four S-parameters are determined.  $\Gamma_G$  for port 2 and port 3 are then calculated from equations (1) and (2), respectively. The measurement setup for the indirect method is shown in Figure 1(b). The output terminals of the splitter are connected to a calibrated two-port network analyzer and measurements are taken with different one-port standards connected to the free input port of the splitter. In contrast to reference [5], we use measurements of multiple reflect standards (four offset shorts, an open and a matched load). The set of two-port S-parameter measurements is described by four equations for each one-port calibration standard. The equations have the form

$$S_{ij}^M = S_{ij} + \frac{S_{1j}S_{i1}\Gamma}{1 - S_{11}\Gamma} \quad (3)$$

where the  $S_{ij}^M$  are the four calibrated measurements of the

scattering parameters made with the network analyzer ( $i = 2, 3$  and  $j = 2, 3$ ).  $\Gamma$  is the reflection coefficient of the one-port standard and is obtained from a model of the standard. With six calibration standards, there is an over-determined system of equations for eight unknowns:  $S_{11}$ ,  $S_{22}$ ,  $S_{33}$ ,  $S_{23}$ ,  $S_{32}$ ,  $S_{13}S_{31}$ ,  $S_{12}S_{21}$ , and  $S_{12}S_{31}$  (note that  $S_{13}S_{21}$  can be expressed in terms of the other unknowns). Equation (3) can be linearized in terms of the eight unknowns by multiplying by  $(1 - S_{11}\Gamma)$ . The linearized set of equations is then solved using a weighted linear least squares technique. The solutions to the linearized problem are subsequently used as an initial guess for an unconstrained nonlinear optimization routine that determines the eight unknowns such that the difference between the measurements and values calculated from equation (3) is minimized. Note that an adapter is used during the measurements to make the splitter compatible with the network analyzer ports. Therefore a subsequent characterization of the adapter is required as part of the analysis.

### III. MEASUREMENT RESULTS

The results of the measurements are shown in Figure 2. Figure 2(a) compares the two methods for port 2, while Figure 2(b) compares the two methods for port 3. The measurements from the Juroshek method (solid black curves) and the measurements from the indirect method (dashed gray curves) generally agree well. The agreement for  $|\Gamma_G|$  for port 2 is closer than the agreement for  $|\Gamma_G|$  for port 3. This is attributed to the introduction of additional uncertainty in the port 3  $\Gamma_G$  measurements in the indirect method due to the adapter and a non-rigid cable connecting port 3 to the network analyzer. This effect could be mitigated by swapping ports 2 and 3 in the indirect method in order to reduce the uncertainty in the measurement of port 3.

While the two methods yield similar results, there are notable differences. The Juroshek method requires fewer connects to determine  $\Gamma_G$ ; however, it yields  $\Gamma_G$  only for one of the splitter ports. The indirect method requires more connects, a two-port calibration of the network analyzer, and the use of an adapter, but provides information about the three-port S-parameters. Consequently, it yields  $\Gamma_G$  for both splitter ports, albeit with the introduction of additional uncertainty on the port that is connected to the adapter.  $|S_{22}|$  and  $|S_{33}|$  as measured by the indirect method are shown in Figures 2(a) and 2(b), respectively.

### IV. REPEATABILITY ANALYSIS

In order to evaluate the effect of random measurement errors on  $\Gamma_G$ , measurements were repeated several times for each of the two methods. For the Juroshek method, the measurements were repeated five times for each output port. For the indirect method, measurements were repeated three times. The effect of redundant measurements was evaluated by varying the number of standards used to calculate  $\Gamma_G$ . In the simplest case, only three measurements of the one-port calibration standards were used: an open, a matched load, and one short. In contrast,  $\Gamma_G$  was also calculated using measurements of all six calibration

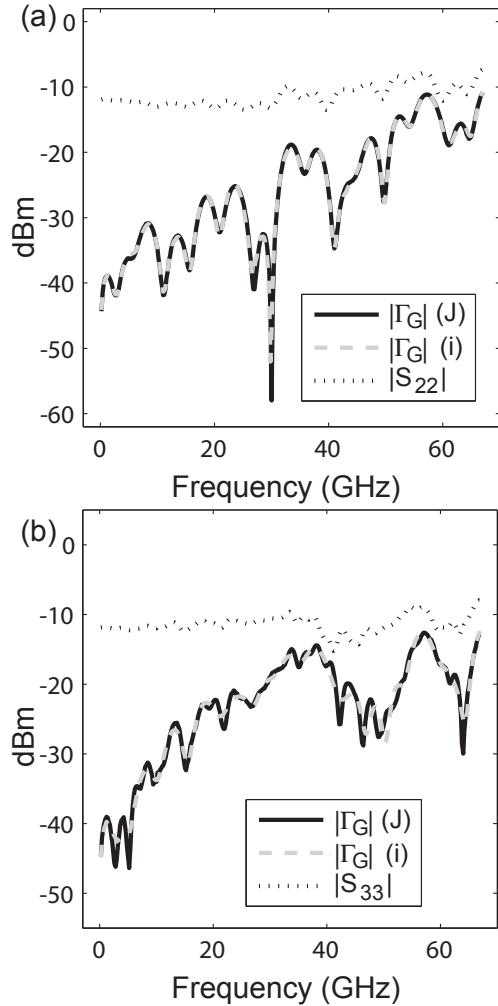


Figure 2. Comparison of the two methods used in this paper for measuring  $\Gamma_G$ . (a)  $|\Gamma_G|$  for port 2 of the 1.85 mm coaxial power splitter. The solid black curve corresponds to  $|\Gamma_G|$  as determined by the Juroshek (J) method and the dashed gray curve corresponds to  $|\Gamma_G|$  as determined by the indirect (i) method. The dotted black curve is  $|S_{22}|$ , as determined by the indirect method. Each curve is the average of five separate measurements. (b)  $|\Gamma_G|$  for port 3 of the 1.85 mm coaxial power splitter. The solid black curve corresponds to  $|\Gamma_G|$  as determined by the Juroshek (J) method and the dashed gray curve corresponds to  $|\Gamma_G|$  as determined by the indirect (i) method. The dotted black curve is  $|S_{33}|$ , as determined by the indirect method. Each curve is the average of three separate measurements.

standards. Figures 3 and 4 show the standard deviations of  $|\Gamma_G|$  for the Juroshek and indirect methods, respectively, calculated using all six standards (solid black lines) as well as just three standards (solid gray lines).

A comparison of Figures 3 and 4 shows that the standard deviation for the indirect method is almost an order of magnitude smaller than the standard deviation for the Juroshek method. This is attributed to the fact that more measurements are made in the indirect method, particularly in the process of performing a two-port calibration. From Figure 3, it is clear that the use of redundant measurements reduces the effect of random measurement errors on  $\Gamma_G$  for the

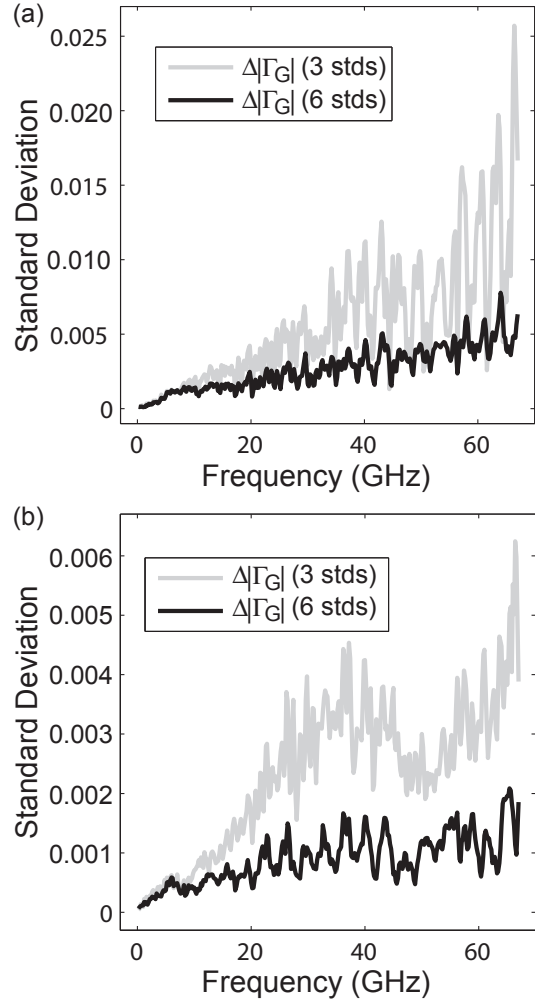


Figure 3. Effect of redundant measurements for the Juroshek method. Standard deviation in five repeated measurements of  $|\Gamma_G|$  with six standards (solid black curve) and three standards (solid gray curve) for (a) port 2 and (b) port 3.

Juroshek method: clearly, when redundant measurements are used, the standard deviation decreases at nearly all frequencies for each port. From Figure 4, the reduction in the effect of random measurement errors on  $\Gamma_G$  for the indirect method is less clear: when redundant measurements are used the standard deviation decreases at some, but not all frequencies. The number of repeated measurements in these experiments represents a small sample size, but from these results it is clear that redundant measurements reduce the statistical uncertainty for the Juroshek method and it appears that there is a similar effect for the indirect method, albeit of a smaller magnitude.

## V. CONCLUSION

These measurements demonstrate that the original methods of [1] and [5] for determining the effective source mismatch  $\Gamma_G$  can be re-formulated in a statistical framework. This allows the use of redundant measurements in characterization of  $\Gamma_G$ , which in turn provides the possibility of reducing the effect

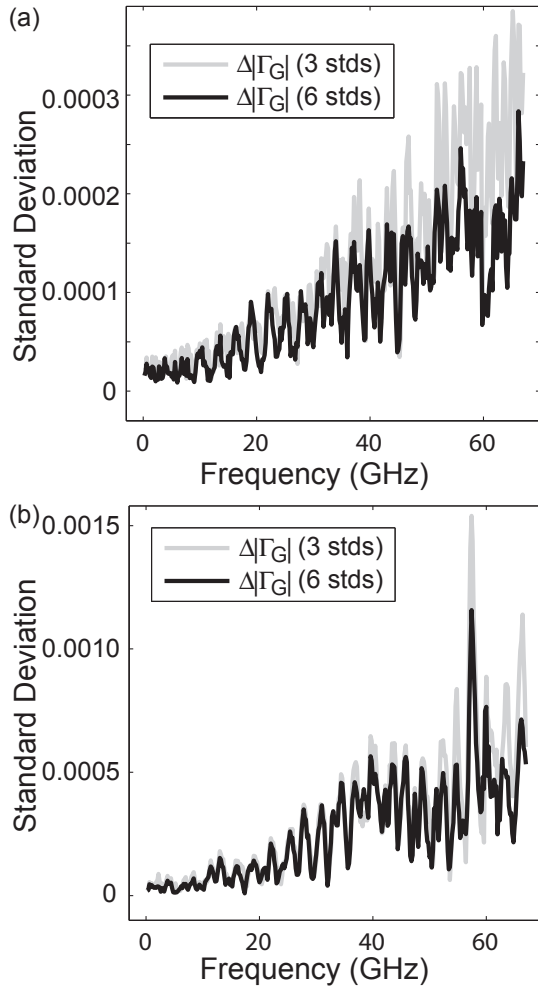


Figure 4. Effect of redundant measurements for the indirect method. Standard deviation in three repeated measurements of  $|\Gamma_G|$  with six standards (solid black curve) and three standards (solid gray curve) for (a) port 2 and (b) port 3.

of random measurement errors. In practical terms, the use of redundant measurements to determine  $\Gamma_G$  will reduce the contribution of random measurement errors to the total uncertainty in direct power comparison measurements and other applications that require three-port devices. Moving forward, a rigorous analysis of the effect of systematic errors in the two methods for determining  $\Gamma_G$  will facilitate further comparison of the methods' respective strengths and limitations.

#### REFERENCES

[1] J. R. Juroshek, "A Direct Calibration Method for Measuring Equivalent Source Mismatch", *Microwave Journal* 40, 106 (October 1997).  
 [2] M. P. Weidman, "Direct Comparison Transfer of Microwave Power Sensor Calibration," *NIST Technical Note 1379*, U. S. Department of Commerce (January 1996).  
 [3] R. D. Moyer, "Techniques for Measuring the Effective Source Reflection Coefficient of Two-Resistor Power Splitters," *IEEE Transactions on Instrumentation and Measurement* 36, 23 (March 1987).

[4] R. C. Powell and A. C. Miller, "Determination of the Reflection Correction when Using a Symmetrical Two-Resistor Power Splitter to Calibrate a Power Sensor," *IEEE Transactions on Instrumentation and Measurement* 36, 458 (June 1987).  
 [5] M. Davidovitz, "Reconstruction of the S-matrix for a 3-port Using Measurements at Only Two Ports", *IEEE Microwave and Guided Wave Letters*, 5, 349 (October 1995).  
 [6] J. C. Tippett and R. A. Speciale, "A Rigorous Technique for Measuring the Scattering Matrix of a Multiport Device with a 2-Port Network Analyzer," *IEEE Transactions on Microwave Theory and Techniques* 30, 661 (May 1982).  
 [7] J. C. Rautio, "Techniques for correcting scattering parameter data of an imperfectly terminated multiport when measured with a two-port network analyzer," *IEEE Transactions on Microwave Theory and Techniques* 31, 407 (May 1983).  
 [8] R. F. Bauer and P. Penfield, "De-Embedding and Unterminating," *IEEE Transactions On Microwave Theory and Techniques* 22, 282 (March 1974).

# An Envelope Domain Measurement Test Setup to Acquire Linear Scattering Parameters

Efrain Zenteno\*, Magnus Isaksson\*, David Wisell†, Niclas Keskitalo\*† and Olav Andersen‡

\*Center for RF Measurement Technology, University of Gävle  
SE-801 76 Gävle, Sweden,

†Ericsson AB, SE-164 80 Stockholm, Sweden

‡Ericsson AB, Box 6206, SE-800 06 Gävle, Sweden

**Abstract**—In this paper, the functionality of a vector network analyzer VNA is implemented using the concept of software defined measurements (SDM) [1], called SDM-VNA.

A general measurement set-up based on a vector signal generator (VSG) and a vector signal analyzer (VSA) is used. The set-up allows complete linear characterization using only one receiver. A calibration procedure to remove the systematic errors is applied to the results and compared with a modern VNA, showing good agreement.

## I. INTRODUCTION

Linear Scattering parameters, or so called S-parameters, are undoubtedly one of the best resources available to characterize linear networks. Even today, they are extensively used, especially in the radio frequency. However, up to now, measurements of S-parameters required the use of several receivers in order to detect the scattered waves in a DUT, as illustrated in Fig. 1.

In this kind of architecture, synchronization requirements as well as similarity in the linear distortion are needed for all receivers.

The operation principle of this type of receiver is down-conversion in a narrow-band Intermediate Frequency (IF), which allows accurate results, but also prevents new forms of signal excitation, which becomes a requirement in the new communication systems.

## II. EXPERIMENTAL

The set-up used is presented in Fig. 2, and it consists of an arbitrary waveform generator plus IQ modulator (source) (SMU 200A, Rohde & Schwarz), a Vector Signal Analyzer (VSA FSQ26, Rohde & Schwarz), acting as a receiver, a test set built with couplers (for signal separation), and a personal computer (for automation and numerical calculations). Finally the set-up is completed by a solid-state switch that allows for the use of a single receiver in the measurements of complex quantities involving ratios of scattered waves.

The benefits of using a general hardware (HW) set-up and implementing the functionality in software (SW) are that it is simpler with regard to e.g. cabling, switches, calibration, etc., and that it is more flexible in that functionality can be more easily enhanced or added. This is certainly an advantage, especially in a production environment where many different measurements are to be executed on the workstation.

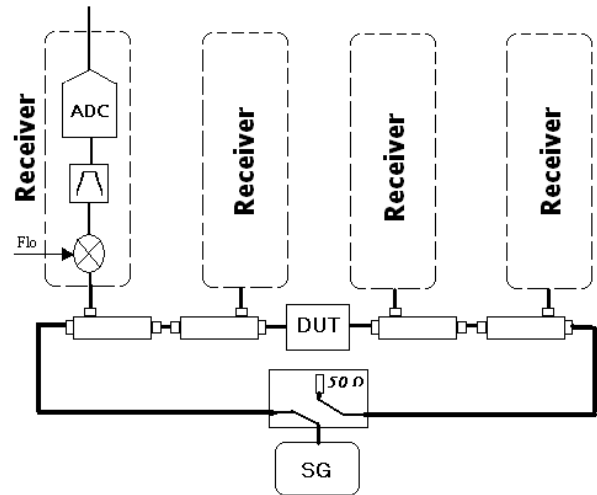


Fig. 1. Typical VNA hardware structure

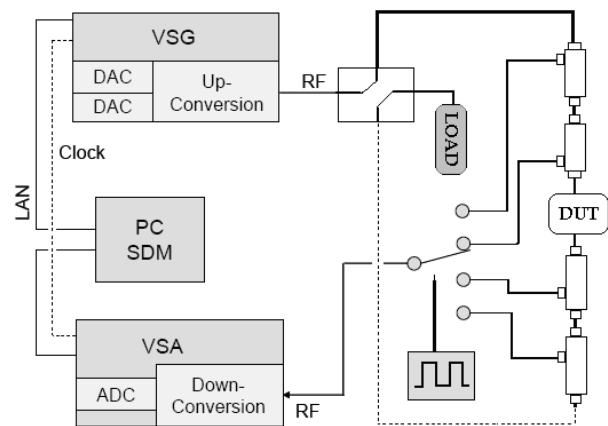


Fig. 2. Proposed hardware set-up

Note that in Fig. 2 a single receiver is used for all measured signals. This decreases the need for calibration since it inherently decreases the influence of the receiver on the measurement result. This obviously requires that the DUT be viewed as time invariant between the measurements of the

different input and output signals. This is certainly the case for passive devices, but it also holds for most active devices such as power amplifiers (PAs).

The use of the combination vector signal generator (VSG) and vector signal analyzer (VSA) provides not only a source capable of reproducing different kinds of stimulus signals, but it also offers the possibility of nonlinear characterization [2], as can be seen in [3].

The stimulus signal chosen is a 10-tone complex exponential,

$$s(t) = \sum_{i=1}^N A_i e^{j(\omega_i t + \phi_i)} \quad (1)$$

with constant tone separation, using phases according to [4] in order to decrease the peak to average power ratio to around 2.5 dB.

The basic idea to compute S-parameters is to perform a fast switching and record enough samples related to all waves in the measurement ports; it will keep the phase reference of the signals, while the switch can run independently from the instruments and computer in the set-up.

The well-known period of the stimulus signal can be used advantageously when coherent averaging [5] is implemented so that the dynamic range of the set-up is maximized.

A critical step to achieve the S-parameter measurement is the digital signal separation, which refers to the ability to extract the different signals in the recorded stream of data of the VSA. For this purpose, the power presented in the reference branch must always be higher than the other branches; this can be achieved by proper selection of the coupling factors or introducing attenuation to the signals reaching the switch. In this way, the power of the stream, numerically calculated for a number of samples that is equal to a period of the signal, will show clear edges in the transitions between the signals, as illustrated in Fig. 3.

### III. EXTRACTION OF AMPLITUDE AND PHASE

Proceeding with the measurement, a magnitude and phase extraction is required, and the modulated 10-tone signal can be seen as

$$s(t) = x(t)\cos(\omega_c t) + y(t)\sin(\omega_c t) \quad (2)$$

where  $x(t)$  and  $y(t)$  are the in-phase and quadrature-phase signals, respectively,  $\omega_c = 2\pi f_c$  is the carrier frequency. In the modulation domain, this signal is written as

$$s_i(t) = x(t) + jy(t) \quad (3)$$

The amplitudes and phases of the tones are found by solving Eq. 4 in the min square sense, as is described in [6]:

$$z = \mathbf{H}\theta. \quad (4)$$

where the column vector  $z$  contains the measured values,  $\theta$  contains the amplitude and phases of the respective frequencies, and  $\mathbf{H}$  is defined as:

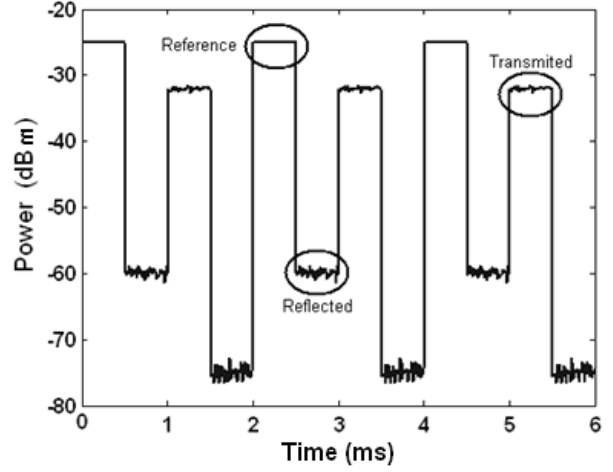


Fig. 3. Signal Separation based on Power difference

$$\mathbf{H} = \begin{pmatrix} 1 & 1 & \dots & 1 \\ e^{-j\omega_0} & e^{-j\omega_1} & \dots & e^{-j\omega_9} \\ \vdots & \vdots & \ddots & \vdots \\ e^{-j\omega_0(N-1)} & e^{-j\omega_1(N-1)} & \dots & e^{-j\omega_9(N-1)} \end{pmatrix} \quad (5)$$

The phase relationship is found by using an estimation of the pseudo delay of the system [7], [8], that can be written as the following:

$$\tau_p = \frac{\psi_6 - \psi_5}{\omega_d} \quad (6)$$

where

$$\psi_i = \angle\theta_i - \phi_i \quad (7)$$

and  $\angle\theta_i$  represents the measured phase, while  $\phi_i$  is the initial phase of the  $i$  tone.

Thus, the phase can be compensated for this delay by using:

$$\varphi_{ci} = \psi_i - \omega_i \tau_p. \quad (8)$$

It is most important that the pseudo delay of the system ( $\tau_p$ ) is considered constant for short time periods, as long as the interval is small enough to avoid any clock variation or drift in the oscillators. Hence, phase calculation is done for the first signal (reference signal) by calculating  $\tau_p$ ; when treating the next signals, that value is assumed to be the same, correcting directly for the phase deviation using equation 8. The procedure for amplitude and phase calculation is summarized in TABLE I

TABLE I  
SUMMARY OF MEASUREMENT PROCEDURE

- |   |   |
|---|---|
| 1 | Separate the different signals of the stream recorded using the VSA.                                |
| 2 | Using the signal corresponding to the reference branch, calculate $\tau_p$ by solving Eqs. 6 and 7. |
| 3 | Use Eq. 4 to find the magnitude and phase of the tones.   |
| 4 | Use Eq. 8 to correct the phase obtained in step 3 by applying $\tau_p$ obtained in step 2.          |
| 5 | Repeat steps 3 and 4 with the rest of the signals.  |

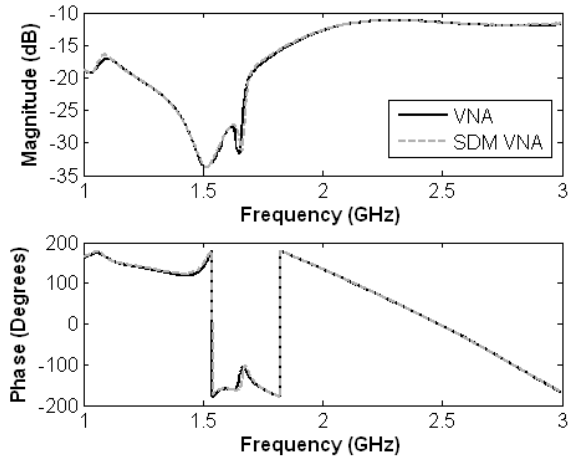


Fig. 4.  $S_{11}$  of an RF power Amplifier

#### IV. CALIBRATION

The difference between the "true" and the measured S-parameters, despite of the noise inherent to every measurement, is caused by the non-ideal test conditions such as limited directivity on the couplers, mismatches in the source as well in the load side.

To get rid of these systematic errors, two calibrations were tested: 'SOLT 12 error term' and 'One path two port' calibration.

#### V. RESULTS

Extensive measurements were performed to test the ability of the set-up to properly acquire S-parameters. Figs. 4, 5 and 6 show a comparison between measurements carried out in the set-up (using one path two port cal) as well as a modern VNA. To decrease the impact of the calibration procedure in the final S-parameters, the same calibration kit was used in the VNA and SDM-VNA.

Fig. 4 shows  $S_{11}$  of an amplifier module, Fig 5 shows  $S_{21}$  of a second amplifier and Fig. 6 shows  $S_{21}$  of a 3 dB attenuator; in these figures, an excellent correlation between measurements is apparent.

Small differences in magnitude and phase are encountered, in the worst cases like 0.2 dB and 1 degree, however such deviations correspond to a very small magnitude of the measured vector, and the uncertainties from both instruments are larger.

To prove the validity of such measurements, the method described in [9] was used to test the concordance of these with measurement R&S ZVA-8 from Rohde and Schwarz.

In Fig. 7, the sum of the repeatability boundaries for VNA and the test set-up proposed are shown, together with the maximum difference boundary for a set of verification devices using two different calibration methods. The set of verification devices is composed of 2 amplifiers and 2 attenuators.

Note from Fig. 7 that even for one-path two-port calibration the difference boundary is slightly off the repeatability bound-

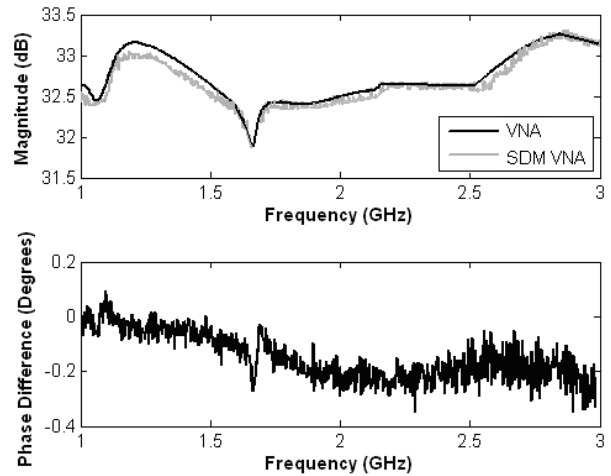


Fig. 5.  $S_{21}$  of Band pass of an amplifier

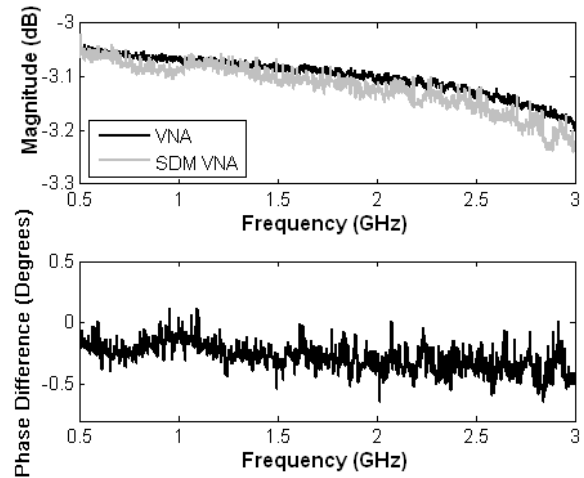


Fig. 6.  $S_{21}$  of a 3 dB attenuator

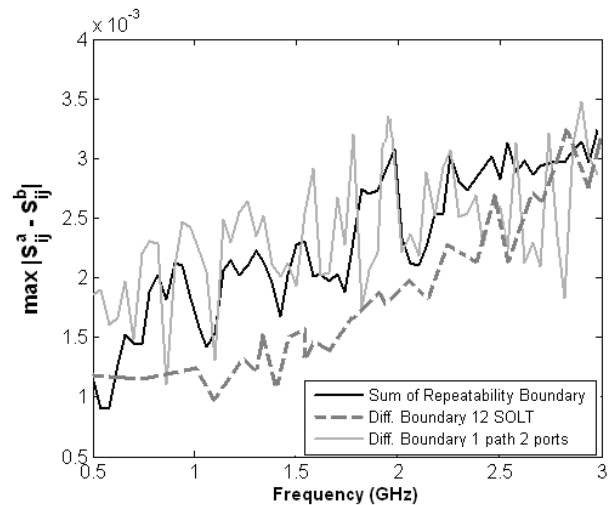


Fig. 7. Repeatability and Difference boundary

dary, but the closeness of both lines suggests a fair agreement between both instruments, with this type of calibration the speed reported in the measurements was around 170MHz/s.

On the other hand, 12 SOLT calibration provides better agreement and speed of 85 MHz/s. this is because 12 SOLT requires more measurements on the DUT performing better correction procedures.

An important limiting factor regarding the speed issue is the bandwidth of the receiver in VSA (20 MHz) that prevents the utilization of the full bandwidth presented in the source (VSG).

## VI. CONCLUSION

The proposed set-up allows the measurement of scattering parameters using a single receiver. The set-up relaxes the requirements of synchronization and calibration in a typical instrument having several receivers.

The repeatability analysis along with the respective difference boundary, shown in Fig. 7 illustrates the agreement of the measurements between the proposed set-up and a normal VNA. Moreover, the speed achieved in this configuration is similar to modern VNAs using narrow IF bandwidths.

## ACKNOWLEDGMENTS

This work was supported by Ericsson AB, Freescale Semiconductor Nordic AB, Infineon Technologies Nordic AB, Knowledge Foundation, NOTE AB, Rohde & Schwarz AB and Syntronic AB.

## REFERENCES

- [1] D. Wisell, P. Stenvard, A. Hansebacke, and N. Keskitalo, "Considerations when designing and using virtual instruments as building blocks in flexible measurement system solutions," in *Proc. IMTC 2007, Warsaw, Poland*, 2007.
- [2] K. Remley, P. Hale, D. Bergman, and D. Keenan, "Comparison of multisine measurements from instrumentation capable of nonlinear system characterization," in *66th ARFTG Conf. Dig., Washington D.C.*, 2006, pp. 34–43.
- [3] E. Zenteno, O. Andersen, M. Isaksson, N. Keskitalo, and D. Wisell, "Nonlinear network analysis for modern communication devices and systems," *submitted at 72th ARFTG Conf., Portland, Oregon*, 2008.
- [4] M. Schroeder, "Synthesis of low-peak-factor signals and binary sequences with low autocorrelation," in *IEEE Trans. on Information Theory*, vol 16, January, 1970, pp. 85–89.
- [5] D. Wisell, M. Isaksson, and D. Rönnow, "Validation of behavioral power amplifier models using coherent averaging," in *Proc. Gigahertz, Uppsala, Sweden*, 2005, pp. 318–321.
- [6] T. Söderström and P. Stoica, *System Identification*, 2nd ed. Upper Saddle River: Prentice Hall, 1989.
- [7] K. Remley, D. Williams, D. Schreurs, G. Loglio, and A. Cidronali, "Phase detrending for measured multisine signals," in *61th ARFTG Conf. Dig., Philadelphia, PA*, 2003, pp. 73–83.
- [8] D. Wisell, B. Rudlund, and D. Rönnow, "Characterization of memory effects in power amplifiers using digital two-tone measurements," in *IEEE Trans. Instrum. Meas.*, Vol 56, No 6, 2007, pp. 2757 – 2766.
- [9] D. DeGroot, R. Marks, and J. Jargon, "A method for comparing vector network analyzers," in *54th ARFTG Conf. Dig., Atlanta, GA*, 1997, pp. 107–114.

# MICROWAVE CHARACTERIZATION OF OPTICALLY MODULATED PHOTO-INDUCED SWITCHES WITH A PASSIVATION LAYER USING AN LSNA

C. Roda Neve<sup>(1)</sup>, G. Poesen<sup>(2)</sup>, D. Schreurs<sup>(3)</sup>, J.-P. Raskin<sup>(1)</sup>, J. Stiens<sup>(2)</sup>, R. Vounckx<sup>(2)</sup>

<sup>(1)</sup>UCL, Belgium

<sup>(2)</sup>Vrije Universiteit Brussel, Belgium

<sup>(3)</sup>K.U.Leuven, Belgium

## Abstract

A measurement set-up has been developed to characterize the electrical response to a pulsed optical excitation on photo-induced switches. The hardware configuration is a combination of a 50 GHz LSNA and a laser modulated by a pulse generator. By making use of vector large-signal measurements, the pulse envelope response is measured which allows the study of transient effects as well as the determination of performance parameters such as excess carrier lifetime. It is demonstrated that depositing a passivation layer beneath the CWP transmission line switch reduces the carrier life time considerably.

## I. Introduction

The interest in microwave components with a tunable switching behavior has grown over the past years. In applications like beam steering, imaging, and switching between receiver and transmitter, components such as MEMS have been implemented. Another known way to make tunable RF-components is by using optoelectronic techniques. Direct optical control permits a high electrical isolation between the optical control signal and the microwave/millimeter wave component. Such control is achieved by creating a photo-induced plasma volume at the illuminated areas of a semiconductor material [1]. The device itself has a simple transmission line structure. The objective of this work is to study the influence of technology variations, and more precisely passivation, on the electrical response of a pulsed optical excitation on such transmission line switches. The measurement set-up is based on the Large-Signal Network Analyzer (LSNA). It builds on earlier work [2] in which the set-up was developed for CW modulated optical excitations only. A pulsed excitation however resembles closer the actual operation in practical applications, and moreover the underlying physics can be analyzed in more depth [3]. The present work expands beyond an earlier reporting on this measurement technique [4] in that its application is extended to the characterization of the excess carrier lifetime and that the influence of passivation on the results is studied.

The devices under investigation are described in Section II. The developed measurement set-up is presented in Section III, and experimental results are discussed in Section IV.

## II. Photo-induced switch

Fig. 1 shows the cross-sections of three versions of photo-induced switches. The standard implementation, depicted in Fig. 1a, consists of a CPW transmission line lying on a high-resistivity silicon substrate (HR-Si). Due to the nature of semiconductor substrates, the photo-induced excess carriers are not restricted to the illuminated zone, but spread within a larger zone as a result of carrier diffusion [5]. The use of a passivation layer between the oxide and the HR-Si (Fig. 1b) has recently been proved to be an effective way to reduce the photo-induced carrier diffusion [6], and therefore it could be used as a way to restrict lateral diffusion to a desired area. In this work, we go one step further by etching a small window of the sandwiched passivation layer, below the CPW, to allow the light to reach the HR-Si substrate (Fig. 1c). The corresponding top view of the proposed new design for a photo-induced switch using a passivation layer is presented in Fig. 2. In this work, these three types of photo-induced switches will be characterized and compared. Also a fourth type has been included in the study by which the passivation layer was completely etched away prior to oxidation and CPW transmission line metallization ('etched HR-Si').

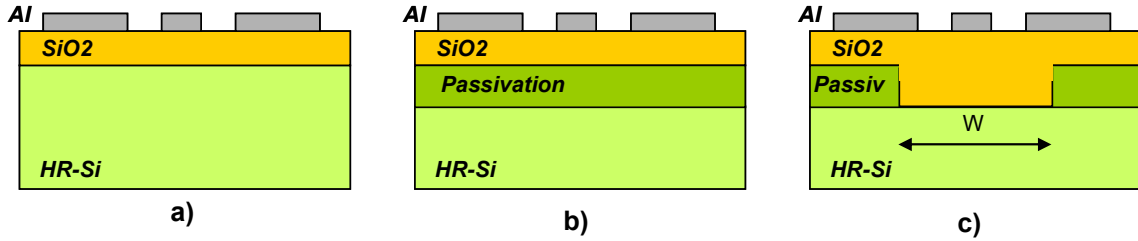


Fig. 1: CPW transmission line on (a) un-passivated high-resistivity silicon substrate, (b) on passivated high-resistivity silicon substrate, and (c) on passivated high-resistivity silicon substrate with an etched window.

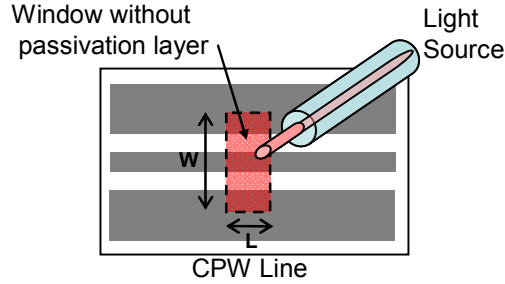


Fig. 2: Use of windows to allow the laser light to illuminate the high-resistivity silicon substrate.

All CPW transmission lines consist of a 1  $\mu\text{m}$ -thick aluminum CPW transmission line of 3385  $\mu\text{m}$  length. The dimensions of the CPW transmission line are:  $W = 58 \mu\text{m}$  for the width of the central conductor,  $S = 36 \mu\text{m}$  for the slot width, and  $W_g = 208 \mu\text{m}$  for the width of the planar ground conductors. For all switches, the silicon resistivity is 2  $\text{k}\Omega\text{-cm}$ . The passivation was done by deposition of a 270 nm layer of amorphous Silicon ( $\alpha\text{-Si}$ ) followed by a rapid thermal annealing step (2 min. at  $950^\circ\text{C}$ ). The passivation was fully etched at the desired zones, by means of a TMAH etching process. Finally, a dry thermal oxidation followed to obtain a 50 nm-thickness  $\text{SiO}_2$  top layer.

The operation of these devices under optical modulation can be understood as follows. When the CPW transmission line is not illuminated, the RF-signal is transmitted undisturbedly and therefore this corresponds to the ON-state. The OFF-state is realized by increasing the substrate conductivity below the CPW transmission line by illuminating one or both slots of the CPW transmission line, i.e., by creating a photo-induced short. When the incident control illumination is modulated the efficiency of the switch depends on the modulation frequency. Time dependent parameters of the carrier substrate are one of the dominating parameters influencing the switch efficiency. Moreover the attenuation mechanism that takes place during the OFF-state, attenuative or reflective, is function of the RF frequency and of the OFF-state duration. By using an LSNA up to 50 GHz, the transient effects due to optical modulation can be studied as function of the RF frequency.

### III. Measurement set-up

Whereas a transmission line switch based on the photoconductivity phenomenon is a linear time-invariant system, one needs a non-linear measurement set-up to characterize the transient electrical response under pulsed optical excitation. The reason is that the optical-electrical effect is a mixing process. Whereas modern network analyzers can measure at other frequencies than the applied frequency, the same functionality can not be obtained. One reason is that one would need an additional external excitation signal, which increases the complexity in terms of both synchronization and calibration. The authors performed some tests in this regard and experienced a number of practical issues. The main limiting factor was that the time it takes for the network analyzer to sweep from one frequency point to the next one takes longer than the pulse duration of the optical excitation. Another aspect was the narrow spacing between frequency points, or in other words, the high number of data points because the pulsed excitation is in base band (1 kHz). The latter is also the main determining factor why an oscilloscope is not suitable to execute this type of measurements. The huge difference between the envelope period (1 ms) and the RF period (20 ps, in case of 50 GHz excitation) would require a huge number of sampling points ( $>100\text{MS/s}$ ) and this in combination with a wide RF bandwidth. The down-conversion sampling principle, on which the LSNA is based, is more appropriate.

The measurement set-up is represented schematically by Fig. 3 and illustrated by some pictures in Fig. 4. The pulse generator modulates the red laser light, which illuminates an area of  $10\ \mu\text{m}$  of diameter on one slot of the CPW transmission line switch through an optical fiber. The oscilloscope is used to monitor the signal generated by the pulse generator. The CW RF signal is generated by the 50 GHz RF source within the LSNA rack, and both the incident signals and responses are characterized by the LSNA. The measurements are controlled via a PC, and all instruments are synchronized via a 10 MHz signal.

The base band optical modulation on the transmission line introduces small modulation tones, with a spacing equal to the modulation frequency  $f_{\text{mod}}$ , around the fundamental carrier frequency  $f_{\text{fund}}$ . Depending on the shape of the base band excitation (square, triangular, ...), higher order intermodulation products appear in the transmitted (and reflected) spectrum, and are located at frequencies equal to  $f_{\text{fund}} \pm N \cdot f_{\text{mod}}$ , with  $2N$  being the number of considered spectral components around  $f_{\text{fund}}$ . Subsequently, the behaviour of the reflection and transmission in time domain can be calculated by the inverse Fourier transformation of the measured spectra.

The calibration of this set-up follows the same procedure as with a regular LSNA calibration, which consists of a relative calibration combined with an absolute power and phase calibration [7]. Due to the way that the downconversion process is achieved within the LSNA, i.e., by the use of a  $\text{freqN}$ , the choice of  $f_{\text{mod}}$  is not completely free [8]. Therefore attention should be paid to the fact that the  $f_{\text{mod}}$  of the pulse generator complies with the frequency grid of the LSNA. Finally, as it can not be controlled at what time instant of the baseband envelope the data acquisition is performed, post-processing alignment [9] has to be applied to be able to compare results of subsequent measurements. In this work, the start of the rising edge of the return loss (see Section IV) has been taken as the common time reference. Finally, it is assumed that the rise and fall times of the laser can be neglected and that the illumination signal can be considered as a perfect square wave.

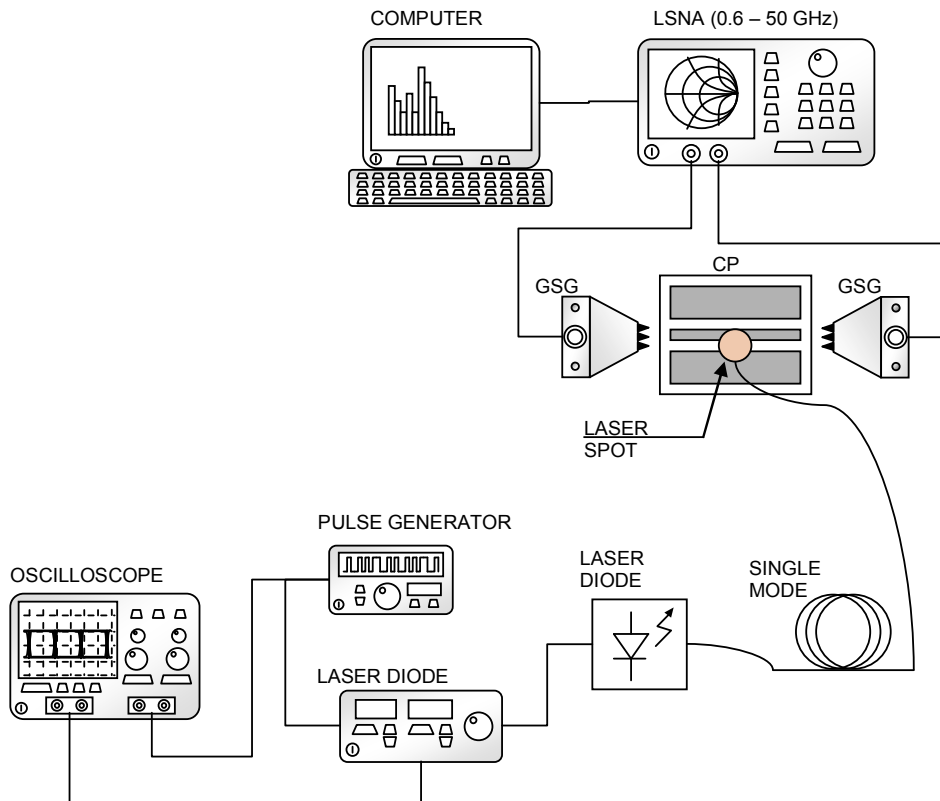


Fig. 3: Measurement bench enabling the characterization of the RF response of a transmission line switch subjected to a pulsed optical excitation.

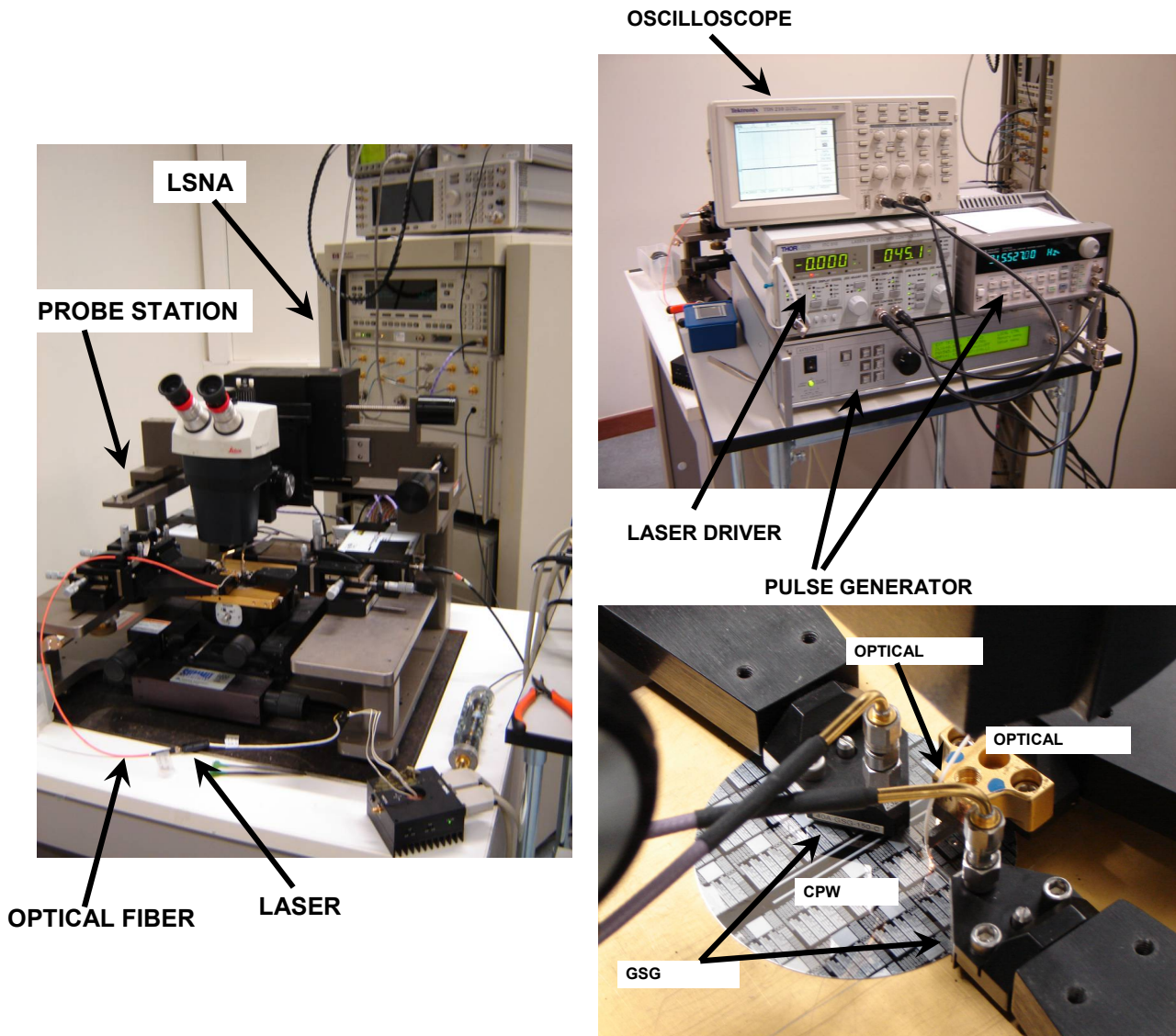


Fig. 4: Pictures of the measurement set-up.

#### IV. Experimental results

The measurement setup described above has been used to measure the incident spectrum (a1) and the response spectra of the reflected (b1) and transmitted (b2) voltage waves of the photo-induced switches under optical modulation. The output load of the LSNA is 50 Ohm and therefore a2 equals zero. The laser was modulated with a square wave signal at 915.527 Hz and the voltage level was adjusted to obtain an optical power of 50 mW during the switch OFF state. As a result of the photo-induced effect, the CW RF signal applied by the RF source of the LSNA is modulated in the CPW transmission line. In the considered experiment, the set-up acquires 500 spectral components in both the lower and upper side bands around the fundamental frequency. By calculating the inverse Fourier transformation of the measured frequency response, we are able to obtain the time-domain signal. By eliminating the carrier frequency (through Hilbert transform), the envelope of the signal represents the time response of the RF signal due to the optical modulation. The down-converted time-signals corresponding to b1 and b2 are normalized with the envelope of the input signal (a1) to obtain the time domain return and insertion losses, respectively.

The measured return loss (RL) and insertion loss (IL) of each of the four different switches investigated in this work are presented in Figs. 5 and 6 for a carrier frequency of 1 GHz and 41 GHz, respectively. As was shown in [10], the wavelength of the carrier frequency and the size of the photoconductivity profile determine whether the attenuation mechanism of the photo-induced switch is due to reflection or to absorption. At 1 GHz the mechanism is purely reflective, as we can deduce from the quasi square form of the RL for all DUTs. However at 41 GHz, the attenuation mechanism is now due to absorption for the non-

passivated samples. For example in case of the HR-Si switch (Fig. 1a), we observe that the RL increases rapidly once the laser is set to ON and then decreases gradually to attain a stable value after 200  $\mu$ s. The physical background is that after this time, the lateral grow of the photoconductivity profile does not continue and the photoconductivity reaches a steady state [10]. As the wavelength of the signal is small compared to the dimensions of the photoconductivity profile, the impedance changes can no longer be considered as an impedance step but should be regarded as a distributed effect. Similar behaviour can also be observed for the etched HR-Si sample, but not for the HR-Si sample with windows. This could be explained by considering that the photo-induced plasma zone is restricted to the window, hence the wavelength of the signal is still large compared to the photoconductivity profile inside the plasma zone.

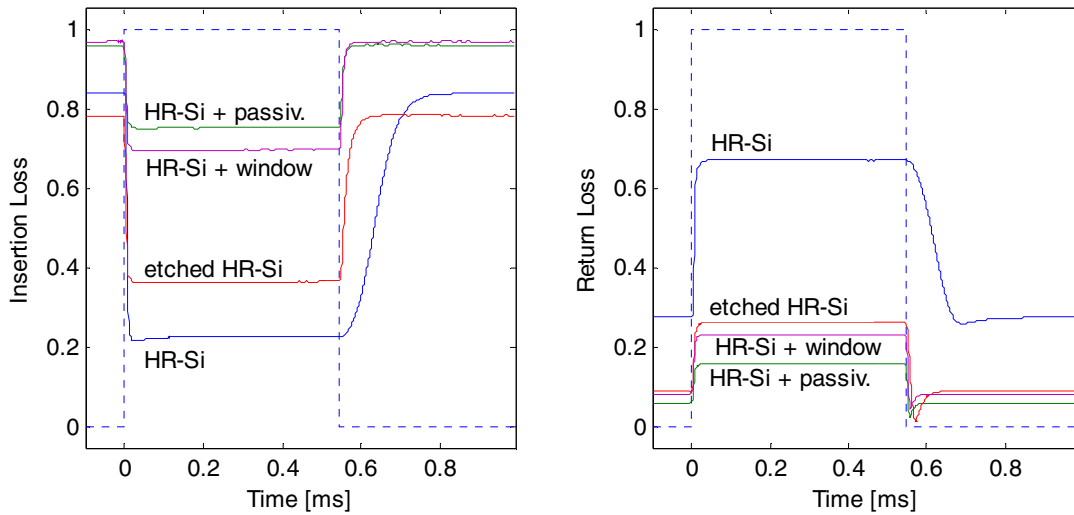


Fig. 5: Normalized envelope signals of the inverse Fourier transformation for the different CPW transmission lines. The CPW transmission lines are optically modulated with a 915.527 Hz square wave signal, and the carrier frequency is 1 GHz. The maximum optical power, corresponding to the switch OFF state, is 50 mW. The square wave signal is represented in dots.

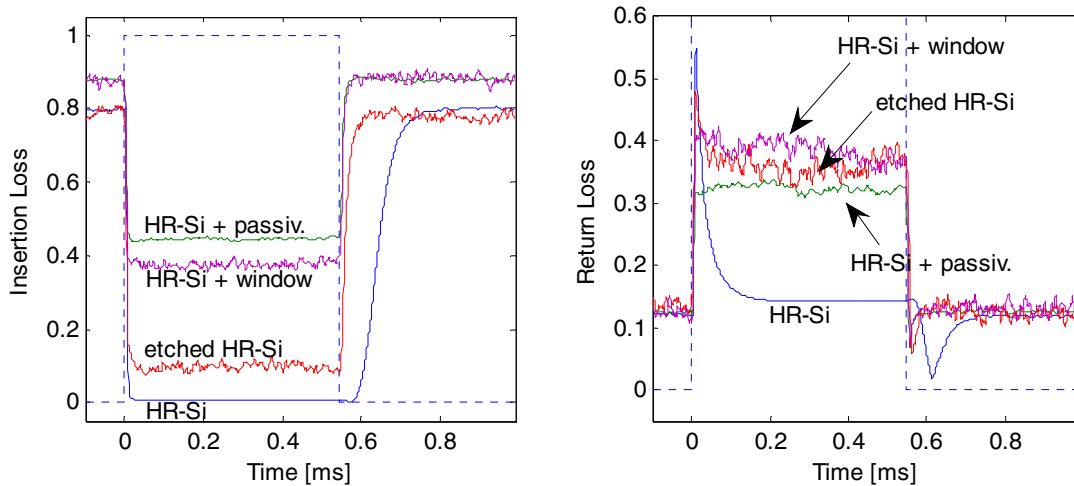


Fig. 6: Normalized envelope signal of the inverse Fourier transformations for the different CPW lines. The CPW-line is optically modulated with a 915.527 Hz square wave signal, and the carrier frequency is 41 GHz. The maximum optical power, corresponding to the switch OFF state, is 50 mW. The square wave signal is represented in dots.

Additionally, the measurement setup allows us to estimate the excess carrier lifetime. From the down-converted time-domain IL, we measure the photo-conductivity decay after the laser is switched off. The carrier lifetime is calculated as the time that it takes to recover 66.6% of the excursion between the steady state when the switch is on (laser off) and when the switch is off. In Fig. 7 the extracted excess carrier lifetime is presented for the different photo-induced switches and at different carrier frequencies. As

expected, the carrier lifetime is not function of the carrier frequency but remains constant over the frequency range. It can be noticed that passivation reduces the excess carrier lifetime significantly, but that the presence of a window has no impact on the excess carrier lifetime.

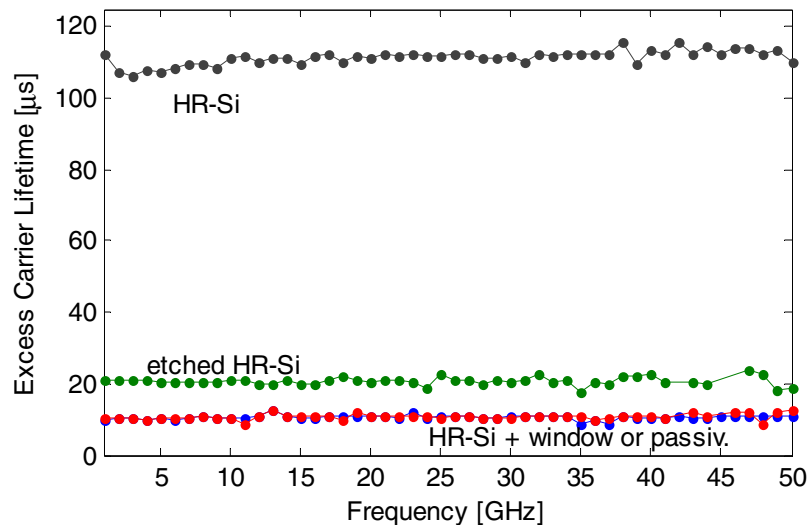


Fig. 7: Estimated excess carrier lifetime for the different frequency carriers, and for an optically modulated square wave signal with a 915.527 Hz, and 50 mW of optical power.

## V. Conclusions

We presented a measurement set-up that allows the characterisation of the electrical response of photo-induced microwave/mmwave switches subjected to pulsed optical excitations. By time-aligning the various measurement results through post-processing, measurements can be inter-compared. By characterising four types of switches, it was demonstrated that the dominant attenuation mechanism may change with varying RF carrier frequencies. It was also shown that performance parameters such as excess carrier lifetime can be extracted from the measured data.

## References

- [1] G. Poesen, G. Koers, J. Stiens, G. Carchon, W. De Raedt, and R. Vounckx, "Photo-induced millimeter wave losses in coplanar waveguide on high resistivity Si," *Microwave and Optics Technology*, vol. 49, pp. 808-810, 2007.
- [2] R. Vandersmissen, D. Schreurs, S. Vandenberghe, and G. Borghs, "Time domain RF characterisation of a thin-film metamorphic HEMT under modulated backside illumination," *Automatic RF Techniques Group Conf. (ARFTG)*, 5 p., June 2002.
- [3] G. Poesen, M. Vanden Bossche, G. Koers, J. Stiens, and R. Vounckx, "Transient effects in optically modulated transmission line switches operating at mm wave frequencies," *8th Topical Symposium on Millimeter Waves*, pp. 29, Feb. 2006.
- [4] G. Poesen, J. Stiens, M. Vanden Bossche, and R. Vounckx, "Time-dependent characterization of an optically modulated CPW line characterized with a large signal network analyzer," *Microwave and Optical Technology Letters*, vol. 49, no. 12, pp. 3124-3128, 2007.
- [5] W. Platte, "Effective photoconductivity and plasma depth in optically quasi-CW controlled microwave switching devices," *IEE Proc. J. Optoelectronics*, vol. 135, pp. 251-254, 1998.
- [6] C. Roda Neve, D. Lederer, and J.-P. Raskin, "Reduction of Photo-Induced excess carriers in optically controlled microwave circuits on HR-Si," *Proc. EuMA Special Issue on Microwave Photonics II*, vol. 4, no. 3, pp. 199-205, 2008.
- [7] J. Verspecht, P. Debie, A. Barel, and L. Martens, "Accurate on wafer measurement of phase and amplitude of the spectral components of incident and scattered voltage waves at the signal ports of a nonlinear microwave device," *IEEE MTT-S Digest*, pp. 1029-1032, May 1995.
- [8] J. Verspecht, "Calibration of a measurement system for high frequency nonlinear devices," PhD dissertation, Vrije Universiteit Brussel, (Belgium), Nov. 1995.
- [9] K. Remley, D. Williams, D. Schreurs, G. Loglio, and A. Cidronali, "Phase detrending for measured multisine signals," *Automatic RF Techniques Group Conference (ARFTG)*, pp. 73-83, June 2003.
- [10] G. Poesen, "Towards an adaptable millimeterwave reflector: Development of an antenna coupled opto-electronic modulator array," PhD dissertation, Vrije Universiteit Brussel (Belgium), Sept. 2008.

# Nonlinear Network Analysis for Modern Communication Devices and Systems

Efrain Zenteno\*, Olav Andersen<sup>†</sup>, Magnus Isaksson\*, Niclas Keskitalo\*<sup>†</sup>, and David Wisell<sup>†</sup>

\*Center for RF Measurement Technology, University of Gävle  
SE-801 76 Gävle, Sweden,

<sup>†</sup>Ericsson AB, SE-164 80 Stockholm, Sweden

<sup>‡</sup>Ericsson AB, Box 6206, SE-800 06 Gävle, Sweden

**Abstract**—This paper presents a novel test setup, based on a vector signal generator (VSG) and a vector signal analyzer (VSA), capable of nonlinear characterization of communications devices such as RF power amplifiers.

Envelope time-domain waveform extraction and correction is applied to the DUT reference plane, preserving vector correction even in modulated environments where ingoing and outgoing signals from the ports of the DUT can be distinguished.

This tool is valuable in the analysis of nonlinear devices, the generation of behavioral models and the study of memory effects..

## I. INTRODUCTION

A problem with the modern power amplifier is that it may not withstand swept continuous wave (CW) signals, since they are designed to work with high peak to average power ratio (PAPR) signals (i.e. 7 – 9 dB for wideband spread spectrum, wideband code division multiple access (WCDMA) or orthogonal frequency division multiplexing (OFDM)). This means that the thermal design of such an amplifier (e.g. a class: AB LD-MOS 50W OFDM power amplifier) is capable of handling a short duration of a modulation envelop peak signal at P-1.5dB, but it is not designed to handle that signal peak for the long time span of a VNA sweep. Consequently, if this amplifier is subjected to such a signal, it will be characterized with the wrong AM-AM, AM-PM.

Therefore, traditional VNA methodology cannot address the need for many nonlinear components that are subjected to a modern wideband high crest-factor communication signal.

Another problem has been also identified except for the 0dB PAPR, a swept sine has all its spectral power confined to one distinct frequency point, contrary to a real world modulated signal. This single point, in many cases, will not be representative of the distortion mechanisms (such as nonlinear memory effects) of a signal spread out over a larger frequency span. Since the important characteristics of a nonlinear component are the behaviors that best represents its true real-life response, this is yet another shortcoming of the traditional VNA method.

For this reason, a multi-tone signal is used in the test setup proposed in Section II. Using 8 or 16 tones will give the ability to set the appropriate relation between the average and the peak power. At the same time, PSD (power spectral density) is confined at discrete spots in the frequency plane to enable a high SNR (signal to noise ratio) in the measurement, thus ensuring high measurement speed and accuracy.

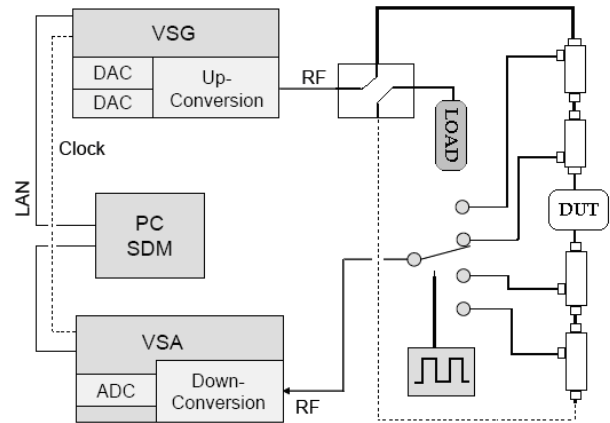


Fig. 1. Proposed hardware setup

## II. EXPERIMENTAL

Contrary to the traditional VSG (vector signal generator) and VSA (vector signal analyzer) approach, the proposed method and test-system maintain the inherent advantage of distinguishing between forward and reflected waves. Thereby, it can enable a calibrated reference plane to the unit under test, and also give both scalar and vector capability. This is identical to the inherent advantages of VNAs; but without sacrificing the valuable modulation capability.

The test setup, shown in Fig. 1, consists of a VSG (acting as the source) (SMU 200A, Rohde & Schwarz GmbH), a VSA (as a receiver), (FSQ, Rohde & Schwarz GmbH), a test set of couplers to separate the signals, and a solid-state switch for multiplexing all signals.

A multitude of nonlinear measurements is currently available to see the different effects caused by operating a device in its nonlinear regime [1]. However, modulated measurements are preferable to simulate daily working environment conditions. Thus results extracted from multitone signals add valuable information and increased accuracy [2], [3].

The harmonics of the envelope can be analyzed even when the harmonics of the carrier are not considered in the analysis. The set-up presented in this study is a powerful tool for

characterization of specially power amplifiers (PAs) working with high crest factor signals in their nonlinear regime.

Calculated from measurements, the dynamic range of the setup was around 65 dB that range is mainly related to the useful dynamic range in the VSA which is setting dependent. In other words, setting a very high reference level (low sensitivity) raises the noise floor and shadows the low-level frequency components [4]. On the other hand, setting a too low reference value can introduce distortion into the measurement from the incoming signal, hence this value should be carefully chosen.

### III. MEASUREMENT PROCEDURE

In order to be reproduced, the N-tone excitation signal is digitally created by a computer in its baseband form and downloaded to a VSG by a LAN connection. A large degree of freedom when choosing the tone's amplitudes and phases in this signal allows for fine control of the PAPR.

From the setup seen in Fig. 1, it can be noted that the waveforms cannot be measured at the same time instant. Hence, the first step in the measurement procedure is an extraction of the data corresponding to each branch in the setup, therefore the amplitude or power criterion were utilized to successfully complete this process [5]. From recent advances in signal processing and multisine engineering, the phase of a multitone signal can be estimated by computing a delay in the measurement system [6], [7].

All phases are related to the fundamental signal, called phase normalization. The waveform ' $a_{1d}$ ' presents zero phase and can be represented as a real number. In cases where the analysis involves intermodulation products, the phases of this spectral components are referred to the corresponding phases of the fundamental tones.

### IV. CALIBRATION

In order to get accurate results from measurements of nonlinear devices, calibration is a necessary stage. The error term model with the reference and DUT planes are shown in Fig. 2.

Basically, the calibration in the setup is divided into three steps [8]. First, relative calibration, using SOLT or any suitable method, is completed to find the terms involved in the classical models for VNA calibration; hence, a natural step was verification of the linear S-parameter measurement, as described in [5].

The remaining two steps are dedicated to find the magnitude and phase of the term ' $e_{01}$ ' shown in Fig. 2. This process is also known as power and phase absolute calibration. As in LSNA case, the power calibration is performed using a power meter (see Fig. 3). However, the calculation of the ' $e_{01}$ ' term varies, since the peak amplitude of a multitone is different from a sinuswave.

$$A_p = \sqrt{N} 10^{\frac{P_e(dBm) - 10}{20}} \quad (1)$$

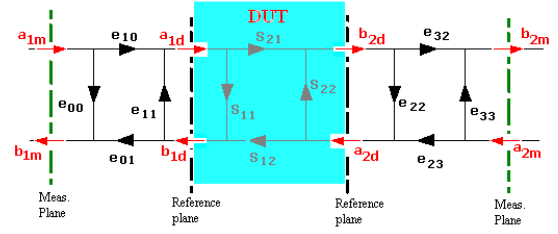


Fig. 2. Error terms in the calibration model

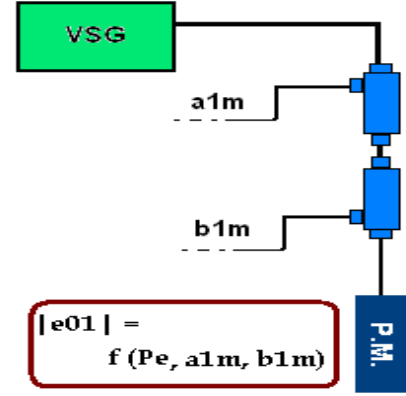


Fig. 3. Power calibration in the setup.

The term ' $|e_{01}|$ ' can be calculated by using Eq. 2:

$$|e_{01}| = \frac{|(e_{01}e_{10} - e_{00}e_{11})a_{1m} + e_{11}b_{1m}|}{A_p} \quad (2)$$

Equation 1 shows the relation of the power meter reading ( $P_e(dBm)$ ) and the peak amplitude ( $A_p$ ) of an N-tone signal with a flat power spectrum and all phases aligned; however Equation 1 could fail to represent the peak amplitude because of frequency variations in the insertion loss in the branch shown in Fig. 3. For this reason,  $|S_{21}|$  of this branch was measured using a VNA. However, either by proper selection of the frequency band or using  $|S_{21}|$  measurement, variations in the insertion loss can be neglected or compensated for. Similar approaches to calibrate new setups have been developed based on use of the LSNA as a reference instrument [9].

In the absolute phase calibration, the time delay in the receiver is assumed to be constant for all scattered waves. This time delay represents the phase distortion of the receiver and, since only one is used in the system (single receiver setup), that assumption presents a good agreement for short time periods.

The waveform correction is found by using Eqs. 3 and 4:

$$\begin{pmatrix} a_{1d} \\ b_{1d} \end{pmatrix} = \frac{1}{e_{01}} \begin{bmatrix} e_{01}e_{10} - e_{00}e_{11} & e_{11} \\ -e_{00} & 1 \end{bmatrix} \begin{pmatrix} a_{1m} \\ b_{1m} \end{pmatrix} \quad (3)$$

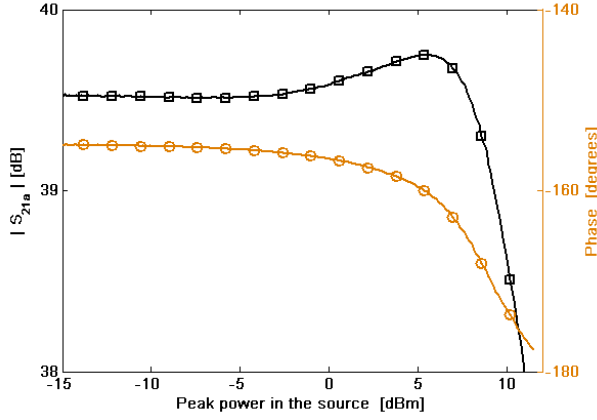


Fig. 4. AM-AM and AM-PM conversion for an amplifier driven with an 8-tone signal with 9dB PAPR at 2.14 GHz.

$$\begin{pmatrix} a_{2d} \\ b_{2d} \end{pmatrix} = \frac{1}{e_{01}} \begin{bmatrix} \frac{(e_{32}e_{23} - e_{22}e_{33})e_{10}e_{01}}{e_{32}e_{10}} & \frac{e_{22}e_{10}e_{01}}{e_{10}e_{32}} \\ -\frac{e_{33}e_{10}e_{01}}{e_{32}e_{10}} & \frac{e_{10}e_{01}}{e_{32}e_{10}} \end{bmatrix} \begin{pmatrix} a_{2m} \\ b_{2m} \end{pmatrix} \quad (4)$$

The model used in the current calibration is the 7 term error model. This model neglects the terms of crosstalking or isolation, so is important to have a good level of isolation between the ports of the solid state switch. This parameter (isolation) was verified by using a typical VNA with an isolation level around 85 dB.

## V. RESULTS

The actual setup capabilities allow us to extract corrected baseband waveforms using a suitable calibration procedure. An eight tone signal with a constant amplitude spectrum and aligned phases (PAPR of 9 dB) was created as the stimulus signal. The device under test was a radio frequency power amplifier AB LD-MOS 50W designed to operate with WCDMA signals at 2.14 GHz.

In Fig. 4 the AM-AM and AM-PM can be seen. These lines were computed using the average independent response of each tone detected in the  $b_{2d}$  waveform.

Fig. 5 presents the ratio  $b_1/a_1$ , using the same stimulus signal. This ratio represents  $S_{11}$  when the device operates in this linear regime. As can be seen in Fig. 5 a change in the return loss and phase deviation from the linear operation point can be clearly distinguished.

The eight-tone signal was created to match the bandwidth of a WCDMA channel (3.84 MHz), so the independent phase distortion of each tone could be valuable in the analysis, as depicted in Fig 6.

In another application example of the capabilities of the setup, a typical two tone test was run, the tone spacing was 800 KHz. The envelope waveforms were corrected from the measurement system, so they represented the behavior of the DUT.

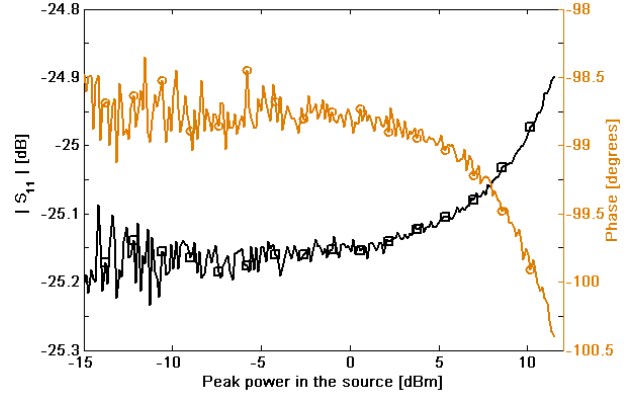


Fig. 5. Measured  $b_1/a_1$  in the amplifier driven with an 8-tone signal with 9 dB PAPR at 2.14 GHz.

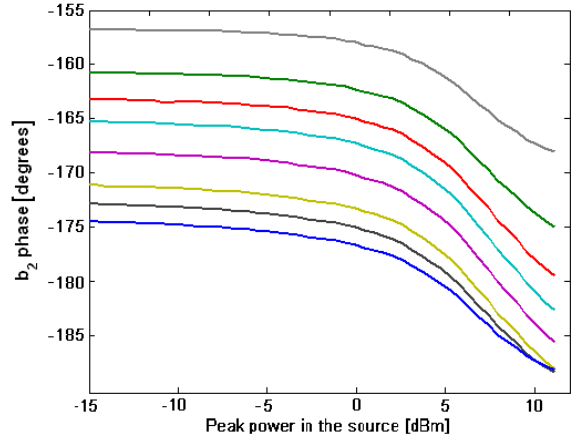


Fig. 6. Measured phase of each independent tone in  $b_2$  signal.

Fig. 7 shows the amplitude spectrum of the waveforms in each port of the DUT; as can be seen from Fig. 7 a survey of the fundamental tones and intermodulation products can be performed by using the setup.

In Figs. 8, 9 and 10 the upper and lower fundamental tones are plotted in black (dashed) and brown (solid) lines respectively, while the upper and lower IMD3 are plotted in purple (dashed) and blue (solid) lines.

In this kind of test it is important to know the input signal ( $a_{1d}$ ) to avoid drawing incorrect conclusions regarding linearity. In this case the spectral purity in the source was always higher than 58 dBc, as can be seen in Fig 8, where the amplitude of the tones and third order intermodulation products (IMD3) are shown; the x-axis represents the peak power set in the source.

The reflected signal ( $b_{1d}$ ) provides new insight, since variations in the return loss can be detected, including the new spectral components related to the intermodulation products. As Fig. 9 shows, the phases of the tones and the IMD3 are measured, where the phases of IMD3 are related to the fundamental tones.

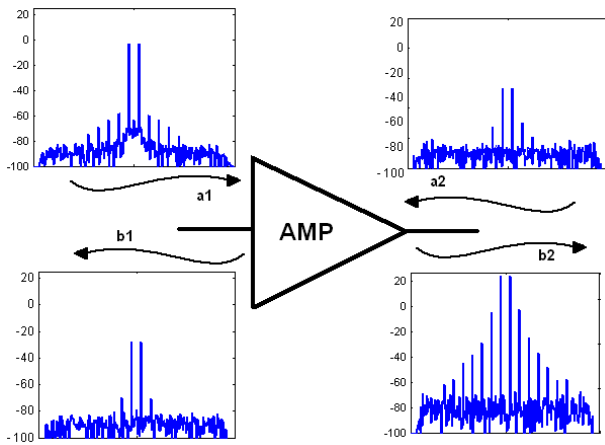


Fig. 7. Two-tone test over a Radio frequency power amplifier.

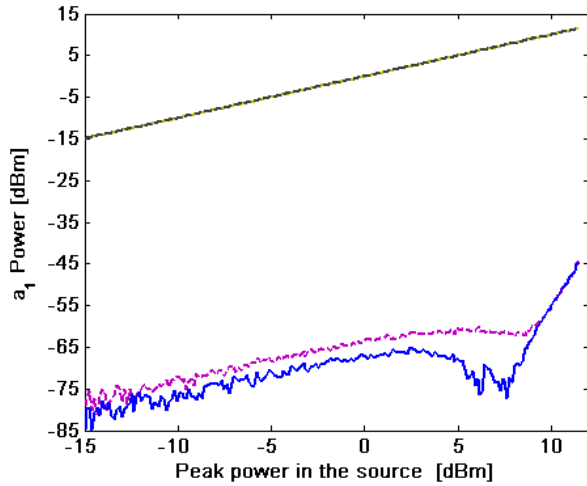


Fig. 8. Waveform of  $a_{1d}$  presented in a two-tone test.

The outgoing waveform at the output of the amplifier ( $b_{2d}$ ) is shown in Fig. 10, the dip in the amplitude of upper IMD3 corresponds to a phase shift of  $\approx 180$  degree as can be noted in the purple line. The IMDs of order superior to three were deleted to avoid confusion, but they can be easily included into the survey.

It is well-known that nonlinear measurements produce a huge amount of data, since basically two dimensions are swept: frequency and power. Hence, the computer in setup that was used to apply signal processing algorithms, can be also used to store the data, so possibilities to display and analyze the data can be performed and enhanced [10] [11]. So using the data collected in the two-tone test, Fig. 11 shows a power / frequency sweep for the magnitude of the third upper intermodulation product. In Fig. 11 is observed that for larger tone spacings a "sweet spot", i.e. dip in the IMD3, can be seen while none is present at more narrow tone spacings.

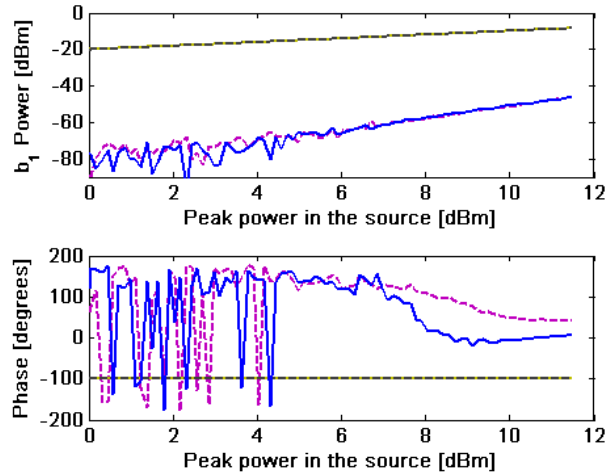


Fig. 9. Waveform of  $b_{1d}$  presented in a two-tone test.

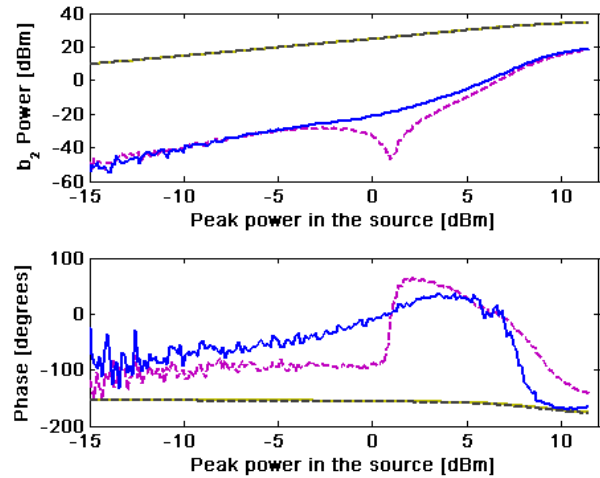


Fig. 10. Waveform  $b_{2d}$  presented in a two-tone test.

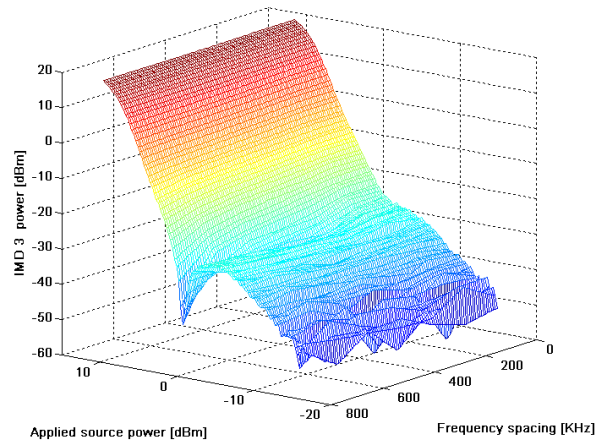


Fig. 11. Magnitude Third upper Intermodulation product.

## VI. CONCLUSION

In this work we described a four channel envelope time-domain measurement test setup capable of characterizing nonlinear devices. Extraction of the waveforms and its correction is possible in each port of the device under test. Additionally, the capability to distinguish ingoing and outgoing signals.

From the setup architecture, the use of a single receiver decreases, to some extent the impact of amplitude and phase distortion over a measurement, reducing the calibration requirement in such system.

The modulation capability, as well as the digital signal processing, included in the setup made it suitable for analysis of nonlinear components, such as radio frequency power amplifiers.

## ACKNOWLEDGMENT

This work was supported by Ericsson AB, Freescale Semiconductor Nordic AB, Infineon Technologies Nordic AB, Knowledge Foundation, NOTE AB, Rohde & Schwarz AB and Syntronic AB.

## REFERENCES

- [1] J. P. Teyssier, D. Barataud, C. Charbonniaud, F. D. Groote, M. Mayer, and J.-M. Nebus, "Large-signal characterization of microwave power devices," *Wiley Periodicals, Inc.*, pp. 479–490, 2005.
- [2] J. Pedro and N. Carvalho, "Designing multisine excitations for nonlinear model testing," in *IEEE Trans. Microwave Theory Tech.*, vol 53, No 1, Jan. 2005, pp. 45–54.
- [3] M. Myslinski, K. Remley, D. Schreurs, M. M. Kinley, and B. Nauwelaers, "Large-signal behavioral model of a packaged rf amplifier based on qpsk-like multisine measurements," in *Proc. of 13th GAAS, Paris, France.*, Oct. 2005, pp. 185–188.
- [4] M. McKinley, K. Remley, M. Myslinski, and J. Kenney, "Eliminating fft artifacts in vector signal analyzer spectra," in *Microwave Journal*, Oct. 2006.
- [5] E. Zenteno, M. Isaksson, D. Wisell, N. Keskitalo, and O. Andersen, "An envelope domain measurement test setup to acquire linear scattering parameters," *submitted at 72th ARFTG Conf., Portland, Oregon*, 2008.
- [6] K. Remley, D. Williams, D. Schreurs, G. Loglio, and A. Cidronali, "Phase detrending for measured multisine signals," in *61th ARFTG Conf. Dig., Philadelphia, PA*, 2003, pp. 73–83.
- [7] D. Wisell, B. Rudlund, and D. Rönnow, "Characterization of memory effects in power amplifiers using digital two-tone measurements," in *IEEE Trans. Instrum. Meas.*, Vol 56, No 6, 2007, pp. 2757 – 2766.
- [8] J. Verspecht, "Calibration of a measurement system for high-frequency non-linear devices," Doctoral Dissertation, Brussel: Vrije Universiteit, 1995.
- [9] F. Macraigne, T. Reveyrand, G. Neveux, D. Barataud, J.-M. Nebus, A. Soury, , and E. NGoya, "Time-domain envelope measurements for characterization and behavioral modeling of nonlinear devices with memory," in *IEEE Trans. Microwave Theory Tech.*, vol 54, No 8, 2006, pp. 3219–3226.
- [10] D. Wisell, P. Stenvard, A. Hansebacke, and N. Keskitalo, "Considerations when designing and using virtual instruments as building blocks in flexible measurement system solutions," in *Proc. IMTC 2007, Warsaw, Poland*, 2007.
- [11] Y. Rolain, W. van Moer, and P. Vael, "Measuring the characteristics of modulated non-linear devices," in *53th ARFTG Conf. Dig., Anaheim, CA, USA.*, Jun. 1999, pp. 1–9.

# RF Waveform Metrology for Characterization of Non-linear Amplifiers

David A. Humphreys<sup>†</sup>, Gavin Watkins<sup>‡</sup>, Kevin A. Morris<sup>‡</sup>, and James Miall<sup>†</sup>

<sup>†</sup>National Physical Laboratory, Teddington, Middlesex, UK; <sup>‡</sup>Centre for Communications Research, Bristol University, Bristol, UK

**Abstract** — Radio Frequency Waveform metrology (RFWM), based on real-time digital oscilloscopes, was used to evaluate the performance of a non-linear E-class amplifier optimized for WCDMA at 840 MHz. A timing error in the modulation signal gave abnormally high EVM values when measured using commercial equipment. The EVM of the source and amplifier were estimated as 0.4% and 2% respectively using RFWM. Simple RFWM evaluation tools show amplifier distortion and may offer insights over parametric measures.

**Index Terms** — RF Waveform metrology, real-time digital oscilloscope, spectrum analyzer, class-E power amplifier (PA), cellular radio, error vector magnitude (EVM), wideband code division multiple access (WCDMA), adjacent channel interference.

## I. INTRODUCTION

The limited power budget in a cellular radio handset drives the requirement for high power-added-efficiency (PAE) of the RF power amplifier. A typical linear amplifier (class-A/AB/B) for Wideband Code-Division Multiple-Access (WCDMA) applications will exhibit a PAE (Power Added Efficiency) of less than 50% [1] and the low efficiency of such an amplifier makes it unfavorable for mobile terminal applications, where battery life is limited. Only a non-linear class-C/D/E/F amplifier can produce a PAE greater 50% [2,3]. Unfortunately unless correction signals are applied these amplifiers also generate large amounts of distortion, which will interfere with other users and degrade the transmitted signal.

The prototype nonlinear amplifier design measured here integrates a highly efficient class-E amplifier into a hybrid Envelope Elimination and Restoration (EER) / Polar Modulator architecture. Pre-distortion of the input signal improves the linearity to a point where the amplifier meets the limits allowed by the 3G Test Specifications [4,5].

The optimization results for the amplifier pre-distortion and EER waveforms in the target application format, in this case WCDMA, are likely to depend on the application. The WCDMA emissions mask parameter for Adjacent Channel Power Ratio (ACPR) was measured using commercial equipment and used to optimize the pre-distortion and EER waveforms. Measurements of in-band distortion in the form of Error Vector Magnitude (EVM), gave significantly higher values than anticipated. The RFWM approach, using a real-time digital oscilloscope was adopted to resolve this discrepancy and determine the true amplifier EVM.

## II. WAVEFORM METROLOGY APPROACH

### A. Overview

The RFWM approach provides a traceable link between the complex modulated RF communications waveform and the NPL electro-optic sampling system (EOS) [6]. Sampling oscilloscopes and real-time digital oscilloscopes are general-purpose instruments with well-understood error behavior that can be used to measure the simple electrical impulse and step waveforms that link to the primary standard. These instruments can also measure the more complex waveforms that occur in wireless communications [7]. The waveforms are acquired and then stored for later off-line processing. An advantage of this approach is that the different analysis algorithms can be tested using the same data and that the uncertainties associated with the modulated waveform can be determined [8].

### B. Measurement system

The measurements were taken using a real-time digital oscilloscope operating at 2.5 Gsamples per second and acquiring data over a 1 millisecond epoch. This epoch is sufficient to capture the 2560 chips at 3.84 Mchips per second (666 microseconds) required to calculate the EVM and ensure that any truncation effects arising from the raised-root cosine filter [4] are insignificant.

A CW pilot-tone at a different frequency has been added to compensate for the oscilloscope timebase variation [7]. Digital oscilloscopes exhibit complex noise and non-linearity behavior which imposes restrictions on the choice of the signal and the pilot-tone frequencies. The frequencies are chosen so that all significant mixing and inter-modulation products fall outside the filter bandwidth. In this case we have also restricted the choice of frequency to harmonics of the 10 MHz reference. Although this restriction is not essential for a real-time oscilloscope, it allowed compatibility with the sampling oscilloscope used to provide traceability to the EOS.

All measurements were made using a dual output signal generator, ensuring good reference-lock between the two oscillators. The digital oscilloscope accepts an external reference signal that ensures that the timebase is disciplined by the synthesizer reference. This is helpful but not essential as the timing reference is derived from the CW pilot signal.

Imperfectly matched RF components could introduce errors due to the superposition of multiply reflected signals. This effect increases the minimum measurable EVM. Well-matched broadband components (attenuators and a resistive power splitter) and short cables have been used to mitigate this effect. The layout of the measurement system is shown in Fig. 1.

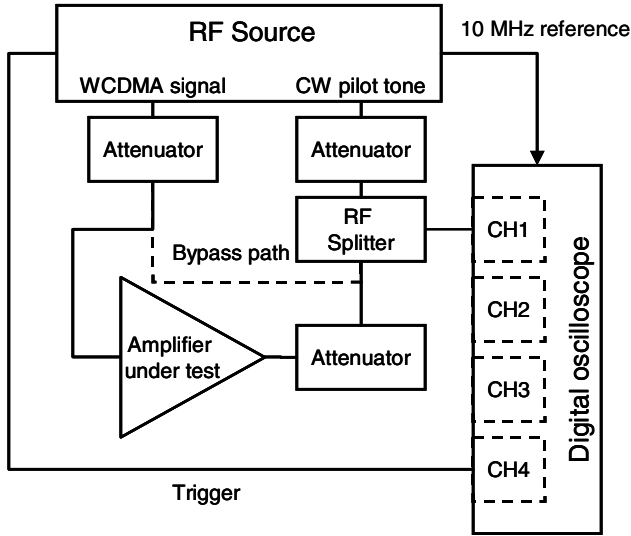


Fig. 1. System used to measure the WCDMA source (Bypass path) or the RF amplifier and WCDMA source.

### C. Measurement process

There are three stages in the measurement process. Firstly the composite waveform comprising the WCDMA signal and the CW pilot tone is acquired from the oscilloscope. The resolution of the oscilloscope's high-speed analogue-to-digital converter is eight-bit but in compensation for this low resolution the over-sampling rate is high (650 samples per chip).

The measurement results are processed to correct for timing errors, RRC filtered, aligned and combined in the complex plane to improve the noise performance and to provide statistics for the results. The RRC filter bandwidth is set at 3.84 MHz for EVM calculations but a wider bandwidth 11.52 MHz is used to investigate ACPR.

The final stage is the analysis of the results to determine parametric measures, such as EVM, or to compare the input and output modulated waveforms.

## III. RESULTS

### A. RF Amplifier optimized performance

The ACPR performance of the prototype amplifier was optimized using measurements taken with a commercial spectrum analyzer. When operated at 840 MHz, it has an

overall PAE of 62.6% at 25.6 dBm  $P_{OUT}$  and 23 dB gain. Without the correction, the  $ACPR_1$  is -32 dBc and  $ACPR_2$  is -41 dBc (respectively at 5 MHz and 10 MHz away from the carrier), exceeding the limits (-33 dBc and -43 dBc) set by the 3G Test Specifications [4]. When the pre-distortion correction is applied, the ACPR figures are improved by 2 dB and 6 dB respectively to give an  $ACPR_1$  of -34 dBc and an  $ACPR_2$  of -47 dBc, taking the prototype amplifier within the specification limits.

### B. EVM performance of the RF Amplifier

Measurements of the amplifier EVM performance using the RF spectrum analyzer gave values in the range 8% to 10% and direct measurement of the RF source also gave high EVM values. Analysis of the WCDMA source waveform acquired using the digital oscilloscope showed that there was a timing error in the modulation data file that shifted the symbol timing by 87.2 ns (0.335 chips) every 2560 chips, as shown in Fig. 2.

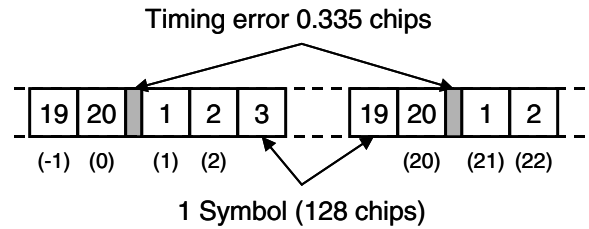


Fig. 2. Following each 20 symbols (2560 chips) there is a timing error of 0.335 chips. The figures in parentheses give a continuous count of the symbol number.

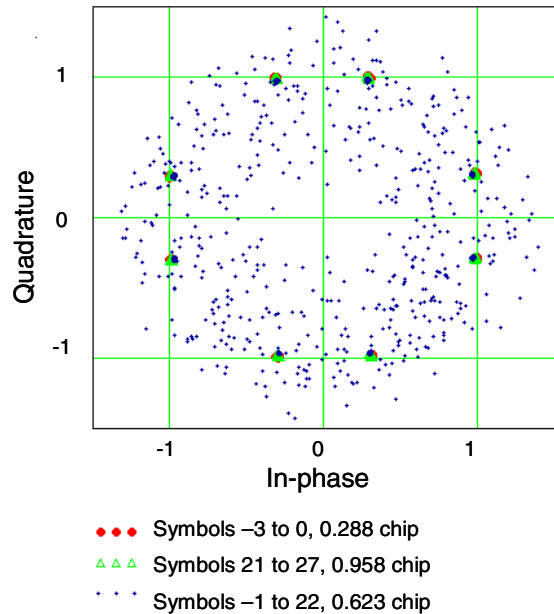


Fig. 3. Constellation diagram showing the effect of the timing error on data sampled at the chip rate.

Since the constellation contains only eight points on the perimeter of a circle, as shown in Fig. 3, the timing of the constellation points can be easily determined by sampling the magnitude of the modulation signal at the chip rate. The results have a well-defined minimum standard deviation at the symbol point.

At 840 MHz, the source showed an EVM of 0.44% and the amplifier yields an EVM of 2% with the compensation applied and an EVM of 3.9% without the compensation correction. The statistical contribution to the uncertainty of the waveform measurements is typically 0.26% at 95% confidence.

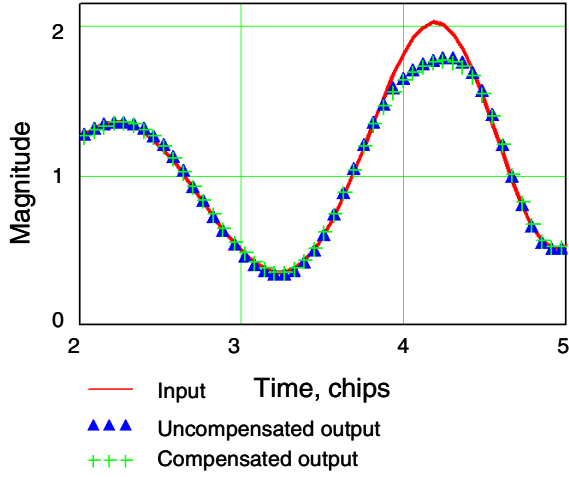


Fig. 4. Output clipping at high signal levels is compensation independent.

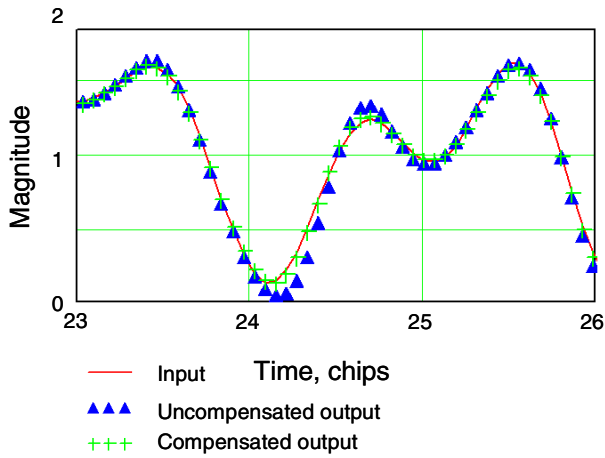


Fig. 5. The overshoot and memory-effects of the amplifier output is corrected by the compensation waveform.

### C. Evaluating the dynamic performance of the RF Amplifier

As an alternative to parametric measures, such as EVM and ACPR, measurements of the source and amplified modulation response can be used to give insights into the behavior of the RF amplifier. The group delay difference between the input

and output modulation waveforms can be determined by cross-correlation of the two waveforms. Since the waveforms are both complex this provides both time-delay and phase rotation corrections. Once these have been determined, the two waveforms can be overlaid to reveal discrepancies. Effects such as clipping (Fig. 4) are fundamentally limited by the amplifier and are independent of the compensation correction whereas at low signal levels, the amplifier shows memory effects that can be improved by the compensation correction (Fig. 5).

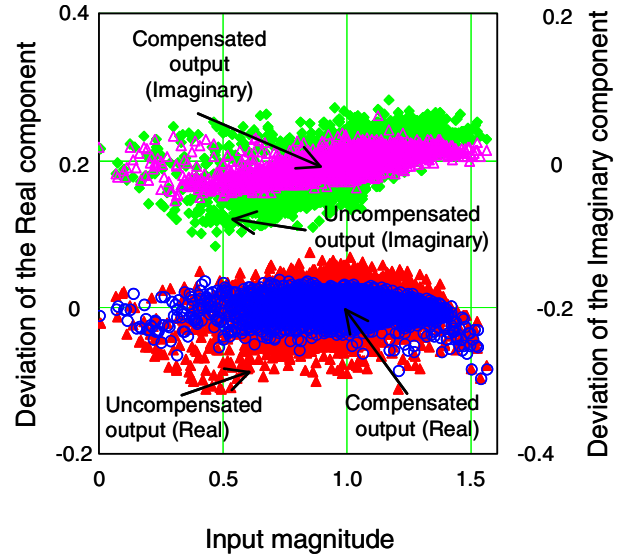


Fig. 6. Deviation of the real and imaginary components of the amplifier output envelope from a linear response to input level, with and without compensation.

This technique provides good detail about features within the trace. An alternative approach, which gives a broader picture of the results, is to view the envelope modulation transfer function properties of the amplifier. Both the input and output modulation waveforms are complex and so a phase correction must be applied to the results.

$$R_c = R_{out} \cdot \frac{R_{in}^*}{|R_{in}|} \quad (1)$$

where  $R_c$  is the phase corrected response,  $R_{in}$  is the complex modulation envelope from the WCDMA source and \* denotes the complex conjugate.  $R_{out}$  is the complex modulation envelopes from the amplifier, corrected for group-delay and phase-rotation.

The results (Fig. 6) show that applying the compensation signal reduces the spread of the results at low signal levels.

### D. Frequency domain analysis

The modulation waveform results can be represented in the frequency domain, to view the ACPR performance. In order to

do this, the bandwidth of the RRC filter must be increased. In this case, the filter bandwidth was 11.52 MHz, which is sufficient to view the adjacent channels. The results (Fig. 7) show  $ACPR_I$  (5 MHz away from the carrier) of -35 dBc for the compensated amplifier and -30 dBc for the uncompensated amplifier. These results are broadly in line with the spectrum analyzer measurements.

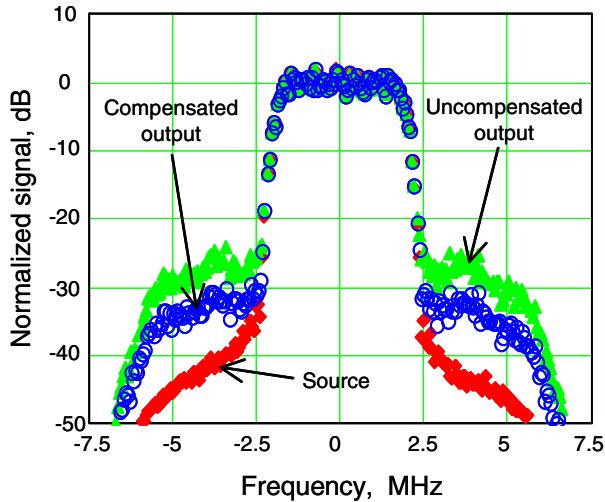


Fig. 7. ACLR produced by WCDMA source, the ACLR of the amplified signal and the ACLR of the amplified signal with correction

#### IV. CONCLUSION

The RFWM approach outlined here is flexible and can be used to provide insights where the parametric measures fail. We believe that the dedicated EVM software was unable to determine the symbol position because of the timing error.

Analysis in the frequency domain gave good agreement with the spectrum analyzer for the (5 MHz)  $ACPR_I$  figures.

Representing the evolution of the modulation envelope in the time-domain and the ‘envelope modulation transfer function’ may prove to be useful tools for measuring and optimizing the performance of non-linear sub-systems as the measurements can be performed in the target format.

#### ACKNOWLEDGEMENT

This work was based mainly on the secondment of a member of NPL staff to the Bristol University Centre for Communications Research funded by the DIUS Measurement for Innovators Program [9]. The authors also wish to thank Matthew Harper, Lindsay McInnes and Andrew Smith of NPL for their useful suggestions regarding this work.

#### REFERENCES

- [1] Mitsubishi Electric, “Mitsubishi BA01232 WCDMA amplifier,” *Semiconductor Product News*, [http://www.mitsubishichips.com/Global/new\\\_pro/no.113/p11\\\_.html](http://www.mitsubishichips.com/Global/new\_pro/no.113/p11\_.html), 2008.
- [2] C. Roff, J. Benedikt, and P. J. Tasker, “Design approach for realization of very high efficiency power amplifiers,” *Microwave Symposium, 2007. IEEE/MTT-S International*, 3-8 June 2007, pp. 143-146.
- [3] S. Gao, C. Sanabria, H. Xu, S. I. Long, S. Heikman, U. Mishra, and R. A. York, “MMIC class-F power amplifiers using field-plated GaN HEMT,” *IEE Proc. -Microw. Antennas Propag.*, vol. 153, pp. 259-262, June 2006.
- [4] 3rd Generation Partnership Project, “Tech. spec. group terminals; terminal conformance spec.; radio trans. and rec. (FDD),” 3GPP TS 34.141, rev 6.0.0, p69, 2005-03.
- [5] Gavin T. Watkins, Paul A. Warr, Kevin A. Morris, Tony R. Horseman, Kaoru Takasuka, Yukihiro Ueda, Yasushi Kobayashi, Shinji Miya, “78.1% PAE 840MHz Transmission Line Class E Amplifier with Low-Pass Output Filter”, *Submitted to IEEE Trans. MTT*, August 2008.
- [6] A.J.A. Smith, A.G. Roddie and D. Henderson, “Electro-optic sampling of low temperature GaAs pulse generators for oscilloscope calibration,” *Optical and Quantum Electronics - 28* (1996) pp 933-943 (July special issue on optical probing of ultrafast devices and integrated circuits).
- [7] D.A. Humphreys, M.R. Harper, P. Roberts. “Preliminary results for a traceable amplitude modulation measurement technique using in-phase and quadrature referencing”, *Waveform Diversity and Design*, 2007.
- [8] D.A. Humphreys, M.R. Harper, L.K.J. McInnes, J. Miall, “Strategy for traceability of complex modulated signals using RF waveform metrology,” *URSI 2008 Commission A*, August 2008.
- [9] National Physical Laboratory, “Measurement for Innovators,” [http://www.npl.co.uk/measurement\\_for\\_innovators/](http://www.npl.co.uk/measurement_for_innovators/), 2008.

# Power Amplifier Behavioral Modeling Performance Comparison of the LSNA and the Modulation-Domain System

Per Niklas Landin<sup>1,2</sup>, Christian Fager<sup>3</sup>, Magnus Isaksson<sup>1</sup>, and Kristoffer Andersson<sup>3</sup>

<sup>1</sup>Center for RF Measurement Technology, University of Gävle, SE-80176 Gävle, Sweden.

<sup>2</sup>Signal Processing Lab, Royal Institute of Technology, SE-100 44 Stockholm, Sweden

<sup>3</sup>Microwave Electronics Laboratory, Chalmers University of Technology, SE-41296 Göteborg, Sweden

email: [perlan@hig.se](mailto:perlan@hig.se).

## Abstract

The performance of power amplifier behavioral models depends strongly on the performance of the system used to measure the amplifiers. In this study two different systems with nonlinear measurement capability are used to model a commercially available PA. One system is a large-signal network analyzer (LSNA) and the second system is a modulation-domain system (MDS) consisting of a vector signal generator and a vector signal analyzer.

The PA was tested with multitone and WCDMA signals and behavioral models were extracted from the measured data. The evaluation criteria normalized mean square error and weighted error spectral power ratio or adjacent channel error power ratio were then computed to compare the performance of the models from the two systems. Cross-validation between the systems, using data from one system to obtain the model and validating its performance with data from the other system, shows that the model performance is mainly affected by the used validation data. Validating the performance of models from the LSNA with data from the MDS indicates that the identified models have almost the same performance as the MDS-identified models, i.e. it does not matter which system is used to identify the models. Cross-validation using a WCDMA-signal and multitone signal from the different systems shows that the normalized mean square error is mainly affected by modeling imperfections introduced by using another signal type. WESPR and ACEPR show a certain difference in performance with somewhat lower values for the MDS. The behavior of the two systems can be explained by different noise levels.

## I. Introduction

In the present study two measurement setups for measuring non-linear radio frequency components and systems are compared when considering behavioral modeling. The two systems are the Maury Microwave MT4463A large-signal network analyzer (LSNA) and the modulation-domain measurement system (MDS) consisting of a vector signal generator, the R&S SMU200A, and a vector signal analyzer, the R&S FSQ26.

The same device under test, a radio frequency power amplifier (PA) intended for the 3<sup>rd</sup> generation of mobile communications, has been measured separately with the two systems. The studied PA is well documented in previous studies [1], [2]. The measured input and output signals from the power amplifier with both the MDS and the LSNA systems were compared. The measured data was used to identify behavioral models and the modeling results were compared using accepted criteria for behavioral modeling performance evaluation.

To the authors' knowledge no study of the above character has previously been reported. However, a study comparing a LSNA, a microwave transition analyzer and a digital sampling oscilloscope was done in [3]. This study focused mainly on identifying error sources due to possible mismatches in the measurement systems.

## II. Prerequisites

When comparing the two measurement systems from a behavioral modeling perspective the model is a critical choice. Note that it is the systems that are under evaluation, not the model. For the present study a well defined, well documented model with excellent modeling properties for the specific device under test, i.e. the radio frequency PA, has been used: the parallel Hammerstein (or the memory polynomial) model [1], [2], [4]-[6]. The model is described by the nonlinear order  $P$  and the memory length  $M$ . Such a model is henceforth denoted  $\text{PH}(P,M)$ . Previously published reports [1], [2] have shown that the modeling error both

in and out-of-band for the particular device under test will not significantly decrease after a nonlinear model order of 9 and a memory length of 2 sample delays. That model order complexity, i.e.  $\text{PH}(9,2)$ , is therefore used in the present study.

The test signals are two sets of 62-tone signals and one WCDMA-signal with a peak-to-average ratio of 6.5 dB. The 62-tone signals were generated to have an amplitude probability density function similar to the WCDMA-signal by optimizing the amplitudes and phases with the algorithm in [7]. The resulting 62-tone identification signal was used in both systems to obtain models and the 62-tone validation signal was used to validate the performance. The WCDMA-signal was also used in the MDS to give a comparison of the modeling performance when using different signal types.

The 62-tone modeling performance of the systems is evaluated by using the two PA behavioral modeling criteria normalized mean square error (NMSE) and weighted error spectral power ratio (WESPR) [8]. NMSE is mainly affected by in-band model errors and WESPR is designed to take account of the out-of-band model errors. The weighting function in WESPR is chosen to be the maximum of the lower and upper adjacent channels to give a criterion similar to the adjacent channel error power ratio (ACEPR) but only the discrete frequencies where IM-products can be found are included. For the comparison when the WCDMA-signal is used as input and output to the model, the adjacent channel error power ratio (ACEPR) and the NMSE are considered.

To compare the performance of the systems for this particular purpose an identification signal measured in one system is used to identify a model. The performance of the model is then evaluated using the validation signal measured in the other system. The difference between modeled and measured output, the model error, is then computed and evaluated using NMSE, WESPR and/or ACEPR. If one system has an advantage in dynamic range this will be shown by consistently having better

performance when using that dataset for validation.

### III. Experimental

The setups are similar in both cases. The LSNA is described in detail in [9] and the MDS in [1] and the references therein. To make the comparison as fair as possible the considered device under test included both the PA and attenuator as shown in Fig. 1.



Fig. 1. The PA setup without the measurement systems. The reference planes are chosen at the input of the PA and the output of the attenuator.

To get the highest accuracy in the modeling of the PA it is necessary to measure both the input and the output signals. Using measured input and output signals in the modeling process reduces some of the distortions introduced by the measurement setup.

The device under test (DUT) is a commercial PA from Ericsson AB. It is a LDMOS-PA with a gain of 52 dB and rated maximum input power of 1 dBm. The used center frequency is 2.14 GHz. In earlier studies [1], [2] the PA has shown significant memory effects when used at high power levels. The power sweep covering 33 different power levels, from 1 W to 38 W were chosen to keep the PA fairly close to normal working conditions. Using higher power levels will result in stronger nonlinearities but also larger modeling errors. This is undesired since this work focuses on comparing performance of the measurement systems and not the model itself.

### IV. Results

Figs. 2 and 3 show the measured input and output signals, respectively, for an input power level of -9.2 dBm. The power is normalized to make the signals from both systems have the same power in-band.

For the input signal the measured differences in the sidebands are large. The difference in input signal is partly taken care of in the

modeling process. Fig. 2 shows that the weakest detectable signals are in the range -60 to -70 dBc. The MDS show lower measured powers below and above the signal band. This could indicate that the MDS is capable of measurements with higher dynamic range than the LSNA.

The output signals show the spectral regrowth of the amplifier. The measured spectrum differs somewhat between the two systems.

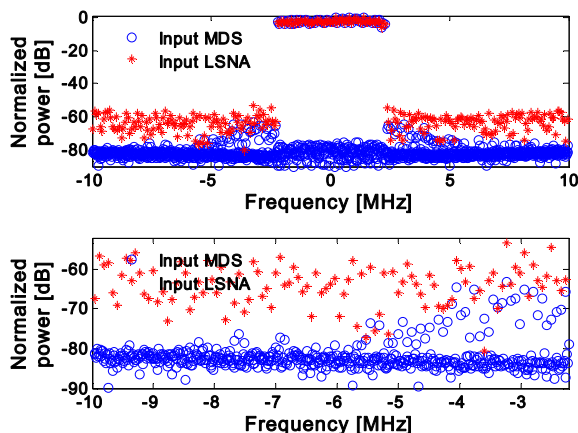


Fig. 2. The measured input signal spectrum using both systems at the power level -9.2 dBm. Blue line shows data from the MDS and red stars show data from the LSNA. The upper part shows data for the measured frequency range of the LSNA and the lower shows the spectrum at frequencies below the channel.

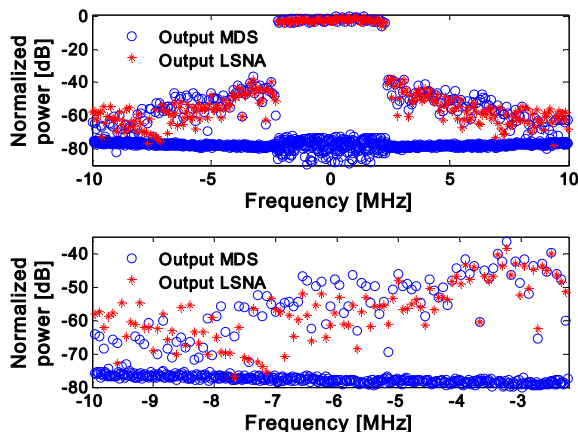


Fig. 3. Spectrum of the measured output signal in the respective system. Upper and lower parts of the figure are as in Fig. 2.

As has been shown earlier [1] the quality of the validation data has the major impact on the evaluation criteria. Fig. 4 shows the NMSE and

the WESPR when evaluated on data within the respective system, i.e. 62-tone identification and validation data are both measured in the same system. PH(9,2)-models for each power level are extracted for each system and then evaluated using the validation data from the same system. The data from the MDS has lower NMSE and WESPR. The difference between overall model performance decreases as the power increases which mainly is explained by the model's inability to completely predict the PA behavior. WESPR, which is an out-of-band modeling error criterion, shows a behavior similar to NMSE but with larger difference at the lower power levels. The behavior at the lower power levels is a clear indication of noise or distortions in the measured data out-of-band. The power levels out-of-band are naturally much lower than the in-band and are thus more easily affected by noise.

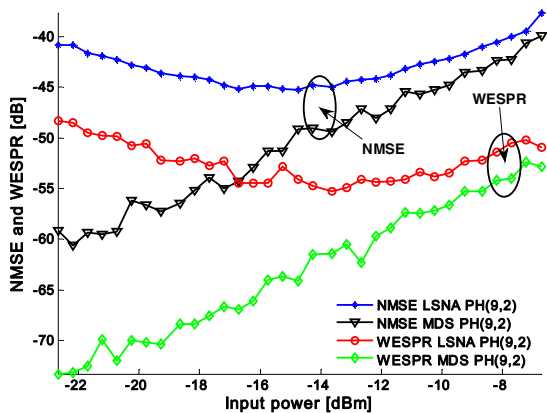


Fig. 4. The NMSE and the WESPR when using data measured within the system. Lower power levels show larger difference than higher powers. This is partly due to the fact that the model cannot completely describe the behavior of the PA.

In Fig. 5 the NMSE and the WESPR are shown when cross-validating the data between the systems, i.e. the identification data comes from one system and the validation data comes from the other system. Fig. 5 shows that when identifying with data from the LSNA and validating using data from the MDS, the NMSE and the WESPR are almost as good as when staying within the MDS. However, identifying

models using data from the MDS and validating with data from the LSNA gives the same performance as when both identifying and validating using data from the LSNA-system. This behavior shows that the LSNA finds approximately the same model parameters as the MDS but is not quite able to validate the performance of the model at the lower power levels.

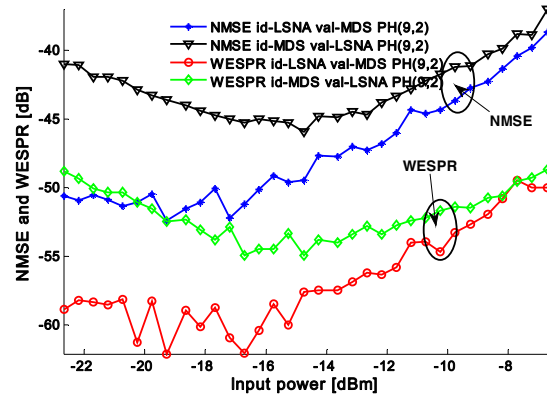


Fig. 5. The cross-system validation performance for NMSE and WESPR is shown. "Id-LSNA val-MDS" means that the model is identified using identification data from the LSNA and the performance is validated using the validation data from the MDS.

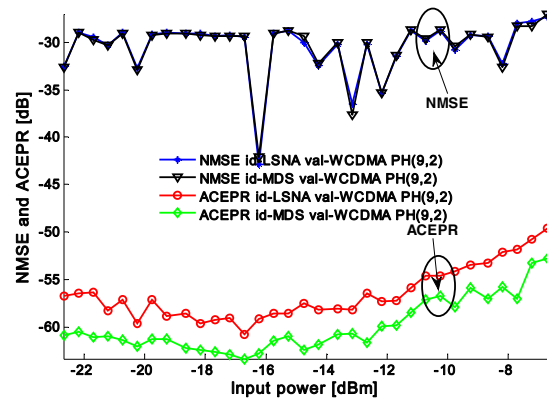


Fig. 6. The NMSE and ACEPR when identifying using 62-tone data from both systems and validating the performance using the WCDMA-signal measured in the MDS. "id-MDS val-WCDMA" means that the model is identified using the 62-tone and the performance is validated using the WCDMA-signal.

Results based on different signal types are shown in Fig. 6 where the models are identified using the 62-tone signals from respective system and validated using the WCDMA-signal measured in the MDS. For NMSE the difference in performance between the systems is negligible whereas the ACEPR is 3-4 dB lower when using the MDS. The negligible differences in NMSE between the systems appear since the models are not identified for the parts of the spectra that fall between the discrete frequencies defined by the 62-tone. A model error much larger than the errors caused by the noise is thus introduced. For the out-of-band effects, measured as ACEPR, the difference between the systems is significant. The out-of-band signal power is lower than in-band and the ACEPR is thus more easily affected by the noise.

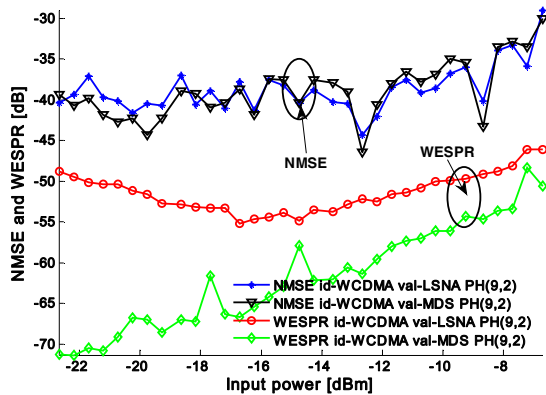


Fig. 7. NMSE and WESPR are shown when using the WCDMA-data for model identification and then validating the performance using the 62-tone signals from the respective system.

The results when identifying the model using the MDS-based WCDMA-signal and validating the performance with the 62-tone signal for the respective system are shown in Fig. 7. The NMSE is almost the same for both systems, but compared to the NMSE in Fig. 4 it is much worse, at least 10 dB, for the MDS-data and approximately 5 dB for the LSNA. For the WESPR the difference between the systems is large. When comparing the difference between the WESPR in Fig. 4 and Fig. 7 there is almost no difference. One possible explanation is again

the noise and distortion levels in the respective systems.

In general, it is seen that the LSNA-system finds models that give approximately the same performance as the models found using data from the MDS, both in-band, measured as NMSE, and out-of-band, measured as WESPR or ACEPR. It has earlier been shown [1] that the main impact on the evaluation criteria is given by the used validation data. The behavior is also clear when considering that an approximate model, like the PH-model, does not consider every aspect of the behavior but only the major. This property provides certain robustness against noise when identifying the models. When computing the model error all the noise in the measured data is directly present and can directly affect the final result.

Other model orders, both with and without memory, have been tested with the same results. One problem that arose in certain cases with more complex models and the less-noisy data from the MDS was over-modeling.

## V. Conclusions

The performance of two measurement systems with nonlinear measurement capabilities has been compared using PA behavioral modeling. The performance is compared through the accepted PA behavioral modeling criteria NMSE, WESPR and ACEPR. The systems are a LSNA and a MDS.

For 62-tone signals it was found that the LSNA-setup gives behavioral models with almost the same performance as the MDS both in-band, measured as NMSE, and out-of-band, measured as WESPR or ACEPR. However, the tested LSNA could not validate the performance of the models.

At the highest power levels the model performance was the limiting factor. The difference in performance between the systems would have persisted also at higher powers if another model structure better suited to describe the PA had been used.

The results based on using different signal types for identification and validation show that

it is not straightforward to use the models if the best performance is desired. The differences between the systems in-band, i.e. the NMSE, were negligible and depended mainly on the signal type. Out-of-band differences between the systems, WESPR or ACEPR, were more pronounced with lower values for the MDS.

It is important to remember that these results are obtained under the assumption of well matched systems. Measurements with the LSNA indicate that this is the case for this particular PA. For other PAs, this may not be the case and the MDS system may then produce erroneous results.

### Acknowledgements

This work was supported by Ericsson AB, Freescale Semiconductor Nordic AB, Infineon Technologies Nordic AB, Knowledge Foundation, NOTE AB, Rohde&Schwarz AB and Syntronic AB.

### References

- [1] M. Isaksson, D. Wisell, and D. Rönnow, "A comparative analysis of behavioral models for RF power amplifiers," *IEEE Trans. Microwave Theory Tech.*, vol. 54, pp. 348-359, 2007.
- [2] M. Isaksson and D. Wisell, "Extension of the Hammerstein Model for Power Amplifier Applications," in *63rd ARFTG Conf. Dig.*, Fort Worth, TX, USA, 2004, pp. 131-137.
- [3] T. Williams, O. Mojón, S. Woodington, J. Lees, M. F. Barciela, J. Benedict, and P. J. Tasker, "A robust approach for comparison and validation of large signal measurement systems," in *IEEE MTT-S Int. Microwave Symposium Digest*, Atlanta, GA, 2008, pp. 257- 260.
- [4] M. S. Heutmaker, E. Wu, and J. R. Welch, "Envelope distortion models with memory improve the prediction of spectral regrowth for some RF Amplifiers," in *ARFTG 48*, Clearwater, FL, USA, 1996.
- [5] J. Kim and K. Konstantinou, "Digital predistortion of wideband signals based on power amplifier model with memory," *Electron. Lett.*, vol. 37, Nov. 2001, pp. 1417-1418.
- [6] H. Ku and J. S. Kenney, "Behavioral modeling of RF power amplifiers considering IMD and spectral regrowth asymmetries," in *IEEE MTT-S Int. Microwave Symposium Dig.*, 2003, pp. 799-802.
- [7] J. C. Pedro, and N. B. Carvalho, "Designing multisine excitations for nonlinear model testing," *IEEE Trans. Microwave Theory Tech.*, vol. 53, pp. 45-54, 2005.
- [8] D. Wisell, M. Isaksson, and N. Keskitalo, "A general evaluation criteria for behavioral PA models, " in *69th ARFTG Conf. Dig.*, Honolulu, HI, 2007, pp. 251-255.
- [9] J. Verspecht, "Large signal Network Analysis," *IEEE Microwave Magazine*, vol. 6, no. 4, pp. 82-93, 2005.

# Simultaneous Measurement of High and Low Frequency Response of Non-Linear Microwave Circuits

G. Avolio<sup>1</sup>, G. Pailloncy<sup>2</sup>, D. Schreurs<sup>1</sup>, M. Vanden Bossche<sup>2</sup>, B. Nauwelaers<sup>1</sup>

<sup>1</sup>K.U.Leuven, Div. ESAT-TELEMIC, B-3001 Leuven BELGIUM

<sup>2</sup>NMDG NV, B-2880 Bornem BELGIUM

## **ABSTRACT**

In this work, measurements of the high frequency as well as the low frequency response of a non-linear microwave circuit are reported. The developed set-up is based on an extension of the LSNA and it enables the simultaneous measurement of baseband response and RF behaviour. Thanks to this capability a direct correlation between the variation of baseband impedance and asymmetry of distortion components around the fundamental carrier is possible. Experimental results of two-tone measurements, carried out on a hybrid GaAs microwave circuit, are shown.

## **I. INTRODUCTION**

The growing complexity of modern wireless telecommunication systems makes the design of PAs a challenging task. The requirement of multi-standard systems as well as the use of wideband modulated signals force characterization and modelling under real applications conditions. For this reason, the single-tone CW test [1] is not longer suitable to study the response of a non-linear device since, amongst others, low frequency dynamics (exciting Long Term Memory (LTM) effects) cannot be captured.

To investigate LTMs, the two-tone test [1] is widely used. As the frequency offset ( $\Delta\omega=\omega_2-\omega_1$ ) between input tones is changed, the response of a non-linear device to baseband intermodulation products, strongly impacts the RF dynamics if LTMs are not negligible. As a consequence, variation and/or asymmetry of magnitude and phase of 3<sup>rd</sup> order intermodulation products appearing around the carrier (namely the lower and upper IM3 at frequencies respectively of  $2\omega_1-\omega_2$  and  $2\omega_2-\omega_1$ ) are observed as function of tone spacing. The set-up that we present is an extension of the LSNA and enables the calibrated measurement of the LF response in combination with the RF response. This overcomes the limitations of the existing set-ups, either capable of measuring LF response only [2] or having low frequency limitations (in [3], due to equipment, the lowest measurable frequency is 200 kHz).

The paper is outlined as follows: in section II the novel set-up is described along with calibration procedure; in section III experimental results are discussed.

## **II. MEASUREMENT SET-UP**

### *II.A. Description*

The measurement set-up is an extension of the LSNA [4]. The latter accurately measures the amplitude and phase of the incident and scattered waves of any two-port component, both at the fundamental and harmonics including a 20 MHz modulation bandwidth, from 600 MHz to 50 GHz. The core of the instrument is based on a sampling downconverter and four ADC channels.

In this work, the instrument has been extended with a LF dynamic bias setup. This setup requires four more ADC channels, enabling the simultaneous measurement of the four RF traveling voltages waves (ports labeled 'RFport1' and 'Rfport2' in Fig.1) and the four induced LF components up to 24 MHz (LF ports 3 and 4 in Fig.1).

Two coupler-like signal separation boards have been developed in order to sense the LF components

flowing through its main input and output ports. These boards are typically placed between the device under test (DUT) and its DC biasing sources, i.e., connected between the DC sources and the input and output RF bias tees or biasing circuits of the DUT. The sensed LF components are separated from the DC voltages and currents. Indeed, the DC biasing conditions of the device can be large compared to the induced LF components, resulting in a poor measurement accuracy. These boards, in combination with the ADC channels, can measure LF components within a 10 kHz to 24 MHz bandwidth with a typical insertion loss of 0.5 dB and presents a minimum VSWR of 4.5 if the input port is left open.

To control the LF impedances presented to the DUT, one needs an LF port different from the DC port. Indeed, any DC source connected to the DC port behaves as short for LF components. For this purpose, two LF bias tees have been developed, allowing separating DC termination and LF termination with a minimum isolation of 35 dB in the 10 kHz to 24 MHz bandwidth.

Finally, a LF Test Set, mainly composed of switches, has been developed. This test set is used in two different modes: the measurement mode and the calibration mode. In the latter mode, it simplifies the calibration of the LF hardware setup by routing automatically the LF calibration source either to the input or to the output test port. In this mode, the LF bias tees are automatically disconnected in order to apply automatically the LF calibration signal or the internal 50 Ohm termination to the sensing module input ports without requirement of user manipulation. In measurement mode, the test-set connects the LF bias tees to the sensing module input ports and give access to the LF source signal through an auxiliary port, in order for example to perform LF active source- or load-pull.

The different parts composing this LF dynamic bias setup have been developed in order to support DC components up to  $\pm 30$  Vdc and up to  $\pm 2$  Adc and to support and sense LF components up to  $\pm 15$ Vpeak and  $\pm 2$ Apeak in the 10 kHz to 24 MHz bandwidth. The sensing modules allow measuring calibrated LF voltages and current as low as 20uV and 3uA respectively.

Unlike the test device used in this article, for devices that do not include their own biasing networks, one needs to combine the DC bias and the RF signal with the help of a RF bias tee. In the case of modulated nonlinear mode of operation, the potential LF induced voltages and currents should flow through the DC path of these bias tees. In order to properly measure them, they should not be filtered out by the RF bias tees. Unfortunately, classical RF bias tees are not suitable as they typically present a high dampening capacitor at their DC input in order to limit oscillation. One needs to use special designed bias tees with a broadband DC path or a diplexer [5] with a LF bandwidth, including DC, and a RF bandwidth covering the application.

## *II.B. Calibration*

One needs to measure the LF induced signals in a calibrated way, synchronized to the high-frequency (RF) part of the signal, in order to properly reconstruct the signals at the device under test (DUT). The RF portion, i.e., fundamental and harmonics in combination with the modulation are measured via the couplers by the LSNA sampler front-end (Fig.1). The LF voltages and currents are measured with the new developed LF dynamic bias setup. Finally the DC measurements are added to the LF and RF measurements to result in the complete voltages and currents at the DUT ports.

Each of DC, LF and RF measurement parts needs to be calibrated to reconstruct the signals at the DUT ports. Moreover, as the LF and RF measurement parts are different, a delay may occur between the LF and RF components. To accurately represent the signals at the DUT ports, one needs to correct for this delay.

For this article, a SOLT calibration has been performed both at RF and LF ports reference planes. These calibrations consist of a classical relative calibration and a power and phase calibration in order to obtain the absolute correction coefficients that one needs to apply to the measured quantities at ADC channels ( $X_{mRF}$  and  $X_{mLF}$  on Figure 1).

While the RF calibration can be performed sequentially at each frequency of interest as the number of frequency points keeps typically lower than 100, the LF calibration would take a very long time when sequential frequency measurements are used. Indeed, to avoid the requirement of recalibration of the measurement system each time the modulation frequency grid is changed, one needs to calibrate the LF measurement part within its full frequency bandwidth (10 kHz to 24 MHz), and with an enough dense

frequency grid to allow interpolation. In the current software implementation, the interpolation function requires an equidistant frequency grid. This means that the maximum frequency spacing needs to be 10 kHz and one ends up with at least 2400 frequency points to measure.

To reduce the calibration measurement time, the full LF bandwidth is calibrated at once using a multi-tone signal generated with the help of an arbitrary waveform generator (AWG). In order to optimize measurements, a Schroeder multi-tone algorithm is selected to obtain a low crest factor output calibration signal:

$$X(f) = \sum_{k=1}^N e^{j\pi \frac{k(k-1)}{N}} * \delta(f - kf_0) \quad (1)$$

where  $N=2400$  corresponds to the number of tones and  $f_0 \approx 10$  kHz is the frequency spacing.

This calibration signal is pre-characterized in amplitude and phase and is used as reference for the LF power and phase calibrations.

As already mentioned, the LF and RF path are different and as such a physical delay occurs between the LF and RF components. Moreover the LF and RF absolute calibrations are performed without triggering between the calibration signal and the ADC channels. In this case, an unknown delay is still present in the correction coefficients. In order to properly reconstruct the signals at the input and output reference planes, both for LF and RF, one needs to compensate for these delays.

A LF-RF delay compensation method has been implemented based on an ESG with synchronized LF and RF modulated output and marker capability. An Agilent E4433B ESG [6] is used to generate a multi-tone modulation signal with its IQ internal generator around the RF fundamental frequency used during the RF SOLT calibration. In addition to the RF output connector, the ESG presents an I (and Q) output connector on its rear panel, allowing to have direct access on the LF modulated signal in the I path (or Q path) of the IQ modulator. Assuming the delay of the modulation signal through the ESG RF and I outputs is negligible, one have a synchronized access to both a RF modulated signal and a LF modulated signal.

Furthermore, a marker is set on the first point of the modulation signal. The purpose of the marker is to generate a trigger signal each time that the first point of the modulation signal is applied internally to the IQ modulator of the ESG. This trigger signal is also available on a BNC connector on the rear panel of the ESG. It is then used to trigger the ADC channels. As such, one can capture the LF output and RF output of the ESG sequentially while keeping a constant phase relationship between the two measurements.

The I output signal of the ESG is connected to one of the reference planes used during the LF SOLT calibration and is measured with the help of the associated LF sensing module. After applying the absolute correction coefficients on the LF measured quantities, one can perform a phase alignment of the calibrated signal with the uploaded multi-tone modulation signal. The same approach is used in the RF path by connecting the ESG RF modulated output signal to one of the reference planes defined during the RF SOLT calibration and aligning the envelope of the measured signal around the fundamental frequency with the uploaded multi-tone signal. The extracted delays during phase alignment are then incorporated in the LF and RF absolute correction coefficients.

After this extra calibration step, the measured and calibrated DC, LF and RF components allow to reconstruct the proper signals at each port of the DUT.

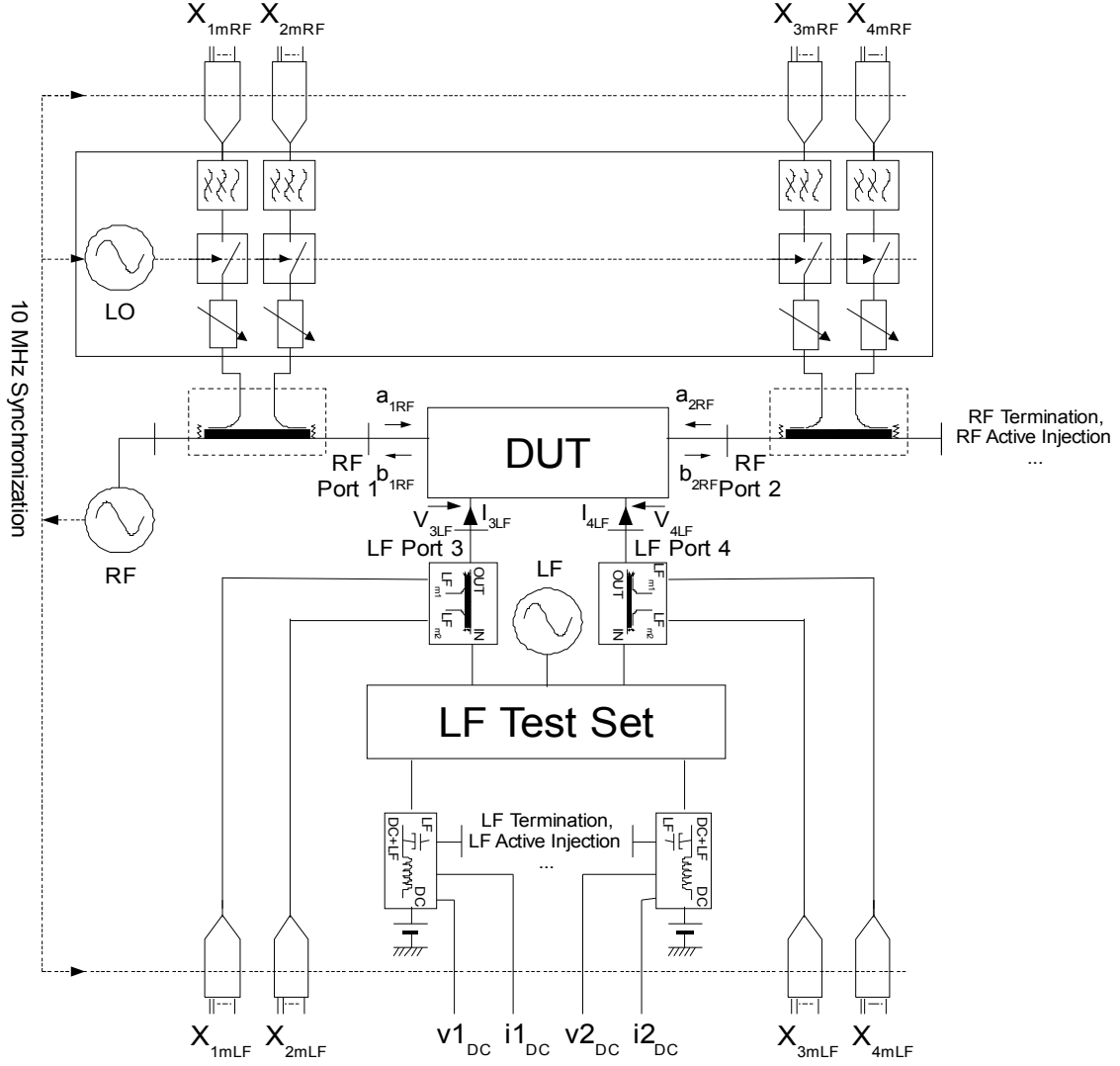


Figure 1: Block Diagram of combined LSNA and Dynamic Bias Setup

### III. RESULTS

The new measurement set-up has been tested performing two-tone measurements on a PCB mounted GaAs circuit (Fig.2). An LC resonant circuit (grey dashed box in Fig.2) was added in the drain bias network in order to induce LTMs [7]. Measurements were carried out at RF and LF reference planes and hence a de-embedding procedure was needed to shift the measured voltages and currents to the unaccessible device terminals. For this purpose, ABCD transformations were applied. The input power was kept constant (0 dBm for each tone) and the spacing was swept (from 10 kHz to 450 kHz). The circuit was biased with 3.1 V on the drain and -0.5 V on the gate resulting in a drain current of 500 mA. In Fig.3a both magnitude and phase of lower and upper IM3 components of  $b_2$  are shown as function of tone spacing. Variation and asymmetry are clearly visible. In Fig.3b experimental results of IM3 asymmetry are plotted along the imaginary part of LF drain impedance (in the inset). The change of the sign of asymmetry can be correlated with the switch of the baseband impedance's reactive part (from inductive to capacitive with related change in phase sign, as emerges from Fig.4) around the resonant frequency (75 kHz). Further, close to resonance, asymmetry is very close to zero dB due to the very high value of the

imaginary part of the impedance whose contribution to IM3 dominates over the one arising from 2<sup>nd</sup> harmonic and reactive non-linearity [8].

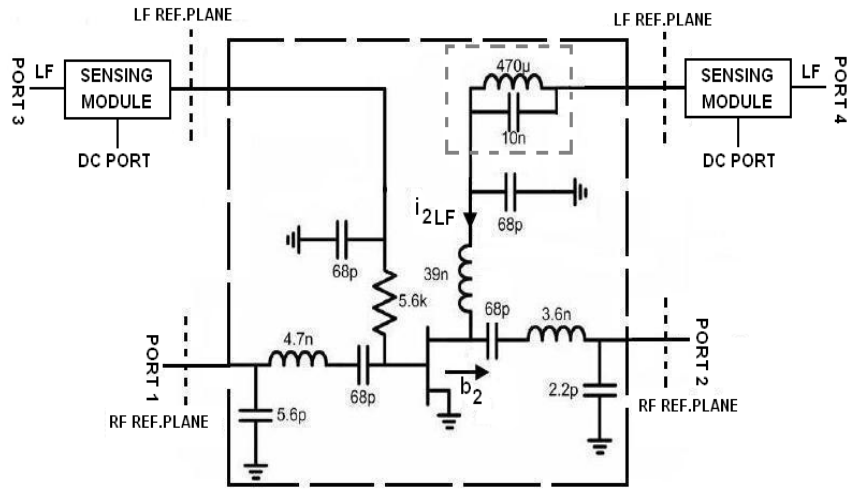


Figure 2: DUT within the measurement set-up

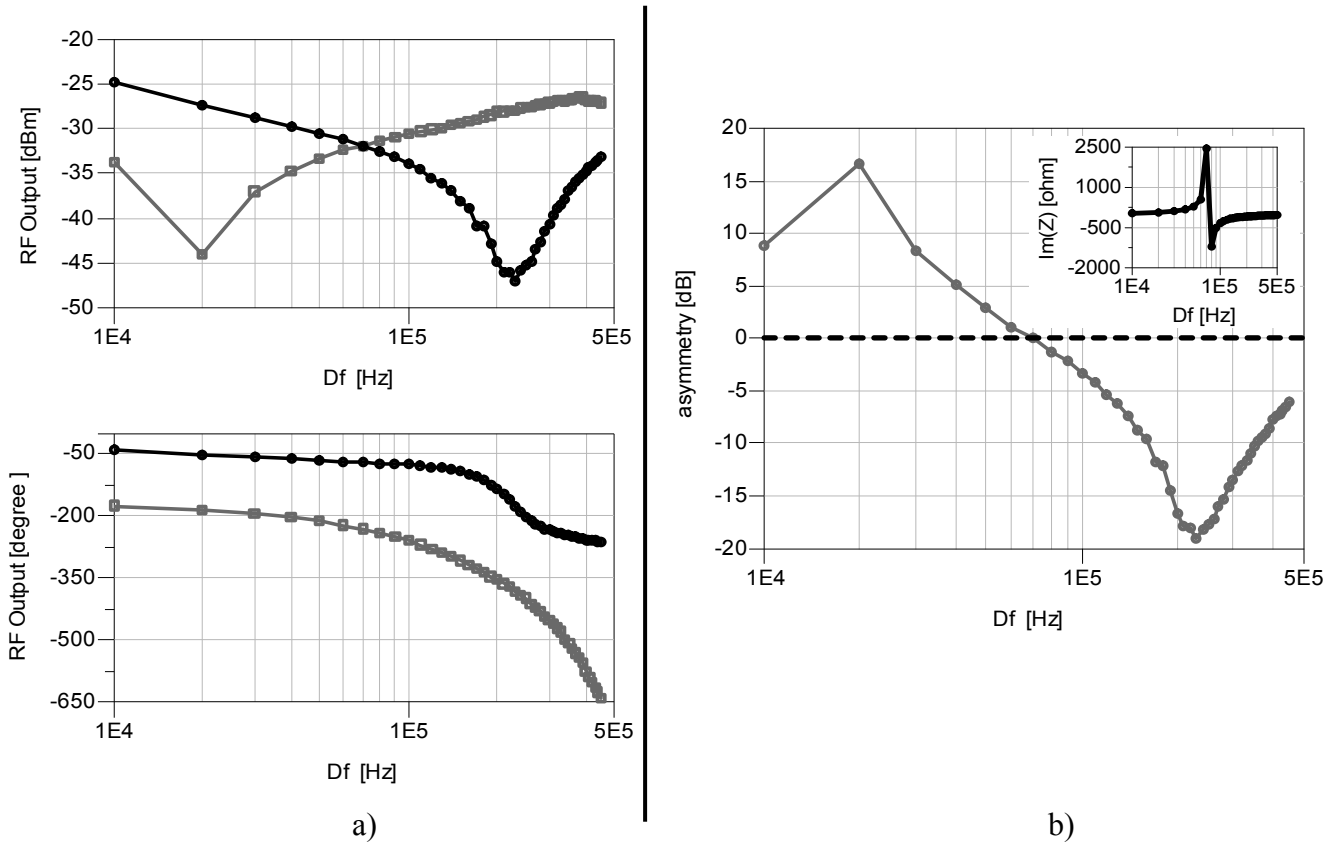


Fig.3: a) Measured amplitude and unwrapped phase of IM3 components of b2 as function of tone-spacing. The lower IM3 product is grey; the upper is black; b) asymmetry (difference between the magnitude of IM3U,L) with the baseband impedance imaginary part(inset)

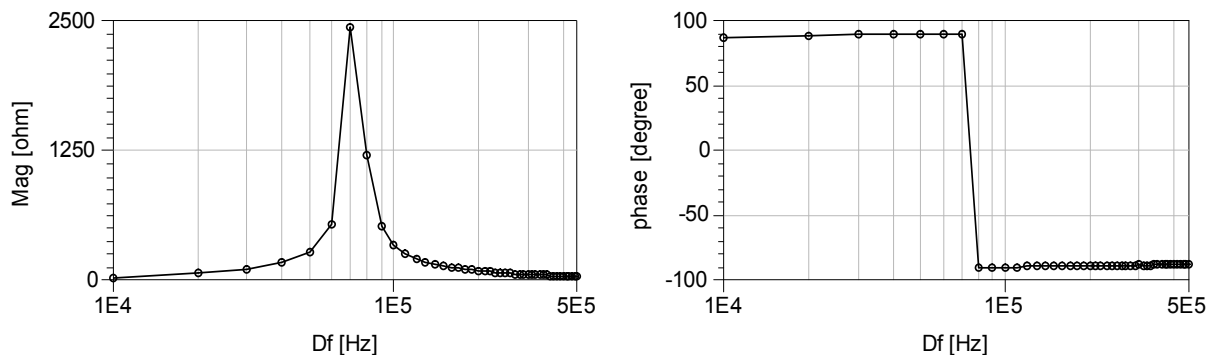


Fig.4: LF impedance at drain side. At resonance (75 kHz) the imaginary part switches from inductive to capacitive and consequently the phase inverts

#### IV. CONCLUSION

In this paper, a novel set-up extending the functionality of LSNA has been presented. The new set-up enables to simultaneously measure both LF and RF responses of a non-linear microwave device allowing a direct correlation between LF dispersive phenomena and LF-bandwidth dependent behaviour of RF dynamics. To assess its capability, measurements were performed on a connectorized amplifier and experimental results of asymmetry of RF response have been shown. Particularly, the relation between frequency dependent baseband impedance and asymmetry of 3<sup>rd</sup> order intermodulation products has been discussed.

#### ACKNOWLEDGMENT

The authors would like to acknowledge J. Portilla and C. Fager for providing circuits.

#### References

- [1] J.C. Pedro and N. Borges Carvalho, *Intermodulation distortion in microwave and wireless circuits*, Artech House, 2003
- [2] J. Brinkhoff and A.E. Parker, "Device characterization for distortion prediction including memory effects," *IEEE Microwave Wireless Compon. Lett.* vol. 15, no. 3, pp. 171-173, 2005
- [3] D.J. Williams, J. Leckey, and P.J. Tasker, "A study of the effect of envelope impedance on intermodulation asymmetry using a two-tone time domain measurement system," in *IEEE MTT-S Int. Microwave Symp. Dig.*, 2002, pp. 1841-1844
- [4] MT4463 Data Sheet, [www.nmdg.be](http://www.nmdg.be)
- [5] J. Benedikt, "Method of combining signals and device therefor," US Patent 7385461
- [6] Agilent E4433 ESG-D Series Digital RF Signal Generator datasheet, [www.agilent.com](http://www.agilent.com)
- [7] J. Brinkhoff and A.E. Parker, "Effect of Baseband Impedance on FET Intermodulation," *IEEE Trans. Microwave Theory Tech.*, vol. 51, no. 3, pp. 1045-1051, 2003
- [8] N. Borges Carvalho and J.C. Pedro, "Two-tone IMD asymmetry in microwave power amplifiers," in *IEEE MTT-S Int. Microwave Symp. Dig.*, 2000, pp. 445-448

# DESIGN AND TESTING OF A SOFTWARE FEEDBACK LOOP FOR RF POWER LEVELING\*

Xiaohai Cui<sup>1,2</sup> and T. P. Crowley<sup>1</sup>

<sup>1</sup>National Institute of Standards and Technology  
MC 818.01, 325 Broadway, Boulder, CO 80305 USA

<sup>2</sup>National Institute of Metrology of China, Beijing, China  
[xiaohaic@boulder.nist.gov](mailto:xiaohaic@boulder.nist.gov)

## Abstract

We have developed a software feedback loop that stabilizes the RF power input to less than 30 ppm during calorimetric measurements. In this system, a bolometric sensor with a Type IV power meter is used to detect the power. Feedback is provided to the Amplitude Modulation (AM) input of an RF generator through a computer-controlled voltage source. The software feedback loop replaces an analog feedback loop that used an NBS Type II Power Measurement System to provide the AM input signal. The new system removes a potential error in the DC substituted power caused by loading of the Type IV when connected to the Type II. The new leveling system is more flexible than the previous system. Both the desired leveling accuracy and real-time feedback rate can be readily modified. The design and evaluation of the software leveling system are presented. It has been tested with a new WR-15 microcalorimeter which will be the national power standard in the US from 50 to 75 GHz.

## Introduction and Motivation

RF generators can typically be leveled either internally or externally. A common external leveling method is shown in Fig. 1. Power leveling feedback is provided by an external power detector connected to the external Automatic Level Control (ALC) input of the generator. The calorimetric measurements determine the effective efficiency  $\eta = P_{sub} / P_{RF}$  of a bolometric detector, where  $P_{sub}$  is the substituted DC power measured and  $P_{RF}$  is the net RF power absorbed by the detector. Because the measurements require that the detector reach thermal equilibrium, we need an RF power stability of better than 100 ppm over several hours. Hence, we use the DUT as the external detector, since it sits in a temperature controlled water bath. However, the ALC circuitry is not designed for use with the Type IV power meters used in these experiments. Although the approach in Fig. 1 could still be used, there are additional complications and so NIST has elected to use the alternate approach described next.

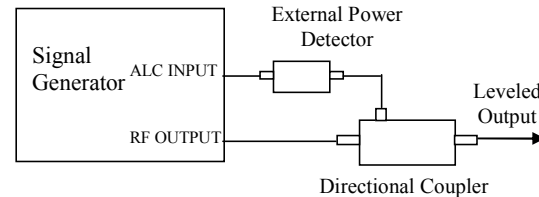


Fig. 1 Typical leveling system of an RF generator

The analog feedback system previously developed for the NIST microcalorimeters is illustrated in Fig. 2 [1]. The bolometric sensor under measurement in the calorimeter is used as the power detector. The calorimeter sits in a water bath stabilized to better than 1 mK. The voltage output of the bolometer's Type IV power meter and a DC reference are inputs to the Type II Power Measurement System [2]. The DC reference is set by a computer to the value of the Type IV output that would produce the desired substituted power level. The deviation between the Type IV power meter voltage and the DC reference drives the Type II feedback signal. The feedback loop is completed by connecting the Type II output to the AM input of the RF signal generator.

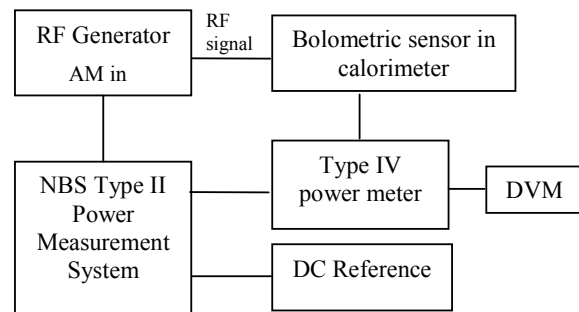


Fig. 2 RF power leveling system previously developed for NIST microcalorimeters.

Although this system has worked well for a number of years, we recently encountered some situations in which the power was leveled properly, but the effective efficiency measurements were inaccurate. Fig. 3 shows an example in which three sets of effective efficiency measurements are shown relative to a common reference from a separate run. The three sets were taken for a single RF connect. Repeated measurements with no changes would typically have effective efficiency values that agree within 0.001.

\* U.S. government work, not subject to U.S. copyright

The only change between the three sets of data was that the source power setting of the RF generator was varied from -20 dBm to +9 dBm. This change caused the Type II output voltage and current to vary considerably. Although the Type II feedback loop was successful in maintaining the desired power level, the effective efficiency measurements vary by up to 0.01, an order of magnitude larger than expected. Additional tests have led us to conclude that if the Type II output current is too high, then the Type II loads the Type IV, so that its output voltage is not an accurate measurement of the bolometer's bias voltage. Incorrect bias voltage measurements result in an inaccurate effective efficiency measurement.

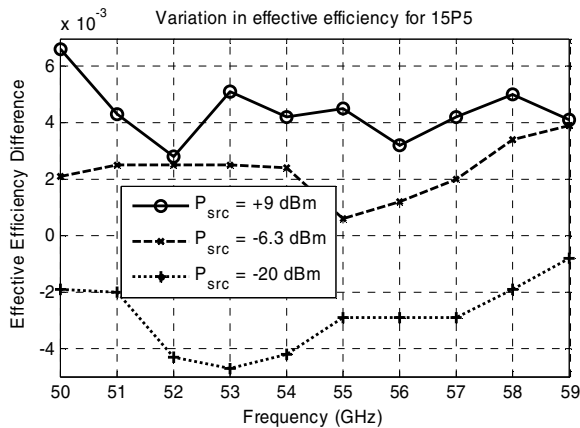


Fig. 3 Effective efficiency deviation between a common reference and data taken with different RF source power settings, which produce different Type II leveling currents.

### Design and Realization

The software feedback loop illustrated in Fig. 4 was developed to level the power without loading the Type IV power meter. The Type II Power Measurement System is not used in the system under software control. Software calculates the measured power level based on the DVM measurement and then increases or decreases a DC generator voltage whose output is connected to the AM input of the RF generator. The system is flexible, and with simple code changes, the desired leveling accuracy and feedback parameters can be adjusted.

Fig. 5 shows the procedure for a calorimeter measurement at a single frequency. The initial and final steps are very similar to those of the Type 2 feedback system. At the start of a measurement, an 'RF off' measurement is made of the bolometer's bias voltage. The computer calculates the bias voltage that will result in the desired substituted

power, initializes equipment, sets the AM properties of the RF generator (linear and usually 50 Ω input), and turns on the RF power. The software feedback loop in the center stabilizes the power at the desired level. The program records the bolometer bias voltage ( $V_{\text{bias}}$ ) and thermopile ( $V_{\text{thermopile}}$ ) voltage every 30 seconds and then re-enters the software feedback loop. The measurement at a given frequency is terminated by a separate algorithm described in [3].

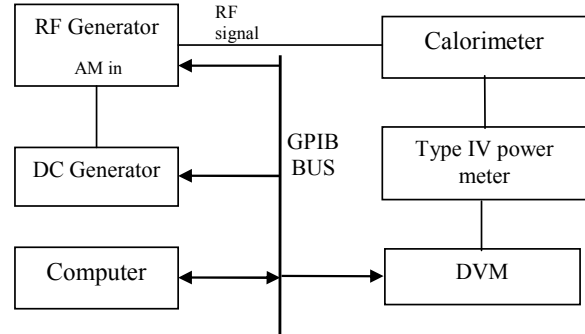


Fig. 4 Software leveling system

The software leveling loop starts with an initial DC generator voltage, and therefore AM input voltage of  $V_{AM,0}=0$ . The code waits a brief period and measures the bias voltage. If the power level is not at the desired level, the new value of the DC generator voltage is set to

$$V_{AM,n+1}=V_{AM,n} + C (P_{\text{setting}}-P_{\text{sub}})/P_{\text{setting}} \quad (n=0,1,2,\dots),$$

where  $P_{\text{setting}}$  is the desired power level,  $P_{\text{sub}}$  is the measured substituted power of the bolometric sensor in the calorimeter, and  $C$  is a constant. The software checks that the  $|V_{AM}| < 1$  in order to avoid damaging the RF generator, and then proceeds to reset the generator voltage. The system delays 1 second after changing the DC generator before reading the bias voltage again and repeating the loop. This continues until the power is leveled. The first pass generally takes about one minute to achieve  $\Delta < \Delta_{\text{tolerance}}$ . Subsequent adjustments take a few seconds. The delays and the coefficient can easily be changed. We have found that a 1 second delay and a coefficient  $C = 0.618$  work well for the WR-15 system.

### Results

Fig. 6 compares the stability of the power sensor using the software feedback loop and the Type II feedback loop. Each data point shows the rms variation during a single frequency measurement that took about 30 minutes. Total run period was over 270

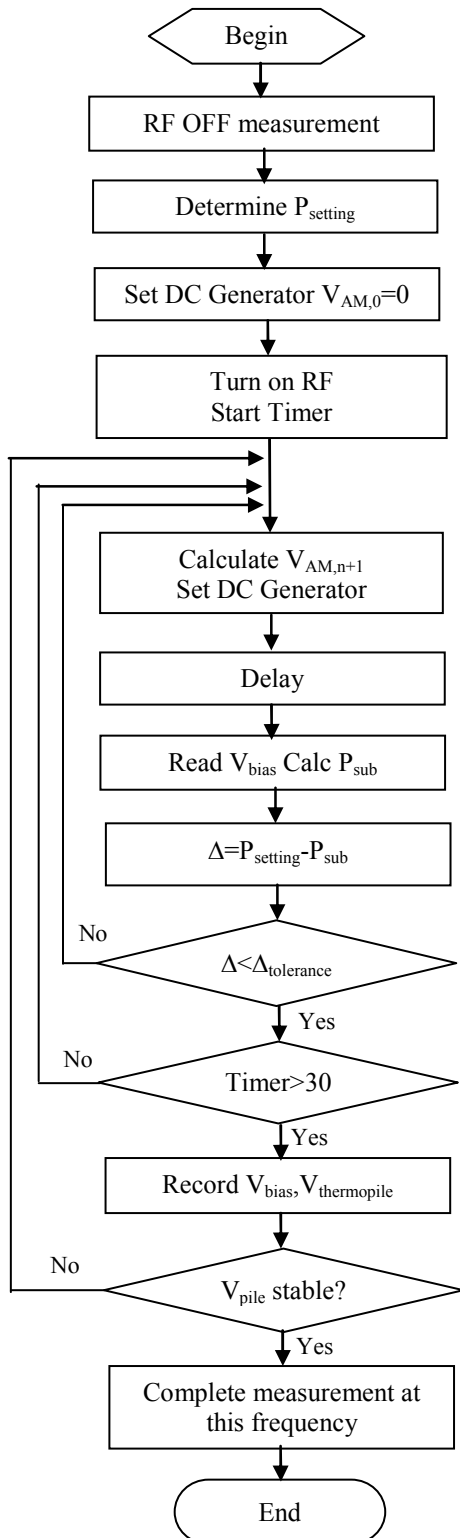


Fig. 5 Flowchart of measurement procedure at each frequency. The software leveling procedure is the loop that ends at the  $\Delta < \Delta_{\text{tolerance}}$  decision step.

minutes. The software leveling case is not as stable as the old analog feedback loop, but it is still well within the measurement requirements, and it provides a more accurate effective efficiency measurement, since there is no loading of the Type IV power meter. In this case, the relative rms variation of the DVM is less than 7 ppm, and it is less than 30 ppm in the other cases we have examined so far.

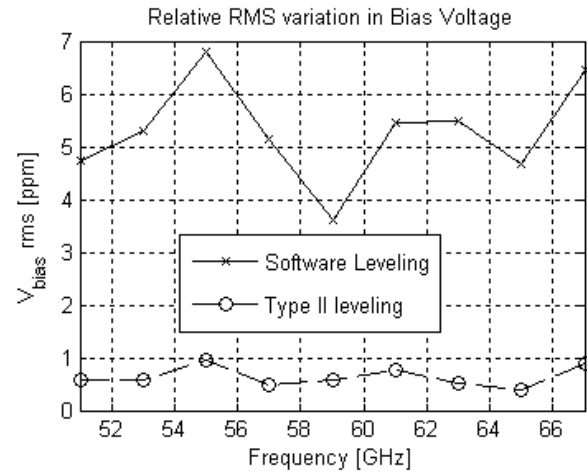


Fig. 6 RMS variation of the bias voltage when using software and analog leveling. For each point, the rms value is calculated from approximately 30 minutes of data.

The software leveling loop has worked well for an extensive set of measurements made for a new WR-15 calorimeter under development. Initial tests with our Type N calorimeter also show that effective efficiency measurements with the software leveling feedback system agree with those from the analog feedback loop to within the repeatability uncertainty.

### References

- [1] J. Wayne Allen, Fred R. Clague, Neil T. Larsen, and Manly P. Weidman, "NIST Microwave Power Standards in Waveguide", NIST Technical Note 1511, Feb.1999.
- [2] N. T. Larsen and F. R. Clague, "The NBS Type II Power Measurement System", *Adv. Instrum.*, vol. 25, Pt. 3, paper no. 712-70 in *Proc. 25<sup>th</sup> Annu. ISA Conf.* (Philadelphia, PA), Oct. 26-29, 1970.
- [3] Fred R. Clague, "A Calibration Service for Coaxial Reference Standards for Microwave Power", NIST Technical Note 1374, May 1995.

# Load-Pull + NVNA = Enhanced X-Parameters for PA Designs with High Mismatch and Technology-Independent Large-Signal Device Models

Gary Simpson<sup>1</sup>, Jason Horn<sup>2</sup>, Daniel Gunyan<sup>2</sup>, and David E. Root<sup>2</sup>

<sup>1</sup>Maury Microwave Corporation, Ontario, CA, 91764, USA

<sup>2</sup>Agilent Technologies, Santa Rosa, CA, 95405, USA

**Abstract** — X-parameters [1-4] are the mathematically correct supersets of S-parameters valid for nonlinear (and linear) components under large-signal (and small-signal) conditions. This work presents an automated application combining a Nonlinear Vector Network Analyzer (NVNA) instrument with automated load-pull measurements that extends the measurement and extraction of X-parameters over the entire Smith Chart. The augmented X-parameter data include magnitude and phase as nonlinear functions of power, bias, and load, at each harmonic generated by the device and measured by the NVNA. The X-parameters can be immediately used in a nonlinear simulator for complex microwave circuit analysis and design. This capability extends the applicability of measurement-based X-parameters to highly mismatched environments, such as high-power and multi-stage amplifiers, and power transistors designed to work far from 50 ohms. It provides a powerful and general technology-independent alternative, with improved accuracy and speed, to traditional large-signal device models which are typically slow to develop and typically extrapolate large-signal operation from small-signal and DC measurements.

**Index Terms** — microwave measurements, design automation, modeling, nonlinear circuits, power amplifiers, simulation, X-parameters..

## I. INTRODUCTION

Device characterization is required for power amplifier design, and the ideal form of the device data is a large signal model. With a model, the performance can be analyzed for varying drive and impedance conditions, so complex or multi-stage circuits can be designed.

Much work has been devoted to large signal model development at microwave frequencies, and improvements have been made in recent years. But though these analytical models can be accurate over certain regions of the device operation, they may fail in other areas. Since they are typically extrapolated from DC and small signal measurements, verification under actual large-signal operation is generally required. In many cases of practical interest, the device is used over a wider range of voltage and current than can even be characterized under DC and linear S-parameter conditions. Load pull is a measurement of a device under actual large signal operation. It may include measuring device performance vs. impedance, drive power, bias, temperature, or other factors. Since it is a direct device measurement, the data

can be used with confidence over the conditions of the measurement.

Load pull data can be used directly for power amplifier design, by determining the impedance terminations required for device operation. A linear simulator can then be used to design the input and output matching networks. But this approach generally works well only for simple amplifiers, not for more complex or multi-stage circuits. This method has been widely used when large signal models are not available or not trustworthy. However, conventional load-pull data typically does not provide the magnitudes and all the cross-frequency phases of the harmonics, and therefore does not provide enough information to reconstruct the terminal waveforms of the device when they are highly distorted under large-signal conditions. It is therefore not sufficient to be used independently in the simulator as a device model.

A second way that load pull data is used for power amplifier design is to validate large signal models. The load pull data is measured during actual device operation, so is used as reference data. The large signal model is compared to the load pull data, and may be adjusted as needed to get accurate analysis in the region of interest. At that point, the large signal model can be used for more complex circuit analysis.

An alternate way of formulating a large signal model is to use a measurement-based behavioral approach, as with the PHD model. This is based on measurements of X-parameters, which are a superset of S-parameters for nonlinear components, and are measured using an NVNA (Non-linear Vector Network Analyzer). S-parameters measure the complex magnitude and phase relationship between small signals at the same frequency at different ports, but don't account for additional spectral components generated by the DUT under large-signals, or the interaction among different frequency signals incident on a device whose state is time-varying due to large-signal stimuli. X-parameters include harmonics and intermodulation frequency components, and also the relationships between all those frequencies for a given drive amplitude and frequency, enabling the complete waveforms – including those corresponding to strongly compressed conditions - to be measured at the device terminals. However, a stand-alone NVNA does not stimulate the device over a wide range of impedance states at which the X-parameters are measured. Therefore, the simplest 1-tone

PHD model [1,4] is extracted only over a limited impedance range around the characteristic impedance of the NVNA, typically 50 ohms, or around an arbitrary but fixed impedance presented by an impedance transformer or matching structure used to present a different impedance environment to the device output. Most high-power transistors and amplifiers have optimal performance far from 50 ohms. It is therefore necessary to acquire X-parameters over large areas of the Smith Chart in order for the resulting model to remain valid over the corresponding range of loads it might be expected to encounter in applications. The limitation is not with X-parameters or the PHD framework for simulating with X-parameters [3], but rather with providing a simple, fast, automated measurement system and application to acquire the X-parameters over the entire complex load-domain of interest.

## II. LOAD PULL WITH X-PARAMETERS

This paper introduces load pull with NVNA measurements of X-parameters that produce data that can be used directly by the PHD model over a wide impedance range. The operator of the combined load pull NVNA system will select an impedance range of interest, possibly over the entire Smith chart. The PHD model can then be used as a circuit element in a non-linear analysis with great confidence, since it is based on measurement at the actual operating conditions of the device.

The load pull X-parameter measurement can include a complete sweep plan. Stimulus variables can include impedance, power drive, bias, and frequency, for example. This can extend the applicability of the PHD model over a much wider range of validity – over the range of actual applications for many high-power and multi-stage PA designs.

The process has three steps:

- 1) The load pull system measures the X-parameters at each impedance setting, like a standard load pull, with X-parameters added to the measurement data set. When the measurements are complete at all the impedances, the measured X-parameters are saved into a single file.
- 2) An enhanced design kit available for use in the ADS non-linear simulator then reads the file saved by the load pull - NVNA system and creates a PHD component associated with the file. This is a very quick step.
- 3) This component can then be dragged and dropped directly into a circuit schematic as a non-linear device, and analysis can start immediately.

This process is a huge simplification over past practice. It provides the simplicity of using load pull and NVNA data directly for simple power amplifier design, but with the ability to analyze complex circuits that require a large signal model. It also is not limited to characterizing a single device, but applies equally to modeling an amplifier section. The process is also independent of the device technology. Extracting full load-dependent X-parameters at multiple harmonics is much

more automated and repeatable than extracting a standard “compact” transistor model, which may have more than 100 parameters that have to be optimized to give overall fits. It is thus ideal for new technologies and new amplifier realizations before any detailed physics-based compact models or accurate circuit-level models are available.

## III. SYSTEM CONFIGURATION

Although the measurement system is capable of taking much more complex measurements than a classic load-pull system, in many ways the setup is actually much simpler. A typical scalar load-pull system may involve a computer running the controlling software, multiple power meters, a spectrum analyzer, DC supplies and meters, one or more sources, and one or more tuners along with attenuators, bias tees, couplers, etc. Utilizing Agilent’s latest premier network analyzer, the PNA-X, many of these separate components and instruments are no longer necessary because they are already contained inside the box. This results in a simpler setup with fewer components, an easier use model, and faster measurements.

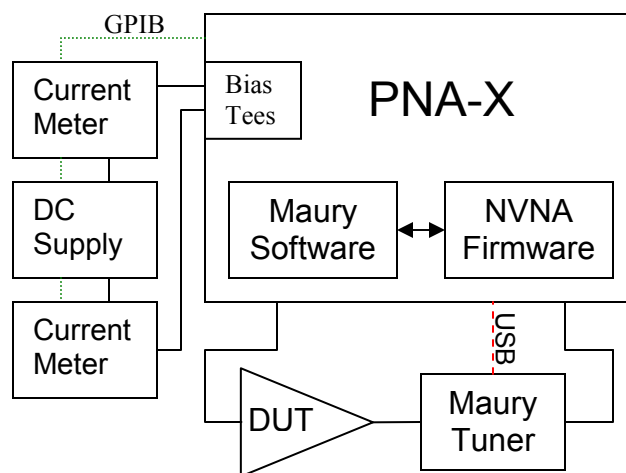


Figure 1. Measurement setup for load pull with X-parameters

The central piece of the measurement setup is the PNA-X with NVNA and X-parameter options. In addition to serving as a time domain measurement system with 26 GHz of bandwidth, the Maury ATS software can run directly on the analyzer for maximum interoperability and speed, eliminating the need for a dedicated measurement computer. The necessary couplers, bias tees, and RF sources are also already included in the box, so connecting the system is relatively simple as seen in figure 1. The USB-controlled tuner plugs directly into the analyzer, and the DC instruments are controlled through the built-in GPIB interface. Since both the NVNA firmware and ATS software have built-in support for external instrument control through GPIB, bias sweeps are

easy to set up and measurement synchronization is automatically handled.

The user interface is primarily handled through Maury's ATS software, with the NVNA firmware used for calibration and made available for advanced settings (configuring internal switches and attenuators, utilizing advanced features of the PNA-X such as pulse modulation or triggering, etc.). Measurement configuration through the UI is similar to standard load-pull configuration, but using a simpler block diagram with the NVNA replacing several typical instruments. The measurement parameter "X-Params" is available when the NVNA is included in the setup. When it is not selected, time-domain load-pull (load dependent waveforms) measurements are taken. When selected, the X-parameters of the DUT are also measured as a function of load and any swept bias conditions. The resulting X-parameters are written to a single file at the end of the measurement that is immediately ready to be imported into ADS and used in simulation and design.

#### IV. SIMULATION

The PHD Design Kit for ADS provides a framework for simulation using measured data. X-parameters measured on the NVNA can be directly imported through the design kit and immediately used for large signal simulation and design. The design kit was updated to support load-dependent X-parameters measured with the system described above. The use model is exactly the same as that of fixed-impedance X-parameters, and consists of copying the MDIF file containing the measured X-parameters into the ADS Project in which it will be used and using the "PHD" menu to create a component that is linked to that file. The entire process typically takes less than one minute, and the component can be immediately used in the Harmonic Balance or Envelope simulators, as shown in figure 2. Full large-signal behavior, including magnitude and phase of harmonics, are captured in the X-parameters and accurately predicted by the component.

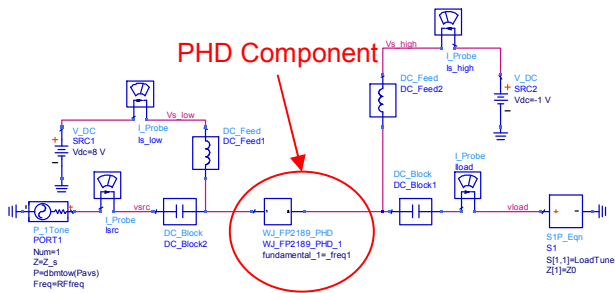


Figure 2. PHD Component linked to a file of measured X-parameters in an ADS schematic.

#### V. RESULTS

The measured data was taken using the Maury tuner model MT982EU30, and the Agilent PNA-X, model N5242A, with

the NVNA and X-parameter options, as shown in figure 1. The DUT measured is a packaged FP2189 1 Watt HFET from WJ Communications (now a part of TriQuint Semiconductor) mounted on a connectorized PC board. All measurements were deembedded up to the package pins.

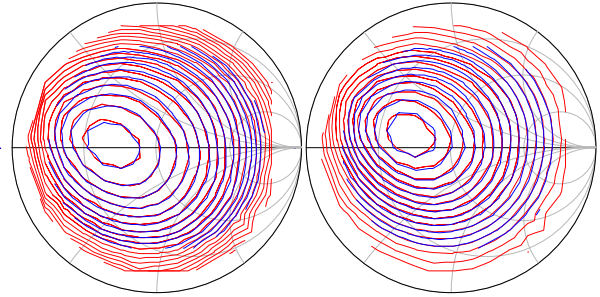


Figure 3. Comparison of simulated (blue) and independent measured (red) delivered power contours (left) and efficiency contours (right)

The first basic validation was done by comparing a standard load-pull measurement of delivered power and efficiency with the results of a load-pull simulation in ADS using the PHD component with measured load-dependent X-parameters. As figure 3 illustrates, the agreement between simulated and the independent measured results is excellent.

In addition to fundamental RF and DC behavior, the X-parameters also capture the harmonic behavior of the device. Since magnitude and phase of harmonics are captured, the full time-domain waveforms are available, as shown in figure 4.

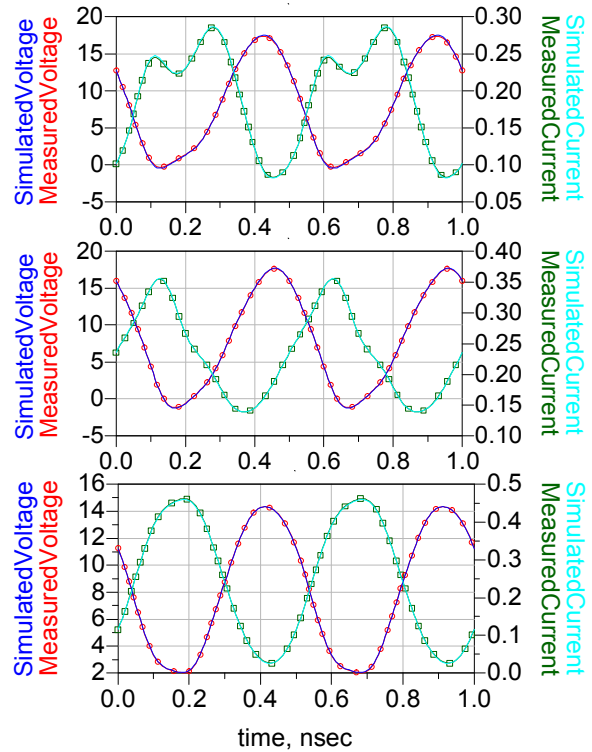


Figure 4. Comparison of simulated and independent measured time domain waveforms at fundamental gamma of 0.383+j\*0.31 (top), 0.387-j\*0.466 (middle), and -0.272+j\*0.048 (bottom).

Again, the agreement between simulation and independent measured results is excellent. The comparison was done by first taking the independent measurements, then presenting the measured load conditions at the fundamental and harmonics to the PHD component in simulation.

The same harmonic load conditions were necessary for a valid comparison because the PHD component uses X-parameters to account for harmonic mismatch. This is an important note, because in addition to providing an automated framework for using nonlinear measured data in simulation, PHD and X-parameters provide an efficient way to capture dependence on harmonic load and upstream source harmonics, as shown in figure 5. Although X-parameters are not a complete replacement for harmonic load-pull in all cases, we anticipate that, for many devices, they will provide sufficient information to use in design without the need for a much longer full harmonic load-pull measurement.

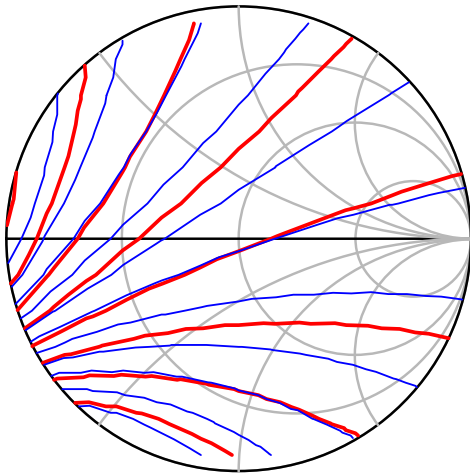


Figure 5. PAE (red) and Delivered Power (blue) contours vs. second harmonic load

## VI. CONCLUSION

Load pull with X-parameters together with the PHD framework provides a simple and direct way to get a large signal model for analysis of complex power amplifier circuits. The load pull measurement creates an X-parameter file which can be loaded directly into the non-linear simulator to use with the PHD component. The data can then be used immediately for analysis of complex power amplifier circuits. The load-dependent X-parameters enable full waveforms to be predicted calibrated to the device terminals – even under high degrees of compression – over all impedance environments.

## ACKNOWLEDGEMENT

The authors wish to acknowledge the assistance and support of the Agilent management.

## REFERENCES

- [1] J. Verspecht and D. E. Root, "Poly-Harmonic Distortion Modeling," in *IEEE Microwave Theory and Techniques Microwave Magazine*, June, 2006.
- [2] J. Verspecht, D. Gunyan, J. Horn, J. Xu, A. Cognata, and D.E. Root, "Multi-tone, Multi-Port, and Dynamic Memory Enhancements to PHD Nonlinear Behavioral Models from Large-Signal Measurements and Simulations," 2007 IEEE MTT-S Int. Microwave Symp. Dig., Honolulu, HI, USA, June 2007.
- [3] J. Horn, D. Gunyan, L. Betts, C. Gillese, J. Verspecht, and D. E. Root, "Measurement-Based Large-Signal Simulation of Active Components from Automated Nonlinear Vector Network Analyzer Data via X-Parameters," in 2008 IEEE COMCAS Conference, Tel Aviv, Israel, March, 2008
- [4] D. E. Root, J. Verspecht, D. Sharrit, J. Wood, and A. Cognata, "Broad-Band, Poly-Harmonic Distortion (PHD) Behavioral Models from Fast Automated Simulations and Large-Signal Vectorial Network Measurements," *IEEE Transactions on Microwave Theory and Techniques* Vol. 53. No. 11, November, 2005 pp. 3656-3664

# A New Technique for Decreasing the Characterization Time of Passive Load-Pull Tuners to Maximize Measurement Throughput

Chris Roff<sup>1,2</sup>, Joshua Graham<sup>1</sup>, Jerome Sirosis<sup>1</sup> and Basim Noori<sup>1,2</sup>

<sup>1</sup> Freescale Semiconductor, Inc., RF Division, 2100 E. Elliot Road, Tempe, AZ. 85284, USA.

<sup>2</sup> Centre for High Frequency Engineering, Cardiff University, 5 The Parade, Cardiff, Wales, CF24 3AA, UK.

**Abstract** — This paper presents a technique for increasing the flexibility and the point density of passive load-pull tuner characterization coverage from a reduced measurement collection cycle. Interpolation methods are used to enhance the resolution of available tuner positions whilst greatly reducing the time required for data collection prior to useful load-pull measurement. Results are presented to demonstrate validation of the method, showing that the mathematical accuracy in the predicted tuner S-parameters is greater than the reported physical reproducibility of the tuners. The impact of the new technique on characterization time is demonstrated to yield a time saving of 80% – significantly increasing potential measurement throughput.

**Index Terms** — high power devices, power amplifiers, load-pull measurements.

## I. INTRODUCTION

Load and source pull techniques are an established tool for the measurement of high power RF amplifier components, whose behavior is often a strong function of load and source impedance. Load and source pull measurements are capable of reproducing conditions similar to the final application and are of great importance in characterizing components operating in the nonlinear regime. By presenting a range of impedance states to the device-under-test (DUT), at the load and source ports, device behavior can be systematically measured and best operating conditions can be determined.

Systematic load-pull mapping of RF amplifiers is usually achieved in one of two ways: passive load-pull using mechanical tuners [1,2] or active load-pull using either closed [3] or open loop architectures [4]. Both passive and active approaches have their advantages and disadvantages but in the majority of industrial RF labs passive tuners are used, primarily due to their simplicity of operation and high power handling capability.

Measurements made using mechanical passive tuners are deterministic, since the loss introduced by the equipment required for real-time measurement of the reflection coefficient (such as couplers) will reduce the achievable tuning range and is therefore undesirable. Although low loss couplers [5] are enabling the synthesis of such systems, the majority of

current architectures are predictive in nature. Consequently, any impedance that the tuner presents to the DUT will need to be measured, typically with a vector network analyzer (VNA). In order to allow flexible use of tuners once they are connected to the DUT for optimizing or “tuning” a device’s performance, it is useful to have a large variety of positions characterized for each frequency of interest prior to commencing load-pull measurements. In this way the impedance presented to the DUT by a tuner in a given position will be known, provided the tuner can reproduce the same state.

Such a tuner characterization process can be extremely time consuming if a high resolution of tuning positions is required. Given the repeatable nature of the automated passive tuners and the power of modern computing and interpolation algorithms, it is possible to reduce the number of points characterized prior to measurement whilst maintaining tuning resolution by interpolating the S-parameters of the tuner at unmeasured positions [6]. This paper presents the development of a new technique to achieve high density tuner characterizations by interpolating a small number of training positions to generate new, unmeasured positions. It will be shown that the time required for a standard tuner characterization can be reduced by approximately 80% using this interpolation approach without reducing the accuracy of the final measurements.

## II. PASSIVE TUNER BEHAVIOR

In the simplest case, an automated passive tuner consists of a conducting line between two ports (typically one end is connected to the DUT and the other is connected to a load). The reflection coefficient presented at the DUT by the tuner can be altered using a perpendicular probe that interacts with the fields around the centre line to varying degrees depending on its position relative to the line. Precise control over the tuner S-parameters is provided by extremely accurate stepper motors that are capable of moving the probe to a wide range of positions.

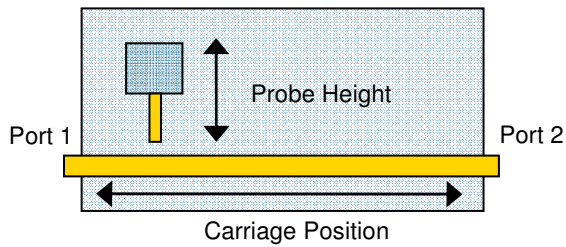


Figure 1 - Simplified diagram of an automated passive tuner.

The position of the probe carriage along the line mainly affects the phase rotation of the reflection coefficient. The vertical probe height primarily controls the magnitude of the reflection coefficient but can also impact the phase as the probe head gets close to the centre conductor and the fringing capacitance becomes significant. A diagram of a rudimentary passive tuner is shown in Figure 1, and an example plot of how tuner position affects the reflection coefficient is shown in Figure 2.

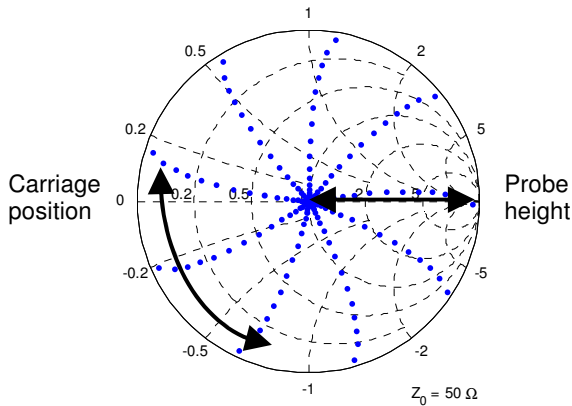


Figure 2 – Plot showing the effect of probe position on reflection coefficient,  $\Gamma$ . The radial “spokes” are measured  $\Gamma$  points at constant carriage positions and varying probe heights. It can be seen that the phase of  $\Gamma$  becomes a function of both the carriage position and probe height towards the edge of the Smith chart.

### III. MODELING TUNER BEHAVIOR

The objective of the interpolation used in this work is to convert tuner S-parameters measured at a small number of positions into S-parameters at any new tuner position with no appreciable loss in accuracy for any frequency of interest. The accuracy of the interpolated S-parameters must be greater than mechanical reproducibility of the tuner, which is stated to be typically better than -40 dB by the manufacturer for the particular tuner models investigated [7].

There is a wide range of interpolation techniques that can be applied to this problem [8]. For each tuner position the S-parameters can be considered the dependent variables which

are a function of two independent variables, the lateral carriage position and the vertical probe height. It was decided that a spline technique would give a fast and flexible implementation and had a proven track record in approximating load-pull measurement data [9].

The Matlab™ spline toolbox provides a simple bivariate spline function in the *thin-plate smoothing spline (TPS)* whose function can be thought of as creating a surface of S-parameter values over a two dimensional matrix of measured position points or centers [10]. The Matlab TPS function creates its surface using a collection of radial basis functions,  $f$ , whose error is minimized according to the following error function:

$$p\mathbf{E}(f) + (1-p)\mathbf{R}(f) \quad (1)$$

where  $\mathbf{E}(f)$  is the error measure,  $\mathbf{R}(f)$  is the roughness measure and  $p$  is a weighting factor. In this way, the weighting factor  $p$  allows control over the degree of smoothing performed during surface creation, trading off fit through measured centers with overall surface smoothness. One drawback of the approach is the increase in calculation times if more than 728 data points are used during surface training [10].

The S-parameter TPS surfaces effectively form a model of the tuner behavior vs. position and can be interrogated to estimate the S-parameters at any new position on the surface. Figures 3 and 4 show the real and imaginary parts of  $S_{11}$  vs. tuner position for a typical tuner, as predicted using a TPS surface. It was found that organizing the S-parameter data in rectangular rather than polar format yielded smoother TPS surfaces, resulting in more accurate interpolated estimates.

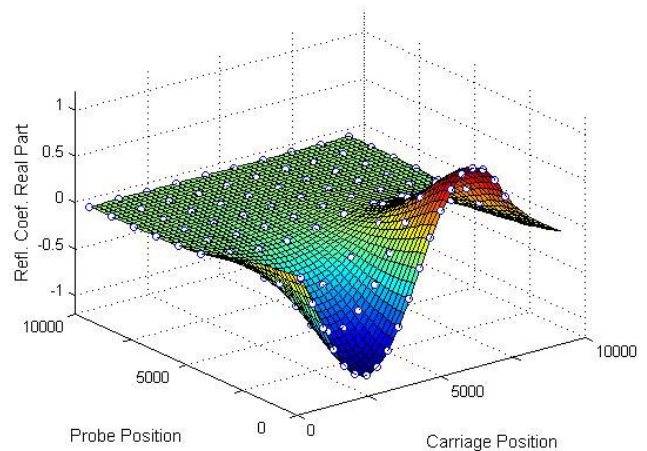


Figure 3 – Surface model of the real part of the reflection coefficient generated from measured training data (shown here as white circle points).

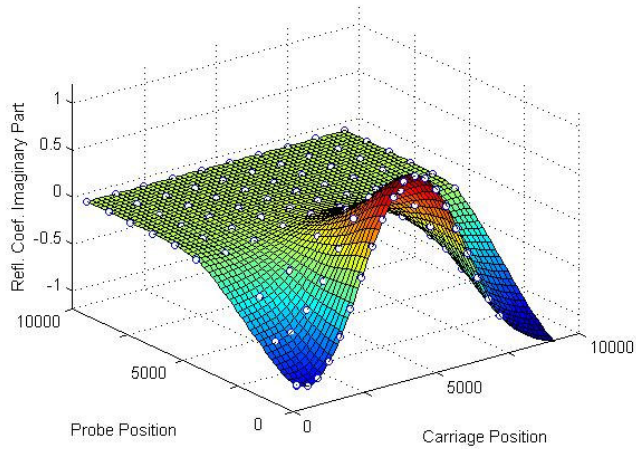


Figure 4 – Surface model of the imaginary part of the reflection coefficient generated from measured training data (shown here as white circle points).

#### IV. RESULTS

In order to test the TPS algorithm, training data sets of varying sizes were collated at 900 MHz using a Maury MT981B tuner from which the TPS surfaces could be generated. Simultaneously, a validation data set was also measured which included 300 points uniformly spaced around the Smith chart that were not used in any of the training data. The measured S-parameters at the validation points were then compared to the results predicted from TPS surfaces built with different training data sets. Figures 5 and 6 show the error results of all 300 predicted points calculated using an optimized training data set. It can be seen that the error delta is lower than -40 dB at all points.

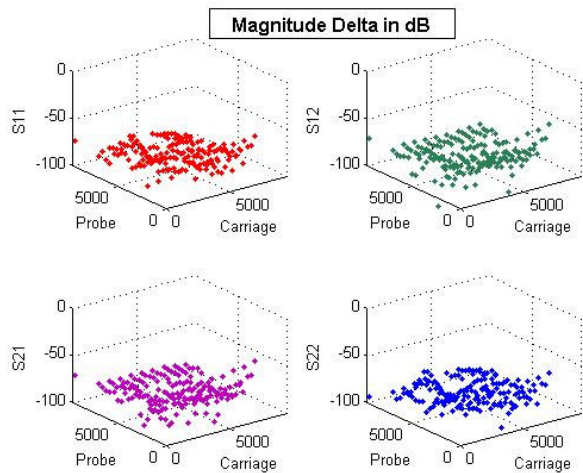


Figure 5 – Magnitude error delta in dB for all four S-parameters as a function of tuner position (probe height and carriage position).

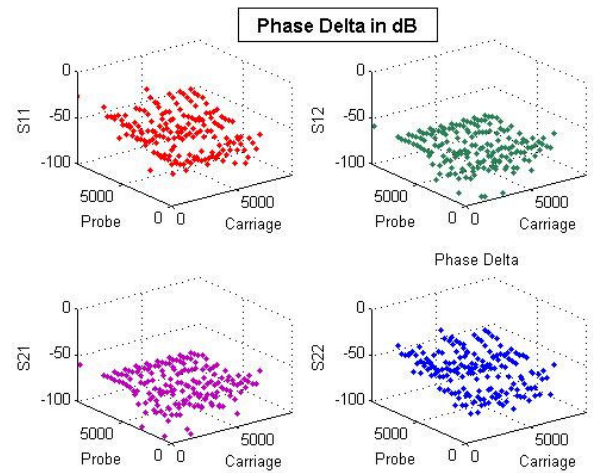


Figure 6 – Phase error delta in dB for all four S-parameters as a function of tuner position (probe height and carriage position).

To further validate the technique, a Maury high gamma tuner model MT981HU was used to generate a 727 point training data file at 2.3 GHz. This file was then used to estimate S-parameters for over 3000 new tuner positions. Each new tuner position was re-measured using a VNA and the raw S-parameters were compared to the estimated values at all 3000 points. It was shown that the error delta was again below -40 dB for every point. The results from this validation are shown in Figures 7 and 8 for reflection coefficient magnitude and phase respectively.

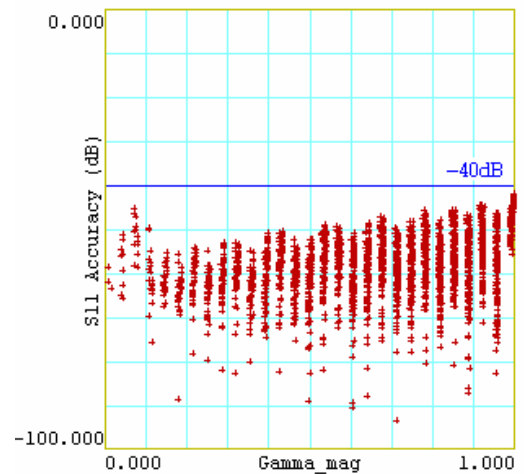


Figure 7 – Delta error in dB between estimated and VNA measured reflection coefficient magnitude for 3000 positions.

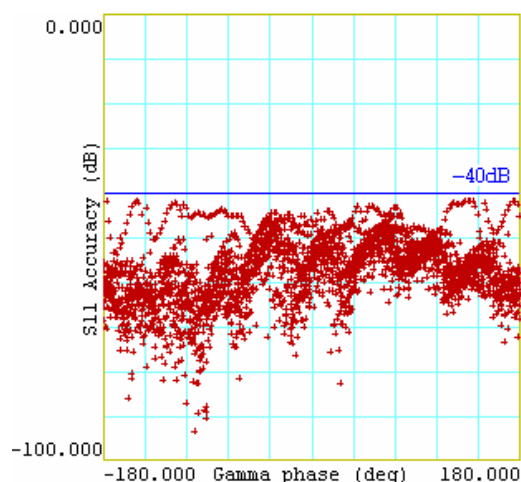


Figure 8 – Delta error in dB between estimated and VNA measured reflection coefficient phase for 3000 positions.

## V. OPTIMIZING INTERPOLATION EFFICIENCY

It was found that the distribution of the training data over various regions of reflection coefficient had a strong impact on the efficiency of the interpolation. Essentially, by manipulating the coverage of the training data set it was possible to reduce the number of points required to achieve the targeted level of accuracy.

Table 1 shows a number of training data set sizes and their accuracy for estimating the 900MHz MT981B validation data described in section IV above, averaged over all 300 points of that validation data set. Training sets (a) and (b) were measured with an even distribution of points across the Smith chart, and fail to meet the specified -40dB of accuracy. Training sets (c) and (d) use non-uniform distributions of training data over the Smith chart and show significant improvement in estimation accuracy, especially with regards to phase.

Label	No. of training points used	Averaged $\Gamma$ magnitude error (dB)	Averaged $\Gamma$ phase error (dB)
(a)	91	-27.99	-4.485
(b)	325	-37.91	-8.107
(c)	206	-46.38	-40.91
(d)	694	-63.96	-42.39

Table 1 – Averaged  $\Gamma$  error in dB for different sized training data sets.

## VI. IMPACT ON MEASUREMENT THROUGHPUT

By reducing the number of measurements required during the characterization stage, substantial time savings can be achieved. This is of great importance in a busy test facility where equipment and engineer time are a costly resource.

Table 2 presents a conservative estimate of the time savings for preparing a single tuner at a single frequency.

	Standard characterization	TPS enhanced characterization
No. of measured points	3000	<800
Approx. duration (~5s per measurement)	5 hrs 49 mins	1 hr 9 mins
No. of available characterization points	3000	>3000

Table 2 – Approximate impact on single frequency characterization times.

Given that a typical load-pull system will have both a load and source tuner and measurements will usually be run at three frequencies (low-band, mid-band and upper-band) the time saving impact is significant. Additionally, it is now possible to achieve extremely dense characterizations containing tens of thousands of characterized tuner points without concern over calibration drift across the measurement duration.

## VII. CONCLUSION

It has been shown that a surface modeling technique can be used to estimate S-parameters at unmeasured tuner positions with accuracy greater than the physical repeatability of the tuners. Validation measurements have been presented showing that many thousands of accurate tuner positions can be characterized by measuring only a few hundred points. Considered distribution of training data enhances the efficiency of the technique. Applying the method in a busy test environment results in drastically streamlined tuner characterization times, allowing for increased load-pull measurement throughput.

## ACKNOWLEDGEMENTS

Thanks to Dr. Aaen, Paul Hart and Dr. Wood, of Freescale Semiconductor for their discussions and advice. The authors also wish to acknowledge the assistance of Maury Microwave Corporation, and in particular Richard Wallace, for their support with tuner automation.

## REFERENCES

- [1] J.M. Cusack, S.M. Perlow, B.S. Perlman "Automatic Load Contour Mapping for Microwave Power Transistors" in *IEEE MTT Microwave Symposium Digest, June 1974*, Vol. 74, Issue 1, pp. 269-271.
- [2] J. Sevic, "Introduction to Tuner-Based Measurement and Characterization," *Maury Microwave Corporation, Application Note 5C-054, 31st August 2004*.
- [3] G.P. Bava, U. Pisani, V. Pozzolo, "Active Load Technique for Load-Pull Characterisation at Microwave Frequencies," in *Electronic Letters 18<sup>th</sup> February 1982*, Vol. 18, No. 4, pp. 178-180.

- [4] Y. Takayama, "A new load-pull characterization method for microwave power transistors," in *IEEE 1976 International Microwave Symposium*, pp. 218-220.
- [5] V. Teppati & A. Ferrero, "A new class of nonuniform, broadband, nonsymmetrical rectangular coaxial-to-microstrip directional couplers for high power applications," in *IEEE Microwave and Wireless Components Letters*, Vol. 13, Issue 4, April 2003 pp.152 – 154.
- [6] "Application Note 15" *Focus Microwaves*, Quebec, Canada. January 1995.
- [7] "MT981HU Tuner Operating Manual" *Maury Microwave Corporation, Ontario, USA. 2007.*
- [8] Neil Gershenfeld, "The Nature of Mathematical Modeling," published by Cambridge University Press, 1999.
- [9] P. Hart, J. Wood, B. Noori and P. Aaen, "Improving Loadpull Measurement Time by Intelligent Measurement Interpolation and Surface Modeling Techniques," *Proceedings of the 67<sup>th</sup> ARFTG Conference, 2006.*
- [10] Mathworks Inc., Matlab™ Spline Toolbox 3.3 (2006a) User Manual.

# Inexpensive Solution to Double RF Bandwidth of Vector Signal Generator

D. Schreurs, J. Alonso Romero, J. Martínez San Román, M. Homayouni, G. Avolio, and B. Nauwelaers

K.U.LEUVEN, Div. ESAT-TELEMIC, Belgium

## Abstract

There is a clear tendency to develop upcoming telecommunication applications at increasing RF carrier frequencies. To enable realistic characterizations of RF building blocks, the use of a vector signal generator, enabling modulated excitations, is indispensable. This paper presents an inexpensive way to extend the RF bandwidth of a commercial vector signal generator. The developed set-up consists of a frequency doubler, one or more amplifiers, and the necessary filters. As it is important to control the excitation applied to the circuit-under-test, a predistortion algorithm has been developed. It is shown that the main difficulty is the suppression of unwanted intermodulation products generated by the frequency doubler. The successful implementation is illustrated by the amplitude and phase controllable generation of two-tone signals.

## I. Introduction

Due to the saturation of the frequency band below 5 GHz by various high-volume consumer applications (cell phone, WiFi, Bluetooth,...), the development of novel applications is happening at increasing RF frequencies (60 GHz and beyond). The major drive is not only congestion, but also the important fact that higher carrier frequencies allow wider IF bandwidths, enabling higher data rates. To test RF building blocks for such applications, it has become clear that measurements under single-tone CW excitations are much too limitative. RF building blocks should be tested under modulated excitation conditions, which require a vector signal generator. Whereas single-tone CW sources (possibly including an external RF mixer) are available up to the frequencies of interest in an early R&D stage, commercial vector signal generators are typically limited to RF carrier frequencies that are in the core attention of present telecommunication applications and therefore do not cover frequency bands that are still in R&D stage. By the time they hit the market, it may no longer be justified for R&D groups to re-invest in such expensive equipment. The objective of this work is to expand the RF bandwidth of a vector signal generator in an inexpensive way. The solution consists of a hardware set-up using off-the-shelf and in-house designed circuits to upconvert the signals (Section II), combined with a correction algorithm to compensate for the linear and non-linear effects introduced by the hardware set-up (Section III). Experimental results on magnitude and phase controllable two-tone excitations are presented in Section IV.

## II. Hardware set-up

The objective of this work is to double the RF bandwidth of a 6 GHz vector signal generator. Even though commercial solutions beyond this doubled RF bandwidth are already available on the market, it constitutes significant re-investment for small R&D groups. Secondly, this study has to be seen as a first step towards vector signal generation at 60 GHz and beyond, which is not yet readily available on the market.

The hardware set-up is schematically depicted in Fig. 1. It consists of the vector signal generator, a frequency doubler, a bandpass filter to suppress the fundamental and the spectral components beyond the second harmonic at the output of the doubler, an amplifier to boost up the power of the generated signal,

and a second bandpass filter to suppress the higher order harmonics generated by the amplifier. Depending on the requirements for the overall output power as well as for the input power level of the frequency doubler, multiple amplifiers may have to be used. Also, depending on the target RF bandwidth, higher order multipliers (e.g., tripler) or a cascade of frequency doublers may be necessary. In addition, small circuitry (not shown here), such as isolators, are part of the set-up. The frequency doubler and amplifier are off-the-shelf components, whereas the filters are designed and fabricated in-house. To meet the specifications in terms of fundamental/harmonic suppression and taking into account fabrication tolerances, the coupled-line filter approach was adopted and Chebyshev filters of 9<sup>th</sup> order were designed and fabricated.

The use of a frequency doubler within this set-up should be clarified as it is more limitative as compared to using a mixer instead. As will be shown in the next section, to be able to control the amplitude and phase of the generated signals, it is necessary to characterise the non-idealities and especially the non-linearities of the frequency-shifting circuit in both amplitude and phase. As the commercial instrument that enables this characterisation is a two-port set-up only, having to characterise a mixer would render the procedure unnecessary difficult and cumbersome, mainly because the phase of the LO signal should be characterised simultaneously with the phases of the RF and IF signals.

It is clear that the circuits within this hardware set-up distort the signal as generated by the vector signal generator. To control the signal at the input of the device-under-test, which corresponds to the output of the second bandpass filter, predistortion is required. In the next section, we present the algorithm to achieve this.

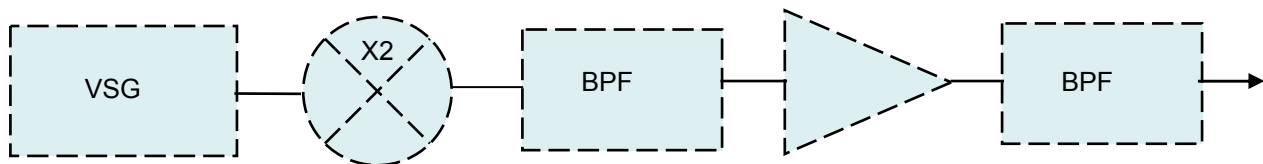


Fig. 1: Schematic of hardware set-up.

### III. Predistortion algorithm

As outlined above, the aim of this algorithm is to predistort the signal being generated by the vector signal generator in order to obtain a pre-defined signal at the input of the circuit-under-test. To this purpose, we first investigated each of the building blocks separately before testing the whole chain. As filters are linear circuits, it is straightforward to determine the required amplitude and phase correction from S-parameter measurements, and therefore this will not be detailed any further. On the other hand, the amplifier and frequency doubler are non-linear circuits, which require specific attention.

#### II.A. Amplifier predistortion

In selecting the amplifier, proper care was taken with respect to the specifications. An amplifier with a good balance between output power, P1dB and IP3 was chosen, such that the amplifier can be operated in its linear operation condition, which simplifies the predistortion. By performing two tone measurements with varying frequency spacings, it was determined also that the considered amplifier does not exhibit long-term memory effects. As a result, the procedure for predistortion reduces to characterizing the AM/AM and AM/PM characteristics of the amplifier using single-tone measurements. Next, it turned out that polynomials are sufficient to represent both the AM/AM and AM/PM characteristics. By inverting

these polynomials, the phase and amplitude of the signals to be generated by the vector signal generator can be calculated. This information can be used not only for single-tone excitations, but also to design multi-tone excitations. As the amplifier is operated in its linear mode, no intermodulation products are being generated and therefore each tone can be treated independently.

Experimental results of two-tone and four-tone excitations are shown in Tables 1 and 2, respectively. The tables compare the realized excitation (at the output of the amplifier) with the target excitation. Excellent agreement has been obtained. The data was collected by a large-signal network analyzer (LSNA), and therefore it is important to note that phase detrending [1] has to be applied to the measured values in order to have the same time reference as the target excitation. The results in these tables correspond to a fundamental frequency of 2 GHz and a frequency spacing of 50 kHz. Similar results have been obtained at other fundamental frequencies. The instrument used to characterize the AM/AM and AM/PM of the amplifier-under-test was the LSNA as well. As will be shown in next subsection, single-tone results are not sufficient to determine the required predistortion in case of the frequency doubler.

	Target	Measured
Tone 1	-4.0 dBm $\angle 90^\circ$	-4.1 dBm $\angle 89.7^\circ$
Tone 2	-4.0 dBm $\angle 90^\circ$	-4.1 dBm $\angle 89.7^\circ$
Tone 1	-5.0 dBm $\angle 45^\circ$	-5.1 dBm $\angle 44.7^\circ$
Tone 2	-2.0 dBm $\angle 135^\circ$	-2.0 dBm $\angle 134.8^\circ$

Table 1: Two-tone results with equal amplitude and phase (upper two rows), and unequal amplitude and phase (lower two rows) at output of power amplifier.

	Target	Measured
Tone 1	-7.0 dBm $\angle 0^\circ$	-7.0 dBm $\angle -0.3^\circ$
Tone 2	-8.0 dBm $\angle 45^\circ$	-8.1 dBm $\angle 44.7^\circ$
Tone 3	-9.0 dBm $\angle 90^\circ$	-9.1 dBm $\angle 89.7^\circ$
Tone 4	-10.0 dBm $\angle 135^\circ$	-10.1 dBm $\angle 134.8^\circ$

Table 2: Four-tone results with unequal amplitude and phase at output of power amplifier.

### II.B. Frequency doubler predistortion

Whereas predistortion of amplifiers, and especially memory-less amplifiers, has already been extensively studied [2], little information about predistortion of frequency doublers is available in literature, and in particular under conditions of multi-tone excitations [3]. The particular problem in case of the frequency doubler is illustrated by Fig. 2. When applying a two-tone signal, the spectrum shows a dominant intermodulation product at  $f_1+f_2$ . It can be easily verified that the amplitude of this spectral component is 6 dB higher than the responses at the second harmonic frequencies of  $f_1$  and  $f_2$ , in the case when the excitation at the input of the frequency doubler consists of two tones with equal amplitude and phase. As it is virtually impossible to filter out this unwanted spectral component, an alternative solution has to be found in order to generate a two-tone excitation with predetermined amplitude and phase at the end of the chain of Fig. 1.

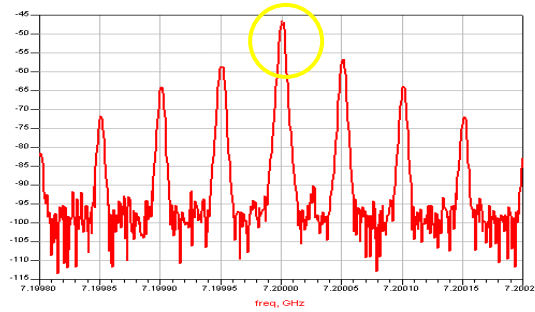


Fig. 2: Spectrum (in dBm) around the second harmonic frequency at the doubler output. The fundamental input frequency is 3.6 GHz. The excitation at the doubler input is a two-tone with 50 kHz spacing.

The first considered solution is to apply a three-tone excitation at the input of the doubler, by which the middle frequency component, at  $(f_1+f_2)/2$ , is designed to generate an output signal at  $f_1+f_2$  that has the same amplitude but opposite phase than that of the signal to be suppressed. As the signal to be suppressed has a 6 dB larger amplitude than the wanted signals, this auxiliary signal would need to have a considerable amplitude as well, resulting in the creation of new unwanted intermodulation products.

The alternative solution is to consider the spectral components at  $(f_1+f_2)/2$  and  $f_2$  as the intended excitation and to consider the spectral component at  $f_1$  as the auxiliary signal that should serve to suppress the intermodulation product at  $2f_1$ . In this way, an adequate solution is obtained, because the required power level of the auxiliary signal is less than in the case above, resulting in a lower level of generated intermodulation products. Table 3 presents the results for two cases. Next to the measured and target values of the two generated tones at the output of the doubler, also the characteristics of the corresponding three-tone excitation as generated by the vector signal generator are indicated. It can be observed that both the amplitude and phase of the two wanted spectral components can be controlled very well. The suppression of the unwanted spectral components is in the order of 25 dB or higher, which is sufficiently adequate. Depending on the application, higher suppression may be obtained by injecting multiple auxiliary frequency components, but a good balance between complexity, obtained accuracy, and cost of the set-up should be kept in mind. When the extended vector signal generator is combined with an LSNA, the actual spectrum being applied to the circuit-under-test can be monitored.

As the information on dominant intermodulation products is essential to determine the required predistortion, it is clear that a single-tone characterisation of the frequency doubler is not sufficient to design multi-tone excitations, as it was the case for amplifiers.

	Target	Measured	Generated at input
$f_1+f_2$	-6.0 dBm $\angle 90^\circ$	-5.9 dBm $\angle 89.9^\circ$	@ $f_1$ : -4.6 dBm $\angle 56.2^\circ$ @ $f_c$ : 7.4 dBm $\angle 144.6^\circ$
$2f_2$	-6.0 dBm $\angle 0^\circ$	-6.0 dBm $\angle 0.1^\circ$	@ $f_2$ : 13.4 dBm $\angle 52.9^\circ$
$f_1+f_2$	-8.0 dBm $\angle 0^\circ$	-8.0 dBm $\angle -0.1^\circ$	@ $f_1$ : -9.0 dBm $\angle 120.4^\circ$ @ $f_c$ : 5.0 dBm $\angle 56.2^\circ$
$2f_2$	-6.0 dBm $\angle 0^\circ$	-6.0 dBm $\angle 0.0^\circ$	@ $f_2$ : 13.0 dBm $\angle 52.8^\circ$

Table 3: Two-tone results with equal amplitude and unequal phase (upper two rows), and with unequal amplitude and equal phase (lower two rows) at the output of the frequency doubler. The fundamental frequency  $f_c$  is 4.2 GHz and the frequency spacing is 50 kHz.

## IV. Overall results

Finally, the complete subsystem as shown in Fig. 1 has been tested. The results for two cases are presented in Table 4. It can be deduced that the proposed solution performs very well under different conditions. It can also be noted that the correction algorithm has to be dependent on the fundamental frequency. Both the characteristics of amplifier and doubler are frequency dependent, but also the ripple in the filter characteristics should not be overlooked. Overall, it can be concluded that the combination of the developed set-up and the supporting predistortion software results in a well controllable two-tone excitation at frequencies beyond the RF bandwidth of the vector signal generator.

Target		Measured	Generated at input	
7.2 GHz	-8.0 dBm $\angle 0^\circ$	8.0 dBm $\angle -0.1^\circ$	3.6 GHz	@ $f_1$ : -13.2 dBm $\angle 138.8^\circ$
	-8.0 dBm $\angle 30^\circ$	8.0 dBm $\angle 29.7^\circ$		@ $f_c$ : 4.8 dBm $\angle -11.1^\circ$
8.4 GHz	17.0 dBm $\angle 100^\circ$	17.3 dBm $\angle 100.0^\circ$	4.2 GHz	@ $f_1$ : -14.1 dBm $\angle -318.0^\circ$
	21.0 dBm $\angle 200^\circ$	21.1 dBm $\angle 199.0^\circ$		@ $f_c$ : 1.9 dBm $\angle -40.3^\circ$
				@ $f_2$ : 11.9 dBm $\angle 57.8^\circ$

Table 4: Two-tone results with equal amplitude and unequal phase (top row), and with unequal amplitude and unequal phase (bottom row) at the output of the developed subsystem.

## V. Conclusions

This paper presented an inexpensive solution to extend the RF frequency range of a commercial vector signal generator. The hardware consists of a doubler, one or more amplifiers, and the necessary filters. To control the excitation generated at the end of this chain, a predistortion algorithm has been developed. Whereas this is straightforward for filters and already well understood for amplifiers, the difficulty was linearizing the doubler under two-tone excitation conditions. An adequate solution in the format of a well designed three-tone excitation was proposed and successfully demonstrated. This set-up enables now to characterise figures of merit like IP3 at carrier frequencies that are up to the double of the RF bandwidth of the vector signal generator. In this way, a framework has been conceived that can lead in future work to extending the hardware and software to even higher RF frequencies and to richer multi-tone excitations.

## References

- [1] K.A Remley, D.F. Williams, D. Schreurs, G. Loglio, and A. Cidronali, "Phase Detrending for Measured Multisine Signals," Automatic RF Techniques Group Conference, pp. 73-83, June 2003.
- [2] "RF Power Amplifier Behavioral Modeling," editors D. Schreurs, M. O'Droma, A. Goacher, and M. Gadringer, Cambridge University Press, 2009.
- [3] Y. Park and J.S. Kenney, "Adaptive digital predistortion linearization of frequency multipliers," IEEE Trans. Microwave Theory and Techniques," vol. 51, no. 12, pp. 2516- 2522, Dec. 2003.

# Real-Time Spectrum Analysis Reveals Time Domain Characteristics of Frequency Domain Signals

Thomas C. Hill  
Tektronix, Inc.  
P.O. Box 500, M/S 50-317  
Beaverton, OR, 97006, USA  
Tom.C.Hill@tektronix.com,

**Abstract**—Many modern RF signals exhibit rapid time-variations, or transient interference. The Real-Time Spectrum Analyzer was developed to discover, trigger on, capture, and analyze such signals. This paper will discuss the differences between traditional and real-time spectrum analysis. The theory behind analysis without gaps will be presented and the types of signals revealed by an RTSA will be shown.

**Keywords**—microwave; RTSA; RF; spectrum analysis; time-correlated.

## I. INTRODUCTION

Spectrum Analyzer technology and design has changed as techniques for RF transmission have changed, and as advancements in measurement technology have become available.

The earliest form was a manually tuned filter and detector combination which simply indicated the signal level at the frequency to which it was tuned. A wave meter is the simplest example of this.

The introduction of electrically tuned signal conversion circuitry created the swept-tuned spectrum analyzer. This provided viewing of a CRT display of the amplitude of all incoming signals spaced horizontally by their respective frequencies.

Digital signal conversion technology along with Digital Signal Processing (DSP) allowed the capture of a much wider band of spectrum which might contain a signal and all of its sidebands, or even multiple signals. Analysis is performed after the signals are captured.

As time variations were added to the more traditional modulation forms, the Real-Time Spectrum Analyzer (RTSA) was developed to show these time-variations and separate multiple time-varying signals overlapping in frequency.

## II. PREVIOUS TECHNOLOGY

### A. The Swept Spectrum Analyzer

Swept frequency analysis inherently can only detect the total power contained within the bandwidth of the detector, as

this detector is effectively swept across a wide frequency band of interest. Fig. 1 is the block diagram of a typical swept spectrum analyzer.

RF activity which might occur in a portion of the band being swept, but not at the frequency the detector is tuned to at the time of the occurrence, will be lost. Therefore, as the detector sweeps, such an analyzer may provide a very low probability of intercept for transient signals of duration less than the entire recurrent sweep time. This makes the frequency-swept analyzer best suited for signals which remain stable for one or more complete sweep cycles.

While most swept analyzers do have the capability to stop the sweeping of the RF conversion oscillator and simply look at one frequency continuously versus time (zero-span mode), this requires knowing the exact frequency in advance. Zero-span can only display amplitude versus time and can not separate multiple signals as in a spectrum plot.

### B. The Vector Signal Analyzer (VSA)

There have been two revolutionary changes in the history of spectrum analyzer architectures. The first was the change from "Swept Spectrum Analysis" to "Vector Signal Analysis". This change moved from the technique of sweeping a narrow-band IF detector across stationary signals to digitizing an entire wideband IF and storing it for later processing.

A Vector Signal Analyzer has a similar RF conversion front end to the swept analyzer, but the IF section has a wide-band filter and Analog-to-Digital converter. Fig. 2 is the block diagram of a typical VSA. The A/D converter digitizes the entire wideband IF of interest and stores the resultant data into a memory. Then a discrete Fourier transform (DFT) process can be applied to the data in memory to analyze the time-variations of the RF signals which may have been captured.

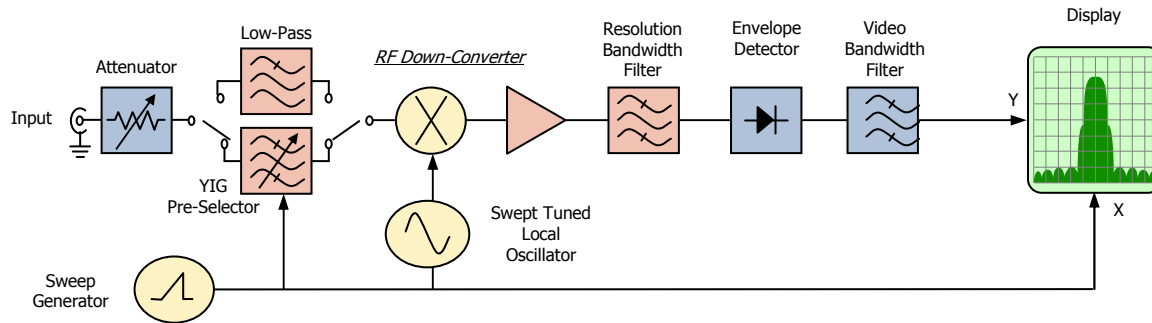


Figure 1. Block diagram of a swept spectrum analyzer.

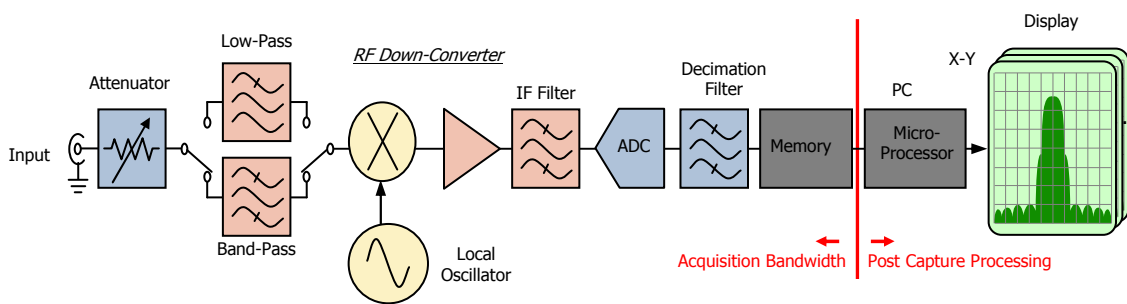


Figure 2. Block diagram of a Vector Signal Analyzer.

In a VSA, the DFT analysis is performed after the data are stored in memory. The frequency spectrum plots available from the DFT are presented to the operator only as fast as the display can update, and then another FFT is initiated. This process eliminates the dead time found in the swept analyzer during the sweep, but is still not continuous. Screen updates still have the processing and display time gaps between spectrum updates where significant input signal activity will be missed.

The digitized data are stored seamlessly in a long memory. After the memory has been filled, the DFT can be used to search the memory to see what has been captured. With this stored data, all frequency events are captured and can be examined.

Fig. 3 is a display of a pulse spectrum produced by a VSA. It is similar to the spectrum display from a swept analyzer. In this case, the resolution bandwidth of the DFT process is wider than the frequency spacing between the fine vertical spectrum lines representing the pulse repetition interval (PRI). Therefore only the  $\text{sin}(x)/x$  envelope of the pulse spectrum is visible, not the dense spectral lines of the PRI.

The pulse is present for only part of the time, and the display will be unstable if the analyzer is not triggered. If the

analyzer is triggered, then it will display only the pulse which caused the trigger.

If, however, triggering is not feasible, then a maximum-hold trace will be needed. In this case the pulse spectrum is the highest amplitude signal at this frequency. If there is a lower amplitude signal present, or a signal varying in time, it can not be resolved. The trace seen in Fig. 3 is a max-hold trace.

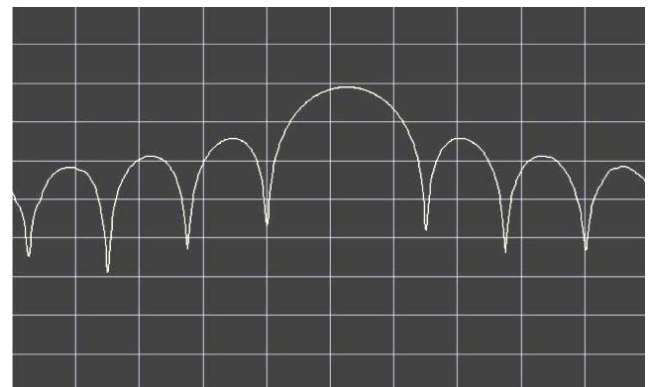


Figure 3. Pulse Spectrum from SA or VSA. No low-level signals visible.

### III. THE REAL-TIME SPECTRUM ANALYZER

Today's RF and Microwave signals often exhibit significant variations in both the frequency and time domains. Some communications formats change modulation methods and bandwidths rapidly to accommodate variable digital bit rates and bandwidth requirements. Some signals may transmit during the time interval between bursts of other transmissions. Measurement techniques that were sufficient for signals that remain stable can not properly characterize rapidly changing signals.

The second major change in the history of signal analysis has been the advent of the Real-Time Spectrum Analyzer. A real-time analyzer must acquire the incoming signal, process it and provide spectrum information without loss of any relevant signal characteristics.

With this fundamental architecture shift, a wideband IF is still digitized, but now the discrete time transform, such as FFT or Chirp-Z (CZT), is performed in a signal processing block that processes the digital data in full real time with no gaps. This is prior to, or concurrent with that data entering the digital memory. Fig. 4 is the block diagram of an RTSA. The real-time processing engine is between the two vertical red lines. The real-time processing engine is a combination of hardware and software optimized to perform the correction, filtering, and DFT processing fast enough to keep up with the digitizer output. This real-time processing block reveals all time-domain changes in the RF signals (frequency-domain) present within the IF bandwidth.

#### A. Probability of Full Intercept (POI)

One reason for the development of the RTSA is the need to increase the probability of fully intercepting wide bandwidth signals exhibiting variations in both frequency and time with no gaps in the observation of the signal. This is not necessarily the same as no gaps in the acquisition of the signal

For purposes of this discussion the definition of 100% full intercept of a short burst of RF has three requirements:

- The resulting spectrum plot must show full amplitude of the signal.
- The amplitude of the signal must not vary if the relative timing of the DFT frames and the signal burst changes.
- The spectrum of 100% of the bursts must have the full amplitude. None are lost.

When signals remain stable for the duration of the complete measurement and observation process, the probability of intercept is 100%. The determination of the probability of intercepting short duration signals or transients starts with an examination of the DFT timing cycle.

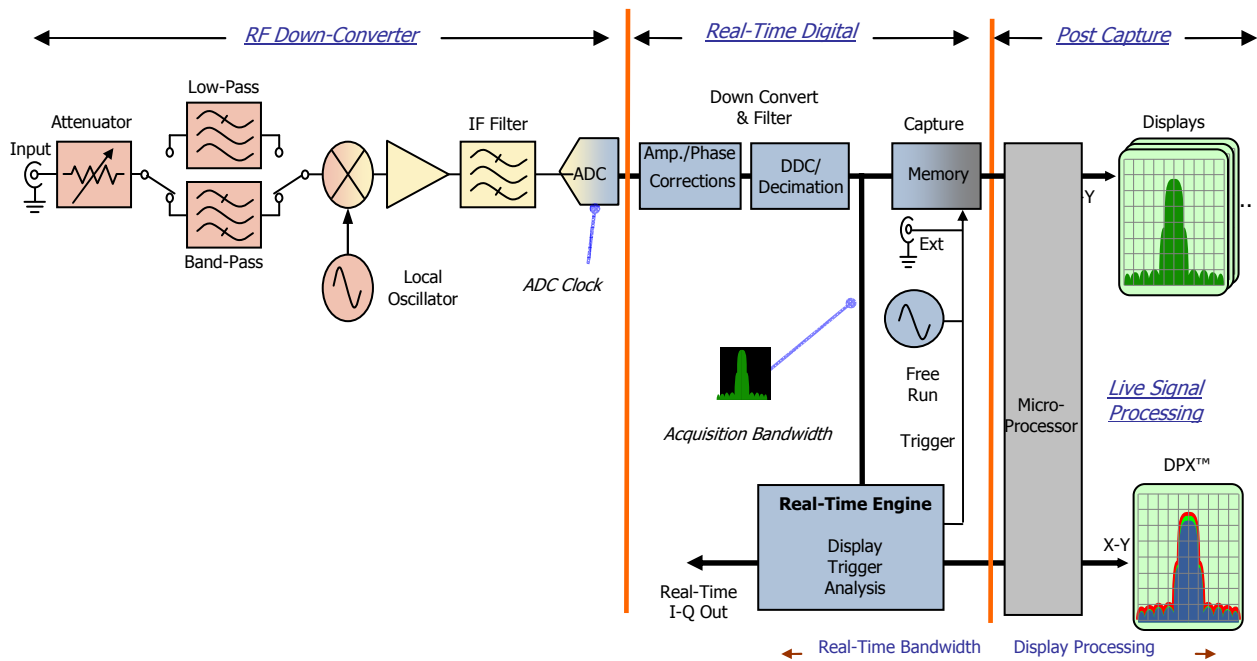


Figure 4. Block diagram of a Real-Time Spectrum Analyzer.

The A/D converter continuously outputs digital samples of the analog input. Once one frame of contiguous samples has been passed to the DFT, the transform process can start. If the display can accept only one spectrum before waiting until the next display cycle, then the minimum signal duration for 100% probability of capture is the same as the display update rate.

If the display update rate is not the limiting factor, then the minimum signal duration for 100% probability of full capture is equal to the time from the start of one DFT frame acquisition until the end of the subsequent one. This assumes that the DFT acquisitions are made periodically.

Fig. 5 illustrates this concept for the case where there is a gap between successive DFT frame acquisitions. For the DFT to produce a spectrum which represents the signal in question at full amplitude, then for full capture the signal or disturbance must exist for at least one entire DFT frame. If the DFT frames and the incoming burst of signal are asynchronous, then the minimum time required is defined when the start of one DFT frame happens to occur one sample prior to the beginning of the signal. In this case, the signal technically can not fill the first frame, and must continue to the last sample of the next frame. The minimum time is therefore more correctly stated as "one sample less than the time from the start of one DFT frame until the end of the subsequent one". An approximation can neglect the subtraction of the one sample and re-stated as "two times the DFT frame length plus the time of the gap between frames".

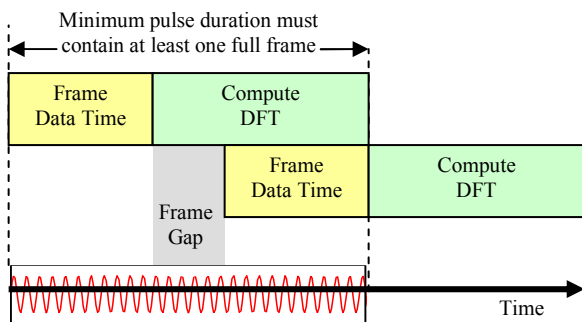


Figure 5. *FFT with gaps between the frames.*

To reduce the required duration of the signal for 100% probability of capture, the DFT frames must be overlapped in time. When overlapped, the DFT processing must either complete before the start of processing of the next DFT, or parallel processing must be utilized. The case of overlapping DFT frames is illustrated in Fig. 6.

Because the incoming signal is still asynchronous to the DFT frame acquisition, the same calculation of signal duration holds. With the frames overlapped, the end result is now two times the DFT frame length minus the time of the overlap of subsequent frames. If the frames overlap by 50%, the minimum signal duration for 100% POI is 1.5 times the DFT frame length.

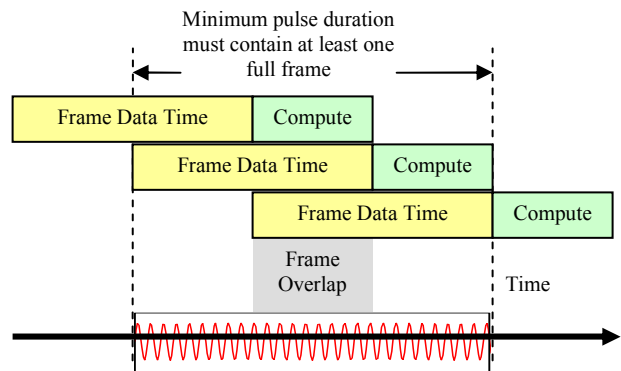


Figure 6. *FFT with Frames Overlapping.*

An example of a practical application for triggering an RTSA with 110 MHz bandwidth:

- Decimated sample rate of 150 MHz, = 6.67 ns per sample.
- Triggering uses FFT frame = 1024 points = 6.83  $\mu$ s.
- 50% overlap is 1.5 frames = 10.24  $\mu$ s minimum burst length.

Another application for the histogram display of an RTSA with 110 MHz bandwidth:

- Histogram CZT = 523 points = 3.49  $\mu$ s.
- CZT process time of 20.48  $\mu$ s forces gaps.
- 3.49  $\mu$ s + 20.48  $\mu$ s = 23.97  $\mu$ s min. burst length.

### B. Spectrum Processing Without Gaps

The difference between 100% probability of full capture and 100% probability of seeing a transient even at reduced amplitude is significant. Processing without any effective gaps allows 100% probability of including transient signals or disturbances in the analysis. If the capture and processing of incoming signals has no effective gaps, then any disturbance or signal with duration less than the definition for full intercept (at full amplitude) can still be captured and observed, but at reduced amplitude. An effective gap results when some portion of the input samples do not contribute to the analysis output.

#### 1) Time Windowing of the DFT samples

The DFT mathematics assumes an infinite input that periodically repeats the set of input samples (frame) that was input to the DFT. This causes a discontinuity where the assumed start of the set of following samples adjoins the end of the input frame. There is a similar discontinuity at the start of the input frame. The solution is to apply a time window function to the frame of samples before processing the DFT.

A commonly used window function is the Kaiser Window. This is represented in Fig. 7. The samples near the ends of the DFT frame are weighted nearly zero. This eliminates the spectral effects which would result from the discontinuities at the frame ends. This also results in an inability to provide spectrum visibility for any input data near either end of the DFT frame.

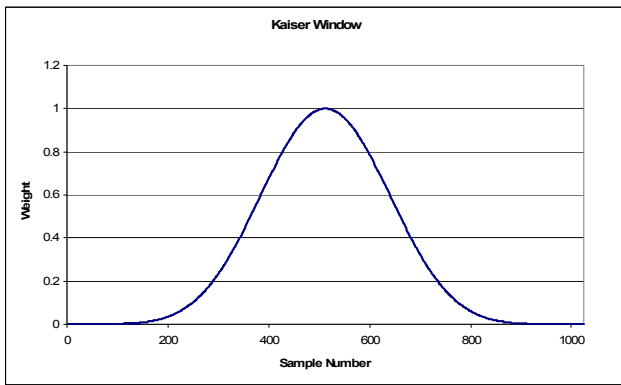


Figure 7. The Kaiser Window function

### 2) Effective Processing Gaps

If the DFT process repeats less often than the time occupied by one frame of input data, then there are inherently gaps in the coverage of the incoming signals.

Such a situation is depicted in Fig. 8. The upper trace is the incoming signal which has an unexpected anomaly, of duration less than one DFT frame, within the left half of the drawing.

The lower traces represent the time-windowed samples delivered to the DFT process. The anomaly of interest happens to fall in the gap between two DFT frames. If the frame repetition rate were less often, the probability of intercepting this signal would be proportionately less.

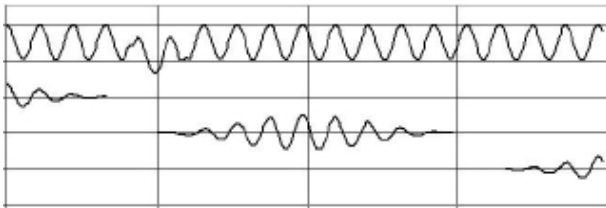


Figure 8. Gaps between FFT Frames misses transient.

If the DFT frames are exactly sequential without gaps, the input data are all part of the analysis, but the end portions of the frames are forced to zero by the window function. There are still portions of the input signal that are in fact not analyzed. These can be termed "effective gaps". In Fig. 9 the anomaly of interest has once again been missed.

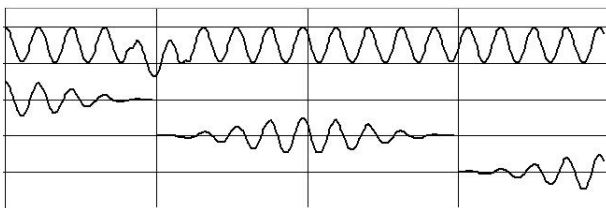


Figure 9. Adjacent FFT Frames still have effective gaps.

To be sure to not miss any of the input signals the DFT frames must be overlapped enough that the window functions do not cause the loss of any of the input data. Fig. 10 depicts the 50% overlap case where none of the input data are lost. This overlap has no gaps and no effective gaps. This guarantees

that the anomaly of interest is not lost. This anomaly will not be displayed at full amplitude, as it has less duration than one DFT frame.

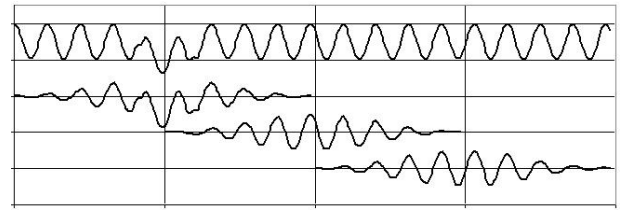


Figure 10. Overlapped FFT Frames captures transient.

### C. Continuously Updated Spectrum Histogram Display

The first result of spectrum processing without gaps is a spectrum display that reveals all spectral variations within the capture bandwidth. The limit of time resolution is approximately the length of the FFT frame. If the FFT frames are significantly overlapped, then shorter signal transients can be revealed, but even if this is done, the time resolution is not made shorter than one frame time, due to any single event now being shared between multiple overlapped frames.

The real-time processing of the spectrum data provides spectrum updates which can surpass 48,000 per second. This greatly exceeds the rate at which current technology can update the display. This requires a display compression method which will provide visibility of a single event within the 48,000 while compressing to a rate compatible with the display. This compression is done as a bitmap display with each pixel accumulating histogram data as the spectra are generated.

#### 1) The histogram:

A bitmap histogram can satisfy these requirements. Each frequency spectrum from the DFT process is converted to a bitmap as if it were to be displayed. It is entered into a display pixel buffer memory. As the DFT outputs more spectra, each is added to the pixel buffer. When the display itself is ready to update, each pixel in the buffer contains a number representing the accumulated number of times that a spectrum plot "hit" in that pixel location.

Each pixel can have a number from zero to the limit of the number of spectra output from the DFT during the time between display updates. These pixels are converted to either gray-scale or color information for the bitmap in the display itself, and the pixel buffer is cleared. This process continues without gaps for all spectra output from the DFT process. Fig. 11 illustrates the process of building the histogram display. This basic histogram erases all spectrum information and re-starts at each display update.

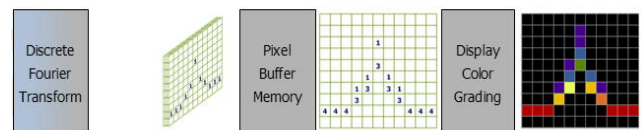


Figure 11. The Display Histogram process

## 2) Pixel decay

For a single event to provide visibility lasting longer than a single display update period (usually in the range of 10 to 100 updates per second) a pixel decay mechanism is added. This can emulate the decay effect found in the phosphor used in a CRT display.

Decay of older spectra is accomplished by retaining a percentage of past pixel data as new data are added. The pixel buffer contents are multiplied by a factor less than one instead of being cleared. As new pixel information is added into the buffer, the percentage contribution from older spectra is reduced each display update cycle. Each pixel is limited to the same maximum value as with no decay.

For infinite display persistence, the buffer is not cleared, the multiplication factor is set to one, and the buffer will accumulate without any reduction in past spectrum information. Each pixel accumulates "hits" until the individual pixel truncation limit is reached.

## D. Spectrum Without Gaps Reveals Time Behavior

The radar pulse spectrum shown in Fig. 12 is the same as seen before in the VSA display of Fig. 3. With the VSA, only the envelope could be seen if the analyzer is triggered to view the pulse, or if the analyzer is set to "max hold" display.

Using overlapped DFT processes and the histogram-derived display, the spectrum can now be seen to contain much more than the intended radar pulse. There is also a lower amplitude frequency-stepped signal interfering with the radar.

The red in the display represents the portions of the spectrum that are nearly continuous due to high "hit" numbers. The noise floor is almost continuous when a pulse has a duty cycle of about 10% as this one does. The dark blue represents the portions of the histogram with few "hits", and the spectral lines due to the pulse repetition interval (PRI) fill this part.

The interfering signal is very infrequent, but does increase the number of hits in the histogram of the spectrum where this signal lands. The blue is brighter in these locations as the histogram has larger numbers there.

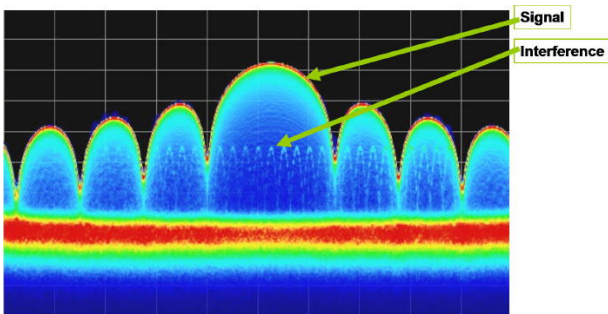


Figure 12. With real-time FFT and display histogram, swept signal is visible.

Fig. 13 is an RTSA histogram display with multiple WLAN signals and a Bluetooth headset. The higher amplitude WLAN signal is blue, signifying that it is relatively infrequent. This is a nearby laptop. The lower amplitude red signal on the same

frequency, is the access point which is further away (and consequently a weaker signal), but transmits nearly constantly.

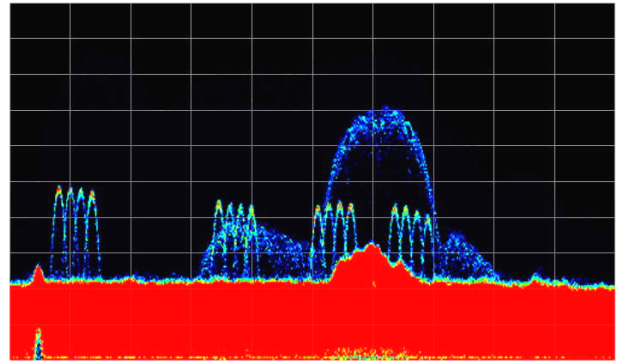


Figure 13. Display histogram shows multiple WLAN and a Bluetooth..

The four groups of four carriers each are from a Bluetooth headset which transmits on these same frequencies. When multiple signals rapidly time-share the same frequency, a spectrum analyzer that represents only the strongest signal does not provide visibility of the time nature of these signals. The histogram real-time display reveals the density of signals over time and which are occupying each portion of the spectrum.

## E. Trigger in the Frequency Domain

Another capability provided by real-time FFT processing is the triggering of measurement processes based on events in the frequency domain as well as time domain. Prior to the development of real-time processing, a trigger could be generated only if the detected power changed. If the FFT is processed at least as fast as the incoming data from the A/D converter, then the output of the sequential FFTs can be compared to a frequency "mask" representing the particular signal of interest. Then when the FFT output matches the mask, a trigger is generated immediately

Overlapping the FFTs removes the same effective gaps that result from the spectrum windowing as was the case for the histogram display.

The frequency mask can be drawn as another trace on the spectrum display. The internal numerical representation of this mask is compared to each of the DFT results as they are generated from the incoming signal data. If any X location of the DFT has a Y-value which exceeds the Y-value of the corresponding X location of the mask, a trigger is generated.

Fig. 14 has a display representative of the frequency mask. The spectrum has nine RF signals across the spectrum of interest. A mask has been drawn between two of these legitimate signals. Any signal that appears in this mask will generate a trigger even if it is 33 dB below the large signals. As this mask is drawn, the large signals will not generate a trigger even if they increase 3 dB above their current amplitude.

This frequency mask triggers on events at specific frequencies even amongst other, much larger signals.

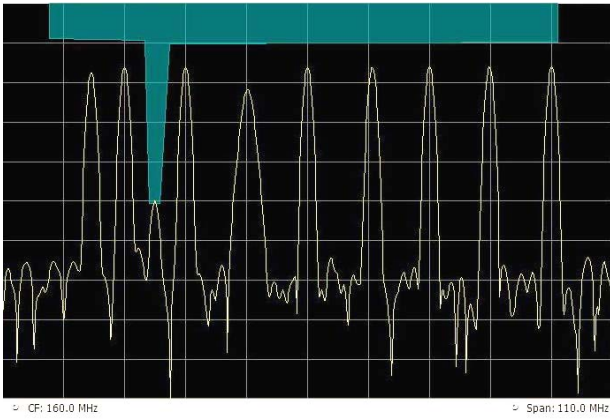


Figure 14. Frequency Mask with low-level transient causing trigger.

#### F. Use of a Frequency Mask Trigger

A spectrogram is a series of spectrum plots put together such that each DFT result is placed in a single display line above the previous one. The x-value of the spectrogram is frequency just as in the spectrum plot. The y-value of the spectrogram is time, each line representing the time between the start of one DFT frame and the next. Each x-value of a spectrum plot is encoded into the spectrogram as intensity or color for the line corresponding to that spectrum plot.

The spectrogram in Fig 15 was triggered by the frequency mask in Fig. 14. The spectrum point of the trigger is circled in Fig. 15. The signal remains in the trigger location for only 400 microseconds.

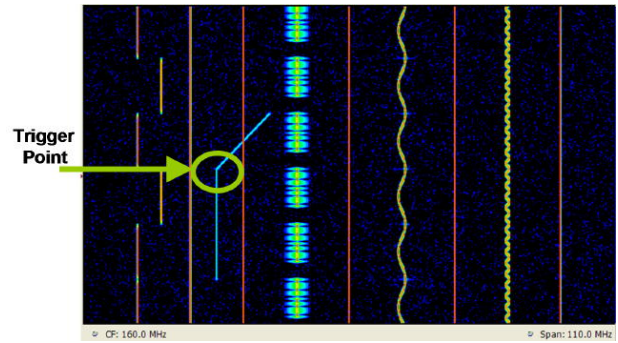


Figure 15. Spectrogram with trigger point marked. Transient recorded.

#### IV. CONCLUSION

Today's RF and Microwave signals often exhibit significant variations simultaneously in the frequency and time domains. Real-Time spectrum processing is required to observe and measure these transient events without losing parts of the observed signals.

#### REFERENCES

- [1] "Fundamentals of Digital Phosphor™ Technology in Real-Time Spectrum Analyzers" Tektronix, Inc. application note.

# Using Spectrum Analyzer to Determine Frequency Modulation Accuracy of a Synthesizer and Its measurement Uncertainty

Yeou Song (Brian) Lee  
Department of Quality  
490 Jarvis Drive  
Morgan Hill, CA 95037  
Tel: 408-201-1976  
E-Mail: [brian-ys.lee@anritsu.com](mailto:brian-ys.lee@anritsu.com)

## Abstract

*The Bessel Null or Carrier Null method is the most accurate way to measure the frequency response of frequency-modulated sources. It is used to control deviation since frequency deviation is independent of the modulating frequency. The actual method of finding a null appears to be accurate and easy. The first null can be observed at the modulation index of 2.4. By numerical solving the Bessel Function and employing the spectrum analyzer, a simplified approach is ideal for accurately determining the frequency deviation. In this paper, we would analyze the results by solving the Bessel functions in determining the accuracy of the frequency deviation and subsequently its measurement uncertainty.*

## Introduction

What is frequency modulation (FM)? It is a method to embed information over a carrier frequency by modulating its frequency. Via modulation and demodulation of signals, any information can be transmitted and received with great fidelity. In today's world, it is important to send digital data by shifting the carrier frequency. FM is a popular specification for any given synthesizer. Modulation analyzer, e.g., 8902, is often used as a tool to determine the FM accuracy. However, 8902 receiver is limited by frequency range (1.3 GHz Max). It often requires adding a mixer to extend its measurement frequency range. Therefore, additional uncertainty will be included into the budget and larger uncertainty can be expected.

The modern spectrum analyzer employs the digital IF technique in the design, which improves the level accuracy. With the aid of the Bessel Null method, we are now allowed to make a more accurate measurement of the frequency modulation. High performance microwave spectrum analyzers are widely available and capable of making accurate measurements. See References [1]-[9].

Users know that spectrum analyzer has an excellent built-in receiver. It is a good substitute for an expensive measuring receiver if you already have a high-performance spectrum analyzer at hands. A high-performance spectrum analyzer is capable of handling wider ranges without external mixers and the FM measurement uncertainty can be highly improved by utilizing this direct method. The total uncertainty for the Bessel

Null method can be calculated and is at best of the order of  $\pm 0.15\%$  according to [9]. This method applies to very broad range of modulation index [10].

### **Modulation Theory and Spectral Density Relationships**

Applying a sinusoidal frequency modulation  $f_m$  to a sinusoidal carrier frequency  $\nu_0$  produces a wave that is sinusoidally advanced and retarded in phase as a function of times. The instantaneous voltage is expressed as,

$$V(t) = V_0 \sin g(2\pi\nu_0 t + \Delta\phi \sin 2\pi f_m t),$$

where  $\Delta\phi$  is the *peak phase deviation* caused by the modulation signal.

The first term inside the parentheses represents the linearly progressing phase of the carrier. The second term is the phase variation (advancing and retarded) from the linearly progressing wave. The effects of modulation can be expressed as residual  $f_m$  noise or as single-sideband phase noise. For modulation by a single sinusoidal signal, the peak-frequency deviation of the carrier ( $\nu_0$ ) is

$$\Delta\nu_0 = \Delta\phi \cdot f_m,$$

$$\Delta\phi = \Delta\nu_0 / f_m,$$

where  $f_m$  is the modulation frequency. This ratio of peak frequency deviation to modulation frequency is called *modulation index*  $m$  so that  $\Delta\phi = \beta$  and  $\beta = \Delta\nu_0 / f_m$ .

For applications where signals with FM need to be provided, signal generators with an external input and/or an internal source are available. The modulation index  $\beta$  is defined as

$$\beta = \frac{\Delta f}{f_m}$$

where  $\Delta f$  is the peak frequency deviation and  $f_m$  is the modulation frequency.

For signal generators employing phase locked loops (PLLs) to stabilize a microwave oscillator there will usually be limitations on the maximum value of  $\beta$  achievable due to limitations in the range of allowable inputs to the phase detectors. This means that there will be a minimum modulation frequency (for a particular deviation) equal to  $\Delta f / \beta_{\max}$ .

### **FM Modulation and Demodulation**

The most common FM modulation involves an LC oscillator with an element that has a changing capacitance-versus-reverse-voltage property, e.g. a varactor diode. Many broadband microwave sources use a YIG oscillator with a current proportional to the modulating signal amplitude.

FM demodulation usually utilizes a network of filter with a linear frequency-versus-voltage characteristic. However, this is extremely difficult for the wide-band FM signals to achieve good linearity over a broad range. Phase-locked loops (PLL) can be used as FM demodulators. The phase synchronization enables the PLL to track FM signals much effectively in the presence of noise. For high-accuracy FM demodulation, a pulse counting demodulation scheme is used. Each time the FM signal crosses zero voltage, a constant-width pulse is generated. The average DC voltage of the pulse train is proportional to the number of pulses with respect to time. The 8902A modulation analyzer uses this charge-count discriminator technique with good results.

However, the range of applications, e.g., 8902 modulation meter, is limited to the modulation from 20 Hz to 200 kHz and carrier frequency from 150 kHz to 1.3 GHz. Today's applications require ranges like: frequency deviation 400 kHz<sub>peak</sub> maximum, accuracy range from 1% to 5% of reading or less, and modulation rate from DC to 8 MHz.

Accurate measurements and the use of Bessel Null method for measuring the FM frequency deviation can be made using a spectrum analyzer featuring a measurement demodulator. The demodulator uses digital signal processing to extract the required signal by digitizing the IF signal. Analysis of the inherent error sources within the spectrum analyzer and measurement demodulator suggest extremely accurate modulation measurements.

### **Why Bessel Null Method?**

The Bessel Null method was used to control deviation since frequency deviation is independent of the modulating frequency. With a fixed frequency of modulation the carrier can be reduced to a null by increasing the amplitude of the modulating signal, and this null point is not dependent on the modulating frequency.

The FM spectrum consists of a set of discrete sinusoids. These sinusoids appear at carrier frequency  $F$  and sidebands on either side of the carrier spaced the modulating frequency apart. There is no end to the sinusoids; theoretically, the FM spectrum has infinite frequency distribution. The amplitudes of the carrier component and the various sidebands are determined by the product of the original carrier amplitude  $A$  and the value of a Bessel function. The order of the Bessel function corresponds to the sideband number counting the carrier as number zero. The argument of the Bessel functions is the modulation index,  $\beta$ .

Since the amplitude of the carrier component is modified by the factor  $J_0(\beta)$ , it follows that the carrier component of the modulated wave is smaller in amplitude than the unmodulated carrier. In fact, the carrier component can actually go to zero. This is called a carrier null and happens when  $J_0(\beta)=0$ . The first carrier null occurs at a modulation index of 2.4. These Bessel zeros are used in determining the frequency deviation.

### **Traceability of Frequency Modulation**

Traceability of frequency modulation measurement can be achieved by use of the Bessel Null method.

Use is made of the relationship  $J_0(\beta)$  that passes through zero at the specific  $\beta$  values. Straightforward spectrum analyzer techniques enable the carrier disappearance at these  $\beta$  values to be detected with great sensitivity. Since the modulating frequency  $f$  can be produced using synthesized sources with a frequency accuracy of better than  $1 \times 10^{-6}$  Hz/Hz, it is possible to calculate the deviation corresponding to a particular disappearance with high precision using the relationship.

$$\text{Carrier frequency deviation } \Delta f = \beta f_m$$

### **Bessel Null Searching**

In practice there are certain basic limitations of the Bessel Null method and some precautions are necessary to minimize the errors. For example, these include the depth of the carrier disappearance, the effect of modulation distortion, audio source distortion on the carrier null position, the effect of the spurious AM on the carrier null position and the accuracy of modulating frequency. If the modulating frequency signal is not a pure sinusoid or if there is any non-linearity in the modulating process, the FM spectrum will be distorted and the effect of this is to alter the values of  $\beta$  at which the carrier amplitude is zero. Since a true zero does not exist, then a position of minimum carrier will be sought [9].

When searching for a Bessel null using zero span on the spectrum analyzer, the displayed trace will appear as a horizontal line. When approaching the Bessel null, the RF carrier becomes much more sensitive to the modulating input level and the displayed trace will drop rapidly. If the carrier null is overshoot, the trace will rapidly rise and begin to fall again when the second carrier null is approached. Automation of this null searching will further mitigate the errors.

The frequency spectrum of the modulated carrier contains frequency components (sidebands) other than the carrier. For small values of modulation index ( $\beta \ll 1$ ), as is the case with random phase noise, only the carrier and first upper and lower sidebands are significantly high in energy. The ratio of the amplitude of either sideband to the amplitude of the carrier is

$$V_{sb} / V_0 = \beta / 2.$$

This ratio is expressed in decibels below the carrier and is referred to as dBc for the given bandwidth  $B$  :

$$\begin{aligned} V_{sb} / V_0 &= 20 \log(\beta / 2) = 20 \log(\Delta v_0 / 2 f_m) \\ &= 10 \log(\beta / 2)^2 = 10 \log(\Delta v_0 / 2 f_m)^2 \end{aligned}$$

If the frequency deviation is given in terms of its rms value, then

$$\Delta v_{rms} = \Delta v_0 / \sqrt{2}.$$

The interrelationships of modulation index, peak frequency deviation, rms frequency, and spectral density of phase fluctuations can be found from the following:

$$\frac{1}{2}\beta = \Delta v_0 / 2f_m = \Delta v_{rms} / \sqrt{2f_m}$$

To demonstrate the Bessel Null method, the Carrier-to-First-Sideband Ratio (CFSR) or Narrowband Approximation Method using the Spectrum Analyzer is shown below.

1. Measure the carrier amplitude as well as the amplitudes of the first pair of sidebands

$$S_0:=-19.4 \text{ dBm}; S_{1A}:=-45.5 \text{ dBm}; S_{1B}:=-45.3 \text{ dBm}$$

Modulation Frequency=10 kHz; Deviation Sensitivity of spectrum analyzer is set at 1 kHz/V.

2. Determine CFSR as follows:

$$CFSR=S_0-(S_{1A}+S_{1B})/2$$

CFSR=26 is obtained.

3. Determine an argument, m which will satisfy the following relationship: (since no closed-form solution exists, the problem is solved iteratively)

**a)**

$$20\log\left(\frac{J_0(\beta)}{J_1(\beta)}\right) = CFSR$$

$$\beta=0.1$$

given

$$20\log\left(\frac{J_0(\beta)}{J_1(\beta)}\right) = CFSR$$

$$\beta:=\text{find}(\beta)$$

$$\beta=0.1$$

$$\text{deviation} = \beta \times \text{mod\_freq}$$

$$\text{deviation} = 1.001 \text{ kHz}$$

$$\text{Modulation Index error} = \left( \frac{\text{deviation}}{\text{dev\_sens}} - 1 \right) \times 100$$

**Or**

- b) Solve the following equation:

$$20\log(2/\beta) = CFSR$$

$$\text{deviation} = \beta \times \text{mod\_freq}$$

$$\text{deviation} = 1.001 \text{ kHz}$$

$$\text{Modulation Index Error} = \left( \frac{\text{deviation}}{\text{dev\_sens}} - 1 \right) \times 100$$

In the determination of FM accuracy, the main uncertainty is due to Modulation Index inaccuracy. This is directly related to the inaccuracy of determining the Bessel Null.

### **Errors and Uncertainty Estimate**

Due to the improved accuracy in the modern spectrum analyzer, which employs the digital IF technique in the design, we are now allowed to make a more accurate measurement of the frequency modulation. High performance microwave spectrum analyzers are widely available and capable of making accurate measurements. The new generation high performance spectrum analyzer and measuring receiver employ a digital demodulator. The modern spectrum analyzers utilize the digital signal processing to improve the digital IF filter for better accuracy. This is a perfect way to demodulate the modulated frequency.

The identifiable uncertainty and error sources in this technique are:

- Inaccuracy of the null detection-resolution of level accuracy: 0.1% linear scale in V (due to spectrum analyzer)
- Error in finding the null
- Lack of assurance that the null is the first Bessel null.

*For example, given  $f_m=240$  kHz,  $\Delta f=99-101$  kHz, the inaccuracy of the null detection could vary from 2.398 to 2.402. Therefore, the uncertainty of modulation index is predicted at  $\pm 0.12\%$ .*

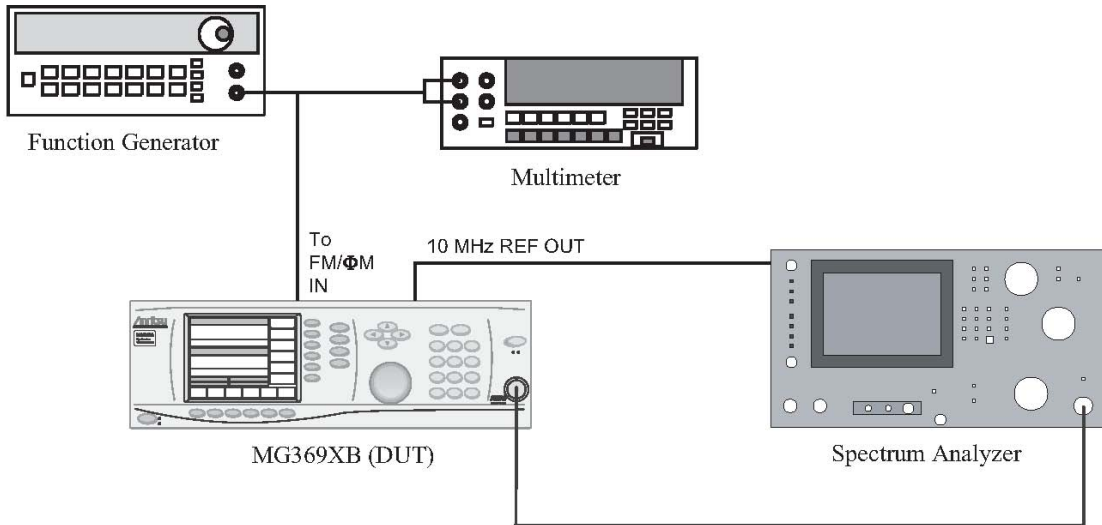
$$J_0(2.4) - J_0(2.398) = 0.12\%$$

$$J_0(2.402) - J_0(2.4) = 0.12\%$$

By automating the procedure, we can eliminate the other two factors: error in finding the null and lack of assurance that the null is the first null. Therefore, their uncertainty contributions are relatively small.

### **Using Spectrum Analyzer to Determine Frequency Modulation Accuracy of a Synthesizer**

A test setup including a spectrum analyzer and a synthesizer-under-test is a perfect example for the Bessel Null method [11]. The test for the locked external FM accuracy at 5 GHz is depicted in the following configuration.



### LOCKED EXTERNAL FM ACCURACY AT 5 GHz Test Steps:

- Step 1.** Set up the test equipment as described above.
- Step 2.** Set up the function generator as follows:
- Press the  $\sim$  key to select the sine wave function.
  - Press the Freq key and use the rotary knob to adjust the frequency output to 99.8 kHz.
  - Press the Ampl key and use the rotary knob to adjust the amplitude to 2.0 Vp-p.
- Step 3.** Set up the MG369XB as follows:
- Reset the instrument by pressing SYSTEM, then Reset. Upon reset, the CW menu is displayed.
  - Press Edit F1 to open the current frequency parameter for editing and set F1 to 5 GHz.
  - Press the **Modulation** | FM | Internal/External keys to select external FM.
  - Press Edit Sensitivity and set the sensitivity to 99.8 kHz/V.
- Step 4.** Set up the spectrum analyzer as follows:
- Press the PRESET key to reset the instrument.
  - Press Aux CTRL
  - Press soft key rear panel
  - Press soft key 10MHz and set to "EXT"
  - Press the FREQUENCY key and enter 5 GHz.
  - Press the SPAN key and enter 10kHz.
  - Press the BW key and set the RBW to 100Hz and the VBW to 100 Hz.
  - Press the PEAK SEARCH key.
- Step 5.** Log the value on the spectrum analyzer as Vmodoff in the test records.
- Step 6.** On the MG369XB, press On/Off to turn the locked FM mode on.
- Step 7.** Log the value on the spectrum analyzer as Vmodon in the test records.
- Step 8.** Using the table X.X "Modulation Index Calculation", calculate modulation index to six decimal places. This value is "mod index".
- Step 9.** Calculate the following to three decimal places and record the results into the test record as FMerror%.

$$\text{FMerror\%} = \text{ABS}[\text{((mod index * 99800) - 99800) / 99800}]$$

Summary of the Overall FM accuracy test is tabulated as follows.

<b>FM Flatness test (note FG Amplitude = 2.0Vp-p)</b>							
<b>Locked External FM Flatness</b>							
FG Freq	FM sensitivity	Vmodoff (dBm)	Vmodon (dBm)	Mod Index	FMflat (dB)	Specification (dB)	Measurement Uncertainty (dB)
10 kHz	10 kHz	-3.4	-6.3	1.1073703	-0.6087	+/-1.0	0.07
20 kHz	20 kHz	-3.4	-6.28	1.1038767	-0.5812	+/-1.0	0.07
50 kHz	50 kHz	-3.42	-6.05	1.0588381	-0.2194	+/-1.0	0.07
99.8 kHz	99.8 kHz	-3.38	-5.87	1.0324293	reference	N/A	N/A
200 kHz	200 kHz	-3.4	-5.97	1.0476302	-0.1270	+/-1.0	0.07
500 kHz	500 kHz	-3.4	-5.8	1.0149617	0.1482	+/-1.0	0.07
1 MHz	1 MHz	-3.38	-5.88	1.0343458	-0.0161	+/-1.0	0.07
9.98 MHz**	9.98 MHz	-3.4	-5.7	0.9950739	0.3201	+/-3.0	0.07
** bandwidth test included.							
<b>Narrow External Phase Modulation Flatness</b>							
FG Freq	Sensitivity	Vmodoff (dBm)	Vmodon (dBm)	Mod Index	PMflat (dB)	Specification (dB)	Measurement Uncertainty (dB)
10 kHz	1.00	-3.4	-5.78	1.0110254	0.0338	+/-1.0	0.07
20 kHz	1.00	-3.38	-5.75	1.0090496	0.0507	+/-1.0	0.07
50 kHz	1.00	-3.38	-5.53	0.9642286	0.4454	+/-1.0	0.07
99.8 kHz	1.00	-3.4	-5.8	1.0149617	reference	N/A	N/A
200 kHz	1.00	-3.42	-5.82	1.0149617	0.0000	+/-1.0	0.07
500 kHz	1.00	-3.38	-5.48	0.9536589	0.5411	+/-1.0	0.07
1 MHz	1.00	-3.4	-5.53	0.9600186	0.6316	+/-1.0	0.07
10 MHz**	1.00	-3.4	-5.23	0.8938146	1.2523	+/-3.0	0.07
** bandwidth test included.							
<b>Wide External Phase Modulation Flatness</b>							
FG Freq	Sensitivity	Vmodoff (dBm)	Vmodon (dBm)	Mod Index	PMflat (dB)	Specification (dB)	Measurement Uncertainty (dB)
10 kHz	1.00	-3.42	-5.92	1.0343458	-0.1309	+/-1.0	0.07
20 kHz	1.00	-3.4	-5.87	1.0285818	-0.0823	+/-1.0	0.07
50 kHz	1.00	-3.4	-5.82	1.0188779	0.0000	+/-1.0	0.07
99.8 kHz	1.00	-3.4	-5.82	1.0188779	reference	N/A	N/A
200 kHz	1.00	-3.4	-5.82	1.0188779	0.0000	+/-1.0	0.07
500 kHz	1.00	-3.4	-5.8	1.0149617	0.0334	+/-1.0	0.07

The following table shows a complete test result using the MetCal procedure.

Test Results						
Test Description	True Value	Test Result	Lower limit	Upper limit	Units	
3-11 FREQUENCY MODULATION TESTS						
Locked External FM Accuracy (99.8 kHz)						
5 GHz		103.23	89.82	109.78 kHz		Pass
20 GHz		103.23	89.82	109.78 kHz		Pass
Locked Low-Noise External FM Accuracy (99.8 kHz)						
5 GHz		100.11	89.82	109.78 kHz		Pass
20 GHz		99.91	89.82	109.78 kHz		Pass
Locked Internal FM Accuracy (99.8 kHz)						
5 GHz		103.23	89.82	109.78 kHz		Pass
20 GHz		106.41	89.82	109.78 kHz		Pass
Locked Low-Noise Internal FM Accuracy (99.8 kHz)						
5 GHz		96.65	89.82	109.78 kHz		Pass
20 GHz		96.65	89.82	109.78 kHz		Pass
Wide External FM Accuracy (99.8 kHz)						
5 GHz		103.23	89.82	109.78 kHz		Pass
20 GHz		106.41	89.82	109.78 kHz		Pass
Narrow External FM Accuracy (99.8 kHz)						
5 GHz		96.65	89.82	109.78 kHz		Pass
20 GHz		96.65	89.82	109.78 kHz		Pass
Wide Internal FM Accuracy (99.8 kHz)						
5 GHz		96.65	89.82	109.78 kHz		Pass
20 GHz		106.41	89.82	109.78 kHz		Pass
Narrow Internal FM Accuracy (99.8 kHz)						
5 GHz		93.02	89.82	109.78 kHz		Pass
20 GHz		93.02	89.82	109.78 kHz		Pass
Locked External FM Flatness @ 5 GHz						
10 kHz		-0.55	-1.00	1.00 dB		Pass
20 kHz		-0.55	-1.00	1.00 dB		Pass
50 kHz		-0.28	-1.00	1.00 dB		Pass
200 kHz		0.00	-1.00	1.00 dB		Pass
500 kHz		-0.28	-1.00	1.00 dB		Pass
1 MHz		-0.55	-1.00	1.00 dB		Pass
9.98 MHz		-0.55	-3.00	3.00 dB		Pass
Narrow External FM Flatness @ 5 GHz						
10 kHz		-0.62	-1.00	1.00 dB		Pass
20 kHz		-0.62	-1.00	1.00 dB		Pass
50 kHz		0.00	-1.00	1.00 dB		Pass
200 kHz		-0.33	-1.00	1.00 dB		Pass
500 kHz		-0.33	-1.00	1.00 dB		Pass
1 MHz		-0.62	-1.00	1.00 dB		Pass
10 MHz		-0.90	-1.00	1.00 dB		Pass
Wide External FM Flatness @ 5 GHz						
10 kHz		0.28	-1.00	1.00 dB		Pass
20 kHz		0.00	-1.00	1.00 dB		Pass
50 kHz		0.28	-1.00	1.00 dB		Pass
200 kHz		0.00	-1.00	1.00 dB		Pass

## Conclusions

Discussions are presented regarding measuring accurate frequency modulation using the spectrum analyzer in conjunction with the Bessel Null method. Example of the Bessel Null method using a spectrum analyzer was applied to the synthesizer FM test. A preliminary result and predicted uncertainty estimate are provided in this report.

## References

1. J. Major, E. Livingston, R. Adair, "Automatic Frequency Response of Frequency-Modulated Generators Using the Bessel Null Method," ARFTG
2. Agilent Application Note 150-1, Spectrum Analysis Amplitude and Frequency Modulation
3. Microwave Theory and Applications, Stephen F. Adam
4. MICROWAVE SIGNAL GENERATORS, William Heinz, Hewlett-Packard Company, Santa Clara, California
5. Agilent Application Note: 1306-1 (5967-5661E)
6. Spectrum Analyzer Fundamentals, 26W-7037, 1989 Tektronix, Inc.
7. Paul Roberts, "The Challenges of Precision Analog Modulation Measurement", Nov. 2007 Automated RF & Microwave Measurement Society (ARMMS).
8. Modern Spectrum Analyzer Theory and Applications, Morris Engelson, ARTECH House, 1984.
9. A.D. Skinner, "Modulation: Fundamental Techniques for Traceability" IEE Colloquium on Accreditation of RF Measurements, 1993.
10. Yeou-Song (Brian) Lee, "A more accurate method to measure the frequency deviation of the modulated signals with modulation index  $\ll 0.2$ ", Measurement Science Conference, 2005.
11. Anritsu Synthesized Signal Generators MG3690B Maintenance Manual, 10370-10367B. September, 2007

# In-Situ Silicon integrated tuner for automated On-wafer MMW noise parameters extraction of Si HBT and MOSFET in the range 60-110GHz

Y. Tagro<sup>1,2</sup>, D. Gloria<sup>1</sup>, S. Boret<sup>1</sup>, Y. Morandini<sup>1</sup>, G. Dambrine<sup>2</sup>

<sup>1</sup>STMicroelectronics, Technology R&D – TPS, Crolles F – 38926, France  
Tél : 33 34 76 92 66 84 ; E-mail : yoann.tagro@st.com

<sup>2</sup>Institut d'Electronique, de Microélectronique et de Nanotechnologie (IEMN)  
Villeneuve d'ascq Cedex 59652, France

**Abstract** — In this paper, for the first time, Silicon integrated tuner is presented aiming silicon transistor (HBT, MOSFET) MilliMeter Wave (MMW) noise parameters ( $NF_{\min}$ ,  $R_n$ ,  $\Gamma_{\text{opt}}$ ) extraction through multi-impedance method. This Tuner is directly integrated in On-wafer tested transistor test structure. The achieved proximity between Device Under Test (DUT) and the developed Tuner allows better impedances (higher  $|\Gamma_{\text{opt}}|$ ) for frequency above 60GHz due to losses reduction between tuner and transistor compared to classical setup using Off-wafer impedance generator. The tuner design is based on variable R, C elements fulfilled with Cold-FET and varactors controlled through biasing and associated to transmission lines (TL) for phase shifting. Design, electrical simulation and MMW measurement of the Tuner are described showing capability from 60GHz up to 110GHz for CMOS and BiCMOS sub65nm technologies characterization.  $|\Gamma|$  of 0.88 have been achieved at the DUT input in the considered frequency range and Tuner losses are less than 20 dB.

**Index Terms** — Active devices, transistors, HBT, MOSFET, in-situ lab., Impedance tuner, noise microwave measurement, multi-impedance, varactor, transmission lines, cold FET.

## I. INTRODUCTION

In the last years, High Frequency (HF) performances of Si devices (CMOS: MOSFETs and BiCMOS: HBTs) have considerably increased and recent Silicon technologies provide dynamic performances (cut-off frequencies higher than 230GHz and  $NF_{\min}$  lower than 2dB@60GHz) very attractive for MMW-band mass market applications (60GHz WLAN & WPAN, Wireless HDMI, Wireless USB, 77GHz automotive radars, ...). One of the key issues to optimize the technology and to develop accurate electrical model is the HF characterization and above all the transistor HF noise parameters extraction. It is well known in the theory of linear noisy networks that a complete characterization of the noise in a linear two-port at one frequency requires the knowledge of the four noise parameters  $NF_{\min}$ ,  $R_n$ ,  $\text{Real}(\Gamma_{\text{opt}})$ ,  $\text{Imag}(\Gamma_{\text{opt}})$  [1] where  $\Gamma_{\text{opt}}$  is the optimum reflection coefficient provided by the source admittance  $Y_{\text{opt}}=G_{\text{opt}}+jB_{\text{opt}}$ . Therefore, the challenge is to characterize these 4 noise parameters of the device up to 110GHz on DUT having  $\Gamma_{\text{opt}}$  very different to 50Ω and  $NF_{\min}$  lower than 2dB in that frequency range. Two extraction methods are well known for the 4 noise parameters measurement:  $NF_{50}$  method in case of MOSFET [3] or multi-

impedance method for Bipolar and MOSFET [2]. The 2<sup>nd</sup> method is based on the use of an impedance synthesizer (Tuner) that is Off-wafer and external to the On-wafer test fixture. This paper presents the development of an in-situ tuner integrated on the On-wafer test structure and used to apply multi-impedance method.

Firstly, existing classical noise extraction methods and their limits are described. Secondly, we describe the proposed approach and its strengths for Silicon device On-wafer automated measurement. Finally, we present tuner results from simulation to measurement.

## II. NF50 AND MUTLI-IMPEDANCE NOISE EXTRACTION METHOD AND THEIR LIMITATIONS

### A. NF50 Method:

Only available for FET devices it is an analytical method assisted by a physical-based noise model [3]. The aim of this technique is to not use systematically a multi-impedance test bench. This kind of approach allows to use only noise measure on 50Ω impedance and the scattering S parameter of the DUT. The scattering S parameter is used to extract the element of the DUT equivalent model, the noise factor on 50Ω allows us to obtain the noise sources of the device. This method is based on (Eq.1) and assumes that  $R_n$  is frequency independent and that  $|Y_{\text{opt}}|^2$  varies as  $\omega^2$ .

$$NF_{50} = 1 + R_n \cdot G_0 + \frac{R_n}{G_0} \cdot (2 \cdot G_0 \cdot G_{\text{cor}} + |Y_{\text{opt}}|^2) \quad (1)$$

These 2 assumptions are verified for MOSFET but not for Bipolar and that is why the proposed lab in-situ method is based on the flow described on part B.

### B. Multi-impedance method:

Introduced by R.Q Lane at the end of the 60<sup>th</sup> year [2], the multi-impedance technique consists in the extraction of the 4 noise parameters by the measurement of 4 noise factors for 4 different source admittances  $Y_S=G_S+jB_S$ .

The method is based on Fig.1-(a) setup using (P1, P2) reference plane and (Eq.2) transformed into (Eq.3) which is

linear regarding 4 new parameters (A, B, C and D) that can be obtained by the measurement of a minimum set of 4 noise factors for 4 different admittances ( $Y_s$ ).

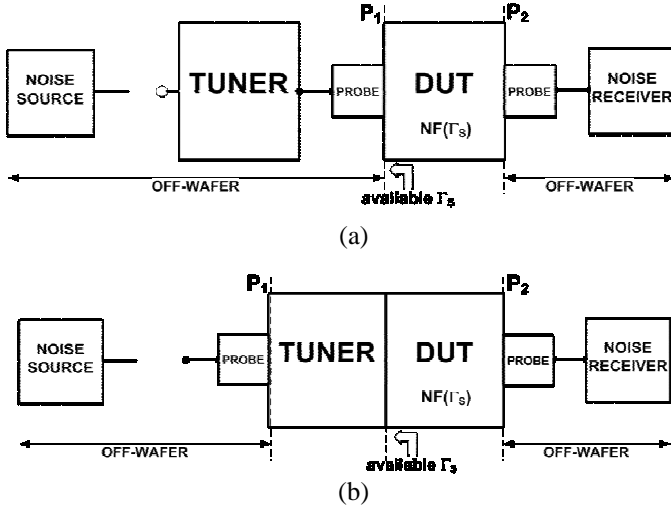


Fig. 1. Multi-impedance method test bench (Tuner Off-WAFER (a) & Tuner On-WAFER (b))

Thanks to (A, B, C, D) determination, and using (Eq.4), we can determine the 4 noise parameters. Nevertheless, for extraction accuracy reason, we approximately use 80 different source admittances ( $Y_s$ ), and deduce A, B, C and D by minimizing the error  $\mathcal{E}$  defined by (Eq.5):

$$NF = NF_{\min} + \frac{R_n}{G_s} |Y_s - Y_{opt}|^2 \quad (2)$$

$$NF = \left[ A + B \left( G_s + \frac{B_s^2}{G_s} \right) + \frac{C}{G_s} + \frac{DB_s}{G_s} \right] \quad (3)$$

$$4 \text{ Noise Parameters} = \begin{cases} NF_{\min} = A + \sqrt{4BC - D^2} \\ R_n = \frac{NF_{\min} - A}{2G_{opt}} = B \\ G_{opt} = \frac{\sqrt{4BC - D^2}}{2B} \\ B_{opt} = \frac{-D}{2B} \end{cases} \quad (4)$$

$$\mathcal{E} = \frac{1}{2} \sum_{i=1}^N \frac{1}{NF_i^2} \left[ A + B \left( G_{Si} + \frac{B_{Si}^2}{G_{Si}} \right) + \frac{C}{G_{Si}} + \frac{DB_{Si}}{G_{Si}} - NF_i \right]^2 \quad (5)$$

The main limitation of this method is the range of  $|T|$  achievable in the DUT reference plane due to losses between external tuner and DUT input (cables, connectors, RF probes) mainly in MMW frequency range. The proposed solution is based on multi-impedance concept but uses integrated tuner in the test structure On-wafer.

### III. IN-SITU TUNER DESIGN

The measurement concept is illustrated on Fig.1-(b) using (P1, P2) reference plane.

#### A. Tuner Concept

The architecture of the tuner uses a cold-nMOS (as variable resistance) in series with a varactor (as variable capacitance) and a TL. Fig.2 shows an electrical schematic of this impedance tuner. All used components are passives.

First of all, to know impedance to be synthesized, a large set of MOS transistors in the tested technology has been studied through electrical model in term of stability circles, optimal source reflection coefficient for  $NF_{\min}$ , and available gain in the concerned frequency range. (see Fig.7).

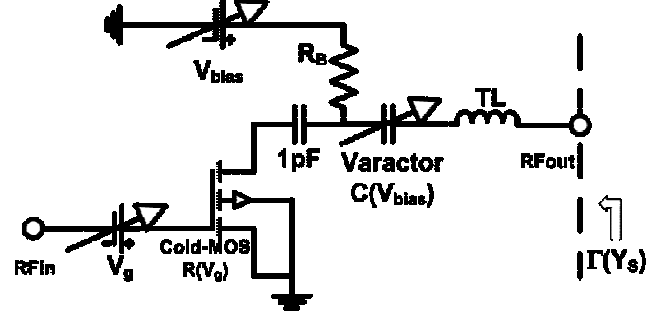


Fig. 2. Electrical schematic of the in-situ tuner in 65nm HR SOI technology.

#### B. Coplanar TL in the 65nm HR SOI technology.

The first prototype has been achieved on STMicroelectronics 65nm HR SOI technology on High Resistivity (HR) substrate providing 6 metallization levels for analog applications and more for digitals as shown on Fig.3.

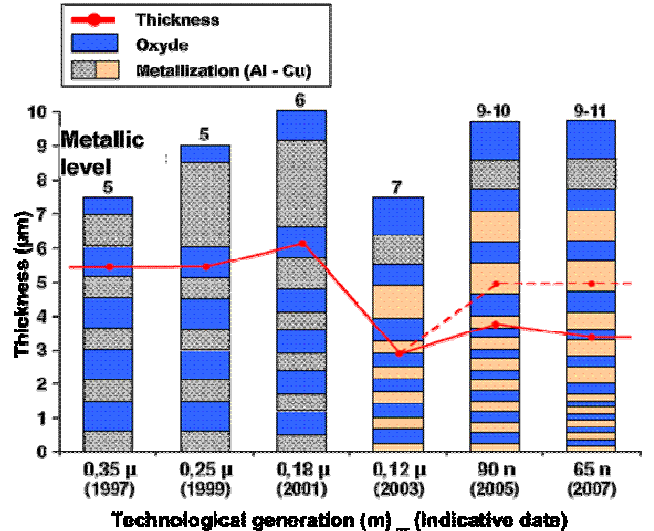


Fig. 3. Evolution of BEOL in silicon technologies [4].

The used TL is a coplanar one described in Fig.4.  $Z_C$  near  $50\Omega$  has been obtained with  $d=70\mu\text{m}$  and  $W=26\mu\text{m}$  [6].

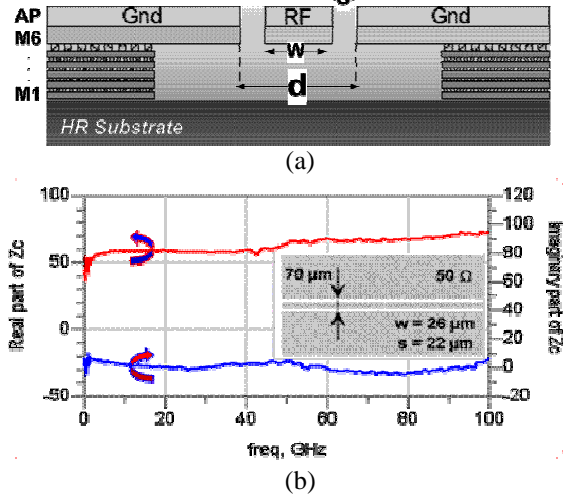


Fig. 4. (a) Coplanar TL in 65nm HR SOI BEOL [5]. (b) Experimental frequency response on 50- $\Omega$  CPW TL.

### C. Varactor used as variable capacitance.

The next passive component used to design the tuner is a varactor based on  $N^+$ poly/Nwell structure. The device is made of 5 poly fingers in parallel. Each finger has  $0.35\mu\text{m}$  length and  $3\mu\text{m}$  width.

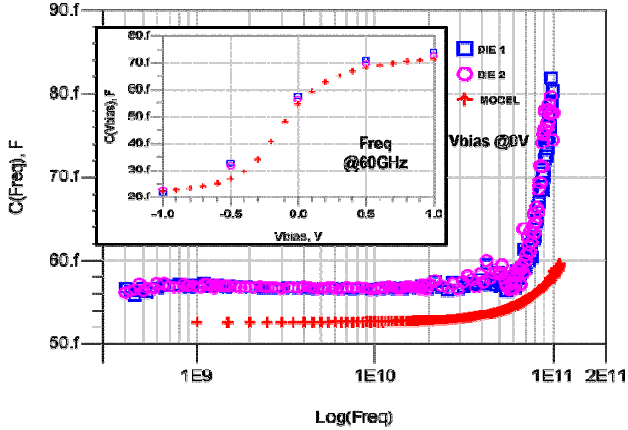


Fig. 5.  $C(V_{\text{bias}})$  versus  $V_{\text{bias}}$  @ 60GHz and  $C(\text{Freq})$  versus  $\text{Log}(\text{Freq})$  @ 0V.

- The criterions to optimize the choice of this component are:
- the cut-off frequency must be higher than the maximum frequency range (100GHz).
  - The  $\Delta C$  over bias must be high ( $\sim 3.5$  in our case).

### D.. Cold-FET used as variable resistance.

Cold-FET is obtained using MOS transistor with floating drain bias (Fig.6). It's made of 80 poly fingers in parallel contacted on both side and each finger has a length of  $0.12\mu\text{m}$  and a width of  $0.5\mu\text{m}$ .

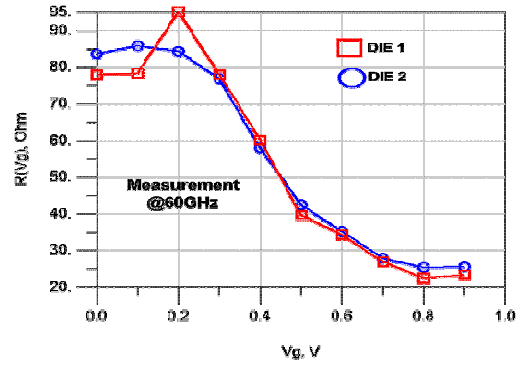


Fig. 6. Measured, Cold-FET versus bias.

The sensitivity and the repeatability of the impedances have to be taken into account in the method robustness and to guarantee the same impedances during alone TUNER characterization and TUNER+DUT one.

## IV. EXPERIMENTAL RESULTS

In this section, we present the experimental data of this study. The measurements are done in 400MHz to 100GHz frequency range even if the used band is 60GHz to 100GHz. These measurements are done on two die of 300mm wafer in 65nm HR SOI technology.

### A. In-situ Tuner measurement results.

On the Fig. 7. we present the results of synthesized admittance  $Y_S$  with the achieved tuner. 3 zones can be identified corresponding to 3 different TL lengths. The lengths have been chosen to move on the smith chart avoiding instability area, and moving across different noise figure circle for the nMOS of the studied technology. Inside each zone obtained for a given TL length, the different admittance are obtained thanks to R(V) (Cold-FET) and C(V) (Varactor).

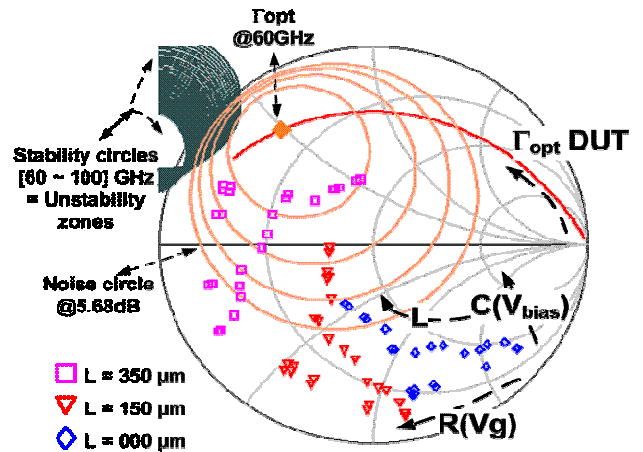


Fig. 7. Impedance synthesis with the in-situ tuner and 65nm HR SOI nMOS ( $0.06 \times 60\mu\text{m}^2$ ) simulated noise characteristics  $V_{gs}=0.65\text{V}$  &  $V_{ds}=1.2\text{V}$ .

On Fig. 7, based on tuner specifications study described on III.A, are plotted the stability (60-100GHz) and noise circle @60GHz (1dB step), and the  $\Gamma_{opt}$  (400MHz-100GHz) of a typical 65nm HR SOI nMOS ( $0.06 \times 60 \mu\text{m}^2$ ). These added characteristics show that the available  $Y_S$  achieved with Tuner provide a good potential for accurate noise extraction on 65nm devices.

The noise features of the considered nMOS provided by its electrical model are:

$$NF_{min}=1.68\text{dB}, R_n=13.6\Omega \text{ and } \Gamma_{opt}=0.72/126.3^\circ$$

Measurements of this transistor with the presented tuner are in progress and will be presented in final paper.

### B. Perspectives of Tuner improvement

As shown in Fig.8, we can see a good agreement between Tuner measurements and electrical simulations. Nevertheless, we observe insertion losses around 20dB in the 60-100GHz range. Reducing the Cold-FET resistance would improve losses as shown in the same figure. This losses reduction will allow higher  $\Gamma(Y_S)$  at the DUT input. In addition reducing  $C_{gs}$  of the cold-FET will also improve losses.

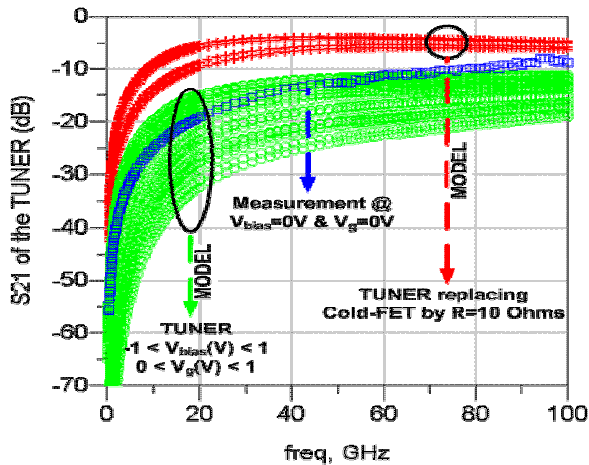


Fig. 8. Tuner  $S_{21}$  simulation versus measurements “Effect of Cold-FET resistance value”.

Fig. 9 shows the variation on tuner  $S_{21}$  over 2 different die and we can note that this dispersion is less than 5% over the frequency range 60-100GHz for all used bias on Cold-FET and varactor. These results are encouraging regarding Tuner characteristics repeatability over different test structures.

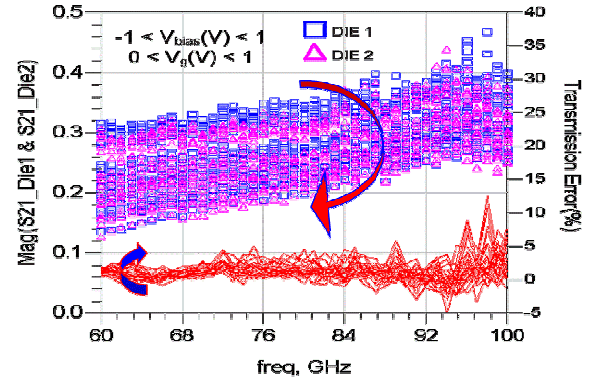


Fig. 9. Transmission error and repeatability of the TUNER transmission on two die.

## V CONCLUSION

A new way to extract the high frequency noise parameters  $NF_{min}$ ,  $R_n$ ,  $G_{opt}$  and  $B_{opt}$  into the frequency range from 60GHz to 110GHz is presented on this paper. This method is based on the multi impedance technique using an in-situ tuner directly integrated on the test structure of HBT or MOSFET devices in sub 65nm technologies. The design of the tuner is based on Cold-FET, and varactor variable with biasing and associated to TL. Obtained electrical results on synthesized impedance are shown and compared to electrical simulations demonstrating a good agreement.

## ACKNOWLEDGEMENT

This work has been carried out within the STMicroelectronics Center R&D, and the authors wish to thank the staff of the 300mm Si facilities in ST Crolles for device fabrication

## REFERENCES

- [1] H. Rothe. W. Dahlke, “Theory of noise fourpoles,” *2003 IEEE Proc. Of the IRE* , pp. 811-818, June 1956.
- [2] R. Q. Lane, “The determination of device noise parameters,” *Proc. Of the IEEE*, vol. 57, pp. 1461-1462, August 1969.
- [3] G. Dambrine and all, “A new method for On-Wafer Noise Measurement,” *IEEE Trans. On Microwave Theory & Tech.*, vol. 41, no. 3, pp. 375-381, March 1993.
- [4] F. Giancesello, “1.8 dB insertion loss 200GHz CPW band pass filter integrated in HR SOI CMOS Technology,” *IEEE Trans. On Microwave Theory & Tech.*, pp. 453-456, 3-8 June 2007.
- [5] S. Montusclat, “Design for Millimeter-wave applications in Silicon Technologies,” *IEEE 33<sup>rd</sup> ESSCIRC*, pp.464-471, 11-13 September 2007.
- [6] S. Boret, “Wide- and narrow-band bandpass coplanar filters in the W-frequency band,” *IEEE Trans. On Microwave Theory & Tech.*, vol. 51, no. 3, pp. 784-791, March 2003.

# A New Noise Parameter Measurement Method Results in More than 100x Speed Improvement and Enhanced Measurement Accuracy

Gary Simpson<sup>1</sup>, David Ballo<sup>2</sup>, Joel Dunsmore<sup>2</sup>, Amar Ganwani<sup>1</sup>

<sup>1</sup>Maury Microwave Corporation, 2900 Inland Empire Blvd, Ontario, CA, USA 91764

<sup>2</sup>Agilent Technologies, 1400 Fountaingrove Parkway, Santa Rosa, CA, USA 95403

*Abstract* – A new method for noise parameter measurements is introduced, with better than 100x speed improvement over traditional methods. The setup is simple and easy to configure, and the entire calibration and measurement process is very fast, making dense frequency spacing practical. The new method produces smoother data with lower scatter, and the dense frequency spacing eliminates shifts due to aliasing and makes it easier to identify the scatter and outliers.

*Index Terms* – microwave measurements, noise figure, noise parameters, low noise amplifiers

## I. Introduction

Noise occurs naturally in any active device or circuit, and limits the minimum levels of useful signals. With a cell phone, for example, it can interfere with a weak signal, and interrupt a call. Therefore, it is important to design circuits to minimize the effects of noise. To do this, the noise must be quantified and measured.

The most common measure of added circuit noise is a figure-of-merit called noise figure, which quantifies the signal-to-noise degradation caused by an amplifier. While noise figure is most commonly measured in a 50-ohm environment, a device's noise figure varies with the source impedance presented to the device. This variation can be expressed in terms of noise parameters, which are essential to know when designing low-noise amplifiers using highly mismatched devices.

Noise parameters may be in different forms, including various versions of the noise correlation matrix, but all forms consist of four scalar numbers, and have the same underlying device information (similar to s-parameters versus y-parameters). A common form of the noise parameters is shown in equation 1. This is shown graphically in figure 1.

$$F = F_{\min} + 4r_n \frac{|\Gamma_s - \Gamma_{\text{opt}}|^2}{|1 + \Gamma_{\text{opt}}|^2 (1 - |\Gamma_s|^2)}$$

Equation 1

Where

$F_{\min}$  = minimum noise figure (linear)

$\Gamma_{\text{opt}}$  = optimum source gamma (to produce  $F_{\min}$ )

$r_n$  = equivalent noise resistance

$F$  = noise figure (linear)

$\Gamma_s$  = source gamma

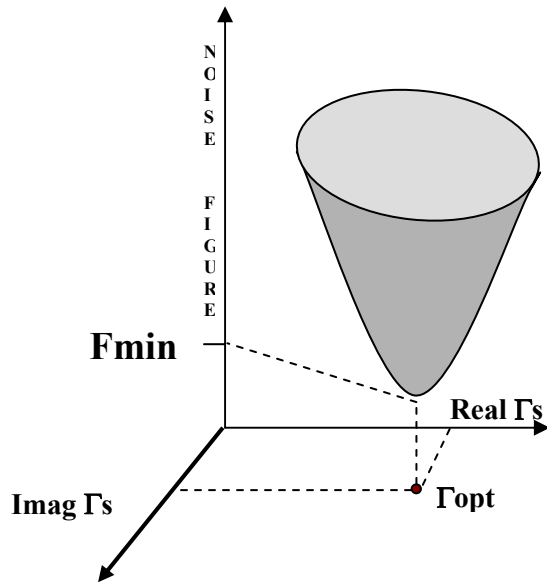


Figure 1 – 3D representation of noise figure vs. source impedance.

The basic approach to noise parameter measurements is to measure the noise figure at multiple source impedance values. For each measurement,  $\Gamma_s$  and  $F$  are plugged into equation 1, resulting in simultaneous equations that can then be solved for the noise parameters. Four measurements give four simultaneous equations, which should be sufficient in theory to solve for the four noise parameters. However, noise measurements are sensitive to small errors, so in practice it is common to measure the noise at more than four values of source impedance, and then use a least-mean-squares algorithm to reduce the over-determined data<sup>[1][2]</sup>.

A better approach than the noise figure equation is to use the noise power equation<sup>[3]</sup>, as shown in equation 2. With this, a noise power measurement with a cold noise source is separate from a measurement with a hot noise source. This allows the reflection coefficient difference between the noise source states to be taken into account rigorously. It also allows any combination of hot and cold measurements, including the “cold only” measurements. Therefore, this method is normally used in practice.

$$P = kB\{[t_{ns} + t_0(F_1-1)]G_{a1} + t_0(F_2-1)\}G_{t2} \quad \text{Equation 2}$$

Where

$P$  = the total measured noise power

$k$  = Boltzmann’s constant

$B$  = the system bandwidth

$t_0$  = 290 kelvins

$t_{ns}$  = temperature of the noise source in kelvins

$F_1$  = the DUT noise figure (function of source impedance)

$F_2$  = the receiver noise figure (function of the DUT output impedance)

$G_{a1}$  = the DUT available gain (function of the source impedance)

$G_{t2}$  = the receiver transducer gain (function of DUT output impedance)

## II. Traditional Noise Parameter Measurements

A traditional noise parameter measurement setup is shown in figure 2. It includes a vector network analyzer (VNA) and a separate noise figure analyzer. For s-parameter measurements, the tuner is set to 50 ohms, and the two RF switches connect the device under test (DUT) to the VNA. For noise measurements, the switches connect the noise source to the DUT input and the noise receiver to the DUT output. An optional load tuner (not shown) is sometimes used when the DUT is highly reflective, to reduce sensitivity to error.

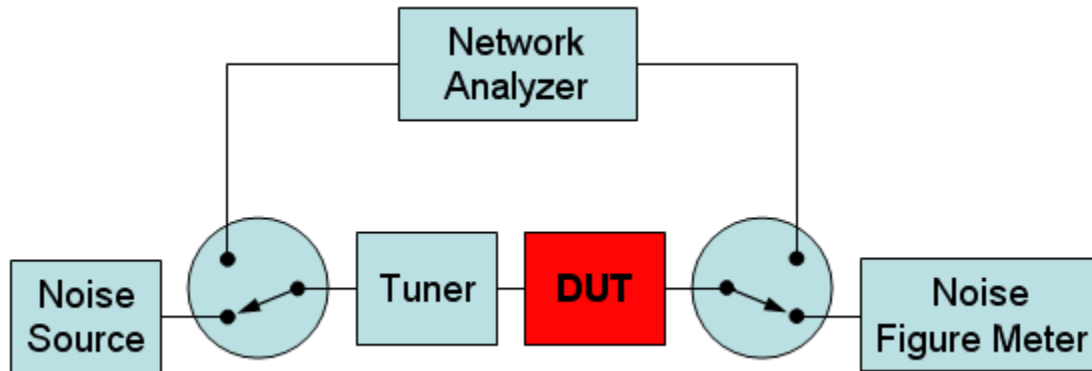


Figure 2 – A traditional noise parameter measurement setup.

The tuner is pre-characterized at every frequency independently. This means that there is a unique set of tuner positions for each frequency, ensuring a good spread of source impedance points at every frequency. The tuner can be characterized separately, or as part of an in-situ system calibration. The advantage of doing it separately is that the same tuner file can be used for a long time, and then a hybrid in-situ calibration can quickly get the remaining s-parameter blocks.

The in-situ system calibration normally uses two VNA calibrations: a 2-port calibration at the DUT reference planes, and a 1-port  $s_{22}$  calibration at the noise source reference plane. By subtracting error terms, the 2-port s-parameters from the noise source to the DUT can then be determined. If the optional load tuner is used, then a 1-port  $s_{11}$  calibration at the noise receiver reference plane is also used to determine the 2-port s-parameters from the DUT to the noise receiver.

A hybrid in-situ calibration uses tuner data that is already characterized. The same VNA calibrations are still used to determine the 2-port s-parameters from the noise source to the DUT plane, which are then de-embedded to remove the tuner s-parameters. The result will be s-parameter blocks that include everything except the tuner.

After the system calibration, the traditional noise receiver calibration and DUT noise parameter measurement are both done one frequency at a time<sup>[3][4]</sup>. This is because the noise parameter extraction involves complex math that is sensitive to small errors, and the pattern of source impedance points is important to get well-conditioned data<sup>[2]</sup>. Measuring one frequency at a time solves this by allowing the impedance pattern to be selected in an optimal manner for each frequency.

One problem with this method is that the measurement time is very long, due the large number of tuner positions that must be set and the high number of associated noise measurements. With s-parameters, it is common to sweep 400 or more points to see details of the amplifier's performance. But measuring noise parameters with that many frequencies can take days, so it is impractical in most cases. If it is done, temperature drift can cause significant errors if the laboratory is not carefully temperature controlled. This is exacerbated by the many lengths of cables required to connect all of the instruments and switches in figure 2.

Since the noise parameter measurements tend to take a long time with the traditional approach, it is typical to only measure a sparse set of frequencies. But this makes the scatter, outliers, and cyclical-frequency errors difficult to interpret. A cyclical error is common with imperfect VNA calibrations, where system errors add at some frequencies and cancel at others. With a small number of frequencies, aliasing can shift the data set up or down if the measurements fall on high points or low points caused by cyclical errors. Smoothing techniques are often employed to make the data look better, but will not correct for shifted data.

### **III. The New Noise Parameter Measurement Method**

A new noise parameter measurement method (patent pending) has been developed that typically speeds up the calibration and measurement time by over two orders of magnitude. This makes it practical to sweep a much larger frequency set.

The new method has two key features that contribute to the breakthrough speed improvement: 1) The tuner is characterized with one set of states (physical tuner positions) that are selected to give a reasonable impedance spread over the frequency band of interest; and 2) the noise power measurement is swept over the frequency range at each state, so that the tuner only moves to each position once. This takes advantage of the fast sweep capability of modern instruments, as well as saving time by minimizing tuner movement.

Since one set of tuner states is used across the entire frequency band, the impedance pattern may not be as ideal as that used with the traditional method. However, one can compensate for this by using more impedance states, and the resulting measurement quality and repeatability indicates well-conditioned data.

The new method is implemented using a new VNA that includes a built-in noise receiver, simplifying the measurement block diagram as shown in figure 3. This arrangement reduces the number of cables and connections, helping to stabilize the setup. Because of the fast measurement time and simpler setup, temperature drift is no longer a significant factor in system errors. A photo of the new setup is shown in figure 4.

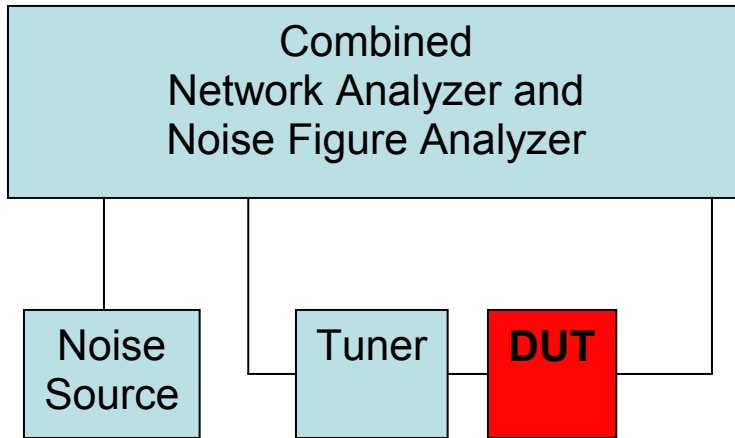


Figure 3 – Noise parameter setup used with new measurement method.

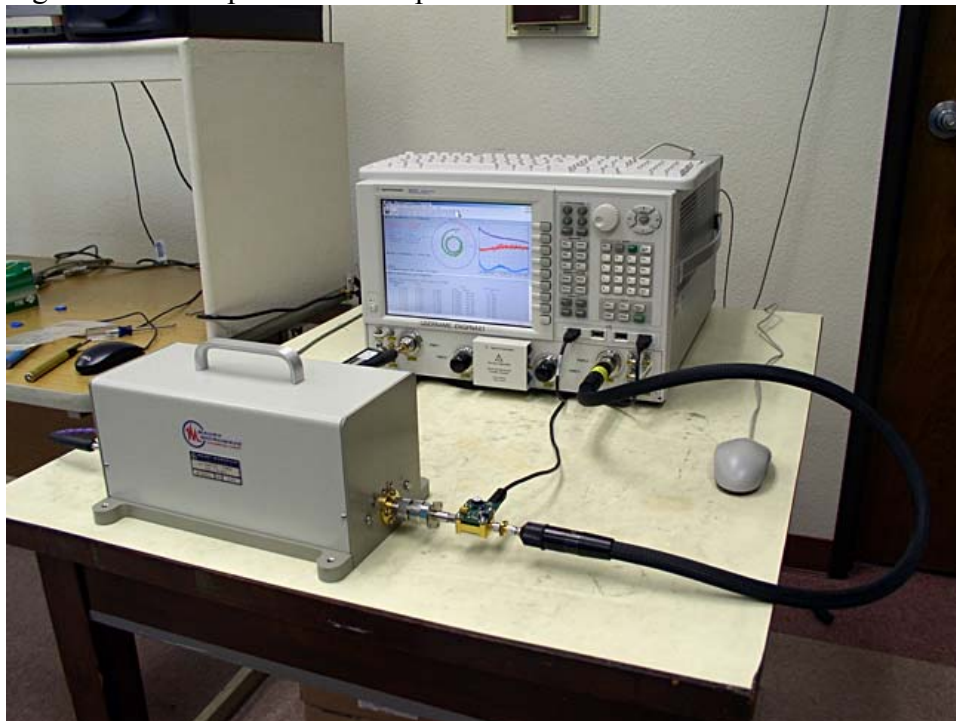


Figure 4 – Photo of the new setup with the coaxial DUT

The new method may be done in multiple frequency bands if the tuner uses different mismatch probes for different frequency ranges. Two frequency bands were used to produce the data shown here, as the tuner was a Maury model MT982EU30, with a low frequency probe covering 0.8 to 2.8 GHz, and a high frequency probe covering 2.8 to 8.0 GHz. The VNA with a noise receiver was an Agilent N5242A PNA-X network analyzer. The measurement was done with Maury noise parameter software running in the PNA-X itself. Alternatively, it could have been run on a Windows-based PC.

The tuner-state selection for a mechanical tuner should use carriage positions that are non-uniformly spaced. Otherwise, the impedance points might overlay or alias at some frequencies and produce poorly conditioned data. An example of this problem is shown in figure 5. Figure 6 shows a typical impedance pattern used with the new method at the low, middle and high end of the band for tuner states chosen with logarithmic spacing along the line.

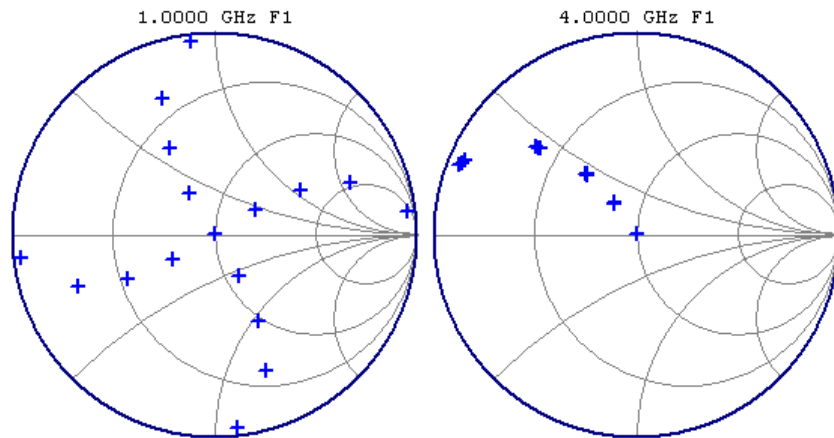


Figure 5 – Example of uniform spacing of tuner states, with aliased results shown at 4 GHz

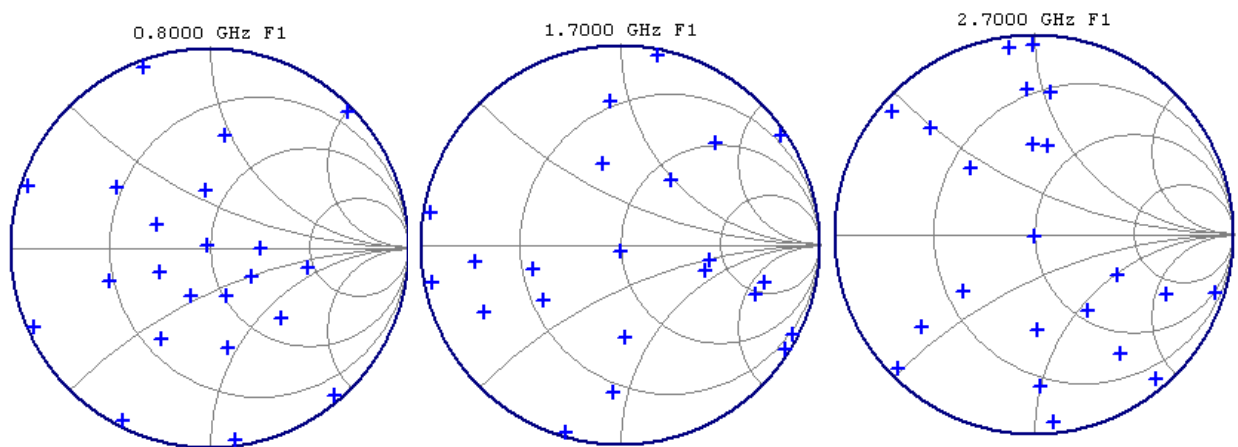


Figure 6 – Example of tuner states of new method

#### IV. Comparison of the Two Methods

To compare the new method with the traditional method, a microwave FET was measured with both methods from 0.8 to 8 GHz, with a step frequency of 0.1 GHz, resulting in 73 test frequencies. Note that this is a much larger number of frequencies than is typically used with the traditional method. The FET was permanently mounted in a 3.5mm fixture with built-in bias tees to make a stable comparison, and the measurement reference planes were at the coaxial connectors. The fixture is shown in the setup of the new method in figure 4.

Figure 7 shows the measured data from the traditional method with 73 frequencies, and figure 7a shows a subset of the same data with only 15 frequencies which is more typical of that method. Figure 8 shows the measured data from the new method with 73 frequencies. No smoothing is applied in any case. A time comparison is shown in table 1.

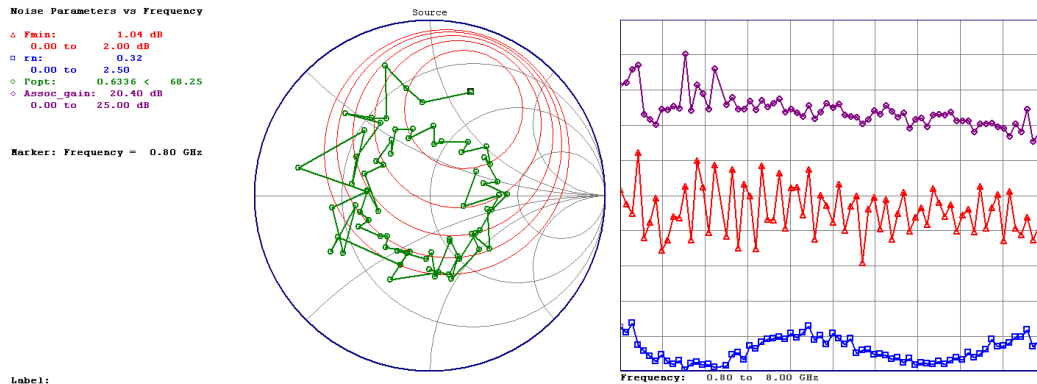


Figure 7 – Measured noise parameter data with 73 frequencies using the traditional method Showing Fmin (red), rn (blue), and Associated Gain (purple)

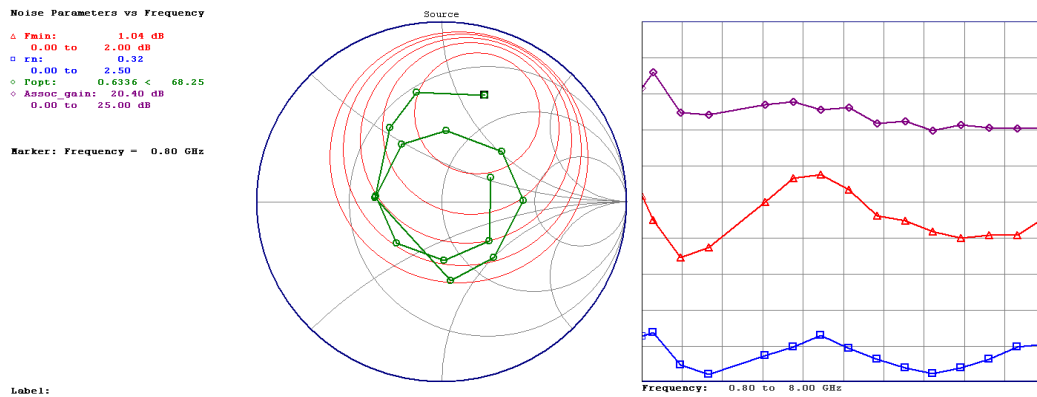


Figure 7a – 15-frequency subset of the measured noise parameter data using the traditional Method Showing Fmin (red), rn (blue), and Associated Gain (purple)

Figure 7a (15 points taken from the data in figure 7), clearly shows that the Fmin readings appear to be shifted, and the data appears smooth, but in reference to figure 7, we can see that it is just an alias of the true measured response. Figure 8 shows the same DUT as figure 7, but the improved method reduces errors, and we can see that the data of the new method is truly smoother.

The data shows the major advantages of the new method: 1) the total measurement time is over two orders of magnitude faster for the examples described here; and 2) the data is much smoother and has lower scatter. The larger scatter in the Fmin data shown using the traditional method is often not observed by RF designers, since many fewer frequency points are typically measured. The smaller number of frequency points may produce data that appears smooth, but the data will vary around the true value shown by the new high-frequency-density method, as shown by Figure 7a. This also means that smoothing techniques may produce offsets with the small number of points but become more meaningful with a larger number of points.

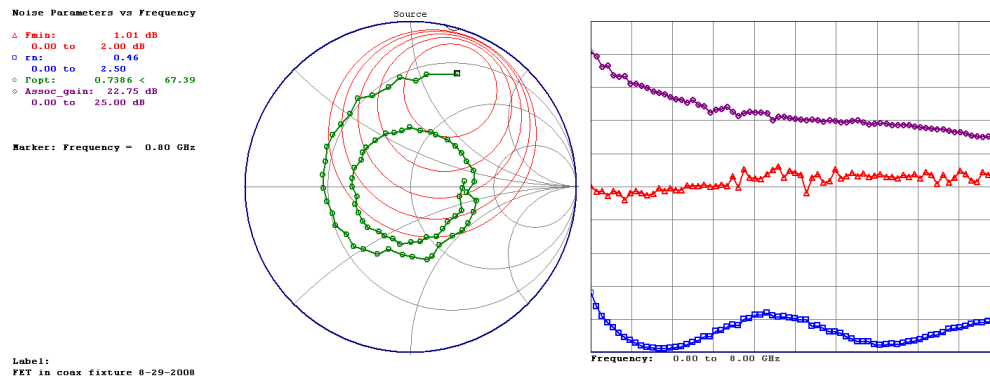


Figure 8 – Measured noise parameter data using the new method, no smoothing applied  
Showing Fmin (red), Rn (blue), and Associated Gain (purple)

Table 1 – Measurement time comparison of the new method vs. the traditional method

	Traditional method measurement time, 73 frequencies	New method measurement time 73 frequencies	Traditional method measurement time, 401 frequencies*	New method measurement time, 401 frequencies
System Cal	25 hrs, 29 min	1 min, 56 seconds	139 hrs, 59 min	3 min, 12 seconds
Noise Receiver Cal	2 hrs, 24 min	2 min, 56 seconds	13 hrs, 13 min	10 min, 44 seconds
DUT Measurement	2 hrs, 22 min	3 min, 15 seconds	13 hrs, 2 min	10 min, 54 seconds
Total Time excluding connections	30 hrs, 15 min	8 min, 7 seconds	166 hrs, 14 min	24 min, 50 seconds
Time Ratio		224X		400X

\*Estimated, based on time to measure per frequency

The speed of the new method also improves the typical calibration methodology. Because of the time required, the hybrid in-situ calibration is often used with the traditional method, because then the same tuner file can be used over and over, saving time. However, that introduces an additional VNA calibration and a number of extra connections, which increases the overall error level. With the new method, there is no need to compromise – a full in-situ calibration including the tuner characterization can be done every time to minimize the errors.

Finally, using one instrument with the VNA and noise receiver functions combined simplifies the setup and eliminates many cables, adapters, and connections that must be held stable. This provides much better system integrity and stability, which also contributes to significantly better and more consistent data. It also requires less operator skill to get good data.

## V. Conclusions

The new noise parameter measurement method provides two orders of magnitude speed improvement. It also produces data that is smoother and has less scatter than the traditional method. The fast measurement speed eliminates temperature drift, and using a VNA with an internal noise receiver simplifies the setup and makes it much more stable and consistent.

The much higher speed makes it practical to always do a full in-situ calibration to minimize errors, and to measure more frequencies to get a better view of scatter and cyclical errors, and to be able to use smoothing with more confidence. The higher frequency density also enhances accuracy by reducing shifts due to aliasing.

### **Acknowledgement**

Thanks to Lynn Rhymes of Agilent Technologies for supplying the connectorized test device.

### **References**

- [1] Lane, Richard Q., "The Determination of Device Noise Parameters", Proceedings of the IEEE, Vol. 57, August 1969, pp1461-1462.
- [2] Caruso and Sannino, "Computer-Aided Determination of Microwave Two-Port Noise Parameters", IEEE Trans. On Microwave Theory and Techniques, Vol. MTT-26, September 1978, pp 639-642.
- [3] Operating Manual, Automated Tuner System, Maury Microwave Corporation, Document number MT993-2.
- [4] Lane, Richard Q., "A 0.5-18 GHz Semi-Automatic Noise Parameter Measurement Technique", 19th ARFTG Digest, June 1982, pp. 42-58.

# Comparison of On-Wafer Multiline TRL and LRM+ Calibrations for RF CMOS Applications

Andrej Rumiantsev<sup>#</sup>, Susan L. Sweeney<sup>\*</sup>, Phillip L. Corson<sup>\*</sup>

<sup>#</sup> SUSS MicroTec Test Systems GmbH, Suss-Str. 1, Sacka, D-01561, Germany, a.rumiantsev@ieee.org

<sup>\*</sup> IBM Microelectronics, Essex Junction, VT 05452, USA, slsweene@us.ibm.com; corson@us.ibm.com

**Abstract** — This paper presents a quantitative comparison of the reference multiline TRL and LRM+ for a customized set of standards in a CMOS process using IBM's 0.13  $\mu\text{m}$  technology. This comparison was undertaken for the first time and covered a frequency range from 1 to 110 GHz. It was demonstrated that the accuracy of the on-wafer multiline TRL and LRM+ calibration were in very good agreement. Both methods outperform the conventional off-wafer calibration with the DUT contact pad parasitics de-embedded.

**Index Terms** — calibration, error correction, calibration comparison, scattering parameters measurement, CMOS, de-embedding.

## I. INTRODUCTION

As technology scaling advances and device performance increases, it is becoming essential to obtain accurate high frequency scattering parameters of on-wafer devices used in applications such as communications circuits. Accurate on-wafer network analyzer calibration and the establishment of the measurement reference plane close to the device under test (DUT) is now necessary to reduce the reliance on inaccurate de-embedding methods of the probe padset parasitics.

Today, the commonly-used method for calibrating a wafer-level measurement setup for RF CMOS application consists of two steps:

- Step 1: off-wafer calibration to the probe tip performed on a commercially-available alumina calibration substrate;
- Step 2: translation of the measurement reference plane to the DUT using contact pad de-embedding techniques.

Such an approach was introduced for the first time at the end of the 1980s [1]. This approach recommended using Open and Short elements as the RF de-embedding test structures. This method provided a reasonable alternative to the on-wafer calibration challenges for silicon at that time, in contrast to the high-frequency GaAs applications [2]. Method [1] required neither a perfectly matched load nor the calibration lines embedded on the test chip.

However, further improvement of RF CMOS device performance and increasing operation frequencies to 110 GHz and beyond requires improved measurement accuracy. The de-embedding procedure has become more and more complicated

[3, 4], and finally, the need to de-embed the load element has been reported [5, 6].

This work is a further development of wafer-level calibration techniques with a customized set of lumped standards for mm-wave frequency applications. The earlier investigations reported in [7] demonstrated implementation of a lumped LRM+<sup>1</sup> calibration methodology on a conductive (SiGe:C) wafer up to 110 GHz. However, results presented in [7] verify the calibration accuracy qualitatively, but the quantitative verification of the LRM+ procedure remained a challenge.

The achievements made in fabricating and characterizing planar distributed standards in conductive wafer processes observed over the last several years has established a solid background for accurate on-wafer calibration on silicon, e. g. [8-10]. This paper presents a quantitative comparison of the reference multiline TRL<sup>2</sup> [11] and lumped LRM+ [7] for a customized set of standards in a CMOS process using IBM's 0.13  $\mu\text{m}$  technology, with an NFET transistor of gate length 0.12  $\mu\text{m}$  as the DUT. This comparison was undertaken for the first time and covered a frequency range from 1 to 110 GHz.

Additionally, this paper considers proper design of planar structures and presents simulated and measured results of wafer-embedded standards.

Finally, key model parameters of an active DUT are extracted with respect to different wafer-embedded calibration schemes.

## II. ON-WAFER CALIBRATION COMPARISON

Different calibration procedures have been developed in the past years [12]. All of them rely on ideal, fully or partly known reference elements (calibration standards), realized in planar design (microstrip or coplanar).

In contrast to coaxial and waveguide applications, a great variety of fabrication techniques makes it almost impossible to trace planar calibration standards to a primary reference. This substantially complicates the task of specifying and verifying planar calibrations. However, research undertaken by the National Institute of Standards and Technology (NIST) provided a procedure for comparing wafer-level calibrations,

<sup>1</sup> Line-Reflect-Match, advanced.

<sup>2</sup> Thru-Reflect-Line

identifying setup drift, as well as verifying calibration standards [13].

In this work, NIST multiline TRL was selected as the benchmark calibration. In conjunction with methods proposed in [14, 15], this procedure allows accurate setting of the measurement system reference impedance to 50 Ohms as well as a precise definition of the measurement reference plane for both semi-insulating and conductive wafers. Thus, it can be successfully applied for verifying the accuracy of a lumped calibration with a wafer-embedded customized set of standards.

### III. ON-WAFER CALIBRATION STANDARDS

The customized calibration set included all standards required for the benchmark TRL and lumped LRM+ calibrations. The standards were fabricated within a typical 2-port AC GSG on-wafer padset. The ground pads, signal pad, and signal launch lines were placed at a high-level metal layer.

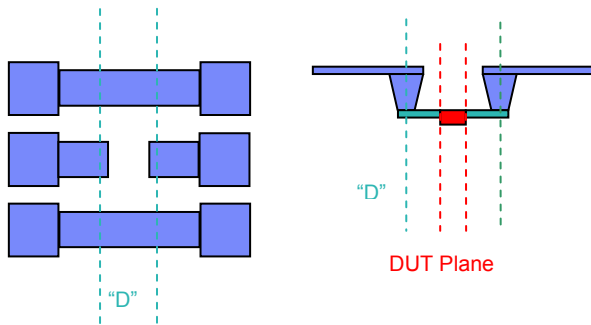


Fig. 1. Design of the customized calibration set.

The transmission lines were fabricated as extensions of the signal launch lines at this high-metal level. Line lengths were optimized to cover a frequency band from 1 GHz to 110 GHz. Lumped load, short, and open elements were developed according to [7] and optimized for the specifics of the bulk CMOS process used and the device under test (DUT) design. These elements were fabricated at the bottom of the via stacks, at plane “D” in Fig. 1, closely coinciding with the placement of the DUT. Thus, both the TRL and LRM+ calibrations establish the reference plane at the via stack, close to the on-wafer DUT.

The electrical parameters of TRL lines were simulated with a simplified model using the 3D full-wave electromagnetic field simulation package Ansoft HFSS<sup>3</sup>. Simulation of the complete physical structure in Fig. 1 with HFSS requires computing resources and solution times that are not practical, so the structure has to be simplified while retaining the correct

<sup>3</sup> HFSS is commercially-available from ANSYS Inc.

response. The simplest approach is a microstrip line, a solid reference conductor, and a single dielectric. This structure was created using the physical dimensions of the launch line, reference plane, and total dielectric thickness.

The cumulative phase of the thru and line standards was used to validate that a single value could be chosen for the real part of the dielectric constant and this would predict the correct phase for all transmission line lengths. The losses of the lines in the model are modulated by the conductivity of the return path and the dielectric loss tangent. These parameters are set in the simplified model to provide a good fit to the measured data.

### IV. MEASUREMENT SETUP

The experimental setup for the 110 GHz wafer-level measurements included an Agilent 8510XF VNA, a semi-automated wafer-probe station, 110 GHz wafer probes with a pitch of 100  $\mu\text{m}$  from GGB Industries, and GaAs reference material RM 8130 available from NIST.

The influence of contact repeatability on measurement data, calibration standards, verification elements, and evaluation transistor S-parameters was reduced by acquiring raw data (with error correction turned off) in three measurement runs. Measurement data from the VNA was recorded with proprietary data acquisition software developed by IBM and with commercial software SussCal<sup>4</sup>. Off-line LRM+ and TRL calibration, error correction, and calibration comparison was performed using SussCal and MultiCal<sup>5</sup> software packages.

### V. EXPERIMENTAL RESULTS

First, the measurement system drift (instrument drift) shown in Fig. 2 was verified within the time interval of the DUT measurements using the calibration comparison technique and a commercially-available alumina calibration substrate. The probe contact repeatability error is significantly less than the measurement instrument instability within the experimental time (about eight hours) due to fabrication of the standards with gold contact pads. Therefore, it was assumed that the error defined from the calibration comparison method represented the instability of the measurement instrument only.

Also, the contact repeatability error of probing on aluminum pads was found from three identical measurement series A, B, and C, of the same wafer-embedded calibration set. Obtained results showed that the error between series AB, BC and AC are comparable and that it is larger than the instrument drift. It follows that the contact repeatability on aluminum pads affects experimental results more than the test instrument instability.

<sup>4</sup> SussCal is available from SUSS MicroTec.

<sup>5</sup> MultiCal software package is available from NIST.

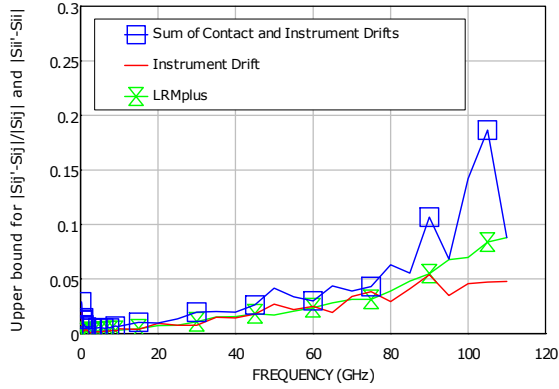


Fig. 2. The accuracy verification of the on-wafer LRM+ calibration.

The line capacitance per unit length was extracted and the characteristic impedance was found using the methods [14, 15]. The extracted value of the line capacitance is 1.5578 pF/cm. The Fig. 3-4 show the measured characteristic impedance, relative phase and attenuation constants of the lines.

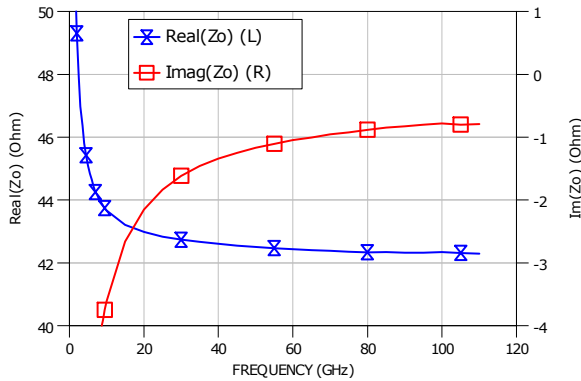


Fig. 3. Measured characteristic impedance of the line standard.

The measured parameters of the customized thru (Fig. 5), load (Fig. 6), and line standards were obtained from the multiline TRL with the reference impedance normalized to 50  $\Omega$ . As shown in the figures, the comparison of the measured parameters of standards and the simulation results exhibited good agreement.

Different resistors were compared to evaluate the influence of fabrication tolerances: the load used for the LRM+ calibration and loads from the Open-Resistor, Resistor-Open, Short-Resistor, Resistor-Short structures as illustrated in Fig. 6. All resistor structures had the same layout geometries. It was found that the load impedance variation error was

comparable with the contact repeatability error of this experiment.

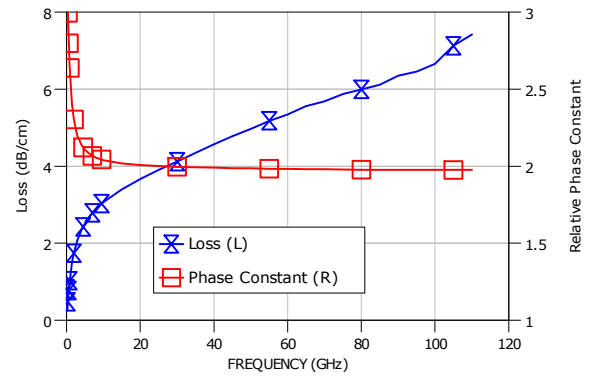


Fig. 4. Measured relative phase and attenuation constants of the line standard.

Next, the on-wafer LRM+ calibration was verified against the benchmark multiline TRL. As shown in Fig. 2, the error of the on-wafer LRM+ is comparable with the system instrument drift and the contact repeatability error for measurements on silicon.

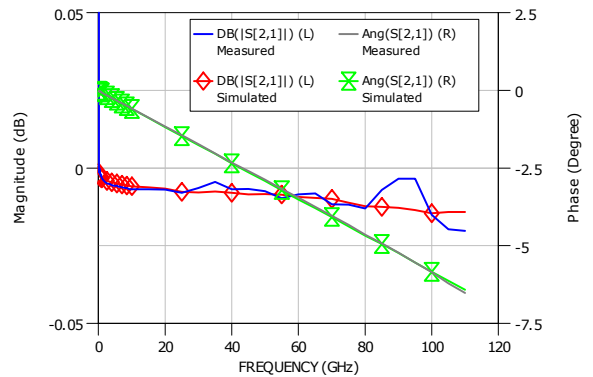


Fig. 5. Comparison of the simulated and measured characteristics of the 24  $\mu\text{m}$  thru standards. The measured parameters were obtained with respect to the multiline TRL calibration method and with the reference impedance normalized to 50  $\Omega$ .

Finally, the same NFET transistor with a gate length of 0.12  $\mu\text{m}$  was measured using the conventional two steps probe-tip (off-wafer) SOLT calibration and the open and short DUT contact pads were de-embedded. This data was compared with the data measured using the on-wafer TRL and LRM+ calibration procedures. Key device parameters  $C_{gs}$  and  $C_{gd}$  were extracted and compared as shown in Fig. 7. These results show both on-wafer calibration methods are comparable and are a significant improvement for critical

parameter extraction over the SOLT calibration with open/short de-embedding over the frequency range of 1 to 110 GHz.

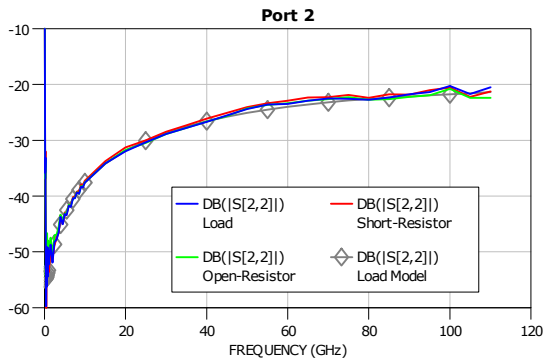


Fig. 6. Comparison of the simulated and measured characteristics of load standard for the second port elements for the LRM+ load, the Open-Resistor, and the Short-Resistor de-embedding structures. The measured parameters were obtained with respect to the multiline TRL calibration method and with the reference impedance normalized to 50  $\Omega$ .

## VI. CONCLUSION

Summarizing, for the first time the LRM+ calibration was quantitatively verified on a challenging high performance RF silicon CMOS technology. It was demonstrated that the accuracy of the on-wafer multiline TRL and LRM+ calibration methods outperform the conventional off-wafer calibration with the DUT contact pad parasitics de-embedded.

Both the LRM+ and the benchmark NIST multiline TRL method are in very good agreement. This proves LRM+ to be a valuable tool as it overcomes the main drawback of multiline TRL: construction of wafer-embedded transmission lines. LRM+ does not require long transmission line calibration standards but nevertheless provides comparable calibration accuracy. LRM+, therefore, saves wafer space, minimizing the test chip size to only three standards, realized in the same padset as the DUT. Thus, a fully automated calibration is possible even when using a fixed wafer probe configuration. The required determination of the electrical model of the load standards needed in the calibration can be done easily, e.g., by means of the approaches presented in [7].

As shown above, LRM+ can be successfully used for advanced RF CMOS applications up to 110 GHz.

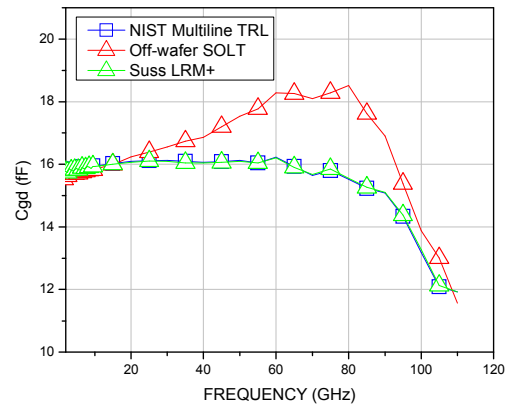
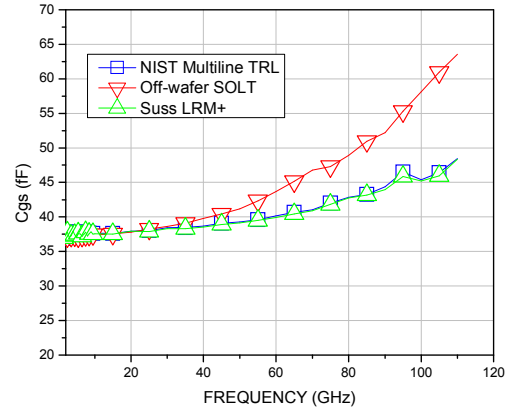


Fig. 7. The test device parameters  $C_{gs}$  and  $C_{gd}$  extracted with respect to the on-wafer multiline TRL and LRM+ calibration procedures and the conventional two-step technique (probe-tip SOLT with the pad de-embedding). The on-wafer TRL and LRM+ shows extremely good agreement over the frequency range and outperforms the conventional method for accuracy of parameter extraction.

## REFERENCES

- [1] P. J. van Wijnen and L. C. Smith, "High frequency characterization of small geometry bipolar transistors," in *Bipolar Circuits and Technology Meeting*, 1988, pp. 91-94.
- [2] D. Williams, R. Marks, K. Phillips, and T. Miers, "Progress toward MMIC on-wafer standards," in *ARFTG Microwave Measurements Conference-Fall, 36th*, 1990, pp. 73-83.
- [3] T. E. Kolding, "A four-step method for de-embedding gigahertz on-wafer CMOS measurements," *IEEE Transactions on Electron Devices*, vol. 47, pp. 734-740, 2000.
- [4] T. E. Kolding, "On-wafer calibration techniques for giga-hertz CMOS measurements," in *International Conference on Microelectronic Test Structures*, 1999, pp. 105-110.
- [5] L. F. Tiemeijer, R. J. Havens, A. B. M. Jansman, and Y. Bouttemont, "Comparison of the "pad-open-short" and "open-short-load" deembedding techniques for accurate on-wafer RF characterization of high-quality passives," *IEEE Transactions on Microwave Theory and Techniques*, vol. 53, pp. 723-729, 2005.

- [6] X. Wei, G. Niu, S. Sweeney, Q. Liang, X. Wang, and S. Taylor, "A general 4-port solution for 110 GHz On-wafer transistor measurements with or without impedance standard substrate (ISS) calibration," *Electron Devices, IEEE Transactions on*, vol. 54, pp. 2706-2714, 2007.
- [7] R. F. Scholz, F. Korndorfer, B. Senapati, and A. Rumiantsev, "Advanced technique for broadband on-wafer RF device characterization," in *ARFTG Microwave Measurements Conference-Spring, 63rd*, 2004, pp. 83-90.
- [8] D. F. Williams, U. Arz, and H. Grabinski, "Characteristic-impedance measurement error on lossy substrates," *Microwave and Wireless Components Letters, IEEE*, vol. 11, pp. 299-301, 2001.
- [9] D. F. Williams, U. Arz, and H. Grabinski, "Accurate Characteristic Impedance Measurement on Silicon," in *ARFTG Conference Digest-Spring, 51st*, 1998, pp. 155-158.
- [10] J. Leinhos and U. Arz, "Effect of uncertainties in the cross-sectional parameters on the wideband electrical properties of coplanar waveguides," in *Signal Propagation on Interconnects, 2007. SPI 2007. IEEE Workshop on*, 2007, pp. 35-38.
- [11] R. B. Marks, "A multilayer method of network analyzer calibration," *Microwave Theory and Techniques, IEEE Transactions on*, vol. 39, pp. 1205-1215, 1991.
- [12] A. Rumiantsev and N. Ridler, "VNA calibration," *Microwave Magazine, IEEE*, vol. 9, pp. 86-99, 2008.
- [13] D. F. Williams, R. B. Marks, and A. Davidson, "Comparison of on-wafer calibrations," in *ARFTG Microwave Measurements Conference-Fall, 38th*, vol. 20, 1991, pp. 68-81.
- [14] D. F. Williams and R. B. Marks, "Transmission line capacitance measurement," *Microwave and Guided Wave Letters, IEEE*, vol. 1, pp. 243-245, 1991.
- [15] R. B. Marks and D. F. Williams, "Characteristic impedance determination using propagation constant measurement," *IEEE Microwave and Guided Wave Letters*, vol. 1, pp. 141-143, June 1991.

# A General Closed-Form Solution to Multi-Port Scattering Parameter Calculations

Peter Wittwer and Peter J. Pupalaiakis, *Senior Member, IEEE*

**Abstract**—measurements using error terms to describe the imperfections of test equipment have been used for a long time, and there are many methods utilized to model the error terms. In all these methods, after having determined the error terms on the basis of calibration measurements, the s-parameters of the device-under-test (DUT) are computed from the measured s-parameters by an appropriate algorithm. One problem that arises in this context is that the methods used for calculating the s-parameters, while widely known for the one- and two-port case, appear to not be generally available for the multi-port situation. This paper addresses this situation by deriving a simple method which allows for calculating the s-parameters of a multi-port DUT from the measured s-parameters, using the error terms obtained in the calibration step. The method generates exact, closed-form solutions, and is applicable to all error models in use today.

## I. INTRODUCTION

S-PARAMETER measurements using error models to describe the imperfections of test equipment have been used for a long time, and there are many methods in use. In all cases the procedure is similar: in a first step calibration measurements are performed, which permit the calculation of the error terms of the error model under consideration, and, in a second step, the s-parameters of the device-under-test (DUT) are determined from the measured s-parameters by using an appropriate error correction scheme.

There is an extensive literature concerning the first step [1], [2], [3], [4], [5], [6], [7], [8], [9], [10], [11], [12], and detailed procedures have been worked out for the general  $N$ -port case, which permit determination of the error terms for a wide variety of error models. In one such error model, called SOLT, a calibrated short, open and load are connected to each port and reflected waves are measured to determine three error terms for each port. In addition, for each driven port, a cross-talk error term is measured between the driven and each undriven port in the system. Finally, a calibrated thru is applied between each possible port connection and reflected waves are measured for waves driven from each of the ports. This makes for a total of  $N_E = 3N^2$  error terms in the case with  $N$  ports. In particular for the two port case we have  $N_E = 12$

P. Wittwer is with the Department of Theoretical Physics, University of Geneva, Geneva, CH, e-mail: peter.wittwer@physics.unige.ch.

P. Pupalaiakis is with LeCroy Corporation, Chestnut Ridge, NY, USA, e-mail: PeterP@LeCroy.com

Manuscript received September 8, 2008; revised October 15, 2008.

and this error model is therefore often also referred to as the twelve-term error model. In some cases, imperfect calibration standards are modelled and applied to the ports of the measurement instrument to improve the accuracy. This leads for the two port case to the so called sixteen-term error model [13].

In what follows we concentrate not on the question of choosing an adequate error model or on the question on how to proceed to determine the error terms of the model by calibration measurements, but we address the question how to determine the s-parameters of the DUT from the measured s-parameters, once the error terms are known. While for the one- and two-port case closed-form solutions for the error correction step are known [10], there appears to be no universally applicable algorithm available for the general  $N$ -port case. Available techniques are either iterative [8], or are based on a change of variables which use the specificities of an error model in order to obtain a closed form solution [2], [3]. In what follows we present a rapid, simple to use algorithm, which solves this problem for the  $N$ -port case and is so general, that it applies without restrictions to any error model satisfying some very basic criteria. It applies in particular to all error models which are in use and for which calibration schemes have been worked out. Since the method is independent of the error model used, we base our presentation here for simplicity on the  $N$ -port version of the twelve-term error model which is widely known and applied, but we maintain that the technique is easily rewritten for any other error model that meets certain simple to verify criteria.

## II. EQUATION SETUP FOR TWELVE-TERM MODEL

A DUT has unknown s-parameters and it is desired to measure and determine these s-parameters in order to characterize the device. Ideally, for a device with  $N$  ports, reflected waves at the  $N$  ports of the device are measured under  $N$  independent measurement conditions. The equations that relate for each measurement condition  $m \in \{1, \dots, N\}$  the reflected waves to the incident waves are:

$$\begin{bmatrix} s_{11} & s_{12} & \dots & s_{1N} \\ s_{21} & s_{22} & \dots & s_{2N} \\ \dots & \dots & \dots & \dots \\ s_{N1} & s_{N2} & \dots & s_{NN} \end{bmatrix} \cdot \begin{bmatrix} a_{1m} \\ a_{2m} \\ \dots \\ a_{Nm} \end{bmatrix} = \begin{bmatrix} b_{1m} \\ b_{2m} \\ \dots \\ b_{Nm} \end{bmatrix} \quad (1)$$

where, for  $i \in \{1, \dots, N\}$ ,  $a_{im}$  is a complex number corresponding to amplitude and phase of the incident

wave at port  $i$  under measurement condition  $m$ , and where  $b_{im}$  is a complex number corresponding to amplitude and phase of the reflected wave at port  $i$  under measurement condition  $m$ . Ideally, one would apply stimuli to each of the  $N$  ports under  $N$  unique measurement conditions (*i.e.*, define the incident waves  $a_{im}$ ) and then measure the reflected waves at each of the  $N$  ports under these  $N$  measurement conditions (*i.e.*, measure  $b_{im}$ ) in order to determine the unknown s-parameters. If we define the matrices  $\mathbf{A}' = (a_{im})$  and  $\mathbf{B}' = (b_{im})$ , then the matrix  $\mathbf{S}' = (s_{im})$  of unknown s-parameters is<sup>1</sup>  $\mathbf{S}' = \mathbf{B}' \cdot \mathbf{A}'^{-1}$ .

In practice, it is of course not possible to make these idealized measurements, so one relies on calibration and error correction. In the above mentioned SOLT calibration, error terms are introduced through additional circuits, so called structures, that are virtually connected to the ports of the device under test. Different structures are used for each port that is driven, and for any undriven port.

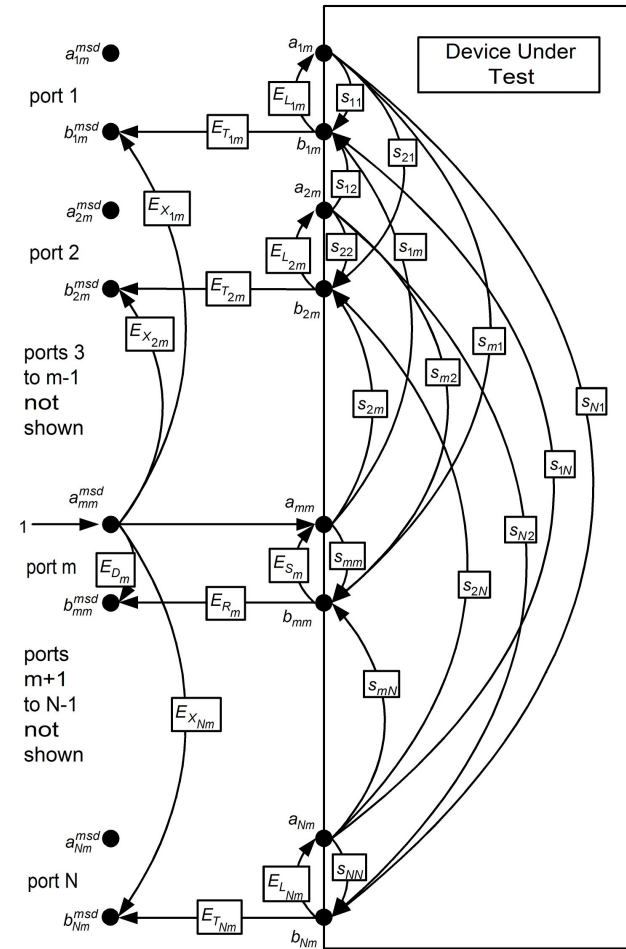


Fig1. Signal flow diagram illustrating the twelve-term error model

Such a situation is illustrated in Figure 1 for the SOLT calibration scheme of the so called twelve-term error

<sup>1</sup>For consistency with the notation that follows we use here for  $N \times N$  matrices names with a prime.

model. Each measurement condition is chosen to have an incident wave on one and one port only, with all other ports terminated in the reference impedance. Instead of the node values  $a_{im}$  and  $b_{im}$  of the device under test one therefore has node values  $a_{im}^{\text{msd}}$  and  $b_{im}^{\text{msd}}$ . The structures on the ports are such that when port  $m$  is driven, one has, on the driven port  $i = m$ , the equations

$$\begin{bmatrix} 1 & E_{S_m} \\ E_{D_m} & E_{R_m} \end{bmatrix} \cdot \begin{bmatrix} a_{mm}^{\text{msd}} \\ b_{mm}^{\text{msd}} \end{bmatrix} = \begin{bmatrix} a_{mm} \\ b_{mm}^{\text{msd}} \end{bmatrix} \quad (2)$$

with

$$a_{mm}^{\text{msd}} = 1 \quad (3)$$

and on each of the undriven ports  $i \in \{1, \dots, N\}$ ,  $i \neq m$ , the equations

$$\begin{bmatrix} 0 & E_{L_{im}} \\ E_{X_{im}} & E_{T_{im}} \end{bmatrix} \cdot \begin{bmatrix} a_{im}^{\text{msd}} \\ b_{im}^{\text{msd}} \end{bmatrix} = \begin{bmatrix} a_{im} \\ b_{im}^{\text{msd}} \end{bmatrix} \quad (4)$$

with

$$a_{im}^{\text{msd}} = 0 \quad (5)$$

whereby:

- $E_{S_m}$  refers to the source match error term for port  $m$ ,
- $E_{D_m}$  refers to the directivity error term for port  $m$ ,
- $E_{R_m}$  refers to the reflection error term for port  $m$ ,
- $E_{L_{im}}$  refers to the load match error term for port  $i$  when port  $m$  is driven,
- $E_{X_{im}}$  refers to the crosstalk error term for port  $i$  when port  $m$  is driven,
- $E_{T_{im}}$  refers to the transmission error term for port  $i$  when port  $m$  is driven.

At this point, we have the equations that govern the system for each measurement condition. Namely, for each  $m \in \{1, \dots, N\}$ , the  $4N$  equations (1)-(5) completely specify the nodal values  $a_{im}$ ,  $b_{im}$ ,  $a_{im}^{\text{msd}}$ ,  $b_{im}^{\text{msd}}$ , for  $i = 1, \dots, N$ , in terms of the (unknown) s-parameters and the (known) error terms. Our goal here is to solve the following inverse problem: for each measurement condition, *i.e.*, for each  $m \in \{1, \dots, N\}$ , and for given nodal values  $a_{im}^{\text{msd}}$ , one measures all the nodal values  $b_{im}^{\text{msd}}$ . This provides  $N$  values per measurement condition for a total of  $N^2$  measured values. Using these values and the known error terms, we now show how to determine the  $N^2$  unknown s-parameters. To this end we rewrite the equations (1)-(5) for each measurement condition in a particular form, namely in the form of equation (14) below. Once this system of equations is written down, we will give a list of properties it satisfies and upon which the extraction of the s-parameters is based. We will also make clear why these properties do not depend on the choice of the error model. In order to explain how to obtain equation (14) we now present two approaches, a first one based on a reordering of equations (1)-(5), and a second one directly based on the flow diagram Figure 1.

The first method for obtaining (14) is as follows: Consider, for fixed  $m \in \{1, \dots, N\}$ , the  $4 \times 4$  block matrices of  $N \times N$  matrices  $\mathbf{S}$  and  $\mathbf{E}_m$ ,

$$\mathbf{S} = \begin{bmatrix} \mathbf{S}' & 0 & 0 & 0 \\ 0 & 0 & 0 & 0 \\ 0 & 0 & 0 & 0 \\ 0 & 0 & 0 & 0 \end{bmatrix} \quad (6)$$

and

$$\mathbf{E}_m = \begin{bmatrix} 0 & 1 & 0 & 0 \\ 1 & -\mathbf{E}'_{m,3} & -\mathbf{D}'_m & 0 \\ 0 & 0 & 1 & 0 \\ 0 & -\mathbf{E}'_{m,2} & -\mathbf{E}'_{m,1} & 1 \end{bmatrix} \quad (7)$$

with  $\mathbf{S}'$  the matrix of s-parameters, with  $\mathbf{1}$  the  $N \times N$  identity matrix, with  $\mathbf{D}'_m$  a diagonal matrix with 1 in its  $m^{\text{th}}$  diagonal element and zero everywhere else, with  $\mathbf{E}'_{m,1}$  a matrix which is nonzero only in its  $m^{\text{th}}$  column, with the  $i^{\text{th}}$  element in this column being equal to  $E_{X_{im}}$  for  $i \neq m$ , and equal to  $E_{D_m}$  for  $i = m$ , with  $\mathbf{E}'_{m,2}$  a diagonal matrix with the  $i^{\text{th}}$  diagonal elements equal to  $E_{T_{im}}$  for  $i \neq m$ , and equal to  $E_{R_m}$  for  $i = m$ , and with  $\mathbf{E}'_{m,3}$  a diagonal matrix with the  $i^{\text{th}}$  diagonal elements equal to  $E_{L_{im}}$  for  $i \neq m$ , and equal to  $E_{S_m}$  for  $i = m$ , and with 0 the  $N \times N$  zero matrix. Define furthermore the vectors with  $N$  components,

$$\mathbf{a}'_m = [a_{1m} \ a_{2m} \ \dots \ a_{Nm}]^T \quad (8)$$

$$\mathbf{b}'_m = [b_{1m} \ b_{2m} \ \dots \ b_{Nm}]^T \quad (9)$$

$$\mathbf{a}_m^{\text{msd}} = [a_{1m}^{\text{msd}} \ a_{2m}^{\text{msd}} \ \dots \ a_{Nm}^{\text{msd}}]^T \quad (10)$$

$$\mathbf{b}_m^{\text{msd}} = [b_{1m}^{\text{msd}} \ b_{2m}^{\text{msd}} \ \dots \ b_{Nm}^{\text{msd}}]^T \quad (11)$$

where  $T$  denotes the transpose, and the vector

$$\mathbf{e}'_m = [0 \ \dots \ 0 \ 1 \ 0 \ \dots \ 0]^T \quad (12)$$

which has the number 1 in its  $m^{\text{th}}$  component and zero everywhere else, and finally the vectors with  $4N$  components  $\mathbf{x}_m$ ,  $\mathbf{b}_m^{\text{msd}}$ , and  $\mathbf{e}_m$ ,

$$\mathbf{x}_m = \begin{bmatrix} \mathbf{a}'_m \\ \mathbf{b}'_m \\ \mathbf{a}_m^{\text{msd}} \\ 0 \end{bmatrix} \quad \mathbf{b}_m^{\text{msd}} = \begin{bmatrix} 0 \\ 0 \\ 0 \\ \mathbf{b}_m^{\text{msd}} \end{bmatrix} \quad \mathbf{e}_m = \begin{bmatrix} 0 \\ 0 \\ \mathbf{e}'_m \\ 0 \end{bmatrix} \quad (13)$$

where 0 denotes the zero vector with  $N$  components. Then the equations (1)-(5) can be written as:

$$(-\mathbf{S} + \mathbf{E}_m) \cdot (\mathbf{x}_m + \mathbf{b}_m^{\text{msd}}) = \mathbf{e}_m \quad (14)$$

Indeed, from the first component in the matrix product in (14) we get that  $-\mathbf{S}' \cdot \mathbf{a}'_m + \mathbf{b}'_m = 0$ , which is nothing else than (1), from the second component we get that  $\mathbf{a}'_m - \mathbf{E}'_{m,3} \cdot \mathbf{b}'_m - \mathbf{D}'_m \cdot \mathbf{a}_m^{\text{msd}} = 0$ , which for  $i = m$  is the first equation in (2) and for  $i \neq m$  the first equation in (4), from the third component we get that  $\mathbf{a}_m^{\text{msd}} = \mathbf{e}'_m$ , which for  $i = m$  is equation (3) and for  $i \neq m$  equation (5), and finally we get from the fourth component that  $-\mathbf{E}'_{m,2} \cdot \mathbf{b}'_m - \mathbf{E}'_{m,1} \cdot \mathbf{a}_m^{\text{msd}} + \mathbf{b}_m^{\text{msd}} = 0$ , which for  $i = m$

is the second equation in (2) and for  $i \neq m$  the second equation in (4).

Alternatively, we can get equation (14) and its ingredients (except for the vector  $\mathbf{x}_m$  which is defined as in (13)) as follows: Examining the symmetry between (2) and (4) we first define the  $N \times N$  matrix of three component vectors  $\mathbf{ET}$ ,

$$\mathbf{ET}_{i,m} = \begin{cases} \begin{bmatrix} E_{D_m} \\ E_{R_m} \\ E_{S_m} \end{bmatrix} & \text{if } m = i \\ \begin{bmatrix} E_{X_{im}} \\ E_{T_{im}} \\ E_{L_{im}} \end{bmatrix} & \text{if } m \neq i \end{cases} \quad (15)$$

Using (15), we get from the equations (1)-(5), by writing them in the specified order, that<sup>2</sup>

$$(\mathbf{S})_{i,j} = s_{ij} \quad (16)$$

$$(\mathbf{E}_m)_{i,N+i} = 1 \quad (17)$$

$$(\mathbf{E}_m)_{N+i,i} = 1 \quad (18)$$

$$(\mathbf{E}_m)_{N+m,2 \cdot N+m} = -1 \quad (19)$$

$$(\mathbf{E}_m)_{N+i,N+i} = -(\mathbf{ET}_{i,m})_3 \quad (20)$$

$$(\mathbf{E}_m)_{2 \cdot N+i,2 \cdot N+i} = 1 \quad (21)$$

$$(\mathbf{E}_m)_{3 \cdot N+i,3 \cdot N+i} = 1 \quad (22)$$

$$(\mathbf{E}_m)_{3 \cdot N+i,N+i} = -(\mathbf{ET}_{i,m})_2 \quad (23)$$

$$(\mathbf{E}_m)_{3 \cdot N+i,2 \cdot N+m} = -(\mathbf{ET}_{i,m})_1 \quad (24)$$

$$(\mathbf{e}_m)_{2 \cdot N+m} = 1 \quad (25)$$

$$(\mathbf{b}_m^{\text{msd}})_{3 \cdot N+i} = b_{im}^{\text{msd}} \quad (26)$$

where  $(\mathbf{A})_{i,j}$  denotes the element of the matrix  $\mathbf{A}$  with row index  $i$  and column index  $j$ . Here,  $m \in \{1, \dots, N\}$  is considered fixed, whereas  $i, j$  are indices varying from 1 to  $N$ . Note that:

- (16) and (17) supply the  $N$  equations defining the nodes  $b_{im}$  for a given  $m$  mentioned in (1) with the unknown s-parameters going into  $\mathbf{S}$ .
- (18), (19), (20) supply the  $N$  equations defining the nodes  $a_{im}$  with (19) connecting node  $a_{mm}^{\text{msd}}$  to node  $a_{im}$  for the driving port  $m$  and (20) connecting nodes  $b_{im}$  to node  $a_{im}$  with a weight of either  $E_{S_m}$  when the port is driven (*i.e.*  $m = i$ ) or  $E_{L_{im}}$  when the port is not driven (*i.e.*  $m \neq i$ ).
- (21) and (25) supply the  $N$  equations for node  $a_{im}^{\text{msd}}$  where (25) supplies the incident wave at  $a_{mm}^{\text{msd}}$  for the driven port.
- (22), (23) and (24) supply the  $N$  equations for nodes  $b_{im}^{\text{msd}}$  with (23) connecting nodes  $b_{im}$  with nodes  $b_{im}^{\text{msd}}$  with a weight of either  $E_{R_m}$  when the port is driven or  $E_{T_{im}}$  when the port is not driven. (24) connects nodes

<sup>2</sup>All matrices are defined to be  $4N \times 4N$  and vectors are defined to be with  $4N$  components, and components of matrices and vectors are equal to zero unless specified.

$a_{mm}^{\text{msd}}$  with  $b_{im}^{\text{msd}}$  with a weight of either  $E_{D_m}$  when the port is driven or  $E_{X_{im}}$  when the port is not driven.

- (26) supplies the  $N$  known, directly measured reflected waves at nodes  $b_{im}^{\text{msd}}$  due to the incident wave on  $a_{mm}^{\text{msd}}$ .
- A total of  $4N$  equations are provided for  $4N$  nodes for each measurement condition  $m \in \{1, \dots, N\}$ .

With these remarks we again get for each measurement condition the system of equations (14).

Up to this point, the paper has concentrated on setting up (14) specifically using the twelve-term error model. This determined the exact number of nodes in the system, and the setup and contents of  $\mathbf{E}_m$ . It is important to note that an analogous system of equations will result also for any other error model. If the error model involves less nodes than the twelve-term error model does, then we can always add the missing nodes with a weight equal one in the flow diagram (this amounts to trivial equalities in (14)), and if the error model contains additional nodes when compared to the twelve-term error model we order the variables such that the additional equations appear after the first  $N$  of the above equations and before the last  $N$  of the above equations. In any case, the list of criteria which is given in the next section, which can be checked at this point and makes the solution for the s-parameters possible, will be naturally satisfied for any system consisting of a DUT plus additional circuitry describing the equipment errors.

### III. THE GENERAL, CLOSED-FORM SOLUTION

At this point it is important to identify some characteristics of the elements that make up the equation (14). Let  $D \geq 4 \cdot N$  (for the twelve-term error model  $D = 4 \cdot N$ ). Then, independent of the error model:

- $\mathbf{S}$  is a  $D \times D$  square matrix containing the unknown s-parameters in the upper left-hand corner (*i.e.* rows and columns 1 through  $N$ ).
- $\mathbf{E}_m$  is a  $D \times D$  square matrix. The matrix is 0 in the upper left-hand corner (*i.e.* rows and columns 1 through  $N$ ).
- $\mathbf{x}_m$  is a  $D$  element column vector and contains all unknown nodal values, but it is 0 in the last  $N$  elements.
- $\mathbf{b}_m^{\text{msd}}$  is a  $D$  element column vector that contains known, measured nodal values in the last  $N$  elements, but is 0 elsewhere.
- $\mathbf{e}_m$  is a  $D$  element column vector containing known applied stimuli.

These are the only ingredients that are necessary in order to be able to solve for the unknown s-parameters. Using this setup one can extract the s-parameters without having to determine all the unknowns of the system. To start we expand the product in (14) and get

$$-\mathbf{S} \cdot \mathbf{x}_m - \mathbf{S} \cdot \mathbf{b}_m^{\text{msd}} + \mathbf{E}_m \cdot \mathbf{x}_m + \mathbf{E}_m \cdot \mathbf{b}_m^{\text{msd}} = \mathbf{e}_m \quad (27)$$

Since  $\mathbf{S}$  is nonzero only in the first  $N$  rows and columns and since  $\mathbf{b}_m^{\text{msd}}$  is zero in the first  $N$  elements, we have that

$$\mathbf{S} \cdot \mathbf{b}_m^{\text{msd}} = 0 \quad (28)$$

Therefore, (27) becomes,

$$-\mathbf{S} \cdot \mathbf{x}_m + \mathbf{E}_m \cdot \mathbf{x}_m + \mathbf{E}_m \cdot \mathbf{b}_m^{\text{msd}} = \mathbf{e}_m \quad (29)$$

Multiplying in (29) from the left by  $\mathbf{E}_m^{-1}$  gives

$$-\mathbf{E}_m^{-1} \cdot \mathbf{S} \cdot \mathbf{x}_m + \mathbf{x}_m + \mathbf{b}_m^{\text{msd}} = \mathbf{E}_m^{-1} \cdot \mathbf{e}_m \quad (30)$$

We now define the vectors  $\mathbf{y}_m$  and  $\mathbf{d}_m$  by,

$$\mathbf{y}_m = \mathbf{S} \cdot \mathbf{x}_m \quad (31)$$

$$\mathbf{d}_m = \mathbf{E}_m^{-1} \cdot \mathbf{e}_m - \mathbf{b}_m^{\text{msd}} \quad (32)$$

so that (30) becomes

$$-\mathbf{E}_m^{-1} \cdot \mathbf{y}_m + \mathbf{x}_m = \mathbf{d}_m \quad (33)$$

Using the definition (13) of the vector  $\mathbf{x}_m$  and the definition (1) of  $\mathbf{S}'$ , namely that  $\mathbf{b}'_m = \mathbf{S}' \cdot \mathbf{a}'_m$ , we see from (31) that the vector  $\mathbf{y}_m$  is of the form

$$\mathbf{y}_m = \begin{bmatrix} \mathbf{b}'_m \\ 0 \\ 0 \\ 0 \end{bmatrix} \quad (34)$$

We now look at the last  $N$  components of (33). These components are equal to zero in the vector  $\mathbf{x}_m$ , and therefore the vector  $\mathbf{b}'_m$  can be determined. Namely,<sup>3</sup>

$$\mathbf{b}'_m = -[\text{submatrix}(\mathbf{E}_m^{-1}, D - N + 1, D, 1, N)]^{-1} \cdot [\text{submatrix}(\mathbf{d}_m, D - N + 1, D, 1, 1)] \quad (35)$$

Finally, now that  $\mathbf{b}'_m$  is known, we can determine the vector  $\mathbf{a}'_m$  by looking at the first  $N$  components in (33). Namely,

$$\mathbf{a}'_m = [\text{submatrix}(\mathbf{d}_m, 1, N, 1, 1)] + [\text{submatrix}(\mathbf{E}_m^{-1}, 1, N, 1, N)] \cdot \mathbf{b}'_m \quad (36)$$

This procedure is now repeated for each value of  $m \in \{1, \dots, N\}$ , which allows us to determine the matrices

$$\mathbf{A}' = \begin{bmatrix} \mathbf{a}'_1 & \mathbf{a}'_2 & \dots & \mathbf{a}'_N \end{bmatrix} \quad (37)$$

$$\mathbf{B}' = \begin{bmatrix} \mathbf{b}'_1 & \mathbf{b}'_2 & \dots & \mathbf{b}'_N \end{bmatrix} \quad (38)$$

and therefore the matrix  $\mathbf{S}'$  of unknown s-parameters, since

$$\mathbf{S}' = \mathbf{B}' \cdot \mathbf{A}'^{-1} \quad (39)$$

This procedure is summarized for the case of the twelve-term error model in the following struktogramm:

<sup>3</sup>Here,  $\text{submatrix}(\mathbf{A}, ri, rf, ci, cf)$  extracts from a matrix (or a vector)  $\mathbf{A}$  the portion between rows  $ri$  and  $rf$  and columns  $ci$  and  $cf$ .

<b>ComplexMatrix CalcSPParams(ET, SM)</b>
<p>Arguments:  Matrix &lt; ComplexVector &gt; ET  {  An N by N matrix of complex vectors representing the error terms such that for  <math>i \in \{1, \dots, N\}</math> and <math>m \in \{1, \dots, N\}</math>,  <math>ET[i][m] =</math>  <math display="block">\begin{cases} \begin{bmatrix} E_{Dm} \\ E_{Rm} \\ E_{Sm} \end{bmatrix} &amp; \text{if } m = i \\ \begin{bmatrix} E_{Xim} \\ E_{Tim} \\ E_{Lim} \end{bmatrix} &amp; \text{if } m \neq i \end{cases}</math>  }</p> <p>ComplexMatrix SM {  An N by N matrix such that for  <math>i \in \{1, \dots, N\}</math> and <math>m \in \{1, \dots, N\}</math>,  SM[i][m] represents the measured reflected wave at port i when port m is driven. }</p>
int N ← Rows(ET)
int m ∈ {1, ..., N}
ComplexMatrix E(4 · N, 4 · N, 0.0)
ComplexVector e(4 · N, 0.0)
ComplexVector b(4 · N, 0.0)
ComplexMatrix A'(N, N)
ComplexMatrix B'(N, N)
int i ∈ {1, ..., N}
E[i][N + i] ← 1.0
E[N + i][i] ← 1.0
E[N + m][2 · N + m] ← -1.0
E[N + i][N + i] ← -ET[i][m][2]
E[2 · N + i][2 · N + i] ← 1.0
E[3 · N + i][3 · N + i] ← 1.0
E[3 · N + i][N + i] ← -ET[i][m][1]
E[3 · N + i][2 · N + m] ← -ET[i][m][0]
b[3 · N + i] ← SM[i][m]
e[2 · N + m] ← 1
ComplexMatrix Ei ← E <sup>-1</sup>
ComplexVector d ← Ei · e - b
ComplexVector b' ← - submatrix(Ei, 3 · N + 1, 4 · N, 1, N) <sup>-1</sup> · ... submatrix(d, 3 · N + 1, 4 · N, 1, 1)
ComplexVector a' ← submatrix(d, 1, N, 1, 1) - ... submatrix(Ei, 1, N, 1, N) · b'
int i ∈ {1, ..., N}
A'[i][m] ← a'[i]
B'[i][m] ← b'[i]
ComplexMatrix S' ← B' · A' <sup>-1</sup>
return S'

#### IV. APPLICATION TO TWO-PORT CASE

To illustrate the algorithm, we use the preceding method to calculate the equations for the two-port case. We have<sup>4</sup>

$$\mathbf{E}_1 = \begin{bmatrix} 0 & 0 & 1 & 0 & 0 & 0 & 0 & 0 \\ 0 & 0 & 0 & 1 & 0 & 0 & 0 & 0 \\ 1 & 0 & -E_{SF} & 0 & -1 & 0 & 0 & 0 \\ 0 & 1 & 0 & -E_{LF} & 0 & 0 & 0 & 0 \\ 0 & 0 & 0 & 0 & 1 & 0 & 0 & 0 \\ 0 & 0 & 0 & 0 & 0 & 1 & 0 & 0 \\ 0 & 0 & -E_{RF} & 0 & -E_{DF} & 0 & 1 & 0 \\ 0 & 0 & 0 & -E_{TF} & -E_{XF} & 0 & 0 & 1 \end{bmatrix} \quad (40)$$

$$\mathbf{E}_2 = \begin{bmatrix} 0 & 0 & 1 & 0 & 0 & 0 & 0 & 0 \\ 0 & 0 & 0 & 1 & 0 & 0 & 0 & 0 \\ 1 & 0 & -E_{LR} & 0 & 0 & 0 & 0 & 0 \\ 0 & 1 & 0 & -E_{SR} & 0 & -1 & 0 & 0 \\ 0 & 0 & 0 & 0 & 1 & 0 & 0 & 0 \\ 0 & 0 & 0 & 0 & 0 & 1 & 0 & 0 \\ 0 & 0 & -E_{TR} & 0 & 0 & -E_{XR} & 1 & 0 \\ 0 & 0 & 0 & -E_{RR} & 0 & -E_{DR} & 0 & 1 \end{bmatrix} \quad (41)$$

and

$$\mathbf{e}_1 = [0 \ 0 \ 0 \ 0 \ 1 \ 0 \ 0 \ 0]^T \quad (42)$$

$$\mathbf{e}_2 = [0 \ 0 \ 0 \ 0 \ 0 \ 1 \ 0 \ 0]^T \quad (43)$$

and finally

$$\mathbf{b}_1^{\text{msd}} = [0 \ 0 \ 0 \ 0 \ 0 \ 0 \ S_{11M} \ S_{21M}]^T \quad (44)$$

$$\mathbf{b}_2^{\text{msd}} = [0 \ 0 \ 0 \ 0 \ 0 \ 0 \ S_{12M} \ S_{22M}]^T \quad (45)$$

We therefore get that

$$(\mathbf{E}_1)^{-1} = \begin{bmatrix} E_{SF} & 0 & 1 & 0 & 1 & 0 & 0 & 0 \\ 0 & E_{LF} & 0 & 1 & 0 & 0 & 0 & 0 \\ 1 & 0 & 0 & 0 & 0 & 0 & 0 & 0 \\ 0 & 1 & 0 & 0 & 0 & 0 & 0 & 0 \\ 0 & 0 & 0 & 0 & 1 & 0 & 0 & 0 \\ 0 & 0 & 0 & 0 & 0 & 1 & 0 & 0 \\ E_{RF} & 0 & 0 & 0 & E_{DF} & 0 & 1 & 0 \\ 0 & E_{TF} & 0 & 0 & E_{XF} & 0 & 0 & 1 \end{bmatrix} \quad (46)$$

$$(\mathbf{E}_2)^{-1} = \begin{bmatrix} E_{LR} & 0 & 1 & 0 & 0 & 0 & 0 & 0 \\ 0 & E_{SR} & 0 & 1 & 0 & 1 & 0 & 0 \\ 1 & 0 & 0 & 0 & 0 & 0 & 0 & 0 \\ 0 & 1 & 0 & 0 & 0 & 0 & 0 & 0 \\ 0 & 0 & 0 & 0 & 1 & 0 & 0 & 0 \\ 0 & 0 & 0 & 0 & 0 & 1 & 0 & 0 \\ E_{TR} & 0 & 0 & 0 & 0 & E_{XR} & 1 & 0 \\ 0 & E_{RR} & 0 & 0 & 0 & E_{DR} & 0 & 1 \end{bmatrix} \quad (47)$$

<sup>4</sup>For comparison with the literature we use here the notation in [13]. We have the following correspondence:  $E_{DF} = E_{D1}$ ,  $E_{RF} = E_{R1}$ ,  $E_{SF} = E_{S1}$ ,  $E_{DR} = E_{D2}$ ,  $E_{RR} = E_{R2}$ ,  $E_{SR} = E_{S2}$ ,  $E_{XF} = E_{X21}$ ,  $E_{TF} = E_{T21}$ ,  $E_{LF} = E_{L21}$ ,  $E_{XR} = E_{X12}$ ,  $E_{TR} = E_{T12}$ ,  $E_{LR} = E_{L12}$ ,  $S_{11M} = b_{11}^{\text{msd}}$ ,  $S_{12M} = b_{12}^{\text{msd}}$ ,  $S_{21M} = b_{21}^{\text{msd}}$ ,  $S_{22M} = b_{22}^{\text{msd}}$ .

and therefore that

$$\mathbf{d}_1 = (\mathbf{E}_1)^{-1} \cdot \mathbf{e}_1 - \mathbf{b}_1^{\text{msd}} = \begin{bmatrix} 1 \\ 0 \\ 0 \\ 0 \\ 1 \\ 0 \\ E_{DF} - S_{11M} \\ E_{XF} - S_{21M} \end{bmatrix} \quad (48)$$

and

$$\mathbf{d}_2 = (\mathbf{E}_2)^{-1} \cdot \mathbf{e}_2 - \mathbf{b}_2^{\text{msd}} = \begin{bmatrix} 0 \\ 1 \\ 0 \\ 0 \\ 0 \\ 1 \\ E_{XR} - S_{12M} \\ E_{DR} - S_{22M} \end{bmatrix} \quad (49)$$

We therefore have that

$$\mathbf{b}'_1 = -[\text{submatrix}((\mathbf{E}_1)^{-1}, 3 \cdot 2 + 1, 4 \cdot 2, 1, 2)]^{-1} \cdot [\text{submatrix}(\mathbf{d}_1, 3 \cdot 2 + 1, 4 \cdot 2, 1, 1)] \quad (50)$$

and therefore that

$$\mathbf{b}'_1 = - \begin{bmatrix} \frac{E_{DF} - S_{11M}}{E_{RF}} \\ \frac{E_{XF} - S_{21M}}{E_{TF}} \end{bmatrix} \quad (51)$$

and similarly that

$$\mathbf{b}'_2 = -[\text{submatrix}((\mathbf{E}_2)^{-1}, 3 \cdot 2 + 1, 4 \cdot 2, 1, 2)]^{-1} \cdot [\text{submatrix}(\mathbf{d}_2, 3 \cdot 2 + 1, 4 \cdot 2, 1, 1)] \quad (52)$$

and therefore that

$$\mathbf{b}'_2 = - \begin{bmatrix} \frac{E_{XR} - S_{12M}}{E_{TR}} \\ \frac{E_{DR} - S_{22M}}{E_{RR}} \end{bmatrix} \quad (53)$$

Using (51) and (53) we get that

$$\mathbf{a}'_1 = [\text{submatrix}(\mathbf{d}_1, 1, 2, 1, 1)] + [\text{submatrix}((\mathbf{E}_1)^{-1}, 1, 2, 1, 2)] \cdot \mathbf{b}'_1 \quad (54)$$

and therefore that

$$\mathbf{a}'_1 = \begin{bmatrix} \frac{E_{RF} - E_{SF} \cdot E_{DF} + E_{SF} \cdot S_{11M}}{E_{RF}} \\ \frac{E_{LF} \cdot (S_{21M} - E_{XF})}{E_{TF}} \end{bmatrix} \quad (55)$$

and similarly we have that

$$\mathbf{a}'_2 = [\text{submatrix}(\mathbf{d}_2, 1, 2, 1, 1)] + [\text{submatrix}((\mathbf{E}_2)^{-1}, 1, 2, 1, 2)] \cdot \mathbf{b}'_2 \quad (56)$$

and therefore that

$$\mathbf{a}'_2 = \begin{bmatrix} \frac{E_{LR} \cdot (S_{12M} - E_{XR})}{E_{TR}} \\ \frac{E_{RR} - E_{SR} \cdot E_{DR} + E_{SR} \cdot S_{22M}}{E_{RR}} \end{bmatrix} \quad (57)$$

We finally get that  $\mathbf{S}' = [\mathbf{b}'_1 \quad \mathbf{b}'_2] \cdot [\mathbf{a}'_1 \quad \mathbf{a}'_2]^{-1}$  and explicitly that

$$\mathbf{S}' = - \begin{bmatrix} \frac{E_{DF} - S_{11M}}{E_{RF}} & \frac{E_{XR} - S_{12M}}{E_{TR}} \\ \frac{E_{XF} - S_{21M}}{E_{TF}} & \frac{E_{DR} - S_{22M}}{E_{RR}} \end{bmatrix} \cdot \begin{bmatrix} \frac{E_{RF} - E_{SF} \cdot E_{DF} + E_{SF} \cdot S_{11M}}{E_{RF}} & \frac{E_{LR} \cdot (S_{12M} - E_{XR})}{E_{TR}} \\ \frac{E_{LF} \cdot (S_{21M} - E_{XF})}{E_{TF}} & \frac{E_{RR} - E_{SR} \cdot E_{DR} + E_{SR} \cdot S_{22M}}{E_{RR}} \end{bmatrix}^{-1} \quad (58)$$

Expanding (58) one arrives at the s-parameter equations in [13].

## V. CONCLUSION

In this article we have addressed the question of how to determine the s-parameters of a DUT from the measured s-parameters once the error terms have been determined through calibration. The method provides an explicit, simple to use algorithm, is completely general, and does not use any of the specificities of an error model. It applies in particular to all the existing error models for which calibration schemes have been worked out. It generalizes without restrictions to any future error model satisfying some very basic criteria. We expect the method to be of direct use in the design of multi-port test equipment.

## REFERENCES

- [1] B. S. H.-J. Eul, "A generalized theory and new calibration procedures for network analyzer self-calibration," *IEEE Transactions on Microwave Theory and Techniques*, vol. 39, pp. 724–731, 1991.
- [2] A. Ferrero and U. Pisani, "Multiport vector network analyzer calibration: A general formulation," *IEEE Transactions on Microwave Theory and Techniques*, vol. 42, pp. 2455–2461, 1994.
- [3] A. Ferrero, U. Pisani, and K. J. Kerwin, "A new implementation of a multiport automatic network analyzer," *IEEE Transactions on Microwave Theory and Techniques*, vol. 40, pp. 2078–2085, 1992.
- [4] H. Heuermann, "Multi-port calibration techniques for differential parameter measurements with network analyzers," in *Rohde and Schwarz workshop, EUMC*, 2003.
- [5] T. Meyer, A. Jostingmeier, N. Spiliotis, and A. S. Omar, "Multiport scattering parameter measuring system," in *ARFTG Microwave Measurement Conference*, vol. 62, 2003, pp. 269–273.
- [6] H. Pham, E. J. Kim, and A. W. England, "An analytical calibration approach for microwave polarimetric radiometers," *IEEE Transactions on geoscience and remote sensing*, vol. 43, pp. 0196–2892, 2005.
- [7] S. Rehnmark, "On the calibration process of automatic network analyzer systems," *IEEE transactions on Microwave Theory and Techniques*, vol. 22, pp. 457–458, Apr 1974.
- [8] I. Rolfes and B. Schiek, "Methods for the calibrated measurement of the scattering parameters of planar multi-port devices," *Adv. radio Sci.*, vol. 5, pp. 439–445, 2007.
- [9] —, "Multiport method for the measurement of the scattering parameters of n-ports," *IEEE trans. microwave theor. tech.*, vol. 53, pp. 1990–1996, 2005.
- [10] D. Rytting, "Network analyzer error models and calibration methods," in *Short Course on Computer-Aided RF and Microwave Testing and Design*, 1998.
- [11] K. J. Silvonon, "A general approach to network analyzer calibration," *IEEE Transactions on Microwave Theory and Techniques*, vol. 40, pp. 754–759, 1992.
- [12] D. F. Williamns, J. C. M. Wang, and U. Arz, "An optimal vector-network-analyzer calibration algorithm," *IEEE transactions in microwave theory and techniques*, vol. 51, pp. 2391–2401, 2003.
- [13] D. C. DeGroot, J. A. Jargon, and K. L. Reed, "Equivalent circuit models for coaxial oslt standards," in *ARFTG Conference*, December 1999.



**Peter Wittwer** was born in Bern, Switzerland in 1955 and received the M.S. degree in Mathematics and Physics from ETH, Zürich, Switzerland in 1980 and the Ph.D. in Physics from the University of Geneva, Geneva, Switzerland in 1984. Until 1985 he was then a visiting member of the CIMS, New York University, New York, and until 1988 Hill assistant professor at the mathematics department of Rutgers University, New Brunswick, New Jersey. In 1989 he returned to Switzerland to join the informatics

department of SwissRe, Zürich, where he worked on the design of relational data base models, and on the formulation of data exchange standards for insurance business. Since 1990 he is a member of the theoretical physics department of the University of Geneva, and since 2005 he is a titular professor of the University of Geneva.



**Peter J. Pupalaiakis** (M'03, SM'08) was born in Boston, Massachusetts in 1964 and received the B.S. degree in electrical engineering from Rutgers University, New Brunswick, New Jersey in 1988.

He joined LeCroy Corporation, a manufacturer of high-performance measurement equipment located in Chestnut Ridge, New York in 1995 where he is currently Vice President and Principal Technologist. He works for the CTO on technology development for high-speed wave-

form digitizing systems and his interests include digital signal processing, applied mathematics, signal integrity and RF/microwave systems. Prior to LeCroy he served in the United States Army and has worked as an independent consultant in embedded systems design.

Mr. Pupalaiakis holds sixteen patents in the area of measurement instrument design and is a member of Tau Beta Pi, Eta Kappa Nu and the IEEE signal processing, communications, and microwave societies.

# Benchmarking Comparison of Thermal and Diode Sensors for Pulsed Power Measurement

Sivalingam Somasundaram Meena<sup>1</sup>, Charles Baylis<sup>2</sup>, Lawrence Dunleavy<sup>3</sup>

<sup>1</sup>Center for Wireless and Microwave Information Systems,  
Department of Electrical Engineering, University of South Florida, Tampa, Florida, USA

<sup>2</sup>Wireless and Microwave Circuits and Systems Program,  
Department of Electrical and Computer Engineering, Baylor University, Waco, Texas, USA

<sup>3</sup>Modelithics, Inc., Tampa, Florida, USA

**Abstract** – A pulsed power system has been constructed to explore conditions under which accurate pulsed power measurements can be made with both a thermal sensor and a diode sensor. For the thermal sensor, pulsed power is estimated from a simple calculation based on the average power of the pulsed RF signal. For the diode sensor, gating is used to enable direct measurement of the pulsed power. As expected, the results of measurements taken with varying pulse lengths and a constant period show that the dynamic range of the thermal sensor is approximately proportional to the pulse length. The results also indicate that, while a thermal sensor can provide accurate results for many situations, the diode sensor can be used to measure with higher precision than the thermal sensor for lower duty cycles. The paper demonstrates a benchmarking procedure that can be used to explore limitations and capabilities of power sensors as well as elements such as the input RF switch used for pulsed power measurements.

## I. INTRODUCTION

Pulsed RF signals are used in a wide variety of applications in modern communication systems. The applications vary from radar systems [1] to the mass production of silver (Ag) nano-sized powder for various industrial applications [2]. Pulsed RF also has become extensively used in characterization of active devices and it is more suitable for many applications than continuous-wave (CW) RF signals [3]. Using pulsed RF for load-pull provides various advantages. First, devices that are operated in pulsed condition in an application, such as radar, can be tested under the same conditions as in the final application. Second, the device temperature during measurement can be lower under pulsed conditions than for CW testing, reducing the chance of device failure during high-power device testing. Devices are often operated in pulsed mode because they can, in many cases, remain linear for higher RF power levels due to the reduction of thermally induced nonlinearities [1]. When both pulsed RF and pulsed DC measurements are combined they can provide insight into the influence of low frequency discrepancy effects (self heating or trapping effects) on the performance of transistors for modeling purposes [4]. Even before examining specific devices under test (DUTs),

however, it is shown herein that the duty cycle of the pulsed signal can have a strong impact on the test system capability (e.g. dynamic range); therefore, an understanding of test system accuracy for varied duty cycles is critical to obtaining reliable pulsed power data. While many publications can be found on the construction of pulsed load-pull systems (e.g. [5]). In the present paper, an experiment in which diode and thermal RF power sensors are compared for pulsed measurements at varying RF power levels and duty cycles to establish a solid baseline for pulsed testing with each of these sensor types.

## II. TERMS AND DEFINITIONS

The duty cycle is given in terms of the pulse width  $\tau$  and the period  $T$  as

$$\text{Duty Cycle} = \frac{\tau}{T} \quad (1)$$

Thus the duty cycle of the RF pulse can be increased by either increasing the pulse width or decreasing the time period of the RF signal. The Pulse Repetition Rate ( $f_p$ ) is the frequency at which the pulses occur and is given by

$$f_p = \frac{1}{T} \quad (2)$$

A thermal sensor was used first in this set-up. A thermal sensor calculates the pulsed power  $P_p$  in terms of average power  $P_a$  as follows [6]:

$$P_p = \frac{P_a}{\tau f_p} \quad (3)$$

where  $f_p$  can be calculated by (2),  $\tau$  is the pulse length and  $P_a$  is the average power. It is important to keep in mind that the above relationship holds good only if the pulses are approximately rectangular in shape. When the pulse shape is irregular it may lead to erroneous power measurements and so a shape factor correction must be applied. Often the shape

factor correction must be estimated and hence may be subject to a relatively large uncertainty [6].

In the second set of measurements, a diode sensor was used. Diode sensors are capable of measuring pulsed power due to their fast raise time. Diode sensors can be used to predict the peak voltage of the RF signal. The relation between the peak RF voltage and the rms power  $P_{rms}$  is given by [7] as

$$P_{rms} = \frac{(V_p \times 0.707)^2}{R} = \frac{V_p^2}{2R} \quad (4)$$

where R is the resistance of the load across which the diode is connected.

To validate or qualify a pulsed power system all the factors that influence it have to be taken into account. In an attempt to isolate the effects of duty cycle on the pulsed measurement results, multiple measurements of pulsed power were taken in which the time period was kept constant and the duty cycle was changed by varying the pulse width. When the pulsed power is derived from an average power measurement (as in the case of the thermal sensor), the dynamic range is reduced as the duty cycle is lowered. The reduction in dynamic range from a CW measurement for a pulsed power measurement with period T and pulse length  $\tau$  is given by

$$\text{Reduction in Dynamic Range} = 10 \log \frac{T}{\tau} \quad (5)$$

### III. EXPERIMENTAL SETUP

A symbolic representation of signals at different ports of the RF switch is depicted in Fig.1. Port A is the input port, port B is the signal applied to the control port of the switch, and port C is the output of the switch that is input to the device under test. In this work, both thermal and diode sensors were used to measure pulsed power. Fig. 2 shows the measurement setup, which includes a sensor (Anritsu MA2422B thermal sensor or Anritsu MA2411B diode sensor), UMCC - model # SR-T800-2S RF switch, power meter (Anritsu ML2496A pulsed power meter or Anritsu ML2438A power meter), HP 8648C signal generator, and a Highland P400 digital delay generator. The Automated Tuner System (ATS) software from Maury Microwave [8] was used to automate the measurements and make system loss corrections as applicable. The delay generator was used to provide the necessary logic control for the RF switch. An active-low switch was used for the measurement: when the digital control pulse is low, the switch passes the RF input through the switch.

### IV. RESULTS

For measurements performed with the thermal sensor, the average power is inherently measured by the sensor. The result is then converted to pulsed power by the software. Before taking any measurements, the duty cycle and the pulse repetition rate  $f_p$  must be input to the ATS software to allow the pulsed power to be accurately calculated.

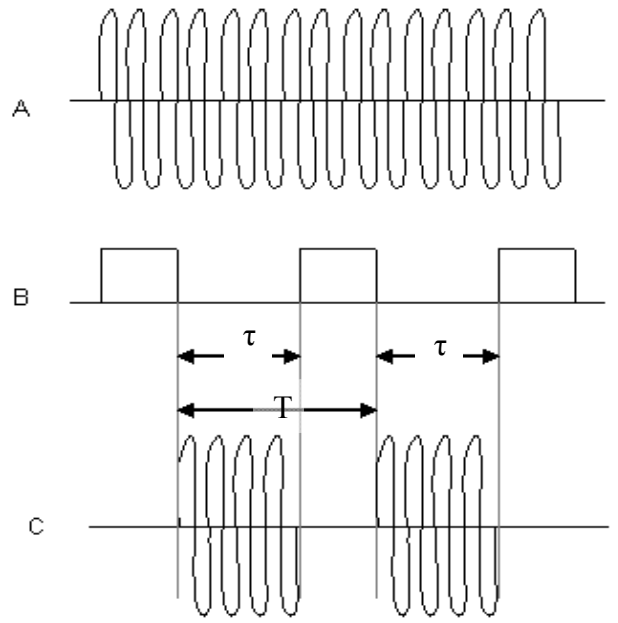


Fig.1: RF signal representation at ports A, B, and C of the RF switch as shown in Fig. 2

The pulsed power calibration is performed by changing the pulse width  $\tau$  of the control logic of the delay generator so that the pulse B shown in Fig. 2 changes. The RF switch allows the RF signal at TTL low to pass through it. The calibration of the system showed that the system had an input insertion loss, before the DUT, of -2.451 dB. The ATS software corrects for such losses as a result of the calibration procedure.

The reduction in dynamic range as pulse length is decreased for a thermal sensor can be seen when a calibration is performed. Fig. 3(a) shows the measured pulsed available power (at the sensor) versus the programmed power for various pulse lengths and a constant period of 100  $\mu$ s and RF signal frequency 2GHz.

In Fig.3 (a) the Y axis ( $P_{available}$ ) is the pulsed power calculated by Maury automatically when  $f_p$  and  $\tau$  are known. It is important to note while observing this data that the thermal sensor measures average power. For reduced pulse length (and hence reduced duty cycle) a reduction in the dynamic range of the sensor was observed due to the fact that the power is applied for a shorter amount of time, thus decreasing the average power delivered to the sensor. The thermal sensor used has a manufacturer specified dynamic range of -30dBm to 20dBm. Fig.3 (a) shows that as expected the sensor actually has an absolute low end that is lower than its specification. For a 50 % duty cycle (in the Fig. 3 case a 50  $\mu$ s pulse length), the average power detected by the sensor at each pulsed power setting is 3 dBm lower than in the continuous-power case. For the 50 % case, it would be expected that a pulsed power of  $-30+3 = -27$  dBm would be the lowest pulsed power measurable by the sensor, based on the specified range.

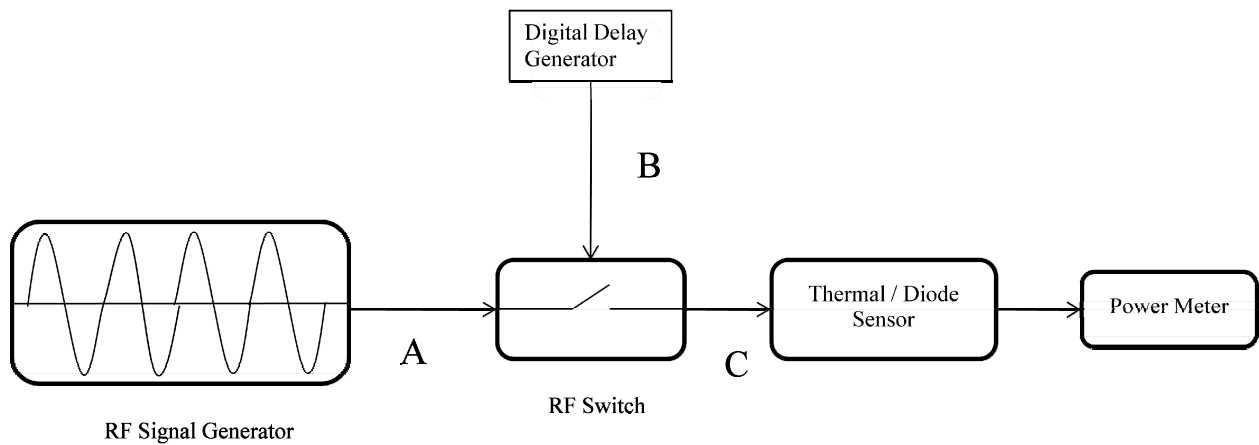


Fig.2: Pulse Power Measurement Set-Up

The duty cycle of 5 percent (5  $\mu$ s pulse length) means that the average power that can be measured in each setting is reduced by approximately 13 dBm, this effect can be clearly observed from Fig.3 (a). In Fig.3 (b) we can see the same plot with Y axis as average Pout (available) in which we can clearly see the lower limit of the sensor is actually around -34 dBm where it hits the noise floor. Because the specification for the low-power measurement limit of the sensor is -30 dBm (the actual observed lower limit during the experiments was -34 dBm), for the case of a 5 percent duty cycle, the lower limit for pulse power is  $(-30 + 13) = -17$  dBm.

This is consistent with the results in Fig. 3a. The results in Fig.3(b) indicate that this setting allows measurements to about -20 or -21 dBm (the sensor seems to show a trend of possessing a “noise floor” about 3 or 4 dB lower than would be calculated from the specification).

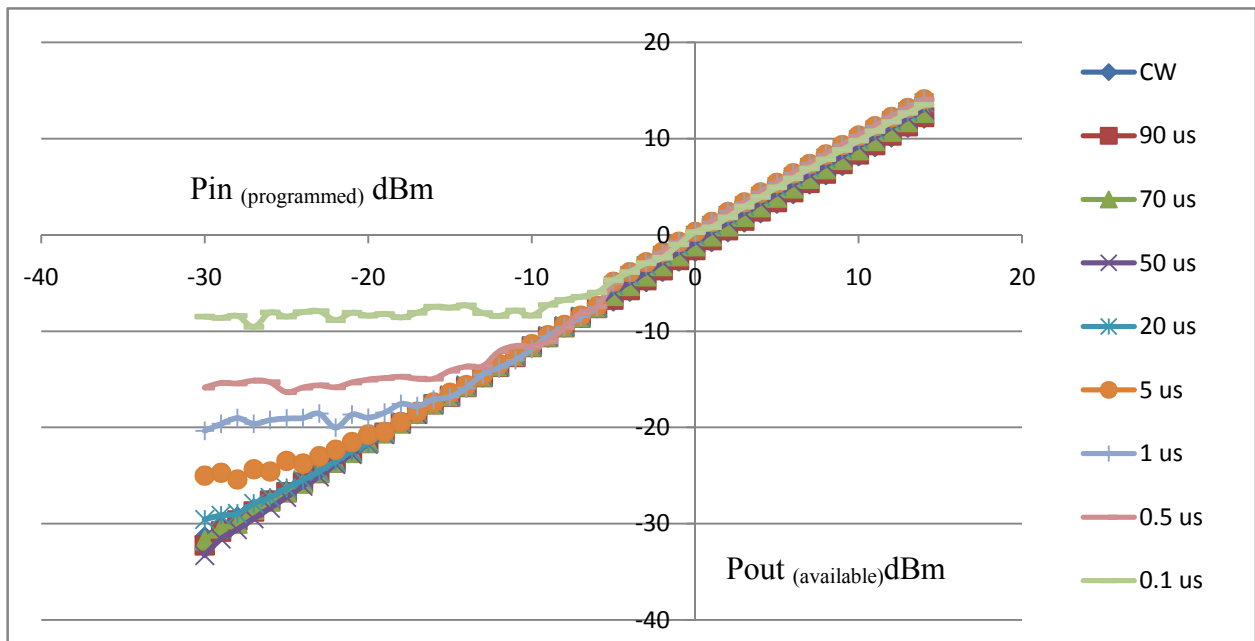
Due to the noise and reduction in dynamic range as the duty cycle is reduced, deterioration in the precision of the measurements can be observed. From Fig.3(a) it can be seen that the low pulsed-power measurement limit of the sensor creeps significantly high for very low pulse lengths and in Fig.3(b) it can be seen that for 0.5  $\mu$ s the sensor is in the noise floor for up until a Pin of -11 dBm. At 0.1  $\mu$ s the lowest power ( $P_{\text{available}}$ ) that could be accurately measured is -4 dBm. This low duty cycle deterioration is present for both calibration as well as DUT testing. Further experimentation was performed using calibration under both pulsed and CW conditions, and these tests showed that the best approach is to calibrate under CW conditions prior to performing DUT testing under the desired duty cycle. The reasoning for this is sound: the sensor measures average power, so calibrating with larger average power values will enhance the precision of both the calibration and the ensuing measurements.

Fig.4 shows the calibration results using a diode sensor (for comparison with Fig. 3(a)). It can be observed that the diode sensor exhibits no low-power dynamic range issue for pulses tested between 90 and 0.5  $\mu$ s. For pulse lengths below 0.5  $\mu$ s, some problems are observed with the diode sensor measurements.

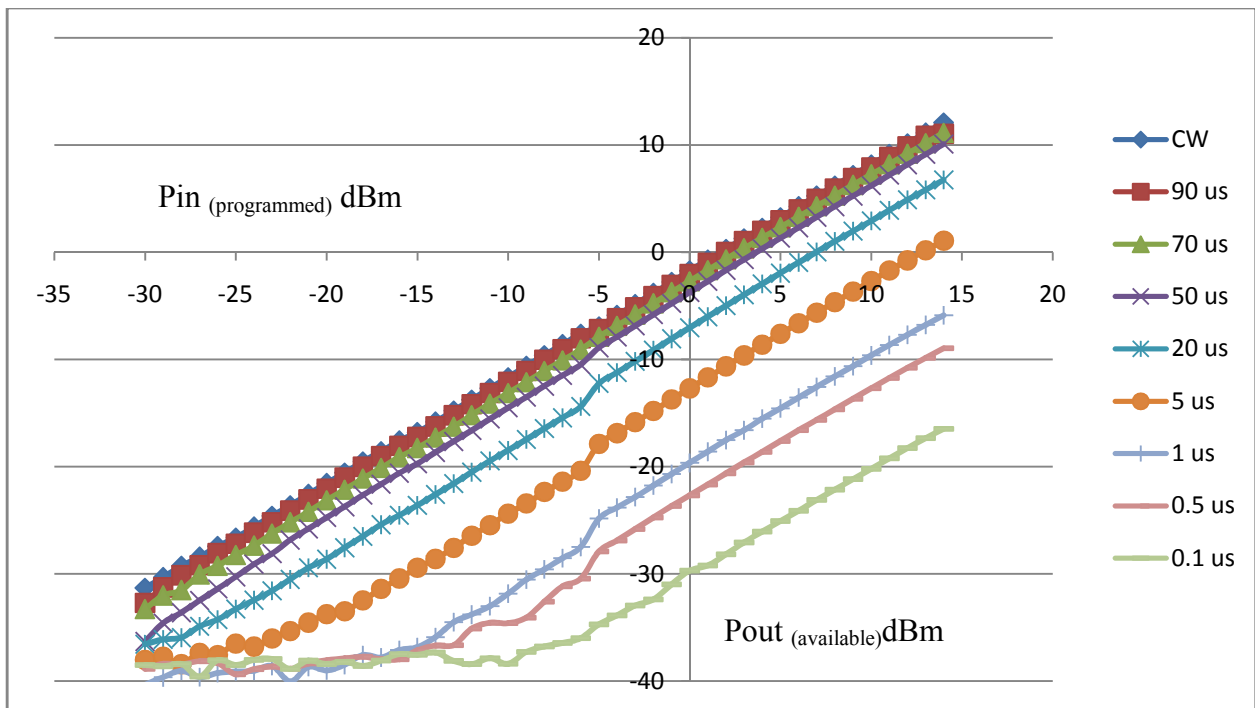
Fig.5 shows power versus time as viewed by the power meter for several different pulse lengths at an input power of 0 dBm. The power meter has been configured to report the average power measured between the two vertical cursors shown on the screen view. Fig. 6 shows the power-versus-time view for a significantly lower input power value (-20 dBm). In this case, it appears that, while a satisfactorily flat region can still be used to obtain a reasonable measurement at the 0.5  $\mu$ s pulse length, the power trace in the 0.2 and 0.1  $\mu$ s cases appears very uneven, and it is difficult to place the cursors to get an accurate measurement. This seems to be a reasonable explanation for the difficulty in obtaining accurate low-power calibrations for the 0.1 and 0.2  $\mu$ s pulse lengths in Fig. 4. It was concluded that caution should be exercised when attempting to use the diode sensor is to measure pulsed power at 0.1  $\mu$ s and 0.2  $\mu$ s pulse lengths for low power values. The use of a different RF switch may produce more favorable results for these lower duty cycles.

Fig. 7 shows a comparison between the measured Gt of the thru for both of the sensors at a pulse length  $\tau = 0.5$   $\mu$ s pulse length during a power sweep. Ideally Gt should be zero for all power levels, but it can be observed that the thermal sensor loses precision at lower input power values. Also note that the diode sensor used in this setup had a stated dynamic range of -20 to +20 dBm, compared to -30 dBm to +20 dBm for the thermal sensor. However, in our application the thermal sensor is being used to measure average power over a large time span including both on and off pulse conditions, whereas the diode sensor is used to measure the signal during a gated interval during the on time of the pulse. Accordingly, the diode sensor has a clear advantage for lower pulse ranges because the signal can be gated and it can be decided under which time period the power should be measured.

From Fig. 7, it can be clearly observed that precision begins to deteriorate significantly for the thermal sensor as the pulsed power goes below about -5 dBm.



(a)



(b)

Fig.3: (a). Calibration Data:  $P_{in_{programmed}}$  Versus pulsed  $P_{out_{available}}$  for Thermal Sensor for Various RF Pulse Width and Constant Period of 100  $\mu$ s (b). Calibration Data:  $P_{in_{programmed}}$  Versus average  $P_{out_{available}}$  for Thermal Sensor for Various RF Pulse Width and Constant Period of 100  $\mu$ s

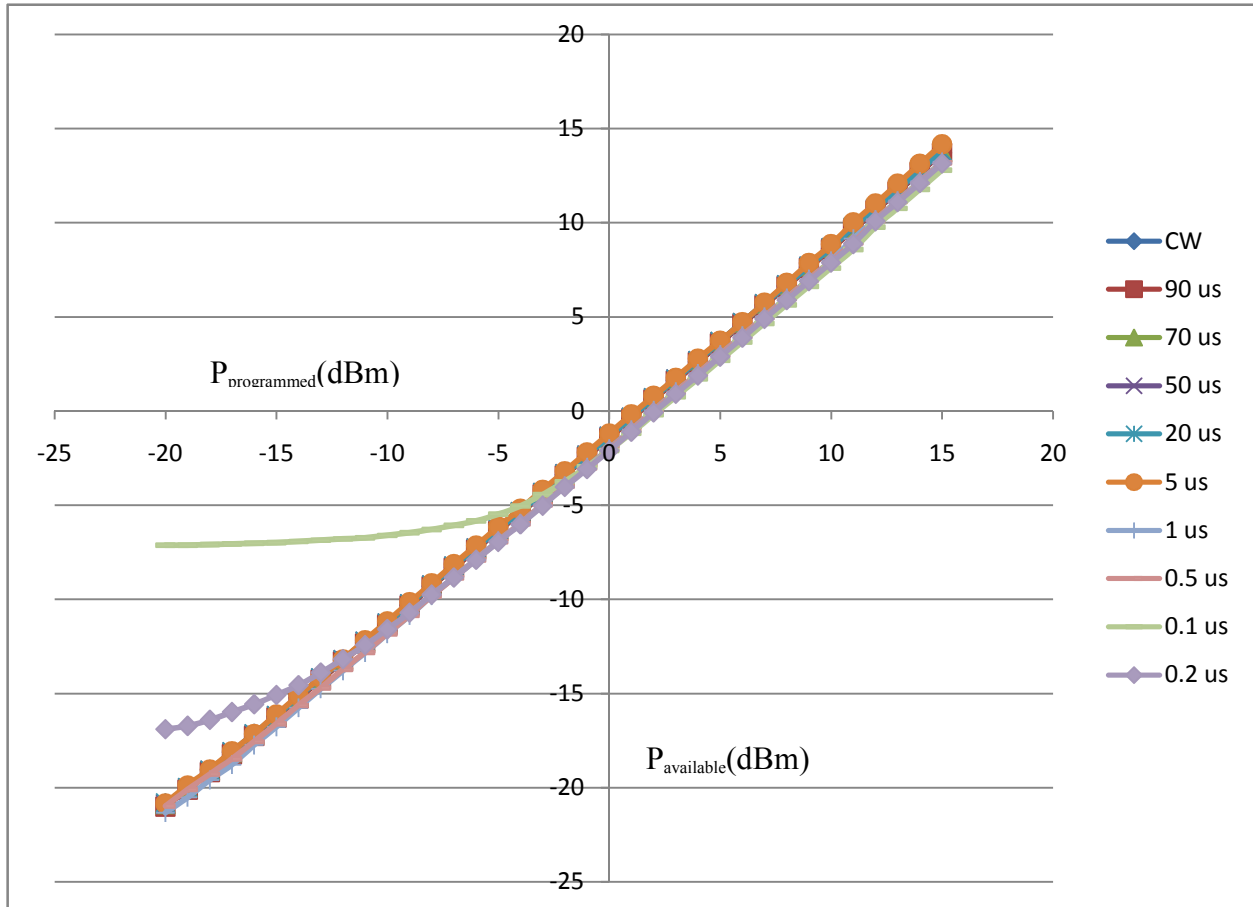


Fig.4: Calibration Data:  $P_{available}$  Versus  $P_{programmed}$  for Diode Sensor for Various RF Pulse Width and Constant Period of 100  $\mu s$

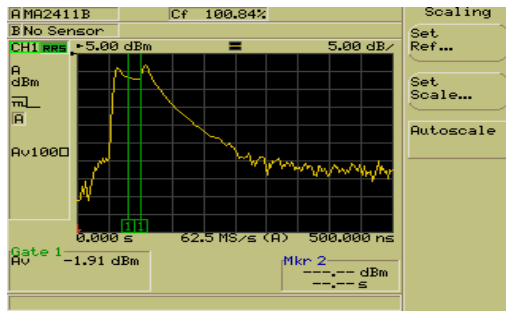
For the thermal sensor, the lower power rating is -30 dBm. Based on equation (5), the dynamic range reduction for  $\tau = 0.5 \mu s$ ,  $T = 100 \mu s$  is

$$\text{Reduction in Dynamic Range} = 10 \log \frac{T}{\tau} =$$

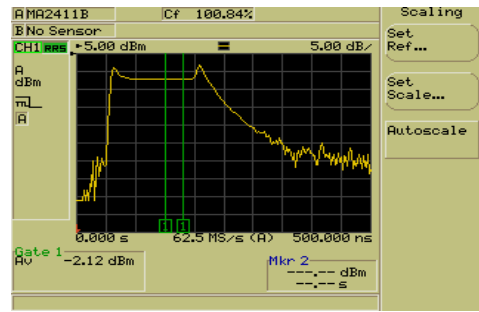
$$10 \log \frac{100}{0.5}$$

$$= 23 \text{ dB}$$

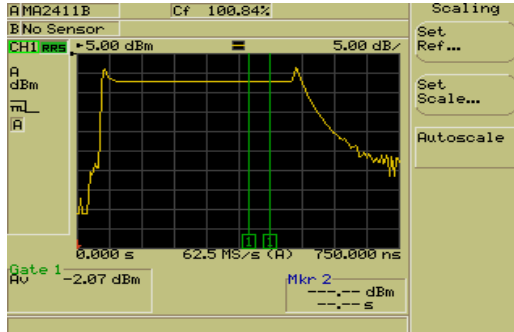
This means that the lower end of the accurately measurable input power range should be -30 dBm + 23 dB + 2.5 dB (insertion loss of the switch) = -4.5 dBm. This coincides exactly with the deterioration of the thermal sensor precision observed in Fig.7.



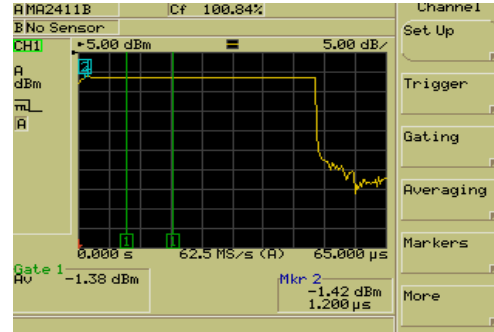
(a) Pulse Width = 0.1  $\mu$ s



(b) Pulse Width = 0.2  $\mu$ s

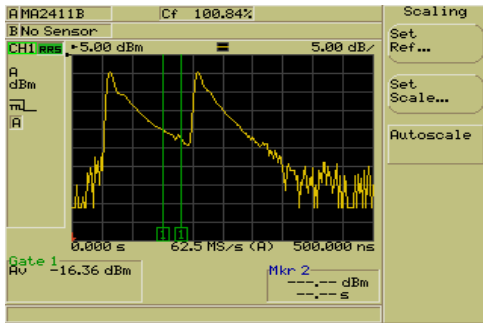


(c) Pulse Width = 0.5  $\mu$ s

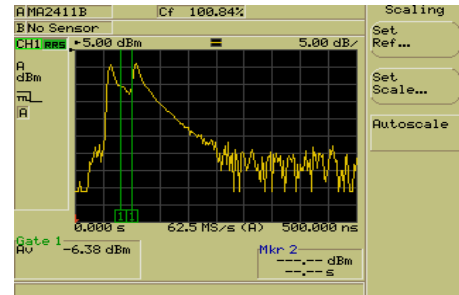


(d) Pulse Width = 50  $\mu$ s

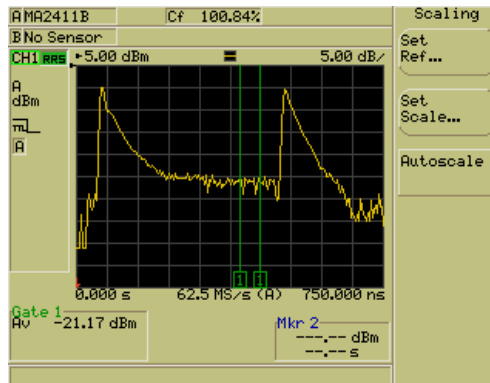
Fig.5: Power Meter Screenshots of Power Versus Time for Different Pulse Widths for  $T = 100 \mu$ s and  $P_{\text{programmed}} = 0$  dBm



(a) Pulse Width = 0.1  $\mu$ s



(b) Pulse Width = 0.2  $\mu$ s



(b) Pulse Width = 0.5  $\mu$ s

Fig.6: Power Meter Screenshots of Power Versus Time for Different Pulse Widths for  $T = 100 \mu$ s and  $P_{\text{programmed}} = -20$  dBm

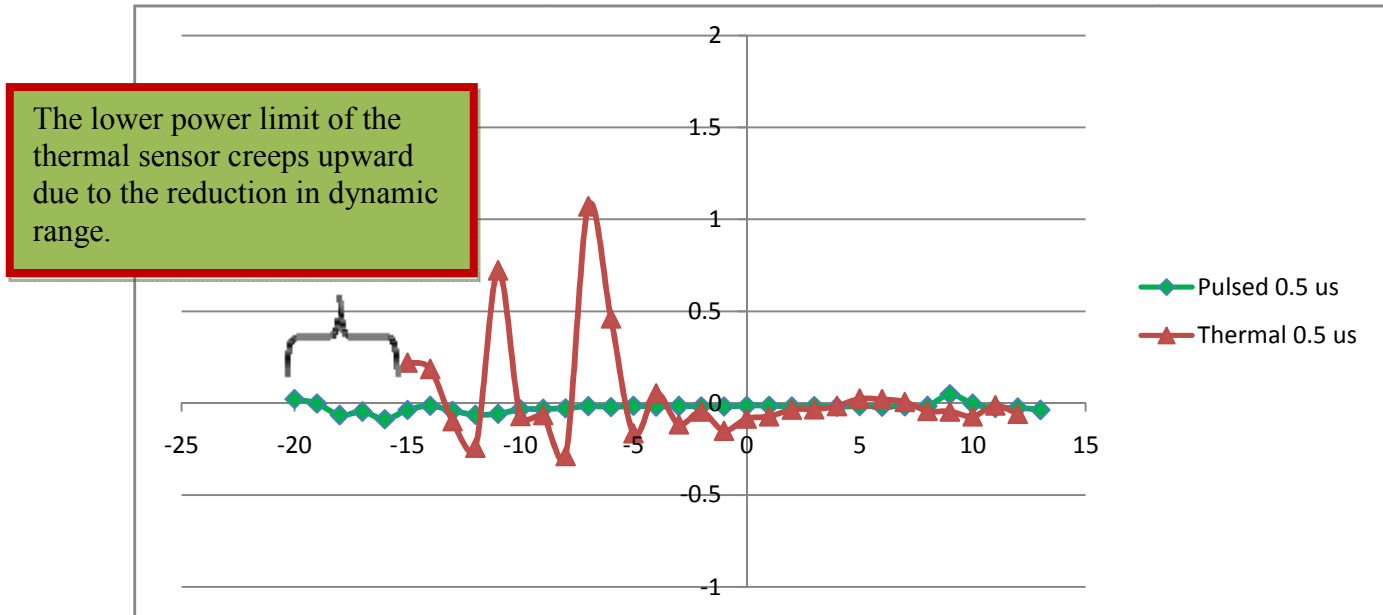


Fig.7: Thru Transducer Gain for the Diode and Thermal Sensors for  $\tau = 0.5 \mu\text{s}$ ,  $T = 100 \mu\text{s}$  (Duty Cycle = 0.5 Percent).

## V. CONCLUSIONS

This work demonstrates the results of an experiment to compare the accuracy and precision of pulsed power measurements using two different types of power sensors. Pulsed power measurements for various duty cycles have been analyzed. As expected, the dynamic range of the thermal sensor used reduces as the duty cycle reduces, while the diode sensor setup produced more accurate readings for lower duty cycle values. Limitations of the diode sensor to measure for low duty cycles at low power values were traced to limitations of the pulse shape generated by the RF switch used. The type of benchmark testing outlined here has proven helpful in developing a pulsed load-pull system in the laboratories of the authors and provides insight on what duty cycles and power ranges can be used with confidence for testing of active devices.

## ACKNOWLEDGMENTS

The authors would like to thank Gary Gentry and Jeff Stevens from Anritsu for providing the instruments used in the experiments and Modelithics, Inc. for providing funding for this work. Also special thanks to Richard Wallace from Maury Microwave for the help with the driver file for the Anritsu's pulsed power meter.

## REFERENCES

- [1] F.C. Beach and I.R. McNabe, "Present and Future Naval Applications for Pulsed Power," *IEEE Pulsed Power Conference*, June 2005, pp. 1-7.
- [2] ZH. Jung, J.S. Kim, ZS. Jin, and GH.Rim, "Pulsed Power Application to Produce Silver Nanopowders," *IEEE Pulsed Power Conference*, Vol. 1, June 2003, pp. 437-440.
- [3] H. Subrata and H. James, "Pulsed vs. CW Power Performance of InGaP/GaAs HBTs," *IEEE Microwave Conference Proceedings*, Vol. 1, December 2005, pp. 3
- [4] C. Baud, D. Barataud, J.M. Nebus, JP. Teyssie, JP. Villotte, D. Floriot, "An Active Pulsed RF and Pulsed DC Load-Pull System for the Characterization of Power Transistors Used in Coherent Radar and Communication Systems," *IEEE MTT Transactions*, Vol.48, No.12, December 2000, pp. 2625-2629.
- [5] J. Teyssier, P. Bouysse, Z. Quarch, D. Barataud, T. Pyretailade, and R. Quere, "40 GHz/150-ns Versatile Pulsed Measurement System for Microwave Transistor Isothermal Characterization," *IEEE Transactions on Microwave Theory and Techniques*, Vol. 46, No. 12, December 1998, pp. 2043-2052.
- [6] C. Baylis, L. Dunleavy, and J. Martens, "Construction and Benchmarking of a Pulsed S-Parameter Measurement System," *Automatic RF Techniques Group (ARFTG) Conference*, Washington, DC, December 2005.
- [7] PA. Hudson, "Measurement of RF Peak Pulse Power," *Proceedings of IEEE*, Vol. 55, No. 6, June 1967, pp. 851-855.
- [8] Maury Microwave, 2900 Inland Empire Blvd, Ontario, California 91764 USA, [<http://www.maurymw.com/index.htm>]

# Reciprocity-based Multiport De-embedding and an Analysis of Standard Sensitivity

J. Martens

Anritsu Company, Morgan Hill, CA, 95037, US

**Abstract** — Multiport de-embedding techniques have been becoming of increasing interest as the paths between probe pads and the DUT become more three-dimensional and more coupled. Circuit-model-based de-embedding schemes often suffer from a lack of adaptability to slightly different layouts. Fully general de-embedding approaches may require too many standards or too much knowledge about those standards. A general approach enforcing reciprocity and a few other constraints on leakage behavior can potentially work around both limitations while providing a reasonable computational framework in the general N-port case. Such a method will be discussed and de-embedding examples presented as a vehicle for a heuristic analysis of the sensitivity of the de-embedding to the quality/knowledge of the standards.

**Index Terms** — S-parameter, de-embedding.

## I. INTRODUCTION

De-embedding and VNA calibrations are, by definition, closely related (e.g., [1]). While there are some subtle computational differences due to the nature of how the calibration is used, the main distinction in the context of on-wafer measurements has been the nature of the standards used to define the final reference planes. The practical de-embedding problem allows a classical calibration at or near probe tips but requires information at an inner reference surface where the allowed standards set is limited (both for space and electromagnetic reasons) and knowledge available about those standards may be difficult to acquire. Many papers have appeared in recent years covering a number of approaches to solving this class of problems (e.g., [2]-[11]).

Consider the structure shown in Fig. 1. While not necessarily representative of any particular technology, it illustrates two features key to this paper: (1) a multiport problem with non-negligible transmission between all ports, and (2) structurally not amenable to treating it as a TRL problem. For such a structure, the approaches have generally been to treat the intervening network as either a circuit model of some type with unknown element values (e.g., [2]-[7]) or as a 2N-port black box that is completely unknown (except presumably linear; e.g., [8]-[11]). As suggested before, both approaches have their limitations. The circuit model approach has applicability limits as the material and structural details change although, for certain structures, it may be very efficient. The black box approach has considerable theoretical support (e.g., [12]-[16]) but many standards may be required at the inner reference surface, particularly as N gets large. Not only may this not be practical for a given structure, but

acquiring the knowledge about the standards could become prohibitive as well due to process variations, etc..

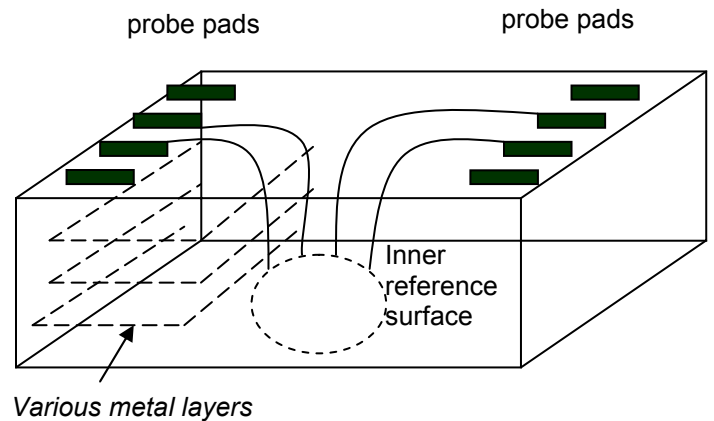


Fig. 1. A possible multiport de-embedding problem where the network between the probe plane and the inner reference surface is fully leaky and the structure is not readily amenable to TRL treatment.

In this paper, a middle ground of a constrained black box will be explored but more as a vehicle to look at sensitivities to some of the standards and the knowledge about them. While, strictly speaking, the conclusions will have to be limited to the algorithmic approach chosen and the standards classes used, it is hoped that some of the concepts will be more generally applicable.

Among the assumptions to be invoked is that of reciprocity. Since the network is assumed to be a passive structure, this is reasonable and has been discussed elsewhere (e.g., [2], [11]). In some cases, the assumption has been used to help the solution of a circuit-model fitting approach (e.g., [2]). In other cases, reciprocity has been used as a secondary check of the de-embedding (e.g., [11]). One reason for avoiding the use of reciprocity is that the avoidance would enable the use of a full-calibration at the inner surface instead of the 2<sup>nd</sup> tier de-embedding being proposed here. Sometimes symmetry is also invoked as an assumption [2] but it was believed this was too geometrically restrictive so that assumption was not made in this work.

## II. DE-EMBEDDING METHOD

Consider the classical de-embedding equation (e.g., [12]) relating inner and outer surface S-parameters ( $S_m$  representing measured parameters at the inner surface and  $S$  representing actual parameters that would be available without the intervening network) and some network-describing matrices  $\Gamma_{xy}$ .

$$S_m = \Gamma_{00} + \Gamma_{01} [I - S \cdot \Gamma_{11}]^{-1} \cdot S \cdot \Gamma_{10} \quad (1)$$

Where the  $\Gamma$ s are diagonal in the leakage-free case. In the present case, the  $\Gamma$ s are clearly non-diagonal but since we are using them to model a passive network between probe tips and the DUT planes, we can make some other assumptions. First, reciprocity is assumed which will make the  $\Gamma_{00}$  and  $\Gamma_{11}$  matrices symmetric and will force  $\Gamma_{10} = \Gamma_{01}^T$ . The latter claim can be seen in how the error terms are defined [12]. While this seems like a tremendous aid, it is somewhat complicated by the method in which this equation is usually recast. Second, the leakages will be assumed to be less than main path transmission (less in the sense of allowing multiplicative convergence, not in the sense of ‘<<<’ or neglect; this will be discussed further in a later section). Equation (1) is normally rearranged to the following (e.g., [12]):

$$K \cdot S_m - S \cdot L \cdot S_m + S \cdot H - M = 0$$

where

$$K = \Gamma_{01}^{-1} \quad (2)$$

$$L = \Gamma_{11} \cdot \Gamma_{01}^{-1}$$

$$M = \Gamma_{01}^{-1} \cdot \Gamma_{00}$$

$$H = \Gamma_{11} \cdot \Gamma_{01}^{-1} \cdot \Gamma_{00} - \Gamma_{10}$$

Using the definitions in eq. 2 and the  $\Gamma_{01}$ - $\Gamma_{10}$  relationship, we can write

$$H = L \cdot K^{-1} \cdot M - (K^{-1})^T \quad (3)$$

Thus  $H$  is entirely dependent on the other three matrices. It is somewhat more complicated to enforce reciprocity on  $L$  and  $M$  since the product of two symmetric matrices need not be symmetric. We can state that of the  $N^2$  terms in each of  $L$  and  $M$ , only  $(N^2+N)/2$  are independent since  $K$  has been solved for and  $\Gamma_{11}$  and  $\Gamma_{00}$  are symmetric. It can be shown, but will not be reproduced here for space reasons, that, without loss of generality, the lower diagonal of  $L$  and  $M$  can be treated as dependent. Although algebraically messy, it is straightforward to solve for the relevant  $\Gamma$  elements from the independent  $L$  and  $M$  terms (and  $K$  terms) and then back-substitute to compute the dependent  $L$  and  $M$  terms using Eq. 2.

In formulating the equations to be solved from Eq. 2, a few things change from the usual approaches. First, we will treat the dependent terms iteratively meaning some convenient value will be used to start and these terms in the master equation will be treated as inhomogeneities. Second, since this is a de-embedding problem and not a classical calibration, we can make no normalizing assumptions (i.e., we desire to know the absolute S-parameters of the network). Thus it is fairly handy to have the dependencies to take the role of the inhomogeneity. Equation 4 shows the system of equations for each standard; the system has a total of  $2N^2+N$  independent variables.

$$-M_{ij}^* - \sum_{p=1}^n \tilde{S}_{ip} \left( \sum_{q=1}^n L_{pq}^* \tilde{S}_{mqj} \right) + \sum_{p=1}^n K_{ip}^* \tilde{S}_{mpj} = M_{ij}^{**} + \sum_{p=1}^n \tilde{S}_{ip} \left( \sum_{q=1}^n L_{pq}^{**} \tilde{S}_{mqj} \right) - \sum_{p=1}^n \tilde{S}_{ip} H_{pj}^{**}$$

Where  $i, j=1, \dots, N$

(4)

Where a single \* is used to denote independence and a \*\* is used to denote dependence when needed. The  $\sim$  denotes the measured and actual S-parameter matrices for the given standard. Note that only one of a given lettered matrix is present for a given index combination. This now becomes a standard over-determined problem that can be solved with least-squares or singular-value-decomposition techniques (e.g., [10]). One can argue about the rate of convergence of this process, as is always the case with such solution approaches, and if there are situations where convergence cannot be guaranteed. While no rigorous analysis has been performed, if the main path conduction and behavior is dominant relative to leakage, then the diagonals of all matrices (particularly  $L$  and  $M$ ) will be weighted. Since the dependent terms are all off-diagonal, it would seem reasonable then that convergence would be relatively quick. This has been observed in practice and a more rigorous convergence analysis is underway. A purely deterministic formulation is possible but, for a general  $N$  port case, the algebra will be challenging and likely not be easily extrapolated to higher port counts.

The next most obvious question is what standards (or dummy measurements) are required at the inner interface. In the fully general 4 port setup without reciprocity assumptions (thus yielding 64 unknowns), on the order of 10 or more measurements are required depending on the types of practical standards available and the level of immunity desired to standards knowledge errors. In the present setup, seven measurements have proven to be adequate with reasonable tolerance to standards errors and noise although six were sufficient in most cases. The purpose of this study has been more to evaluate sensitivities under practical conditions rather than to determine the absolute minimum number of possible measurements so the analysis in the latter respect has been minimal to date.

The set of standards examined was desired to be as simple and as easily modeled as possible to avoid the usual problems, particularly with loads and similar structures. While a quasi-TRL scheme is, of course possible, it may not be practical for

geometry reasons. A quasi-LRM scheme is a more attractive possibility and is partially invoked here although some additional defined-standards help makes it much easier to get at the leakage terms with fewer connections. It is believed that the modeling accuracy on these reflects is high enough that there is less of a practical penalty in using them. This quasi-minimalist set used for the computations is then

Standard code	Inner port 1	Inner port 2	Inner port 3	Inner port 4
A	Open-like	Open-like	Open-like	Open-like
B	Short-like	Short-like	Short-like	Short-like
C	Load-like	Load-like	Load-like	Load-like
D	1-3 thru	2-4 thru	1-3 thru	2-4 thru
E	1-4 thru	2-3 thru	2-3 thru	1-4 thru
F	1-3 thru	Open-like	1-3 thru	Short-like
G	1-3 thru	Short-like	1-3 thru	Open-like

From a defined-standards point-of-view, this is only two additional dummy sets relative to the minimal set. For some studies on better standards immunity we will add some additional standards in certain experiments:

- H: 1-2 thru, 3-4 thru
- I: 2-3 thru, port 1 open, port 4 short
- J: 2-3 thru, port 1 short, port 4 open.

### III. RESULTS

To evaluate the sensitivities, we will perform a set of analyses based on the parameters of a commercial 4 port VNA setup in an on-wafer environment but leakage simulation will be done coaxially for simplicity and better control. It will be assumed that reasonably wide IF bandwidths will be used for measurement speed (of order 1 kHz) and that the cables/bias tees normally associated with an on-wafer measurement are employed. As a result, the dynamic range will be considerably worse than in a simple coaxial environment setup for metrological conditions but it may be a more practical manifestation. The leakage levels will target 15-20 dB as might be the case in a small feature size scenario. The leakage can be simulated with a collection of hybrids as suggested in Fig. 2....splitters will not be used in order to better mimic expected through losses (a few dB of through loss in this case).

A variety of DUTs will be studied including low loss transmissive structures that typically form a challenging test of de-embedding quality. Beatty lines will be used as well since the mismatch they present may be of importance in evaluating leakage terms. While a variety of standards defects (or, more precisely, defects in knowledge about those standards) could be analyzed, we will focus on a few

- line length defects
- load reflection coefficient defects
- reflect phase defects

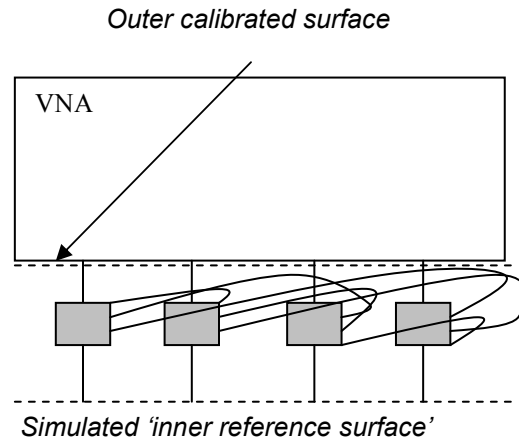


Fig. 2. The structure used to simulate the de-embedding environment of Fig. 1. The boxes shown (hybrid networks connected for all possible leakage paths) represent the region between the probe pads and the inner reference surface.

The studies will consist of looking at the response of a given measurement to defects in the knowledge of the standards. That is, deviations will be introduced into the standards' assumed properties before the de-embedding proceeds. The reaction to these defects will then be analyzed somewhat loosely to try to detect trends.

We will split the impact of these defects into two main categories: those affecting the main line paths and those affecting the leakage paths. The main line sensitivities are fairly straightforward and many of the concepts have been covered for various two-port calibration algorithms in the past (e.g., [17]-[18]). Converting to the language of de-embedding, many of the issues that affect calibration directivity, source match or load match will impact the return loss elements of the de-embedded network. Some of the dependencies are exceedingly obvious such as an error in the load (for SOLT or LRM) or reflects (SOLT) will cause match problems. Line length problems in a defined-standards calibration lead to transmission phase issues which can propagate to match issues and so on.

As a first example, consider a delay line as a DUT connected between ports 1 and 4. In Fig. 3, the effects of an error on the load standard are shown. In this plot, the load model reflection coefficient was varied from the starting value (~-40 dB). As might be expected, the resulting issues with network match appear as ripple in the main line transmission measurement. If certain asymmetries are introduced in the assumed load models, the results change but only because the damage to inferred network match can be more or less severe depending on how many standards measurements have been degraded. The magnitude of the resulting ripple is consistent with the inferred match levels for the de-embedded network. In Fig. 4, the effects of an open phase problem are shown that have similar network match impacts.

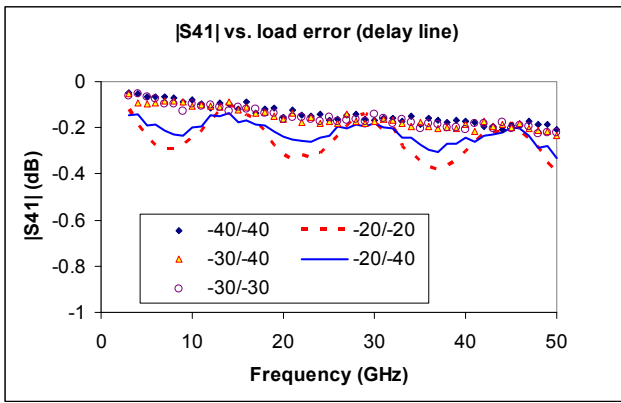


Fig. 3. The effect of load errors on the main transmission path is shown here. The first number in the legend is the load reflection coefficient (in dB) used for ports 1 and 2 at the inner reference surface while the second number is that used for ports 3 and 4.

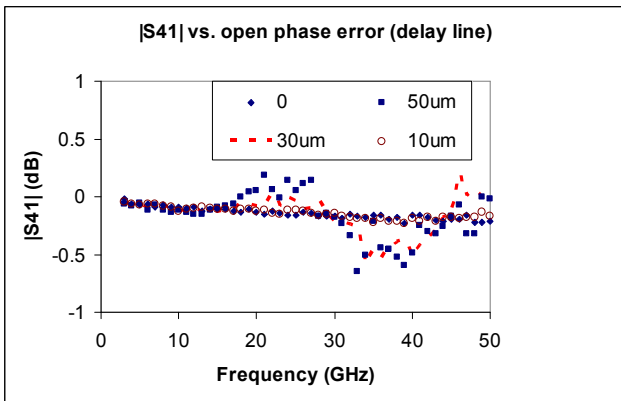


Fig. 4. The effects on main path transmission of an error in open standard phase length (air equivalent length error is shown) is shown here.

Leakage-like terms in the network, however, behave quite differently with respect to standards errors. Consider  $|S_{12}|$  for the same delay line DUT (see Fig. 5). Ideally the result will be in the noise floor and for standards matching the definitions, this is the case (again the noise floor is fairly high here as is consistent with a lossy setup and a relatively high IF bandwidth). Even for a fairly poor load standard definition (-20 dB), the deviation from the floor is fairly small. Only when the errors are made asymmetric, does the apparent leakage term grow significantly. As with many leaky-like algorithms, this approach relies on measurements of partial thru structures to deconvolve the leakage terms. Once the load standards are made asymmetric, the partial thru arms now have varying degrees of inferred mismatch and the deconvolution becomes corrupted.

A similar kind of symmetry dependence can be seen when one introduces a line length error but only on some of the dummy measurements. If only the 1-3 length in the 1-3, 2-4 (standard D) measurement has an error (and not the 1-3 2-open 4-short and 1-3 2-short 4-open measurements...standards F and G), the result is far worse than if one consistently had the length wrong on these measurements.

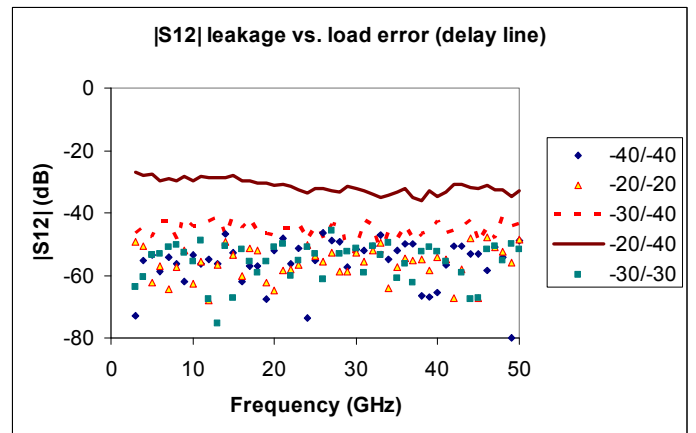


Fig. 5. The effect on a network leakage term of errors in the load standards is shown here. The legend is the same as in Fig. 3 with load model reflection coefficients in dB. Note that the asymmetry in the load error is more important than the return loss problem itself.

Since the change in off-path responses between these standards is a primary basis for establishing the leakage terms, it is perhaps not surprising that distorting the relationship between these three standards introduces additional error. An additional feature of Fig. 6 is that additional standards do not always help, even if they include the leakage path in question. The first additional standard was the 1-2 thru, 3-4 thru identified as standard H previously. The second additional standard was identified as I: 2-3 thru, port 1 open, port 4 short previously. The level of distortion introduced by certain errors can be fairly large (particularly in this case since we affected the prime leakage determining group as well as transmission phase in multiple paths) and this should probably be considered when selecting standards sets.

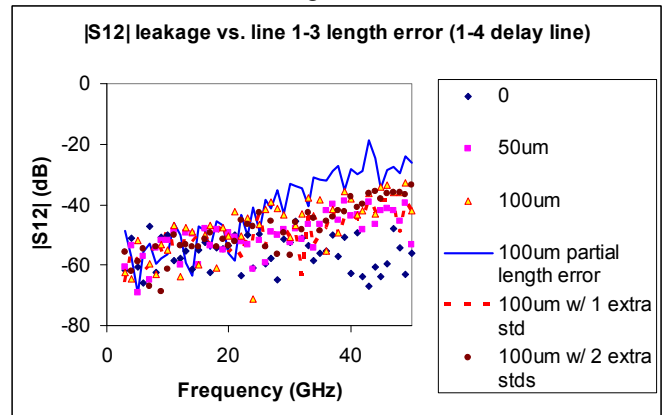


Fig. 6. The effect on a network leakage term from a line length error is shown here. Note that the consistency of line length is even more important than the absolute error.

The load error asymmetry effects of Fig. 5 can be seen using a different type of DUT, a Beatty line in this case (see Fig. 7). The physics is similar but this DUT is somewhat more sensitive to other leakage paths due to the increased mismatch. The asymmetry effect is thus somewhat magnified, particularly in the frequency ranges where the DUT match

worsens (notice the cusped shape to the erroneous -20/-40 curve in Fig. 7).

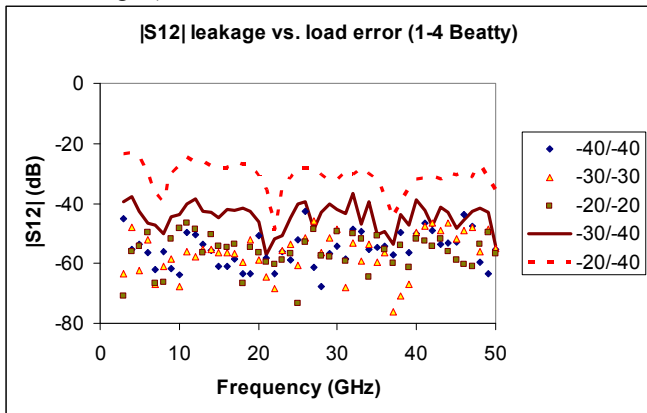


Fig. 7. The effect on a network leakage term from a load error is shown here for a more reflective DUT (legend the same as in Fig. 3). The effects are more obvious but the behavior is similar to Fig. 5.

Because of the key role that the partial thru structures with reflective terminations play in determining leakage for this standard set, it follows that the phase of those reflect standards can be quite critical. This dependence is shown in Fig. 8 and only about 4-5 degrees of error is needed to see a deviation. Fortunately, this type of standard is probably among the easier to model in a wafer environment.

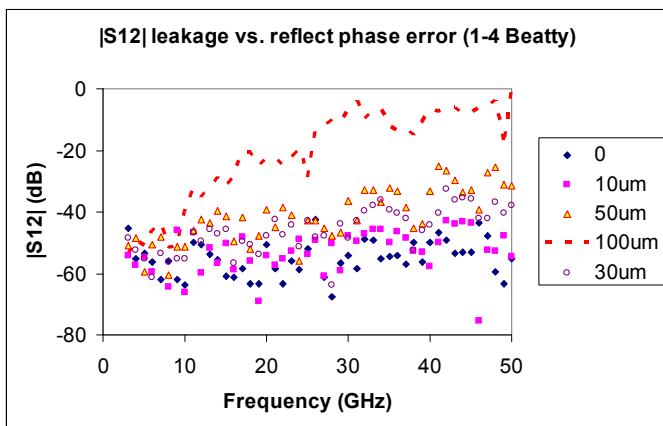


Fig. 8. The effect on a network leakage term from a phase error in a reflect standard is shown here (air equivalent electrical length).

This is one situation where additional standards can help, particularly those that provide direct information about the leakage path in question. In Fig. 9, an additional 1-2 3-4 thru standard (standard H) was added to the set and there was some improvement. The damage done by the standard error is more localized (only affecting the reflect phasing and not all of the transmission terms) and there is then a better chance at repair than in some other situations.

A final example looks more specifically at the dependence on the number of standards used. Consider a pad-like structure (about 3 dB insertion loss between ports 1 and 4 but with only about 20 dB return loss) and look at the leakage between ports 1 and 3. With no standards defects, using either

6 standards (A-F in the earlier table) or 10 standards (A-J) produced about the same result as shown in Fig. 10: the residual floor.

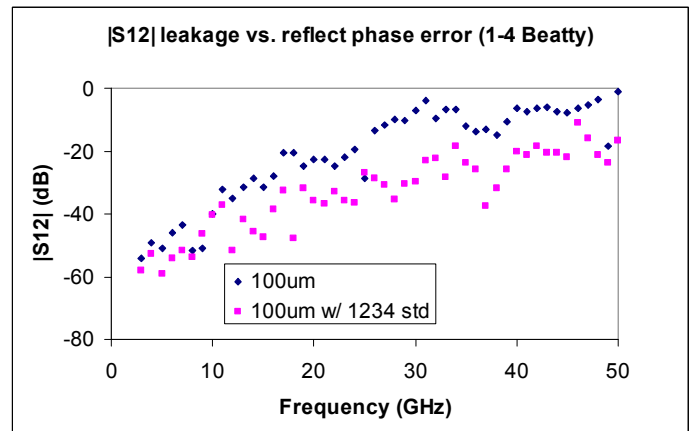


Figure 9. The effect on a network leakage term from a reflect phase error is shown here along with the impact of adding an additional standard.

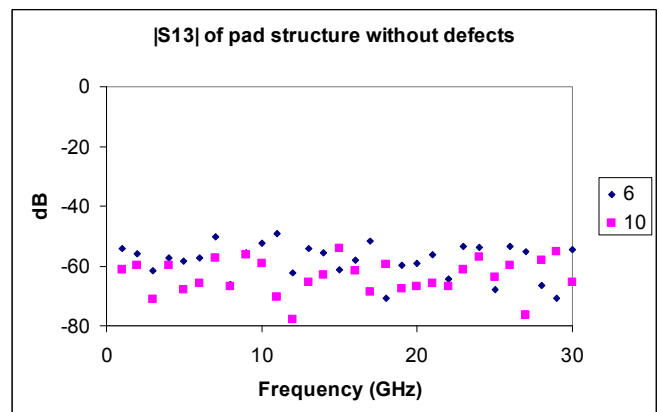


Figure 10. The effect of number of standards (the legend) on a leakage measurement with no defects introduced into the de-embedding process is shown here.

Introducing an asymmetric -20dB/-40dB load model problem produces a very different result (the loads used on ports 1 and 2 assumed to have a 20 dB return loss while those on 3 and 4 were assumed to be left at 40 dB). This result, shown in Fig. 11, illustrates that additional standards can help here as well. Adding an additional thru pair improves the performance beyond that using our original basis set by about another 5 dB. Adding additional partial thru structures (standards I and J) did not help any more and the result seems to have asymptotically approached a value related to the contradictory reference impedance situation we have introduced. The additional thru line pair helped to resolve some of the effects of the reference impedance problem on the leakage deconvolution but could not completely fix it based on Fig. 10.

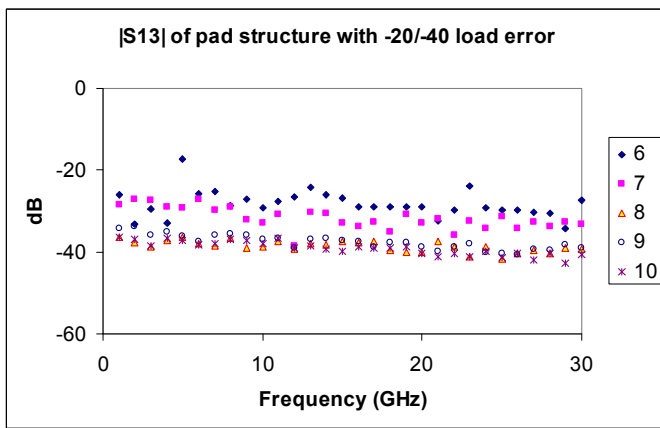


Figure 11. The effect of the number of standards on a defective de-embedding of a  $|S_{13}|$  leakage terms is shown here. A 20 dB return loss load used on ports 1 and 2 was assumed instead of the more correct 40 dB return loss.

#### IV. CONCLUSION

A reciprocity-based multiport de-embedding scheme has been presented with a particular intent at solving some geometrically complex on-wafer de-embedding problems. The approach makes a few key assumptions about the intervening network that reduce the required number of standards without extremely limiting the applicability of the model. The particular focus has been to look at some standards dependencies and a few observations can be drawn:

- A much smaller standard set can be used than if neither reciprocity nor leakage containment was assumed.
- While an intermediate impedance standard seems to be practically required, its sensitivity is more closely tied to symmetry of that standard than knowledge of the actual impedance.
- Reflect phasing and line length can be important dependencies but these can often be well-modeled.
- Additional standards can be used to mitigate standards sensitivities but more so for those standards whose effects are somewhat localized.

#### REFERENCES

- [1] R. Bauer and P. Penfield, "De-embedding and unterminating," *IEEE Trans. Micr. Theory Tech.*, vol. 22, pp.282-288, Mar. 1974.
- [2] L. F. Tiejmeijer, R. J. Hvaens, A. B. M. Jansman, and Y. Bouttement, "Comparison of the 'pad-open-short' and 'open-short-load' de-embedding techniques for accurate on-wafer RF characterization of high-quality passives," *IEEE Trans. Micr. Theory Tech.*, vol. 53, pp. 723-729, Feb. 2005.
- [3] J. Brinkhoff, S. C. Rustagi, J. Shi, and F. Lin, "MOSFET model extraction using 50 GHz four-port measurements," *Proc. RFIC Symp.*, Honolulu, pp. 647-650, June 2007.

- [4] K. Goverdhanam, Y. Tretiakov, G. Ali Rezvani, S. Kapur, and D. E. Long, "De-embedding considerations for high Q RFIC inductors," *Proc. RFIC Symp.*, Honolulu, pp. 449-452, June 2007.
- [5] M. Cho, G. Huang, L. Wu, C. Chiu, Y. Wang, K. Chen, H. Tseng, and T. Hsu, "A shield-based three-port de-embedding method for microwave on-wafer characterization of deep-submicrometer silicon MOSFETs," *IEEE Trans. Micr. Theory Tech.*, vol. 53, pp. 2926-2934, Sept. 2005.
- [6] E. P. Vandamme, D. M. M. P. Scheurs, and G. Van Dinther, "Improved three-step de-embedding method to accurately account for the influence of pad parasitics in silicon on-wafer RF test structures," *IEEE Trans. Electron Devices*, vol. 48, pp. 737-742, Apr. 2001.
- [7] R. A. Purcel, W. Struble, R. Hallgren, and U. L. Rohde, "A general noise de-embedding procedure for packaged two-port linear active devices," *IEEE Trans. Micr. Theory Tech.*, vol. 40, pp. 2013-2024, Nov. 1992.
- [8] Q. Liang, J. Cressler, G. Niu, Y. Lu, G. Freeman, D. Ahlgren, R. Malladi, K. Newton, and D. Harame, "A simple four-port parasitic deembedding methodology for high-frequency scattering parameter and noise characterization of SiGe HBTs," *IEEE Trans. Micr. Theory Tech.*, vol. 51, pp. 2165-2174, Nov. 2003.
- [9] T. O'Sullivan and P. Asbeck, "Investigation of RF de-embedding approaches for device characterization," *70<sup>th</sup> ARFTG meeting digest*, Phoenix, Nov. 2007.
- [10] X. Wei, G. Niu, S. L. Sweeney, and S. S. Taylor, "Singular-value-decomposition based four port de-embedding and single-step error calibration for on-chip measurement," *Proc. Int. Micr Symp.*, Honolulu, pp. 1497-1500, June 2007.
- [11] X. Wei, G. Niu, S. L. Sweeney, Q. Liang, X. Wang, and S. S. Taylor, "A general 4-port solution for 110 GHz on-wafer transistor measurements with or without impedance standard substrate (ISS) calibration," *IEEE Trans. Electron Dev.*, vol. 54, pp. 2706-2714, Oct. 2007.
- [12] V. Teppati and A. Ferrero, "On-wafer calibration algorithm for partially leaky multiport vector network analyzers," *IEEE Trans. Micr. Theory Tech.*, vol. 53, pp. 3665-3671, Nov. 2005.
- [13] A. Ferrero and F. Sanpietro, "A simplified algorithm for leaky network analyzer calibration," *IEEE Micr. And Guided Wave Lett.*, vol. 5, pp. 119-121, Apr. 1995.
- [14] K. Silvonen, "LMR 16- A self-calibration procedure for a leaky network analyzer," *IEEE Trans. Micr. Theory Tech.*, vol. 45, pp. 1041-1049.
- [15] J. V. Butler, D. K. Rytting, M. F. Iskander, R. D. Pollard, and M. Vanden Bosche, "16-term error model and calibration procedure for on-wafer network analysis measurements," *IEEE Trans. Theory Tech.*, vol. 39, pp. 2211-2217, Dec. 1991.
- [16] A. Ferrero, U. Pisani, and K. J. Kerwin, "A new implementation of a multiport automatic network analyzer," *IEEE Trans. Micr. Theory Tech.*, vol. 40, pp. 2078-2085, Nov. 1992.
- [17] U. Stemper, "Uncertainty of VNA S-parameter measurement due to nonideal TRL calibration items," *IEEE Trans. Instr. and Meas.*, vol. 54, pp. 676-679, Apr. 2005.
- [18] J. Martens, "LRM: A quantitative look at reference impedance contradictions and other uncertainty impacts," *69<sup>th</sup> ARFTG meeting digest*, Honolulu, June 2007.

# Traceability of Vector Network Analyzer Measurements

by Ken Wong

Agilent Technologies, Inc.  
1400 Fountaingrove Parkway, Santa Rosa, CA USA 95403

**Abstract – Measurement traceability is NOT just a requirement in ISO quality standards. It is a necessity to ensure the accuracy of any measurement system. For vector network analyzers (VNA), the traceability of S-parameter measurements is not obvious. The latest generation of VNA is also capable of making measurements beyond S-parameters. This paper will present the latest developments in VNA measurement traceability chain, the key traceable parameters, calibration and verification standard traceability and some verification techniques and results.**

## I. INTRODUCTION

Traceability is the “property of the result of a measurement or the value of a standard whereby it can be related to stated references, usually national or international standards, through an unbroken chain of comparisons all having stated uncertainties.” [1] Furthermore, international standards such as ISO17025 has made it clear that measurements have traceability to the designated standards if and only if scientifically rigorous evidence is produced to show that the measurement process is producing measurement results that the total measurement uncertainty relative to national or other designated standards are quantified. This defined the interrelationship between traceability, calibration, verification and measurement uncertainty. Since vector network analyzer (VNA) measurement uncertainty analysis is quite complex, this paper will not deal with this topic. The reader is encouraged to seek more in depth coverage on this topic in many ARFTG papers [2], [3], [4], [5]

It is through the traceability chain that measurement system specifications are established. The traceability of VNA measurements, however, is often confusing. S-parameters are ratios of measured voltage waves and yet, S-parameter measurements are traceable to impedance standards. It is not obvious how the measurement parameters are linked to the basic fundamental constants such as frequency, volt, length, etc.

Soon after the introduction of the Hewlett Packard (HP) 8510 Vector Network Analyzer, a white paper [6] was published to address this issue. It was suggested that traceability of VNA may be established using verification standards, such as those provided in HP verification kits. Figure 1 shows the traceability chain as stated in the white

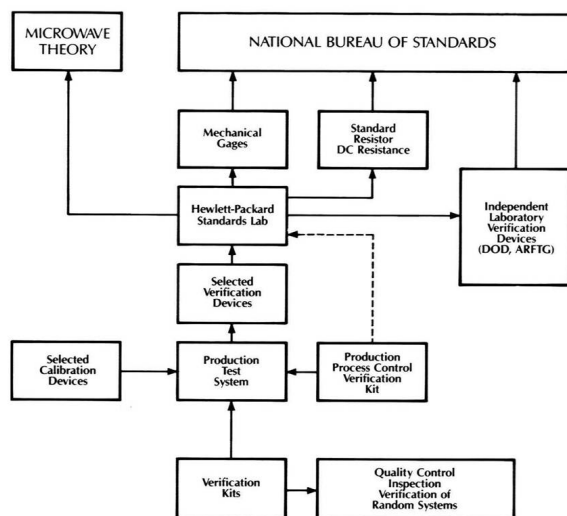


Figure 1: Initial Traceability of VNA

paper. The verification standards usually consist of a precision matched beadless air dielectric transmission line, a mismatch line, a 10 dB fixed attenuator and a 50 dB fixed attenuator. These devices are readily traceable directly to national primary standards. Traceability of calibration devices, back then, was less direct.

It wasn't until the introduction of the TRL calibration method and calibration kits that VNA measurements are traceable through the calibration standards as well as the verification standards. The VNA traceability chain was updated, as illustrated by Figure 2 [7].

An updated traceability paper was published in 1996 [8]. Traceability of VNA through primary calibration standards was firmly established.

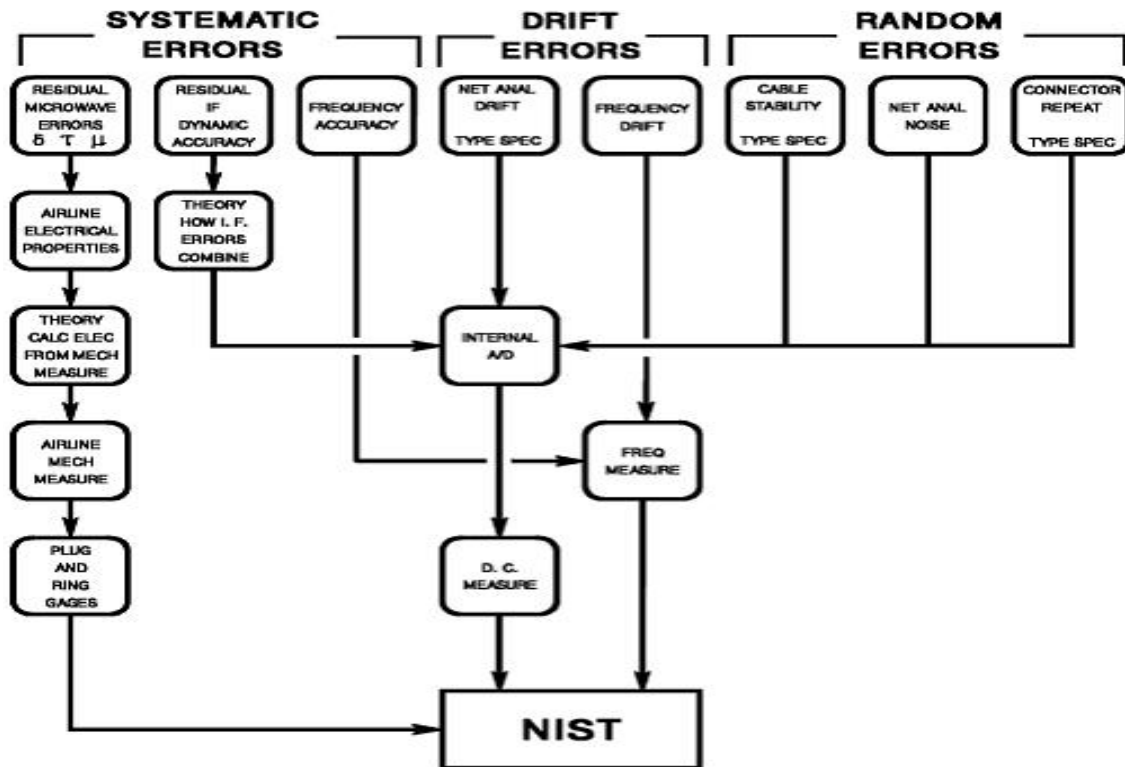


Figure 2: Revised Traceability of VNA

The latest generation of VNA is capable of making measurements beyond S-parameters. These new capabilities also required a new look at its overall traceability. Figure 3 shows the key traceable parameters of new VNA measurements.

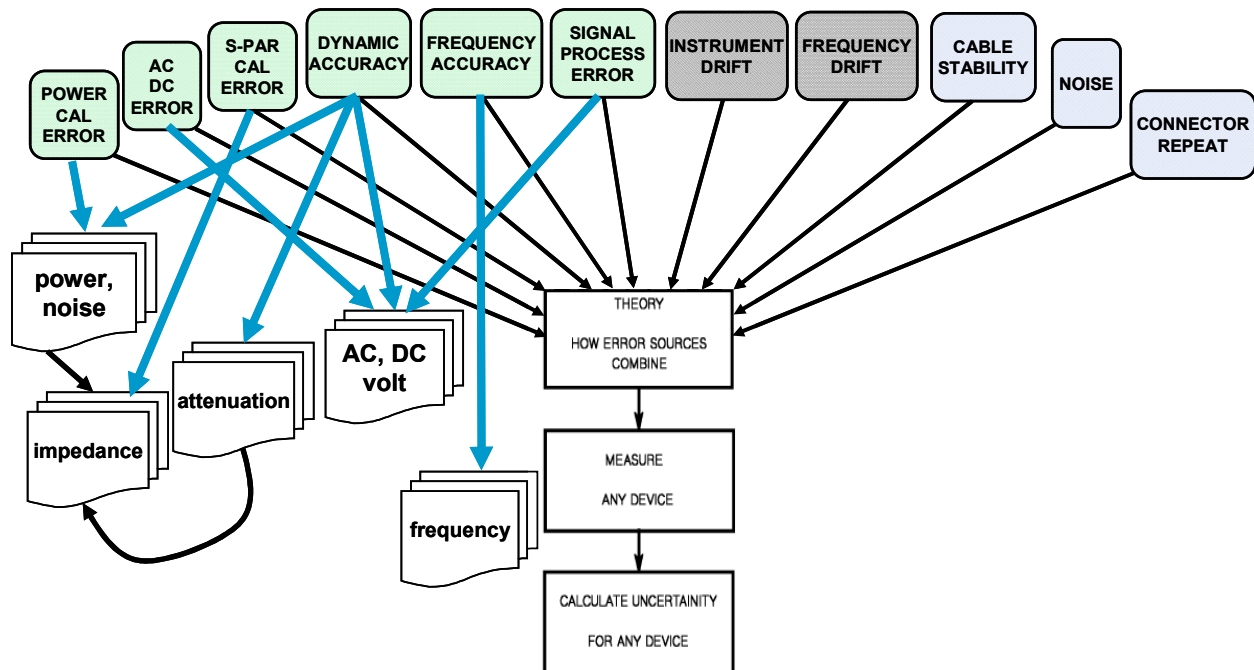


Figure 3:: Traceability of modern VNA

## II. VNA CALIBRATION

VNA S-parameter measurements measures the magnitude and phase relationships between incident waves and reflected and transmitted waves. The measurement equations of a two port VNA can be derived from the signal flow graph representation of the measurement set up, figure 4, and is expressed in the generic form, equation (1).

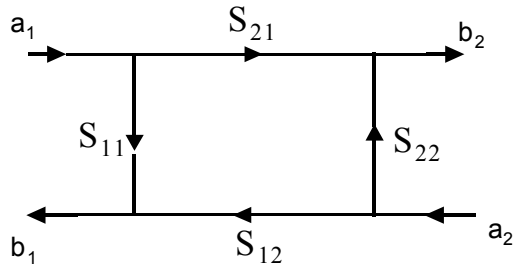


Figure 4 S-Parameters Signal Flow Graph

$$\begin{aligned} b_1 &= S_{11} a_1 + S_{12} a_2 \\ b_2 &= S_{21} a_1 + S_{22} a_2 \end{aligned} \quad (1)$$

where the incident and reflected waves are define with respect to a reference impedance ( $Z_{ref}$ ) [9]. All the terms in equation (1) are vector quantities and can be expanded to N number of ports.

To minimize measurement uncertainties, VNAs are calibrated using a set of “known” impedance calibration standard, at  $Z_{ref}$ , such as open, short and loads. Measurement uncertainty of the

calibrated VNA system is directly proportional to the uncertainty of these standards’ known quantity. The sensitivity of measurement uncertainty to each of the standard's uncertainty depends on the calibration method used, stability of the measurement system, and uncorrected performance of the system. Figure 5 shows the relationship between calibration standards and VNA system measurement specifications.

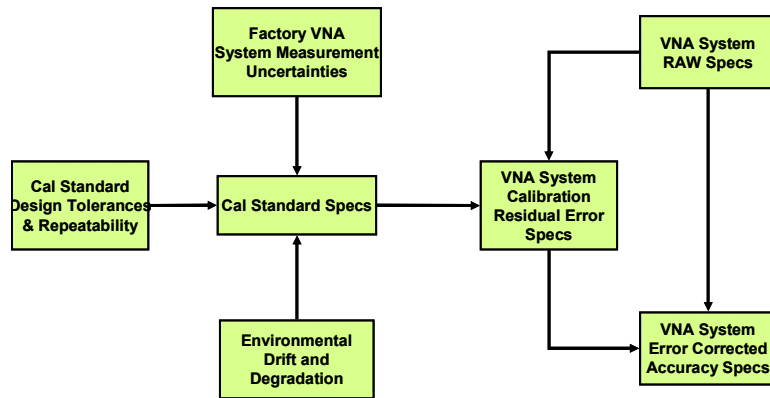


Figure 5: VNA Error Corrected Accuracy and Cal Std Specifications

used [10]. The uncertainty of these devices is a function of the physical metrology systems, uncertainty of the applicable natural constants.

Metrology grade devices are fabricated to the tightest specifications possible using the most advance state of the art equipment and methodology. Precision coaxial airlines can be fabricated with a diameter tolerance of  $\leq 2 \mu\text{m}$  and diameter consistency of  $\leq 1.5 \mu\text{m}$ . This is equivalent to an impedance accuracy of 0.2% for 7mm devices and 0.6% for 2.4mm devices.

For coaxial devices, the female contact should be slotless to minimize performance dependency on mating devices, a prerequisite of metrology grade coaxial connectors [11]. Metrology grade standards reduce calibration uncertainties by at least 50% over instrument grade standards. Because of physical size limitations, slotless female contact for some coaxial connectors, such as the 1.85mm and 1.0 mm connectors, is not feasible. For these connectors, an accurate model of the slotted contact was developed [12] so that the electrical characteristics are calculable from physical dimensions and properties. Uncertainty caused by male pin to female contact interactions is also accounted for. The electrical characteristics of other calibration devices can be derived from these physically calculable standards.

### B. Traceability of Calibration Standards

Today’s VNA measurements required traceability of all the fundamental RF/microwave parameters – impedance, power, attenuation, frequency, and noise. Figures 6 through 10 illustrate the traceable chain of these fundamental parameters. Other than frequency, all fundamental parameters have impedance as a traceable parameter.

VNA impedance calibration standards are traceable to the meter, through precision airlines and shorts and mechanical gages. These are the most precise standards available. Figures 11 to 13 show the traceable parameters of these impedance standards.

The measurement uncertainties of all the applicable mechanical measurement systems are vigorously quantified. An accurate electrical model, based on accepted microwave theory and practices and verified data, is created to convert

the mechanical/physical properties into microwave S-parameters. The input variable uncertainties are used in a Monte Carlo simulation to propagate through the S-parameter calculations and accounted for in the uncertainties of the S-parameters, as diagramed in Figure 12.

The modeled S-parameters are then used to calibrate a reference VNA measurement system. This calibration method removes the imperfections that the airlines and shorts may have and provides the link to the fundamental units of measure - length and other physical constants. Uncertainty of such standards can be as low as 0.0005 at GHz frequencies and around 0.003 at mm wave frequencies. Except for the simple 1-port calibration case, the propagation of calibration standard uncertainties through the calibration process, the error correction process and then the device measurement process is quite complex [13]. Derivation of the sensitivity functions is quite involved. Again, Monte Carlo simulation technique may be employed to obtain VNA system measurement uncertainties.

### III. VNA VERIFICATION

To ensure that the VNA's measurements are accurate as specified after calibration, the measurement system must be verified. An internationally accepted method of VNA verification uses a set of verification standards, such as a low loss matched airline, a mismatched device and 2 attenuators. These devices are first measured by a reference laboratory. The measured data from the VNA in question is compared with the data obtained from the reference laboratory. If the two measurements are statistically similar, then the system is considered verified. This method is also known as the "tops down" verification. Important considerations for verification standards selection are:

- 1) the devices must be physically different from the calibration devices; and
- 2) the devices cover an adequate range of reflection and transmission characteristics.

Unfortunately, the best verification standards and the best calibration standards are at the same accuracy level. Therefore, it is NOT possible to verify a VNA system's accuracy by measuring a set of verification devices the traditional tops down way. The main purpose of this "tops down" verification is to confirm that the VNA calibration was performed correctly, the measurements are within the expected range and the VNA is operating correctly [14]. In addition to the "tops down" verification, statistical data of the verification results should be kept to access statistical control limits. Participation in national and international measurement comparison programs, such as the ARFTG Measurement Comparison Program, will provide the added assurance of the VNA's performance and proof of traceability.

A "bottoms up" verification approach has been proposed and used by many calibration laboratories. This approach uses precision airlines, and other physical standards in a different calibration method to extract the "residual errors" of the original calibration [15]. The "ripple" technique, for example, had been used to extract residual directivity and residual source match of a calibrated system, Figures 14-17. It uses a electrically long precision transmission line plus a short to measure the residual source match of the system. Replacing the short with a load, the directivity term may be extracted. This method assumed that precision transmission line has zero reflection. This assumption is invalid at low frequencies and marginally valid at mm frequencies. Again, since the original calibration used similarly derived standards, calibration accuracy to verification accuracy ratio is essential one. Measurement comparisons of inter-laboratory standards are still needed. A zero delay short (flush short) is the most precise device available. If it wasn't used in a calibration as a defined standards, it can be used as a verification device as illustrated in figure 18. All residual systematic errors are combined in this measurement and therefore is a good way to check total system calibration error. Other error sources of the measurement system also need to be individually quantified at the most fundamental level. This method provides a more thorough treatment of VNA system performance verification, but much more time consuming and costly.

### IV. NEW DEVELOPMENTS

While microwave coaxial and waveguide standards are reasonably well defined, mm-wave impedance standards still need further investigation. The effect of surface roughness becomes more important at these frequencies. On-wafer measurement traceable standards are still being developed. VNA measurements are moving beyond the basic S-parameters. Nonlinear networks, multitone distortion, and differential device measurements are just some of the new capabilities that need further development in traceable standards. Recent developments in mm wave to terahertz measurements made it necessary to redefine the waveguide interconnect standards. Requirements for traceable high impedance measurements of nano electronic devices are getting more attention. The list keeps on growing.

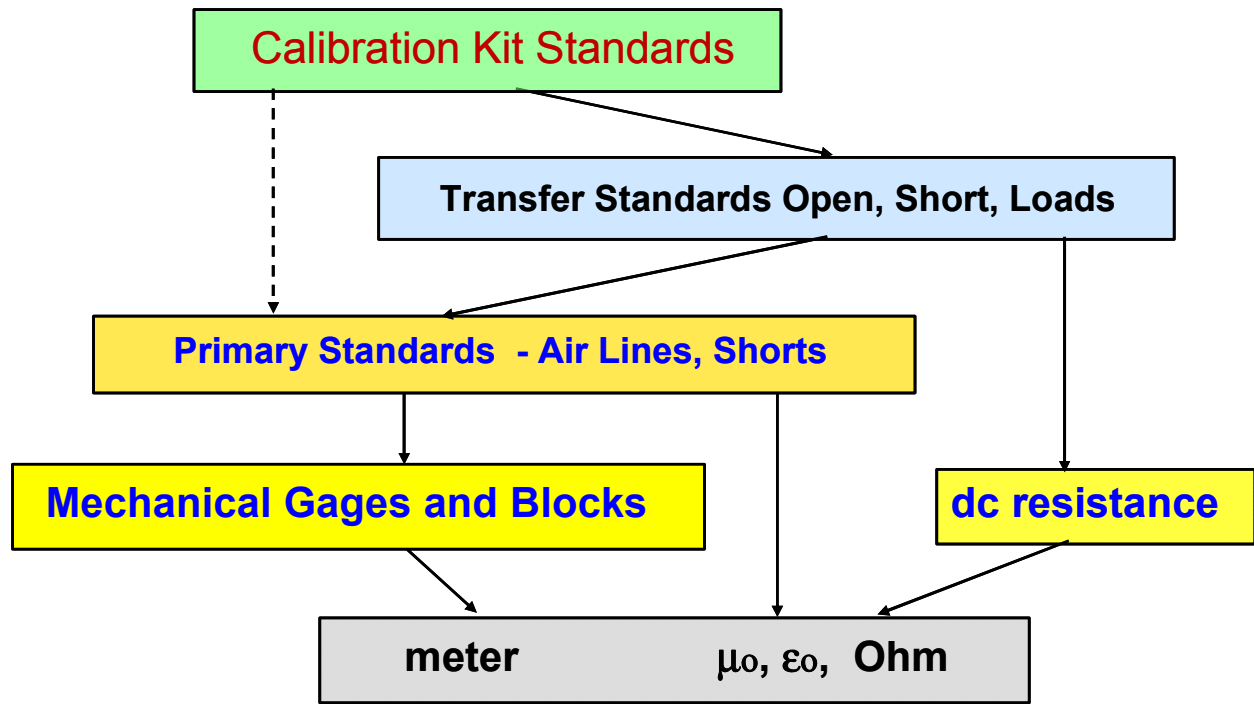


Figure 6: Traceability of Impedance

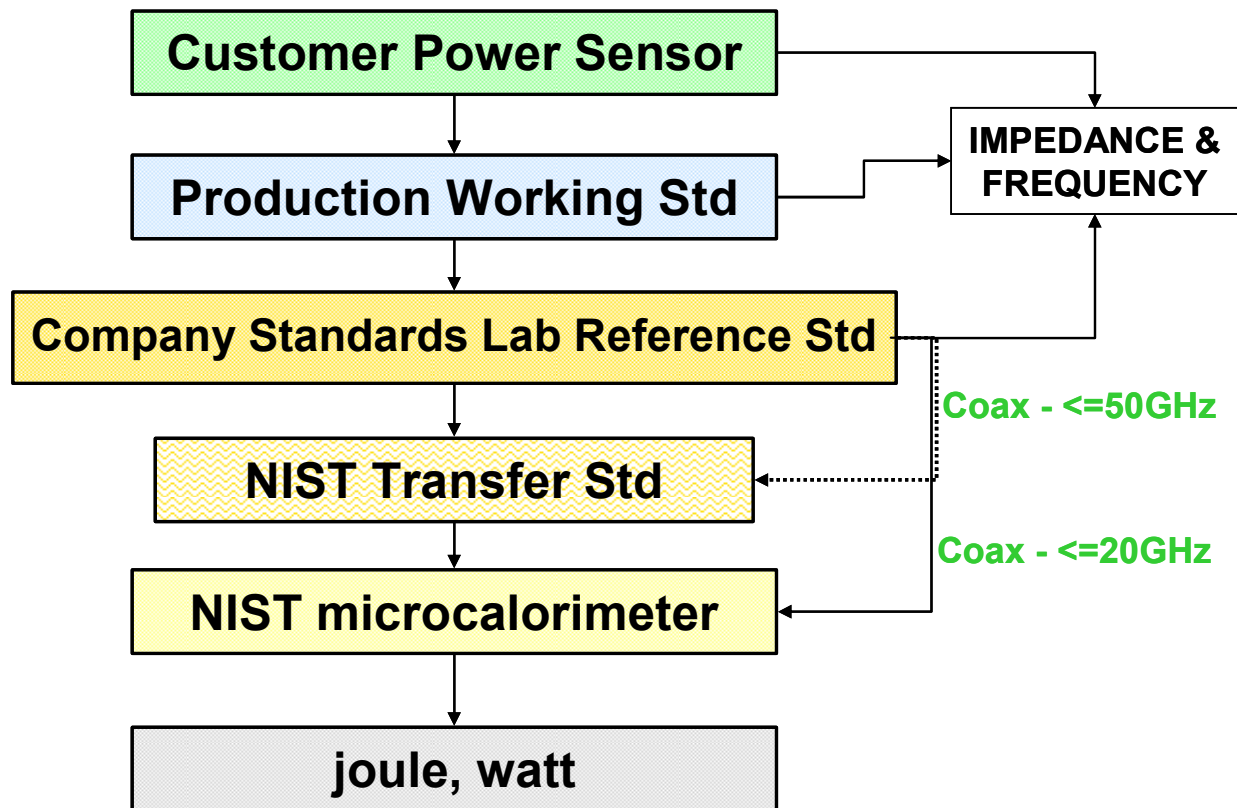


Figure 7: Traceability of Power

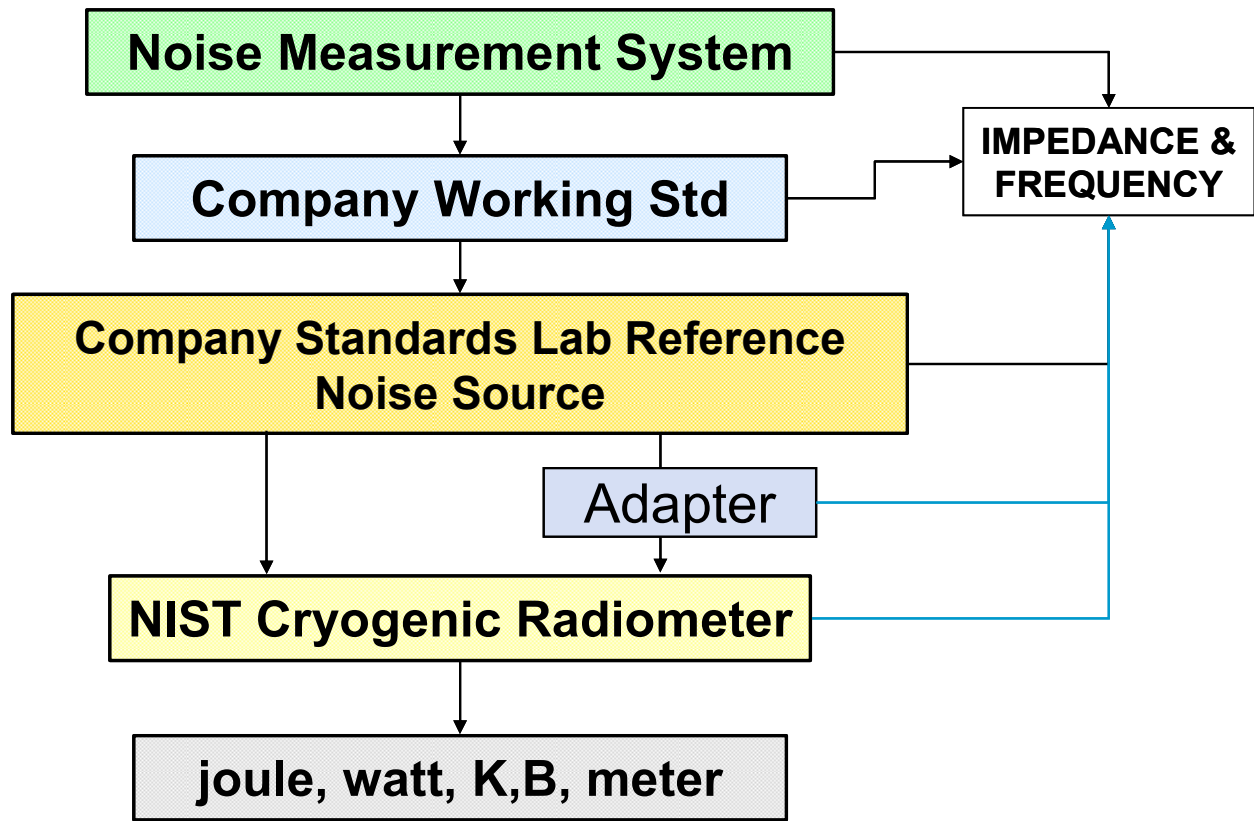


Figure 8: Traceability of Noise

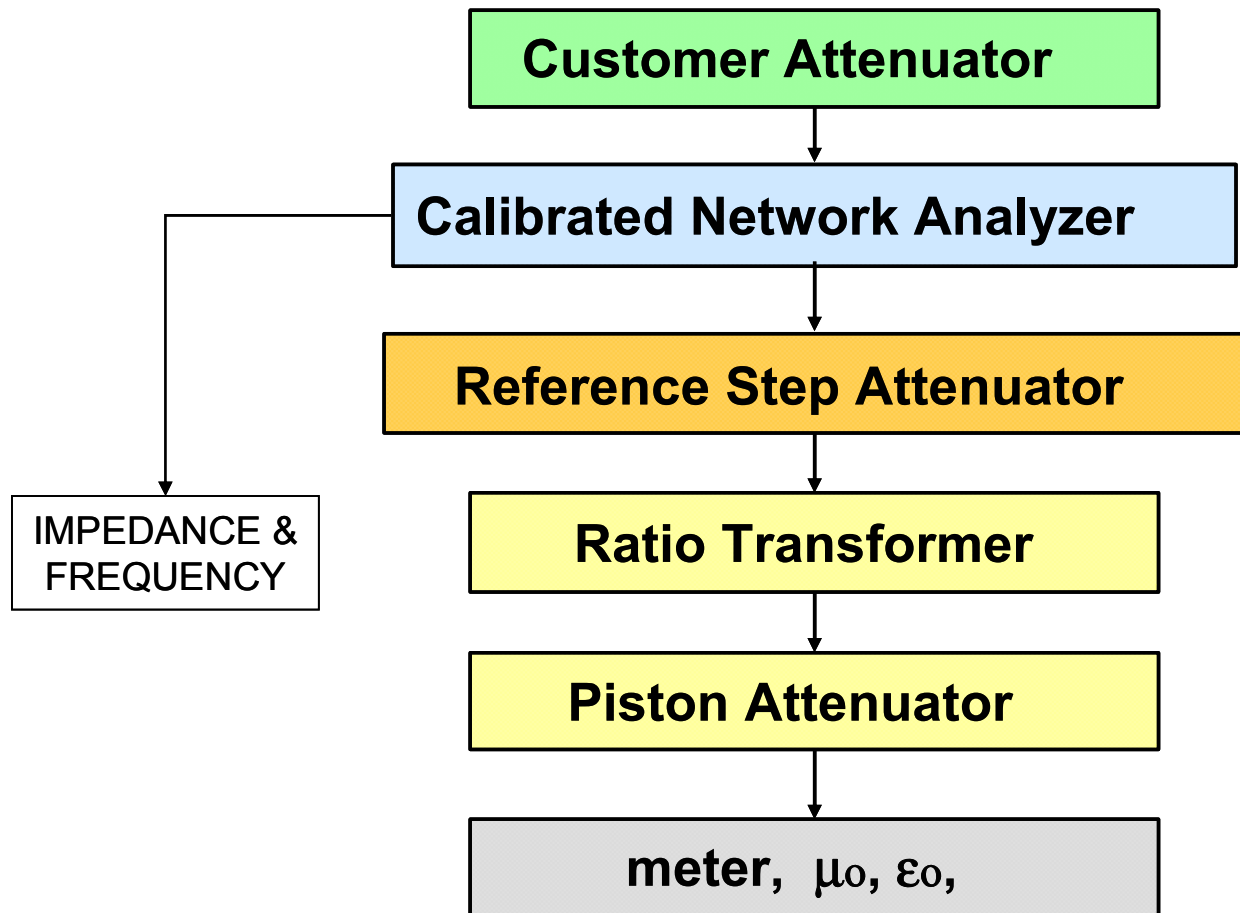


Figure 9: Traceability of Attenuation

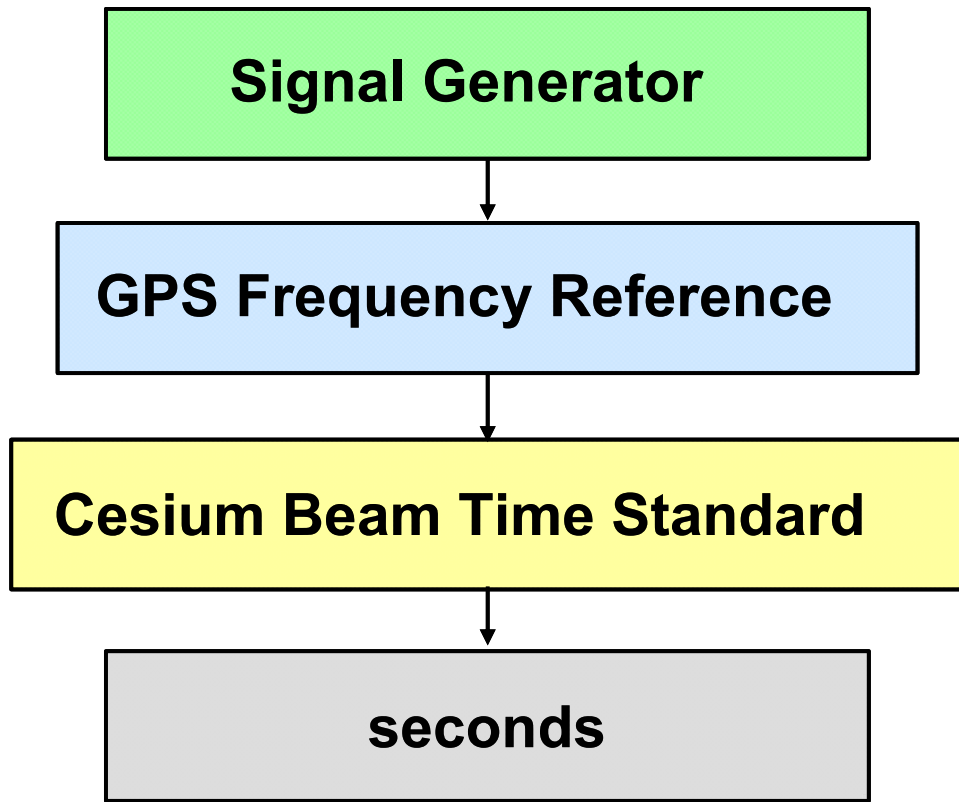
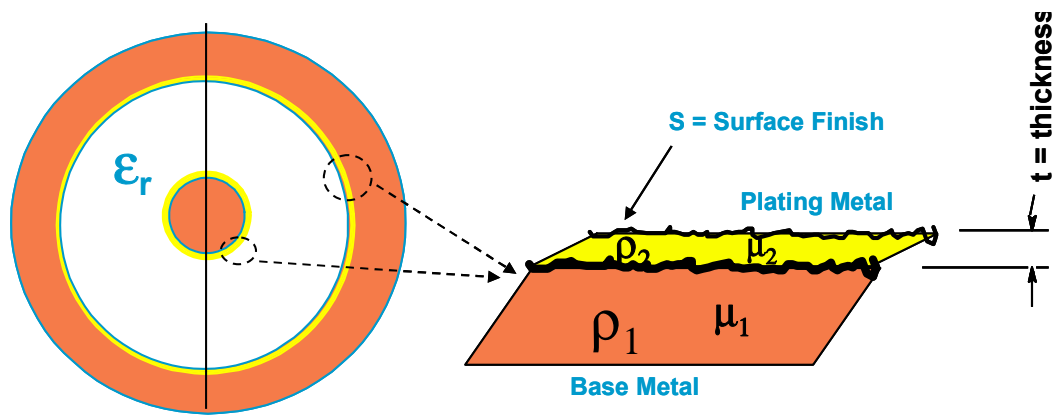


Figure 10: Traceability of Time/Frequency



$$Z_c = F(f, \text{CCOD}, \text{OCID}, \mu_0, \epsilon_0, \epsilon_r, \rho_1, \rho_2, \mu_1, \mu_2, t, 'K, c)$$

$$\gamma = G(f, \text{CCOD}, \text{OCID}, \mu_0, \epsilon_0, \epsilon_r, \rho_1, \rho_2, \mu_1, \mu_2, t, 'K, c)$$

Figure 11: Coaxial Impedance and Loss Dependent Variables

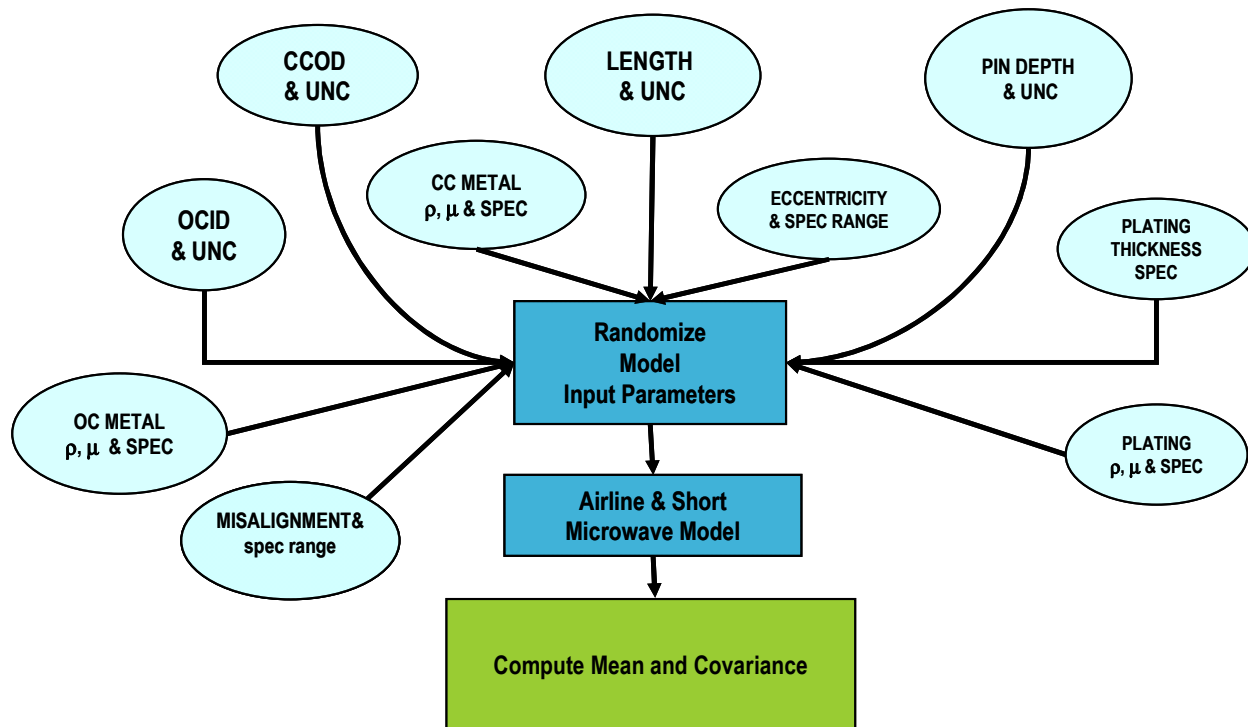
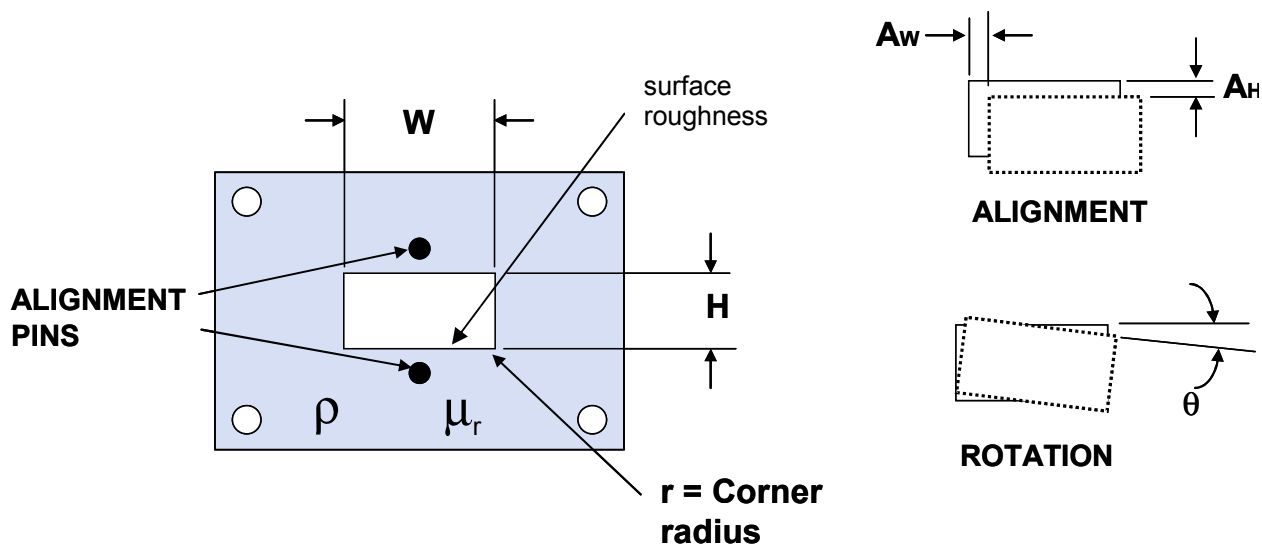


Figure 12: Monte Carlo Simulation of Precision Transmission Line and Short Standards



$$\Gamma = F(f, W, H, r, A_w, A_H, \theta, \mu_0, \epsilon_0, \epsilon_r, \rho, \mu_r, K, c)$$

Figure 13: Waveguide reflection dependent variables

Known Long Airline

LOAD

Known Short

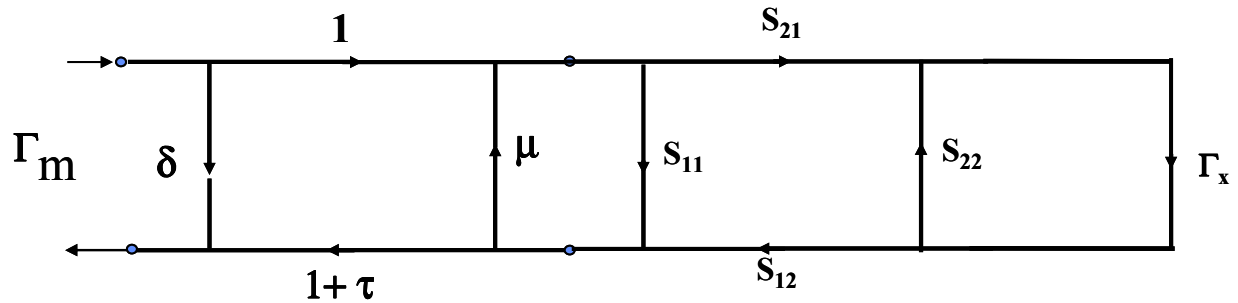


Figure 14: Ripple extraction technique and signal flow graph

## Residual Directivity

$$\Gamma_{m1} = \delta + \frac{(1+\tau) \Gamma_L}{1-\mu \Gamma_L} \quad \Gamma_{m2} = \delta + \frac{(1+\tau) [S_{11}(1 - S_{22} \Gamma_L) + S_{21} S_{12} \Gamma_L]}{1-\mu S_{11} - \mu S_{21} S_{12} \Gamma_L - S_{22} \Gamma_L}$$

Assume that  $S_{11} = S_{22} = 0$  and ignoring 2<sup>nd</sup> order and higher terms.

$$\left| \Gamma_{m1} - \left( \frac{\Gamma_{m2}}{S_{21} S_{12}} \right) \right| \approx \left| \delta \left( 1 - \frac{1}{S_{21} S_{12}} \right) \right|$$

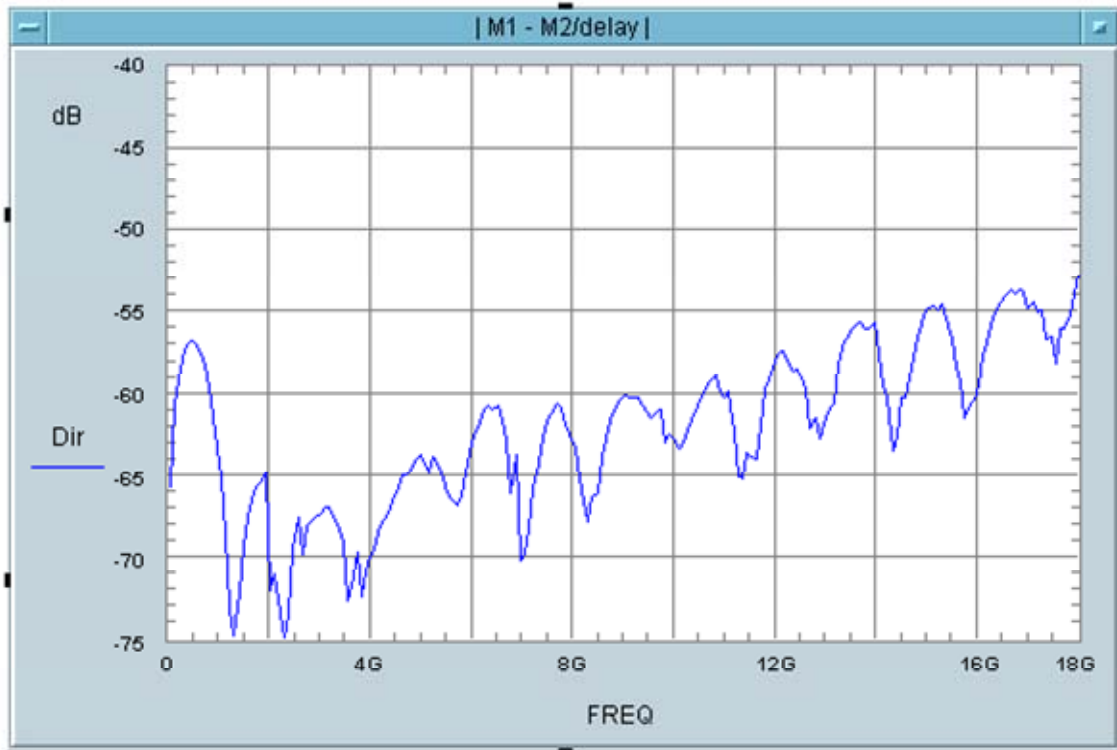
If  $|S_{21}^* S_{12}|$  is  $\sim 1$

$$\left| 1 - \frac{1}{S_{21} S_{12}} \right| \approx |1 - \cos(2\theta) - j \sin(2\theta)| = \sqrt{2 - 2\cos(2\theta)} = \sqrt{2 [1 - \cos(2\theta)]} = 2 \sin(\theta)$$

$\theta = -(\text{phase delay of airline})$

$$\left| \Gamma_{m1} - \left( \frac{\Gamma_{m2}}{\exp(-2j\theta)} \right) \right| \approx 2 |\delta| |\sin(\theta)| \quad ; \quad \left| \Gamma_{m1} - \left( \frac{\Gamma_{m2}}{\exp(-2j\theta)} \right) \right|_{\text{peak}} = 2 |\delta|$$

Figure 15: Residual directivity extraction computation



$$20 * \log_{10} \left\{ \left| \Gamma_{m1} - \left( \frac{\Gamma_{m2}}{\exp(-2j\theta)} \right) \right| \right\} - 6 \text{ dB}$$

Figure 16: Residual Directivity Ripples

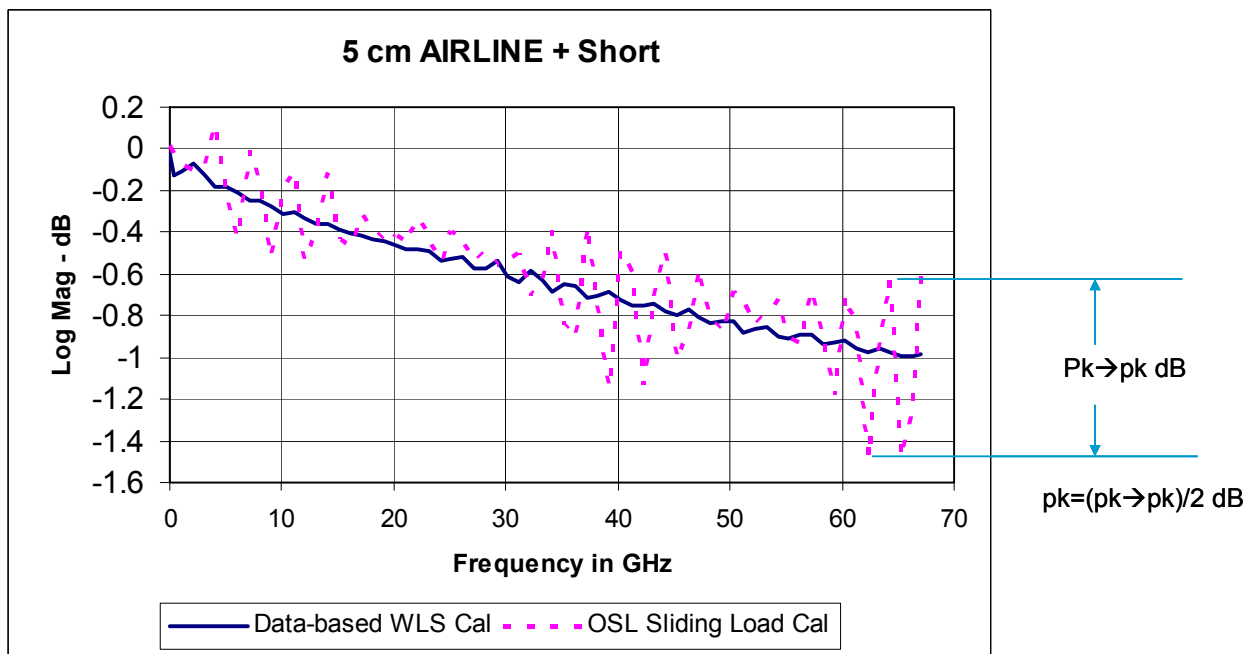


Figure 17: Residual Source Match Ripples

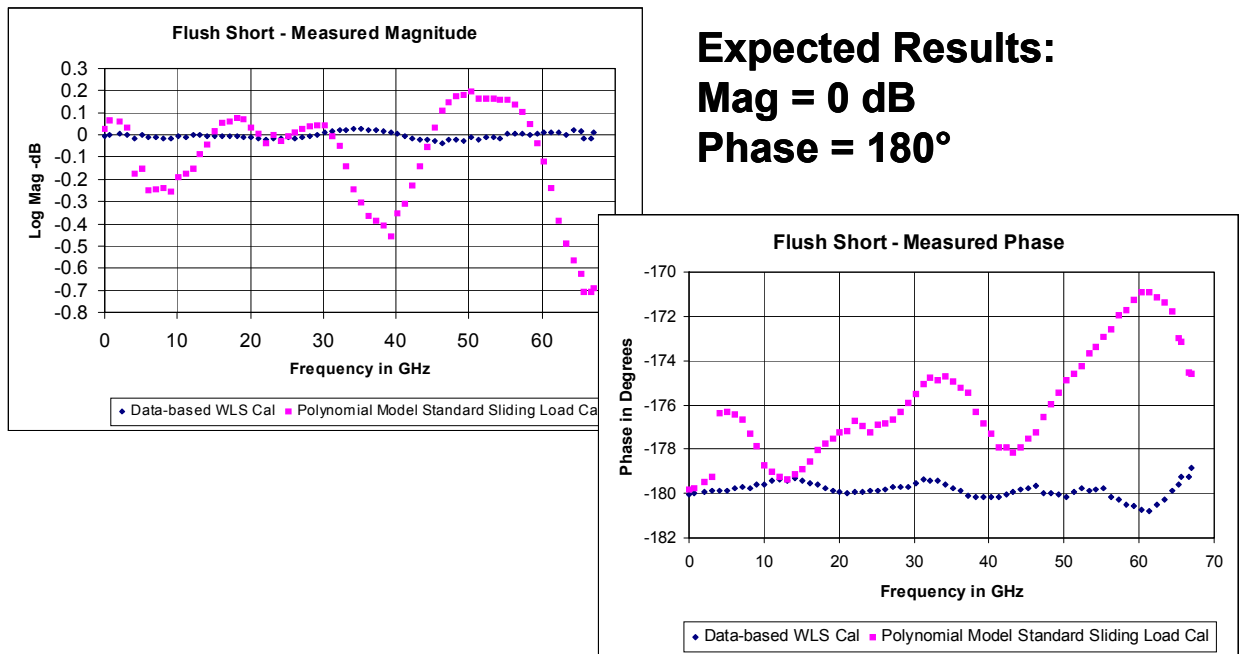


Figure 18: Verification using a flush short

## V. SUMMARY

The ISO definitions of traceability and its relationship to calibration, verification, and uncertainty of measurement were presented. The traceable path of VNA measurement parameters, S-parameters, power, attenuation, and noise were discussed. Traceability of impedance standards, also required for power, attenuation and noise traceability, was discussed in greater detail. VNA performance verification methods were discussed. Limitations of tops down and bottoms up verifications were brought up. Participation in national and international measurement comparison programs was suggested to augment the traditional verification processes. New VNA measurement capabilities and new applications are pushing the need to development new traceable standards.

## References:

- [1]. Belanger, B.C., "Traceability: An Evolving Concept", ASTM Standardization News, Vol 8, No. 1 1980, pp 22-28
- [2] D.K. Rytting, "Network analyzer accuracy overview", 58<sup>th</sup> ARFTG Conference Digest, Nov. 29-30, 2001
- [3] M.J. Salter, N.M. Ridler, "A generalized approach to the propagation of uncertainty in complex S-parameter measurements", 64<sup>th</sup> ARFTG Conference Digest, Dec. 1-2, 2004
- [4] B.D. Hall, "Calculations of measurement uncertainty in complex valued quantities involving 'uncertainty in the uncertainty'", 64<sup>th</sup> ARFTG Conference Digest, Dec. 1-2, 2004
- [5] K. Wong, "Uncertainty analysis of the weighted least square calibration", 64<sup>th</sup> ARFTG Conference Digest, Dec. 1-2, 2004
- [6] "Traceability and the HP 8510 Network Analyzer", HP White Paper, Nov. 1, 1985
- [7] D.K. Rytting, "Advances in Microwave Error Correction Techniques", HP RF & Microwave Symposium, 1987.
- [8] K. Wong, "Traceability of Vector Network Analyzers", Test and Measurement World Europe, Feb. March, 1996
- [9] R.B. Marks, D.f. Williams, "A general waveguide circuit theory," J. Res. National Institute of Standards and Technology, vol. 97, Sept.-Oct. 1992.
- [10]. K.H. Wong, "Characterization of Calibration Standards by Physical Measurements", ARFTG Digest Spring 1992
- [11]. IEEE Standard 287-2007, "Precision Coaxial Connectors"
- [12] J. P. Hoffmann, P. Leuchtman, and R. Vahldieck, "Pin Gap Investigations for the 1.85 mm Coaxial Connector", 37<sup>th</sup> European Microwave Conference 2007, pp. 388-391, October 2007.
- [13] N.M. Ridler, M.J. Salter, "Evaluating and expressing uncertainty in complex S-parameter measurements", 56<sup>th</sup> ARFTG Conference Digest, Nov. 2000
- [14] R. Ginley, "Microwave Network Analyzers: A Discussion of Verification Methods.", Cal Lab, Sept, Oct. 1999, pp. 22-25
- [15] R. Pollard, "Verification of System Specifications of a High Performance Network Analyzer", 23<sup>rd</sup> ARFTG Conference Digest, June 4,5, 1984

# The Influence of Calibration Substrate Boundary Conditions on CPW Characteristics and Calibration Accuracy at mm-Wave Frequencies

Andrej Rumiantsev<sup>\*</sup>, Ralf Doerner<sup>\*\*</sup>, and Edward M. Godshalk<sup>\*\*\*</sup>

<sup>\*</sup> SUSS MicroTec Test Systems GmbH, Suss-Str. 1, Sacka, D-01561, Germany, a.rumiantsev@ieee.org

<sup>\*\*</sup> Ferdinand-Braun-Institut fuer Hoechstfrequenztechnik (FBH),

Gustav-Kirchhoff-Str. 4, Berlin, D-12489, Germany, ralf.doerner@ieee.org

<sup>\*\*\*</sup> Maxim Integrated Products, Inc. 120 San Gabriel Drive, Sunnyvale, CA 94086, USA,  
Ed\_Godshalk@or.mxim.com

**Abstract** — This paper presents new experimental investigations of the influence of calibration substrate boundary conditions on CPW transmission line characteristics and calibration accuracy at millimeter wavelengths. A new configuration that decreases insertion loss of CPW transmission lines and improves calibration accuracy is suggested.

**Index Terms** — calibration, error correction, calibration comparison, scattering parameters measurement, surface waves.

## I. INTRODUCTION

Accurate calibration of RF and microwave wafer-level test and measurement setups is a crucial part of the device characterization process. Its success strongly depends on the calibration method and precision of calibration standards used. Substrate-based calibration standards have been used in the wafer probing industry since the early 1980's. Commonly used calibration substrates (also often called Impedance Standard Substrate or ISS) include short, load and thru calibration standards, and frequently some relatively long transmission lines for different lumped (e.g. SOLT<sup>1</sup>, LRRM<sup>2</sup>, LRM<sup>3</sup> etc.) and distributed (e.g. conventional [1] and multilayer TRL<sup>4</sup> [2]) calibration techniques. Some substrates also contain open standards. Often these standards and transmission lines are based on the coplanar waveguide (CPW) design, since this geometry is compatible with the ground-signal-ground (GSG) wafer probe configuration.

Recommendations for characterizing and improving performance of planar standards have been previously published e.g. [3-6]. The work [4] observed influences of surface wave modes in dielectric substrates that can be propagate at mm-wave frequencies and affect electrical characteristics of standards. Recommendations, such as suspending the calibration substrate, decreasing its thickness,

and the use of radiation-absorbing materials (RAM) were presented. However, experimental results were limited to 50 GHz due to wafer-level measurement capability available at that time.

Investigation [5] recommended placing the calibration substrate on the RAM (versus being suspended 3.8 mm above it as described in [4]) and showed that a 625  $\mu\text{m}$  thick ISS resulted in worse error than a 250  $\mu\text{m}$  thick ISS above 70 GHz.

This paper presents the results of investigations of the influence of calibration substrate boundary conditions on:

1. The propagation characteristics of CPW lines.
2. The accuracy of various calibration methods.

A new configuration is suggested that significantly decreases the coupling of the unwanted substrate modes with the CPW standards beyond 50 GHz. Section II presents background theory and analysis methods that were used. Section III describes the experimental setup, and Section IV presents the experimental results. The conclusions are in Section V.

## II. VERIFICATION AND CHARACTERIZATION PROCEDURES

### A. Variable Calibration Boundaries

Traditionally the substrate thickness for an ISS is in the 250 to 625  $\mu\text{m}$  range. As described in [4], at higher frequencies the substrate can support Transverse Electric (TE) modes and Transverse Magnetic (TM) surface wave modes, that can couple to the CPW transmission line mode at critical frequencies. These critical frequencies are a function of mode number, substrate thickness and substrate boundary condition. Some boundary conditions are:

1. The calibration substrate resting on a metal plate. This is a "grounded" condition.
2. The calibration substrate suspended in air. This is an "open" condition.
3. The calibration substrate resting on RAM. This is a "lossy" condition.

Table 1 shows the predicted critical frequencies as a function of substrate thickness for the first two boundary

<sup>1</sup> Short-Open-Load-Thru

<sup>2</sup> Line-Reflect-Reflect-Match

<sup>3</sup> Line-Reflect-Match, advanced

<sup>4</sup> Thru-Reflect-Line

conditions. The critical frequency is defined at the frequency where the propagation phase constant of the CPW mode is equal to that of the surface wave in the substrate.

To avoid coupling of energy from calibration standards into surface waves, a common solution is to use a calibration substrate that is thin enough to assure that these critical frequencies occur above the band of interest. For example, a CPW transmission line on a 254  $\mu\text{m}$  thick alumina substrate has critical frequency of 122 GHz for the  $\text{TE}_0$  mode and 120 GHz for the  $\text{TM}_0$  mode. Hence, this substrate thickness is suitable for use through W-band (75-110 GHz). Often these substrates are placed over RAM [5] to further attenuate unwanted surface waves by absorbing the evanescent fields that exist outside of the substrate itself.

**TABLE 1.**  
CRITICAL FREQUENCIES FOR TE AND TM SURFACE WAVE  
MODES IN AN ALUMINA SUBSTRATE ( $\epsilon_r = 9.9$ )  
VERSUS SUBSTRATE THICKNESS

Substrate Thickness in mm	Critical Frequency in GHz			
	Suspended "Open" Substrate			"Grounded" Substrate
	TE0	TM0	TE1	TM0
0.254	122	240	-	120
0.508	60	120	-	60
0.762	46	85	-	43
1.016	33	64	-	32
1.270	26	54	-	25
1.524	23	42	-	21
1.778	18	37	-	18
2.032	17	33	$\sim 50$	16

As frequencies increase to the higher millimeter wave bands, it is not practical to continue to reduce the substrate thickness out of concern for breakage of the ISS during handling. For this reason, the approach of placing the ISS on an extremely thick substrate (i.e. about 10 mm) has been investigated. The initial concern is that CPW transmission lines on such a thick substrate will suffer from multiple resonances due to coupling to the numerous critical frequencies shown in Table 1. However, by using small enough CPW dimensions such as recommended in [4], the coupling between the CPW and surface wave modes can be minimized.

### B. Extraction of CPW Transmission Line Parameters

The propagation constant and the characteristic impedance of the experimental CPW lines were found using the method from [7]. This method was originally developed for GaAs applications and later proven suitable for commercially-available alumina calibration substrates [6].

### C. Calibration Comparison

The accuracy of distributed and selected lumped calibration methods was verified for each boundary condition using the calibration comparison technique [8]. This technique provides

the worst-case deviations of the measured S-parameters of passive devices for the examined (first-tier) calibration with respect to the benchmark (second-tier) calibration. Deviations are treated as  $|S_{ij} - S_{ij}'|$ , for  $ij \in \{11, 12, 21, 22\}$ , where  $S_{ij}'$  is the S-parameter measured by the calibration to be tested, and  $S_{ij}$  is the S-parameter measured by the benchmark calibration. In the ideal case, both calibrations, benchmark and examined, are equal, and the error bounds  $|S_{ij} - S_{ij}'|$  are zero.

The NIST multilineTRL method was selected as the benchmark, SOLT and LRM+ [9] as examined calibrations.

## III. EXPERIMENTAL SETUPS

The experimental setup for the 110 GHz wafer-level measurements included an Agilent 8510XF VNA, a semi-automated wafer-probe system PA200HF from SUSS MicroTec, and the two different models of a 110 GHz wafer probe tips: the Infinity and the ACP probes with a pitch of 100  $\mu\text{m}$  and 125  $\mu\text{m}$  respectively. To minimize the influence of the measurement setup on results of this work, an alternative system was used to run the same test plans. The second system consisted of an Agilent PNA 110 GHz VNA and the manual probe system PM8HF from SUSS MicroTec and the same wafer probes.

A commercially available 250  $\mu\text{m}$  thick alumina calibration substrate model 104-783A was evaluated. Standard elements on the substrate included the coplanar short, match, and line structures. The six line standards had lengths of 200  $\mu\text{m}$ , 450  $\mu\text{m}$ , 900  $\mu\text{m}$ , 1800  $\mu\text{m}$ , 3500  $\mu\text{m}$ , and 5250  $\mu\text{m}$ , respectively. The shortest line is used as thru. Typical dimensions of the coplanar structures were 50  $\mu\text{m}$  center conductor width, 25  $\mu\text{m}$  gap, 275  $\mu\text{m}$  ground metal width and 5  $\mu\text{m}$  metallization thickness. In contrast to the longer line standards the ground metal width for short, match and thru standard structures was 125  $\mu\text{m}$ .

The substrate was measured on both systems under the following conditions (Fig. 1):

1. Placed directly on the metal chuck
2. Placed directly on a ceramic chuck (approximately 1 cm thick)
3. Same as 1, but with the absorber between the substrate and the metal chuck;
4. Suspended above the metal chuck by about 1.2 cm.

SussCal<sup>5</sup> Professional and MultiCal<sup>6</sup> high-frequency calibration packages were used for data acquisition, offline error correction and result analysis.

All measurement series were taken at room temperature and under environmentally controlled conditions.

<sup>5</sup> Commercially available from SUSS MicroTec

<sup>6</sup> Available from NIST

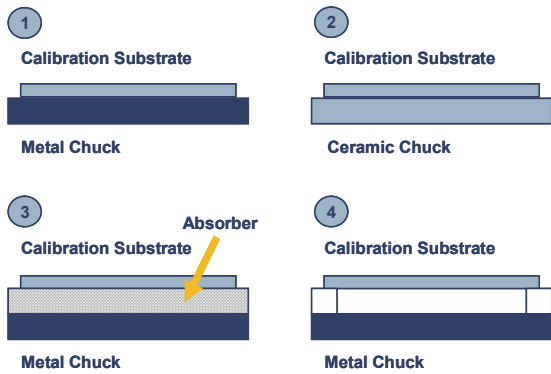


Fig. 1. Experimental setups providing different calibration boundary conditions: 1) Metal “grounded”, 2) Ceramic “matched”, 3) Absorber “lossy” and 4) Suspended “open”.

#### IV. EXPERIMENTAL RESULTS

To avoid additional uncertainty due to contact repeatability, all data were acquired in one measurement series in raw format and saved externally for further analysis. The experimental data included measurement results of all calibration standards that are required for the lumped (SOLT and LRM+) as well as for the multilineTRL calibrations.

##### A. Influence of the Measurement Setup

The propagation constant and the characteristic impedance of the CPW lines were extracted from the NIST multilineTRL for each measurement boundary condition and from measured data taken on both experimental setups, but with the same wafer probes. As expected, both measurement systems provided comparable results (Fig. 2). It proved that the experimental results are independent from the probe system and the VNA used.

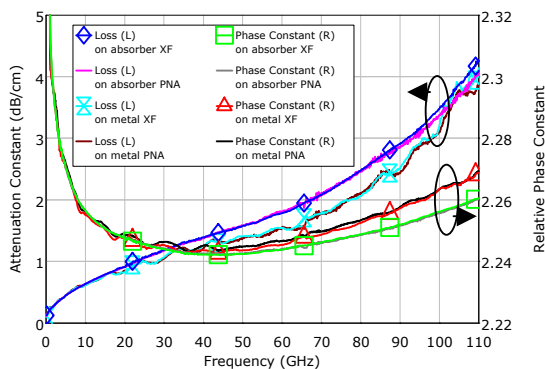


Fig. 2. The attenuation and the relative phase constants of the 250  $\mu\text{m}$  substrate CPW lines measured on two different setups. Two boundary conditions were taken: the metal and absorber boundaries. Both measurement systems gave comparable results.

##### B. CPW Line Characterization

CPW line attenuation and relative phase constants were found from the multilineTRL method. The line capacitance per unit length was extracted applying the lumped resistor method [6, 10] (Table 2) and the line characteristic impedance was measured for all four boundaries (Fig. 1).

TABLE 2.  
THE EXTRACTED LINE CAPACITANCE VALUE

Boundary	Grounded	Lossy	Open	Matched
C in pF/cm	1.489	1.483	1.478	1.478

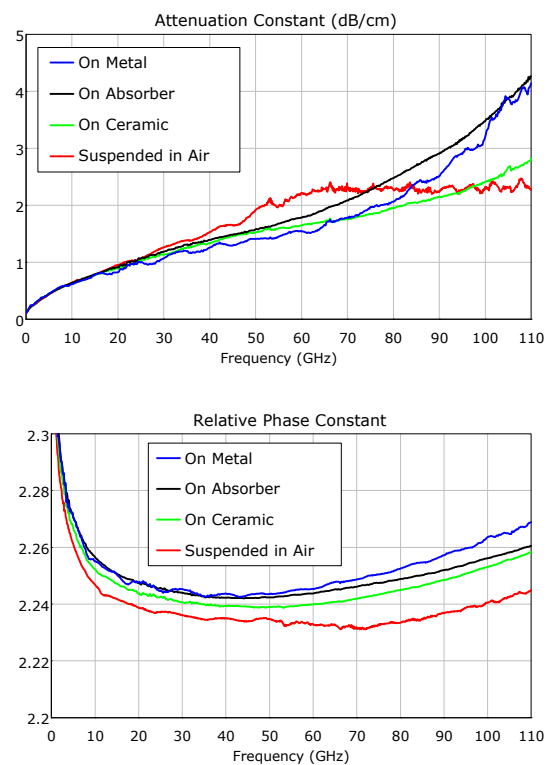


Fig. 3. The extracted attenuation and relative phase constants of the same CPW line from the 250  $\mu\text{m}$  thick substrate for four measurement boundary conditions: direct on the metal chuck (“grounded”), on metal chuck and absorber (“lossy”), suspended in air (“open”), and on ceramic chuck (“matched”).

Figures 3 and 4 show the measured characteristics of the CPW line. The “grounded” and the “lossy” boundaries are commonly-used practices. The “grounded” case shows a periodic ripple from about 20 GHz and beyond. In contrast to this, the line attenuation constant for the “lossy” case is “smoother”, but about 60 GHz and it rises faster than expected. Owing to its erratic behavior the “open” boundary is not a viable alternative.

Figure 3 shows that the CPW line on the “matched” ceramic chuck gives the lowest attenuation and a monotonic response up to 110 GHz. Figure 4 shows that the CPW on ceramic has the least reactance as frequency increases, which is as expected for an ideal transmission line. For these reasons it appears that the CPW line on the ceramic behaves more ideally than for the other boundary conditions.

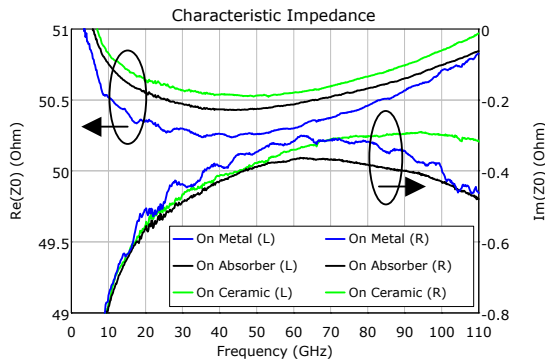


Fig. 4. The characteristic impedance of the same CPW line from the 250  $\mu\text{m}$  thick substrate extracted for three measurement boundary conditions: direct on the metal chuck, on metal chuck and absorber, and on ceramic chuck.

### C. Calibration Accuracy Verification

Next, the multilineTRL, SOLT, and LRM+ were performed. The same set of standards was used while the substrate boundary conditions were varied. The upper error bounds of measurement deviations for passive devices were calculated for each boundary condition using the calibration comparison method. A multilineTRL performed on the ceramic chuck was used as the reference calibration, since the CPW characteristics were the least perturbed from their expected behavior when using this boundary condition.

A significant dependency of the calibration accuracy versus the boundary condition was observed for all evaluated methods. For example, Figure 5 presents the comparison for selected calibration schemes: multilineTRL (mTRL) on the metal chuck and on ceramic, SOLT on the metal chuck and LRM+ (LRMplus) on ceramic, with multilineTRL on the ceramic chuck being the benchmark (i.e. “baseline reference”) calibration.

SOLT on the metal chuck is the worst case for the evaluated lumped-standard calibration methods. It showed an error of about 0.15 at 75 GHz and erratic results above this frequency. The most accurate lumped-standard calibration scheme was found to be LRM+ on ceramic. It demonstrated measurement error of less than 0.13 up to 110 GHz.

For the multilineTRL method the absorber case has the closest agreement (to the benchmark multilineTRL results on the ceramic chuck) with an error of 0.08 at 110 GHz. Presumably the disagreement is due to the lossy boundary

condition of the absorber. When the multilineTRL is performed with the calibration substrate on metal the error increases to 0.18 at 110 GHz.

Hence, measurement of the same test device may significantly differ depending on the boundaries set for calibration. It could introduce uncertainty into modeling and parameter extraction and can mislead device design and optimization.

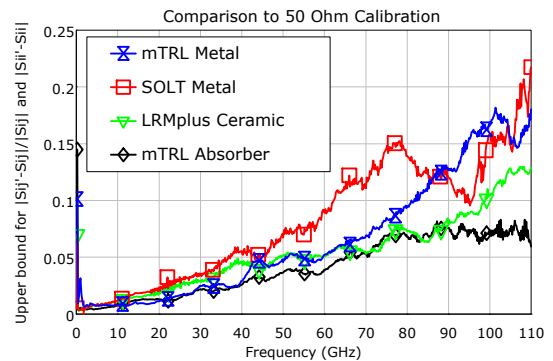


Fig. 5. The upper error bounds of measurement of a passive DUT after multilineTRL, SOLT, and LRM+ performed on the 250  $\mu\text{m}$  thick ISS for selected boundary conditions. The most accurate lumped-standard calibration is the LRM+ on ceramic. The worst lumped-standard calibration case is the SOLT on metal.

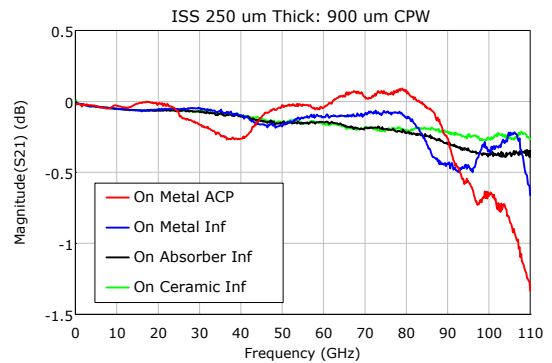


Fig. 6. Insertion loss of 900  $\mu\text{m}$  CPW line from the 250  $\mu\text{m}$  thick alumina calibration substrate, measured with respect to the multilineTRL for different measurement boundary conditions: direct on the metal chuck “grounded”, on metal chuck and absorber “lossy”, and on ceramic chuck “matched” with Infinity probes. The red curve presents the results for the “grounded” boundary and the ACP probes.

### D. Measurement of DUTs

To evaluate the impact of calibration boundaries on the measurement accuracy, three elements were used: the short standard, the 900  $\mu\text{m}$  line standard and the probes contacting the bare ceramic on the substrate (“open on ceramic”). All

measurements were corrected by multilineTRL using the short as the reflect standard.

Because the TRL algorithm does not require the definition of the return loss of the reflect as well as the insertion loss of the line [11], all selected elements can be referred as *a priori* unknown DUTs. The evaluated boundaries were: “grounded”, “lossy”, and “matched”. Also, to identify the impact of wafer probes, the same calibration and measurement were repeated for the “grounded” boundary with the ACP probes (Fig. 6-8).

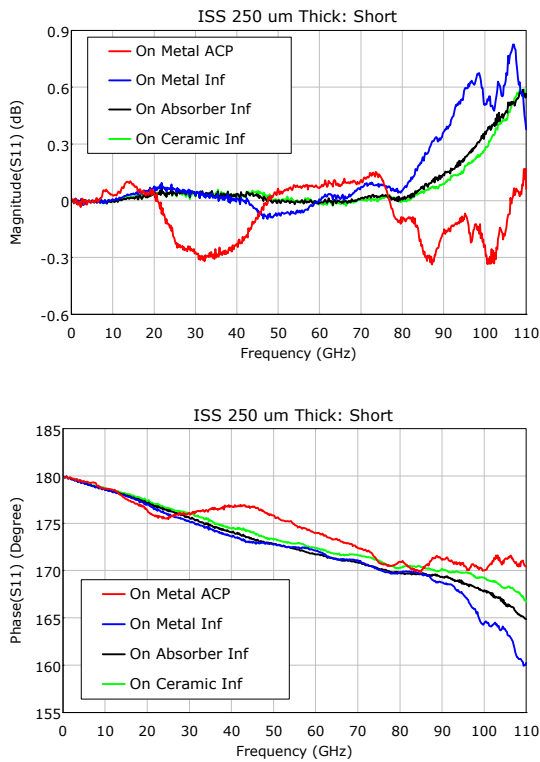


Fig. 7. The return loss of a short standard from the 250  $\mu\text{m}$  alumina calibration substrate, measured with respect to the multilineTRL for different measurement boundary conditions: direct on the metal chuck “grounded”, on metal chuck and absorber “lossy”, and on ceramic chuck “matched” with Infinity probes. The red curve presents the results for the “grounded” boundary and the ACP probes.

The change of the probe type should not influence the TRL calibration results; CPW parameters such as capacitance per unit length, characteristic impedance, and propagation constant are probe independent. They are defined by the CPW design, the properties of the dielectric, and, as proved above, measurement boundaries. Additionally, TRL is not sensitive to the variations of the equivalent model of the reflect standard. This may occur when changing the probe type and the probe pitch.

However, the results from Fig. 6-8 demonstrate that there is a strong influence of the wafer probe design on the measured

data, due to interaction with the measurement system (i.e. calibration substrate, chuck, etc.).

Figure 6 shows insertion loss versus different boundary conditions and probes. Note that the thick ceramic chuck generally results in the lowest loss above 85 GHz.

Furthermore, it was found that the measurement of highly-reflective devices (the short and the “open on ceramic”) did not meet expectations from above 70 GHz for both probe types. The use of a ceramic chuck or absorber reduces the measurement error. However, the return loss of the short still shows an unrealistic value, achieving +0.6 dB at 110 GHz and a non-linear phase above 100 GHz. The same concerns the “open on ceramic” element: its return loss rolls off to -0.94 dB at about 100 GHz for the “grounded” boundary and the Infinity probes. The results for the ACP probes give the same kind of effect. Changing to the “matched” boundary of the ceramic chuck reduced the deviation to 0.4 dB at 110 GHz the magnitude.

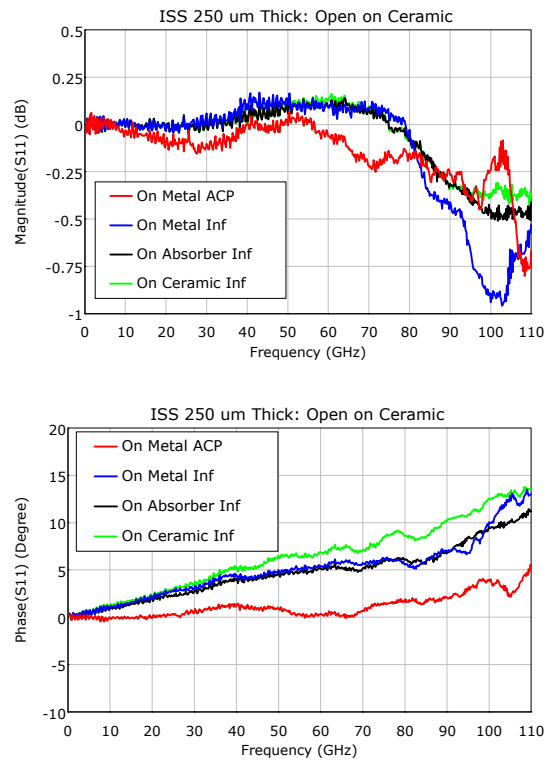


Fig. 8. The return loss of a “open on ceramic” standard from the 250  $\mu\text{m}$  alumina calibration substrate, measured with respect to the multilineTRL for different measurement boundary conditions: direct on the metal chuck “grounded”, on metal chuck and absorber “lossy”, and on ceramic chuck “matched” with Infinity probes. The red curve presents the results for the “grounded” boundary and the ACP probes.

The phase mismatch of about 5 degrees in the “open on ceramic” measurement between probes (Fig. 8) could be

explained as an impact of the different fringing capacitances of the probes.

## V. CONCLUSION

Different calibration boundary conditions were investigated: the commonly used methods to place the substrate on the metal chuck (the “grounded” case) and on absorber (the “lossy” case). It was demonstrated that the “metal” boundary is the worst case for measurement and calibration for frequencies above about 60 GHz.

The change to the “lossy” boundary impacts the loss and the relative phase constants as well as the characteristic impedance of the CPW line. It leads to the non-linear increase of the attenuation constant and increases the roll-off of the imaginary part of the line characteristic impedance. As a result, the definition of the calibration reference impedance will not be ideal for frequencies from 60 GHz and above.

A new method of using a thick ceramic support was proposed. It was shown that new method significantly reduces the impact of higher modes, and at the same time does not negatively influence the characteristics of a CPW line, such as its propagation constant and the characteristic impedance. As a result, the calibration and measurement accuracy is improved. Specifically, this experimental series demonstrated an improvement up to 0.18 of the upper error bounds for the multilineTRL calibration scheme up to 110 GHz. Also, using this new method, lower insertion loss is observed for CPW transmission lines above 85 GHz.

The accuracy of lumped SOLT and LRM+ calibrations was calculated over the 0.1 to 110 GHz frequency range. Both the worst-case SOLT on “grounded” boundary and the best-case LRM+ on “matched” boundary lumped calibrations were comparable with the reference TRL results below 50 GHz. Above 50 GHz, the difference in calibration boundaries increases, and the measurement error grows.

A strong influence of the probe tip design on the distributed calibration accuracy was found. This needs to be investigated further to determine how much is due to the probe itself versus the network formed by the combination of the CPW, boundary condition and probe type.

Also, some unexpected effects were identified at measurement frequencies above 70 GHz for highly-reflective devices independent from the probe types. Improvement of the calibration standards design should reduce such measurement errors.

Summarizing, the use of the new method – the ceramic support chuck instead of metal or an absorber – has demonstrated characteristics, such as more ideal CPW characteristics, that should facilitate improved calibration and measurement accuracy for mm-wave frequency applications.

## ACKNOWLEDGMENT

The authors wish to acknowledge Falk Korndorfer from IHP for excellent assistance and support with an alternative 110 GHz wafer-level measurement system.

## REFERENCES

- [1] G. F. Engen and C. A. Hoer, "Thru-Reflect-Line: an improved technique for calibrating the dual six-port automatic network analyzer," *Microwave Theory and Techniques, IEEE Transactions on*, vol. 27, pp. 987-993, 1979.
- [2] R. B. Marks, "A multilayer method of network analyzer calibration," *Microwave Theory and Techniques, IEEE Transactions on*, vol. 39, pp. 1205-1215, 1991.
- [3] F. Williams, "Characterization of thin-film calibration elements," in *ARFTG Microwave Measurements Conference-Fall, 38th*, vol. 20, 1991, pp. 25-35.
- [4] E. M. Godshalk, "Surface wave phenomenon in wafer probing environments," in *ARFTG Microwave Measurements Conference-Fall, 40th*, 1992, pp. 10-19.
- [5] A. Lord, "Comparing the accuracy and repeatability of on-wafer calibration techniques to 110GHz," available online: [http://www.home.agilent.com/upload/cmc\\_upload/All/AR132.pdf](http://www.home.agilent.com/upload/cmc_upload/All/AR132.pdf).
- [6] A. Rumiantsev, R. Doerner, and S. Thies, "Calibration standards verification procedure using the calibration comparison technique," in *36th European Microwave Conference*, 2006, pp. 489-491.
- [7] R. B. Marks and D. F. Williams, "Characteristic impedance determination using propagation constant measurement," *IEEE Microwave and Guided Wave Letters*, vol. 1, pp. 141-143, June 1991.
- [8] D. F. Williams, R. B. Marks, and A. Davidson, "Comparison of on-wafer calibrations," in *ARFTG Microwave Measurements Conference-Fall, 38th*, vol. 20, 1991, pp. 68-81.
- [9] R. Doerner and A. Rumiantsev, "Verification of the wafer-level LRM+ calibration technique for GaAs applications up to 110 GHz," in *ARFTG Microwave Measurements Conference-Spring, 65th*, 2005, pp. 15-19.
- [10] D. F. Williams and R. B. Marks, "Transmission line capacitance measurement," *Microwave and Guided Wave Letters, IEEE*, vol. 1, pp. 243-245, 1991.
- [11] A. Rumiantsev and N. Ridler, "VNA calibration," *Microwave Magazine, IEEE*, vol. 9, pp. 86-99, 2008.

# Software Solutions for Linear and Non-Linear Microwave Measurements and Calibrations

Andrea Ferrero, Valeria Teppati, Marco Garelli, Serena Bonino, Umberto Pisani

**Abstract**—In modern microwaves systems, software plays a fundamental role for the organization and handling of different types of measurements and its impact is often underestimated.

This paper presents some criteria and software technologies that proved to be very effective for the development of multipoint/load-pull measurement systems.

## I. INTRODUCTION

It is well known that as the frequency increases the difficulties in performing accurate measurements raise up. The hardware set-up becomes more and more complex and great care in performing the system calibration is needed.

Moreover, some measurement require interacting with multiple instruments, which is particularly error-prone if proper software automation is not used. For instance, load-pull measurements require to record a significant set of DUT performances, at the fundamental and harmonic frequencies, while tuning the load and measuring/setting different bias conditions.

There is a number of commercial and freely available microwave measurement softwares [1]–[4], but generally they are tailored to a specific application (only load-pull or scattering measurements) or restricted to a particular brand of instruments. Difficulties therefore may arise for laboratories needing to use their instrumentation in new set-ups or for those that need to share the same instruments between two specialized benches.

However, most of the set-ups used in the microwave field share a common point, i.e. the need for an accurate calibration in order to remove the effects of non-idealities in the system. This fact leads to the widespread use of Vector Network Analyzers in small signal and large signal measuring systems.

This paper's aim is to present effective software solutions for such measurement problems, and to detail some peculiarities that led to the results presented in recent papers [5]–[7].

## II. SOFTWARE REQUIREMENTS AND ARCHITECTURE

A general microwave measurement software should fulfill to the following requirements:

- 1) easy graphical user interface (GUI)
- 2) large hardware support and hardware interchangeability
- 3) test-set flexibility, e.g. performing multiple tasks with the same hardware configuration
- 4) transparency to the user, e.g. the user should perform a scattering parameter measurement in the same way,

The authors are with Politecnico di Torino, Department of Electronics, Torino, Italy.

independently from the Vector Network Analyzer model and brand.

These requirements can be fulfilled with a layered software architecture, as Fig. 1 shows.

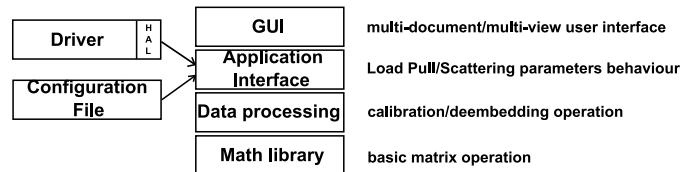


Fig. 1. Proposed software layers.

Graphical languages implement very well the driver and hardware interface, as well as the graphical user interface, but are typically unsuitable for the core processing layer. The C++ programming language is recommended, since it provides an extensive object-oriented framework with a high degree of abstraction, while maintaining high performance.

The application must contain a well structured mathematical library, with complex numbers and matrix operations. This layer also implements Fast Fourier Transforms and chirp-z transform for time-domain computations.

The core layer is the data processing one, where the calibration and deembedding procedures are implemented. It must be able to handle the various error models associated with the hardware and the respective calibration schemes.

The main programming effort is spent in the application interface layer, which is the abstraction layer that models the hardware test-set in software. On the user side, it provides different interfaces for the different measurement tasks, for example, the scattering parameter interface. It should be designed to be easily expanded with new interfaces, thus reducing the programming time when adding a new software capability.

The application layer should provide very high flexibility in modeling the test-set. A text configuration file can be used to define the test-set structure and instrument drivers. On the hardware side, the layer must provide an extensible hardware support, implemented as an Hardware Abstraction Layer (HAL in Fig. 1), as Fig. 2 shows. The different in-

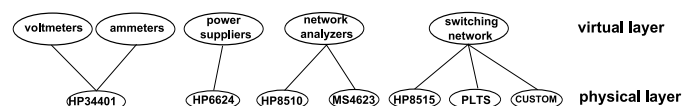


Fig. 2. Proposed hardware layer implementation.

struments are grouped by capabilities. Voltmeters, ammeters,

network analyzers become software classes of instruments that share a common set of capabilities, independently on the manufacturer.

The use of software interfaces enables to transparently use a multifunction instrument (e.g. a programmable power supply with current and voltage meters) as different single-function ones. This approach has recently been codified by IVI foundation and will be adopted in most modern instruments for the future [8].

The top layer is the Graphical User Interface, which is implemented as a single application, with multi-document and multi-view capabilities.

### A. System Calibration

Depending on the application, the system calibration may vary. Traditionally, the calibration problem has been solved with respect to a specific error model, like two-port non-leaky model (8 error coefficients: 7 plus one power term, or the ten-terms scattering parameter error model) or two-port leaky model (15+1 error terms). Multiport (leaky, non-leaky, partially leaky) error models were treated apart.

Actually, the calibration problem can always solved in the same way: first a scattering parameter calibration is performed, then a (optional) power and time-reference calibration is made. The application layer should be able to formulate the problem depending on the user-selected error model (specified for example in the configuration file), and to give a consistent sequence of calibration standards to be measured. Some techniques have already been found [6], [7], [9], [10].

A user-friendly graphical interface should allow the user to define a calibration scheme, from which a consistent standard sequence is computed (Fig. 3).

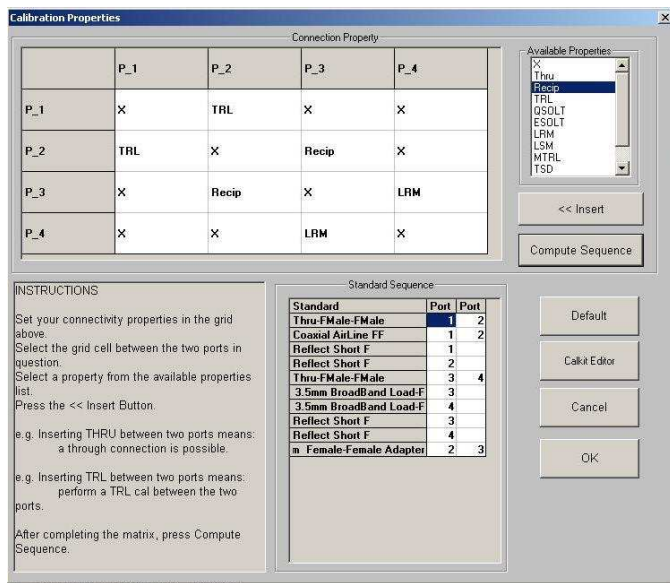


Fig. 3. Example of a scattering parameter calibration dialog.

### B. Multi-Document and Multi-View GUI

Due to the multitude of measurement types and visualization options, the software should be organized as a multi-document

and multi-view application. Each document represents a particular measurement task: a scattering parameter measurement is associated with one document, and a load-pull session is held by another document (Fig. 4). Depending on which document

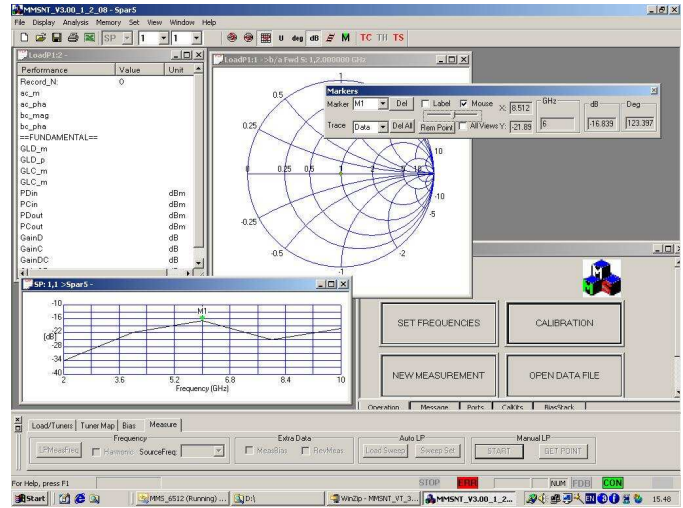


Fig. 4. Example of multi-document GUI. A scattering and a load-pull document are opened

is selected, the behavior of the main application menus and toolbars changes and the respective measurement is triggered and updated by the corresponding window.

A document can be split in multiple views, e.g. enabling the visualization of different parameters or graphs in multiple windows. For example, the scattering parameter  $S_{11}$  can be visualized in two views, one showing the frequency response, the other displaying the time domain reflectometry computed from the frequency response. This is particularly useful in load-pull measurements, where the user needs to have both a numerical output of the parameters of interest and a Smith chart showing in real-time the load reflection coefficient.

Each view should be configurable, i.e. the user can select the graph type, scales and so on. Moreover, it is mandatory to have a marker capability, either associated with each view or globally operating on all views of the same document. An example is given in Fig. 5. The load-pull document is split in four views:

- the Smith chart view, representing the measured differential load reflection coefficient points;
- the parameter view lists the measured performances;
- the time domain view shows the various waveforms for the different power levels associated with the marker-selected load reflection coefficient;
- the sweep view is configured to plot the  $P_{in}/P_{out}$  graph for the selected load reflection coefficient.

Finally, this approach is similar to the one used in simulator environments but requires more sophisticated error handling and hardware checking capabilities.

### C. Automation Interface and scripting

A modern software has to provide an extensive collection of automation interface methods, that enable the control from external environments like Matlab or LabView.

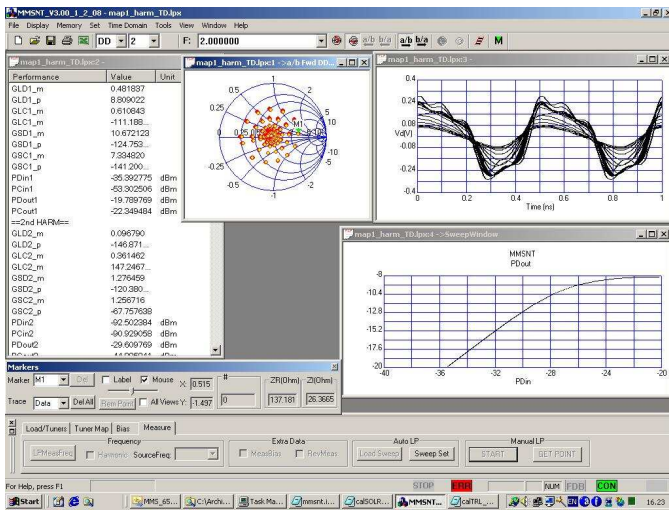


Fig. 5. Example of multi-view GUI showing a differential load-pull measurement.

An interesting aspect is the support for macro scripting, where the user can customize in detail a measurement by writing a script in Visual Basic from within the main program. This is intended for those who need a high degree of customization while avoiding the use of external programming environment, since one can use the built-in GPIB or RS232 primitives to communicate with specific instrumentation. This tends to be fundamental in production environments, where long custom scripts are used to test a specific product.

Fig. 6 shows a macro window example, the Visual Basic script is used to measure the harmonic magnitude and phase of a comb generator with a Microwave Transition Analyzer.

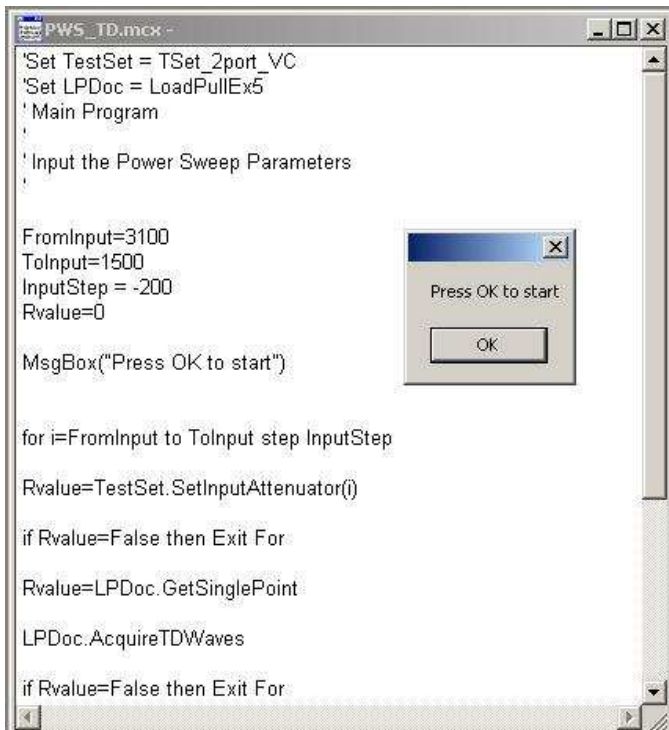


Fig. 6. Example of macro document.

### III. CONCLUSIONS

The paper has presented a set of software solutions tailored for microwave measurements. A well defined software architecture is the key point for a reliable measurement program. Methods used in modern graphical user interface programming were also found to be very effective.

### ACKNOWLEDGMENT

The authors would like to thank Alessandra Neri for her help during part of the design and debugging work.

### REFERENCES

- [1] *Automated Tuner System Software*, Maury Microwave, 2008.
- [2] *Product Catalogue*, Focus Microwaves, 2008.
- [3] *WinCal XE Software*, Cascade Microtech, 2008.
- [4] *Multical User Manual*, National Institute of Standards and Technology, 1995.
- [5] A. Ferrero and V. Teppati, "A novel active differential/common-mode load for true mixed-mode load-pull systems," in *IEEE MTT-S International Microwave Symposium Digest*, San Francisco, CA, Jun. 2006, pp. 1456–1459.
- [6] A. Ferrero, V. Teppati, M. Garelli, and A. Neri, "A novel calibration algorithm for a special class of multiport vector network analyzers," *IEEE Trans. Microw. Theory Tech.*, vol. 56, no. 3, pp. 693–699, Mar. 2008.
- [7] T. G. Ruttan, B. Grossman, A. Ferrero, V. Teppati, and J. Martens, "Multiport VNA measurement," *IEEE Microw. Mag.*, vol. 9, no. 3, pp. 56–69, Jun. 2008.
- [8] *Getting Started Guide*, IVI Foundation, 2008.
- [9] H. J. Eul and B. Schiek, "A generalized theory and new calibration procedures for network analyzer self-calibration," *IEEE Trans. Microw. Theory Tech.*, vol. 39, no. 4, pp. 724–731, Apr. 1991.
- [10] A. Ferrero, F. Sampietro, and U. Pisani, "Multiport vector network analyzer calibration: a general formulation," *IEEE Trans. Microw. Theory Tech.*, vol. MTT-42, no. 12, pp. 2455–2461, Dec. 1994.